Universidad de Alcalá
Escuela Politécnica
Departamento de Electrónica

PhD Thesis

CONTROL CONTRIBUTIONS TO THE UNIVERSAL OPERATION OF WIND TURBINES

Mario Rizo Morente

Supervisors: Dr. Emilio Bueno Peña
Dr. Marco Liserre
Prof. Francisco Javier Rodríguez Sánchez.

2013

Universidad de Alcalá

DEPARTAMENTO DE ELECTRÓNICA
Edificio Politécnico
Campus Universitario s/n
28805 Alcalá de Henares (Madrid)
Teléfono: 91 885 65 40
Fax: 91 885 65 91
eldep@depeca.uah.es

Dr. Emilio José Bueno Peña, Profesor Titular de la Universidad de Alcalá, y
Dr. Francisco Javier Rodríguez Sánchez, Profesor Catedrático de la Universidad Alcalá,

INFORMAN: Que la Tesis Doctoral titulada "**Control Contributions to the Universal Operation of Wind Turbines"** presentada por D. Mario Rizo Morente, y realizada bajo la dirección de los doctores D. Emilio José Bueno Peña, D. Marco Liserre y D. Francisco Javier Rodríguez Sánchez,, dentro del campo de la aplicación de los VSCs como interfaces entre la red eléctrica y sistemas de generación de energía eléctrica, reúne los méritos de calidad y originalidad para optar al Grado de Doctor.

Alcalá de Henares, 09 de Septiembre de 2013

Fdo. Emilio José Bueno Peña

Fdo. Francisco Javier Rodríguez Sánchez

Universidad de Alcalá

DEPARTAMENTO DE ELECTRÓNICA
Edificio Politécnico
Campus Universitario s/n
28805 Alcalá de Henares (Madrid)
Teléfono: 91 885 65 40
Fax: 91 885 65 91
eldep@depeca.uah.es

Dr. Marco Liserre, Profesor asociado del Politecnico di Bari.

INFORMA: Que la Tesis Doctoral titulada "**Control Contributions to the Universal Operation of Wind Turbines"** presentada por D. Mario Rizo Morente, y realizada bajo la dirección de los doctores D. Emilio José Bueno Peña, D. Marco Liserre y D. Francisco Javier Rodríguez Sánchez, dentro del campo de la aplicación de los VSCs como interfaces entre la red eléctrica y sistemas de generación de energía eléctrica, reúne los méritos de calidad y originalidad para optar al Grado de Doctor.

Bari, 06 de Septiembre de 2013

Fdo. Marco Liserre

Universidad de Alcalá

DEPARTAMENTO DE ELECTRÓNICA
Edificio Politécnico
Campus Universitario s/n
28805 Alcalá de Henares (Madrid)
Teléfono: 91 885 65 40
Fax: 91 885 65 91
eldep@depeca.uah.es

Dr. Sira Elena Palazuelos Cagigas, Director del Departamento de Electrónica de la Universidad de Alcalá,

INFORMA: Que la Tesis Doctoral titulada "**Control Contributions to the Universal Operation of Wind Turbines"** presentada por D. Mario Rizo Morente, y dirigida por los doctores D. Emilio José Bueno Peña, D. Marco Liserre y D. Francisco Javier Rodríguez Sánchez, cumple con todos los requisitos científicos y metodológicos, para ser defendida ante un Tribunal, según lo indicado por la Comisión Académica del Programa de Doctorado.

Alcalá de Henares, 03 de Septiembre de 2013

Fdo. Sira Elena Palazuelos Cagigas

ABSTRACT

The continuously growth of the energy consumption is taking the current electric system close to certain limits where the power supply reliability is seriously affected by voltage interruptions. Besides, some factors like the downturn in the economy and the drive of developing countries (i.e. China and India) have forced the companies to extend their products to weaker power systems, where the power quality has not been treated with a strong regulation yet.

This Thesis is framed in the improvement of the power supply reliability through the isolated operation of Wind Turbines. The concept of Universal Operation addresses the island operation of Wind Turbines when the connection to the grid is not longer required after a voltage interruption. In constrast with other tendencies, the peculiarity resides on avoiding the use of expensive external storage devices. This concept is just proposed in the low and medium power level scenarios of on-shore Wind Turbine to face power interruptions of minutes.

With the general objective of extending the island operation to cover the most of the interruption, this work approaches the main challenges of the Universal Operation from the control point of view: regulation of the island power mismatch by means of the inherent storage and dissipation capacities, transition between the island and grid-connected modes, power sharing, etc. On the other hand, an important research line of this Thesis is focused on the optimization of the system response under unbalanced conditions. The proposed control enhancements deal with the oscillating power and the distortion of control references caused by unbalanced conditions.

RESUMEN

Ante la creciente dependencia energética de los países de la Unión Europea y los informes de contaminación atmosférica, la generación distribuida mediante energías renovables está modificando el sistema eléctrico actualmente basado en el paradigma centralizado. Dentro de las energías renovables con mayor impacto actual se encuentra la energía eólica.

Un aspecto importante a mejorar en el marco de la calidad de potencia por parte del operador de la red de transmisión, es la continuidad del suministro. En estas circunstancias se define el concepto de microgrid como un sistema compuesto de al menos una fuente de generación distribuida asociada a cargas locales que pueden intencionalmente desconectarse del sistema de distribución con el objetivo de mejorar la fiabilidad del suministro. Este trabajo introduce la Operación Universal de aerogeneradores, donde éstos pueden trabajar conectados a red eléctrica y desconectarse de ella cuando ocurre un hueco o interrupción del suministro operando en modo isla. Es una aplicación específica del concepto de microgrid a aerogeneradores que evita el uso de sistemas de almacenamiento empleando únicamente las capacidades de almacenamiento y disipación intrínsecas de los aerogeneradores y se centra en contrarrestar interrupciones del suministro eléctrico del orden de unidades de minutos.

Este trabajo se centra en abordar la problemática asociada a la Operación Universal de aerogeneradores desde el punto de vista del control de los convertidores de potencia: regulación del balance energético, compartición de la carga y control de la tensión local en modo isla y transiciones suaves entre modos de operación. Además, el sistema debe seguir manteniendo un rendimiento óptimo en modo conectado a red respetando los códigos de red: respuesta en potencia, calidad de potencia y respuesta ante perturbaciones.

AGRADECIEMIENTOS

El resultado de estos cuatro años se debe en gran parte al apoyo y ayuda de todas las personas que se encuentran a mí alrededor. Estas líneas son solo una pequeña muestra de mi gratitud hacia ellos. Aunque suene a tópico, el final se ha hecho agotador y espero no olvidarme de nadie, si es así, gracias a tí también.

En primer lugar, quisiera mostrar mi más sentido agradecimiento a mi director principal, el Dr. Emilio José Bueno Peña, gracias por darme brindarme esta oportunidad, por haberme guiado y aconsejado, por apostar por mi, y sobretodo, por hacerme descubrir algo con lo que realmente disfruto.

El segundo lugar está reservado para el Dr. Marco Liserre. Sin duda alguna, él tiene gran parte de culpa del rumbo que ha tomado esta tesis. Muchas gracias por orientar mi trabajo durante mi estancia en Bari, los viajes a Aalborg ó a través de la infinidad de mails intercambiados a lo largo de estos tres años.

He de agradecer también la labor realizada por el Dr. Francisco Javier Rodríguez Sánchez, en general para con el grupo GEISER y en particular, por sus consejos y orientación.

Sin duda, dentro de mis compañeros de laboratorio, Carlos Girón Casares merece también una mención especial. Gracias por concederme tu ayuda desinteresada y porque tu trabajo nos ha facilitado la tarea a los que veníamos por detrás. ¡Ánimo! que eres el siguiente. No me puedo olvidar tampoco de todos aquellos con los que he compartido esta experiencia: Paco, Ana, Iván, Santi, Dani, Miguel, Inés, Jorge, Manu, Javi, Vane, Christina, Bernechea, Laura y Arantxa.

También debo recordar a la gente que he conocido durante las estancias y que me han acogido de una manera inigualable (aunque no creo que nunca vayan a leer esto). Muchas gracias Paola Falcone, nunca podré devolverte todo lo que hiciste por mí. Sin tí, Bari no hubiera sido lo mismo. A vostros también: Mimmo, Antonella, Stefanno y Rosa (Bari), Anping, Sebastián y Victor (Toronto).

Lógicamente, la labor de desconectar (muy importante) viene a cargo de los "colegas", siempre dispuestos a hacerte pasar un buen rato con deporte y salidas nocturnas. Borja, Carlos (ánimo que te va quedando poco), Palop, Dani, David, Borja, Enrique, Murci, Diego, Samper, don Pablo, Navarro, Castro, Libia, Cris, Karol, Martis, Worren, Zama, Francho, Angel y Alber. Alba, gracias.

Dejo para el final a los más importantes: mi familia. Muchísimas gracias a mis padres que me han ayudado tantísimo durante estos 26 años. Sin vuestro cariño, apoyo y trabajo, esto no hubiera sido posible. Gracias a mi hermano, Jose, que siempre ha ido abriéndome el camino.

GLOSSARY

Notation

Vector variables are expressed in stationary reference frames (αβ-frames) by default. On contrary, the superscripts dq or abc are used to denote that the vector is expressed in synchronous reference frames or three-phase frames, respectively.

Acronyms

CCVSC	Current Controlled Voltage Source Converter.
CL	Circular Limit Method.
DG	Distributed generation.
DPM	Dynamic Phasor Model.
DS	Distributed Storage.
DVR	Dynamic Voltage Restorer.
EEA	European Environment Agency.
EU	European Union.
FFT	Fast Fourier Transform.
GDP	Gross Domestic Product.
GHG	Greenhouse gas.
GM	Gain Margin.
GS	Grid side.
IG	Induction Generator.
IIR	Infinite Impulse Response.
JPDF	Joint Probability Density Function.
LIFO	Last Input First Output buffer.
LVRT	Low Voltage Ride-Through.
MPPT	Maximum Power Point Tracking.
MA	Maximum Area Saturation technique.
MS	Machine side.
NPC	Neutral Point Clampled.
OPC	Oscillating Power Control.
PCC	Point of Common Coupling.
PD	Proportional + Derivative Controller.
PDF	Probability Density Function.
PI	Proportional + Integral Controller.
PLL	Phase-locked loop.
PM	Phase Margin.

PMSG Permanent Magnet Synchronous Generator.
PR Proportional + Resonant Controller.
PS Proportional Saturation technique.
PWM Pulse-width modulation.e
SL Single loop.
SOGI-QSG Second Order Generalized Integrators-Quadrature Signal Generator.
SRF Stationary Reference Frames.
TA Trajectory Analyzer.
THD Total Harmonic Distortion.
UPS Uninterruptible Power Supply.
USD United States Dollar.
UWT Universal Wind Turbine.
VCO Voltage-Controlled Oscillator.
VCVSC Voltage Controlled Voltage Source Converter.
VQSG Virtual Quadrature Signal Generator.
VSC Voltage Source Converter.
WT Wind Turbine.
ZOH Zero Order Hold.

INDEX

Chapter 1.

Introduction

1.1. Framework.

The world economical progress and the energy market are two concepts intimately linked. The worldwide economy is mainly running on fossil fuels. In such conditions, the European Union (EU) analyzes its critical energy dependence in its green and white papers [Whi, 1997] [Gre, 2006]. More than half (54.1 %) of the EU-27's gross inland energy consumption in 2010 came from imported sources [Estat, 2009], which supposes a 35% increment in the last three decades. If the forecasts are correct, the imported resources will raise up to 66 % before 2020. The tendency of world oil prices and the oligopolistic nature of the market evidence an unsustainable situation for the EU.

This very bleak picture of the future is even worse if environmental issues are considered. Energy related emissions account for almost 80% of the EU's total greenhouse gas (GHG) emissions. The agreement undersigned in the Kyoto protocol [Kyo, 1998] established a set of minimal objectives for reducing CO_2 emissions and reduce the global energy consumption. Europe's Kyoto commitment for 2020 consists in a 20 % reduction of GHG emissions.

1.1.1. Renewable energy.

During the past decade, the EU has emerged as the world's leading region in developing and implementing renewable energy technologies. About one third of the estimated global investment of 150 billion USD in energy efficiency and renewable energy was in the EU in 2007. As a consequence, the European Environment Agency (EEA) have recently determined that emissions from the EU-27's have fallen 18 % since the 1990 baseline year, including 2.5

percent in 2011 when compared to 2010 [Eea, 2012]. However, big efforts are still required in order not to fail in its energy ambitions. The Commission proposes a new energy strategy towards 2020 [Ene, 2012].

- A 20% enhancement of the energy efficiency.
- A 20% of renewable energies contribution in the primary energy generation.
- A 20% reduction of the GHG emissions.

This strategy should help to create market conditions which stimulate higher energy savings and more low carbon investments, to exploit a wide range of centralized and distributed renewable energy.

Within the Spanish national framework, the renewable energy generation has been grown more than 500 % in the last decade. In 2011, it covered almost a third (32.4%) of the total electric demand. The wind power generation supposed the 16 % of the total electric demand, experiencing an expansion of 500 % of the installed power in the last decade. In 2010, the electric generation of renewable energies has avoided the import of oil barrels with a total cost of the 0.22% of the gross domestic product (GDP). As a consequence, in the last five years, the CO_2 emissions related to electric generation was reduced a 42%.

The Spanish energy policies closely follow the European guidelines. The national strategies are collected in [Per, 2011] for the period 2011-2020. The global objective is mainly focused on covering a 20.8% of the primary energy generation with the participation of renewable energies, in contrast with the current 11.3%. It will suppose a 38.1% of the total electric demand and a saving cost of € 1.700 M of fossil fuel imports per year.

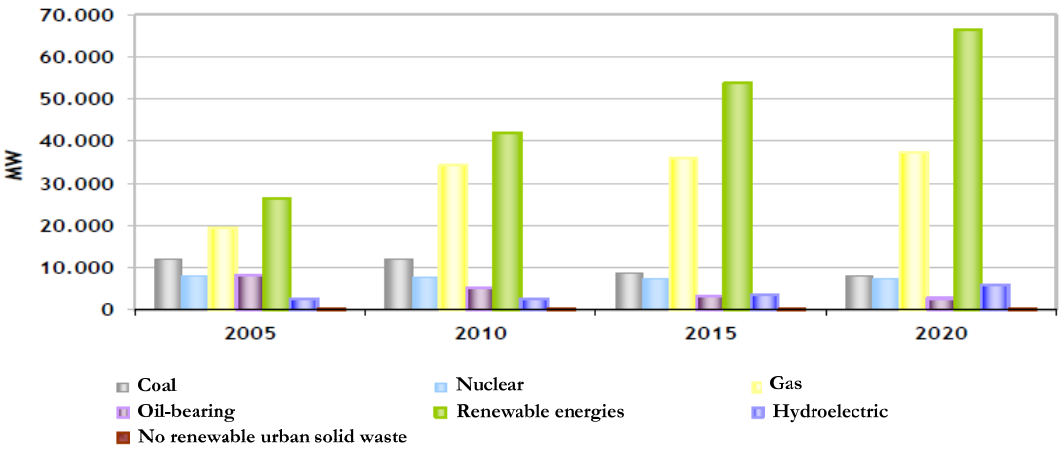

Fig. 1.1: Evolution of the installed electric capacity in Spain. *Source: MITyC/ IDEA.*

1.1.2. Distributed power generation.

The great part of the structure of the current electric system is based on the centralized paradigm. The electricity generation points are highly concentrated and integrated far from the consumption points. The centralized scheme was the result of: 1) economies of scale where the marginal cost of electricity production was reduced with higher ratings of steam turbines, 2) innovation in electricity transmission reducing the losses 3) environmental constraints such as the distance between generation units and the cities, among others.

However, the centralized philosophy has become antiquated and currently presents clear disadvantages: 1) the distances covered by the transmission and distribution networks still lead to remarkable transport and transformation losses, 2) the continuously increasing electricity demand makes necessary a notorious investment on the transmission and distribution networks in the following twenty years, 3) in the 1960s the marginal cost started to increase with the sizing of centralized sourced, 4) the rural electrification supposes connecting remote areas with small consumptions, quite inefficient from the economical point of view, etc.

Although the distributed generation (DG) has historically been used to complement centralized generation, the causes of the recent explosion resides on the liberalization of the electricity markets and the concerns over the GHG emissions [Iea, 2002]. The voltage source converter (VSC) has become the most widespread interface unit within the electric DG. Within the DG, the microgrids play an important role in the enhancement of the power system reliability. The term microgrid accepts many definitions. In [Lasseter, 2002], it is defined as "*a cluster of loads and microsources operating as a single controllable system that provides both power and heat to its local area"*. A more modern and accurate definition is given in [Kroposki, *et al.,* 2008]: *"systems that have at least one distributed energy resource and associated loads and can form intentional islands in the electrical distribution systems with a variety of benefits including improved reliability"*.

As indicated in Fig. 1.2, a classic microgrid mainly consists of DG units, loads, distributed storage (DS) systems and switches. The control of the microgrid is a centralized architecture with communication links. It usually operates grid-tied until a fault occurs. In that instant, the low voltage ride-through (LVRT) requirements should be initially fulfilled and after that, the switch is opened and the microgrid becomes an island. The principal function of the DS system is to regulate/absorb the power mismatch between the generation and the consumption during the island operation. However, this feature is limited to the storage capacity and incrementing it is not always physically feasible or economically assumable. Due to the constraints that it supposes, the total aggregated power of a microgrid hardly ever exceeds 100 kW. A global problem like the high penetration of DG is analyzed from a local point of view by means of the microgrid concept in [Piagi, *et al.,* 2006].

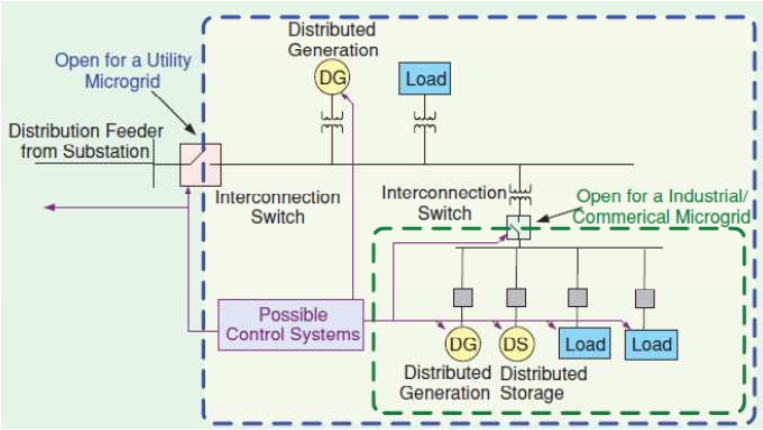

Fig. 1.2: Microgrids and components. *Source: [Kroposki, 2008].*

1.1.3. Power quality.

Power quality, "voltage quality", "current quality" and "service quality", among others, are usually referred as the measure, analysis and improvement of the bus voltage to maintain a sinusoidal waveforms at rated magnitude and frequency [Fuchs*, et al.,* 2008]. In general, the power quality phenomena: leads to the tripping of equipment and the interruption of production operation, endangers power system operation, inserts additional losses, etc. Electronic equipment and companies have become much more sensitive to voltage disturbances in the recent decades. The electric supply is more and more considered as a basic resource and an interruption can suppose a sensitive loss in the companies' profits. Besides, the tripping of the electronic equipment has been considered by the electric companies as one of the principal causes of poor power quality. On the other hand, the high increment of power electronics in consumer equipment and renewable energies has raised the harmonic content in the bus.

There are several criterions for classifying the power quality phenomena. The standard [IEEE-1159, 2009] uses the magnitude and duration of the phenomena while [Bollen, 2002] distinguishes between voltage and current variations and events. Interruptions, dips and swells are categorized as power quality events:

- An interruption occurs when the bus voltage is reduced below the 10%. Grid faults that trigger protections, broken conductors and operation interventions are the main causes of interruptions. It can be further categorized as function of the duration or what is equivalent, regarding the way of restoring it (automatic switching, manual switching or repair/replacement of the faulted component). According to [IEEE-1159, 2009]: a momentary interruption lasts between 0.5 cycles and 3 s, the duration of a temporary interruption is from 3s up to 1 min and a long-duration or sustained interruption lasts more than 1 min.

- A dip or sag supposes a reduction of the rms voltage from 90% up to 10%. Voltage dips are usually caused by the energization of heavy loads, the starting of large induction motors, line-to-ground faults and the load transferring form one power source to another. Long-duration dips are usually referred as undervoltage.

- A swell is defined as the increment of the voltage magnitude between 1.1 and 1.8 p.u. Long-duration swells are usually referred overvoltage.

Voltage unbalances and waveform distortion are included within the steady-state phenomena:

- The voltage unbalance is produced when the magnitudes of the three-phase voltages are not identical or the phase differences between them are different from 120 degrees. The voltage unbalance can be assessed by means of the computation of the zero and negative sequence components.

- The waveform distortion is referred as the deviation from a sinusoidal wave. Harmonic distortion is the most representative phenomena. It is based on the voltage and current contamination with frequency components that are integer multiples of the fundamental frequency. Industrial nonlinear loads and residential loads based on power electronic devices are frequent harmonic sources. Many detrimental effects are related with the presence of harmonics component in the utility.

The standardization and utility efforts have resulted in a good power supply in most developed countries. The consumer's perception is that the electric resource is always available and their position becomes more and more demanding. However, the continuously growth of the energy consumption is taking the current electric system to the limit [Iea, 2011]. In fact, according to [Iea, 2005], the most recently cases of blackouts are related with the power system design weaknesses, overexploitation and lack of redundancy. Besides, some factors like the downturn in the economy and the drive of developing countries (i.e. China and India) have forced the companies to extend their products to weaker power systems, where the power quality has not been addressed with a strong regulation yet. All these facts make clear the following two statements:

- The continuous power supply avoiding any kind of interruption or dip is still a trendy power quality issue.

- There is still a wide range of improvement regarding the power supply reliability.

The use of series and shunt VSC for improving the power quality issues is quite widespread. The power supply reliability can be increased with Voltage Controlled Voltage Source Converters (VCVSCs), like Dynamic voltage restorer (DVR) [Wessels, *et al.,* 2011], Uninterruptible Power Supply (UPS) systems [Guerrero, *et al.,* 2005] or grid-connected converters working in stand-alone mode [Balaguer, *et al.,* 2011]. The voltage stability and

harmonic distortion are also a matter of Current Controlled Voltage Source Converters (CCVSCs), such as Static Synchronous Compensators (STATCOMs) [Ortiz, *et al.,* 2008], active filters [Yuan, *et al.,* 2002] and any DG system connected to the main grid.

1.1.4. Ancillary services: voltage and frequency regulation.

In electric grid systems with a high penetration of DG units or with a certain degree of weakness, the demand of ancillary services becomes quite interesting. The grid codes require the grid-connected DG units to modify the active and reactive power injections with the purpose of increasing the regulation capacity of the system frequency and voltage.

Fig. 1.3 shows the frequency regulation demanded to WTs connected to the Distribution Network in Demark. Generally, the WT can inject the maximum available power in the frequency range indicated by the dead-band. If the frequency rises, as a consequence for example of high load shedding, the WT is forced to reduce the injected power. The power mismatch between available wind power and injected electric power can be initially solved with the kinetic storage and after with the pitch control. With the 50 % down-regulation, the WTs are also dotted with regulation capacity over lower frequencies. Fig. 1.4 depicts the voltage regulation curve demanded in the South African grid code by means of the injection of reactive power. These ancillary services where the active and reactive powers are modified in function of the frequency and voltage are intimately linked with the inverse droop. It is important to distinguish it with the direct droop employed as a power controller in grid-connected where the phase and magnitude of the voltage injected by the DG unit are configured with the aim of tracking the active and reactive power references (see subsection 2.1.2).

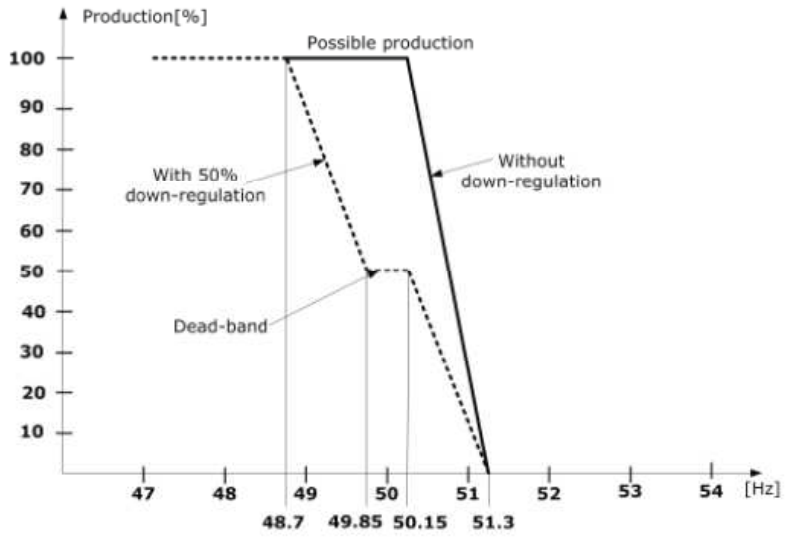

Fig. 1.3: Frequency regulation curve in Danish grid code [UNIFLEX-PM, 2006].

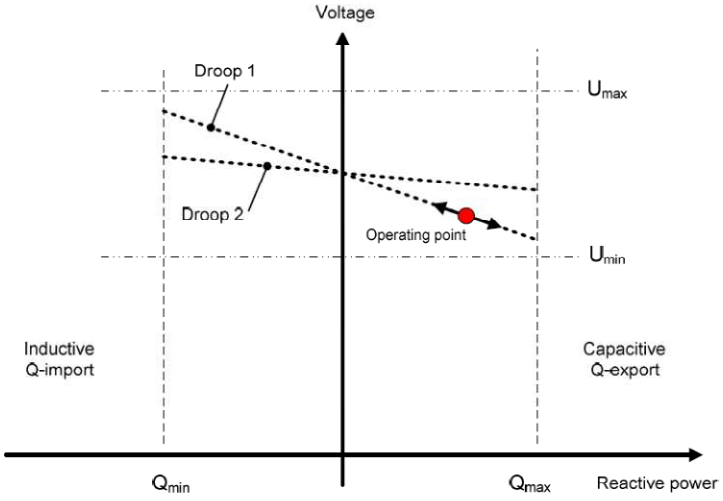

Fig. 1.4: Voltage regulation curve in South African grid code [GCSA, 2012]

1.2. Thesis development context.

In a general framework, this Thesis introduces the concept of Universal Operation. This term just proposes a revision of the microgrid philosophy. Given the necessity of further improving the power supply reliability, the Universal Operation's goal is providing a flexible and economically feasible adaptation of the existing low and medium power (up to 100kW) DG units working as grid-connected sources into potentially island-forming units. Once fault is cleared, the parallel sources are again connected to the grid. This procedure is already covered by the grid-interconnection standards [IEEE-1547.4, 2011]. The microgrid philosophy makes use of a complex and extensive system structure (diesel generators, storage systems and high combination of different DG units) to indefinitely extend the autonomous operation. In contrast, the target of the Universal Operation philosophy is keeping the power supply under interruptions in the range of minutes as an ancillary service to the local loads. Longer interruptions are less likely to occur.

To that concern, the Universal Operation philosophy implements a distributed control architecture following the minimization of communication links and enhancing the flexibility and scalability. In this Thesis, the Universal Operation is particularly applied to on-shore low and medium power WTs. The proposed concept perfectly matches with wind power due to the current high penetration. Besides, the inherent storage capacities of this technology offer the possibility of removing any expensive external storage system to balance the power consumption and generation, given the mentioned duration of the interruptions to be covered. The external storage doubtlessly increases the regulation of the power mismatch and the redundancy and thus, the continuous supply. However, the objective is to provide a direct and economical solution restricting the modification of the existing plants.

Therefore, the Universal Operation of WTs a priori represents several challenges. As global requisites, during the island operation, each isolated source should participate in the regulation

of the local voltage and the load should be efficiently shared between them. As particular requirement, in order to extend the island operation, each WT should delay the shut down condition by means of an optimum management of the balance between injected and generated powers. In the grid-connected mode, the requisites are well-known: a power control with good robust stability and efficient response to grid disturbances. Although the power supply reliability is the main power quality factor this work is focused on, it does not lose the insight of other issues like the harmonic distortion and unbalanced conditions. On the other hand, the control strategy of the isolated network should assure smooth transitions between island and grid-connected modes, avoiding any harmful situation that would lead to the activation of the protections.

To cover all these requirements, this Thesis proposes a list of hardware and control modifications applied to common WTs. A two level full-power converter WT with a permanent magnet synchronous generator (PMSG) is taken as the base model to set out the proposed modifications. The full-power converter is composed by an inverter or grid-side (GS) converter and a rectifier or machine-side (MS) converter. With the adequate regulation strategy, this hardware configuration offers a good response under voltage dips and other types of faults. In contrast with induction generators (IG), the PMSG provides a high power density and a reduced power factor. A common WT with the proposed hardware and control modifications results in the renamed universal wind turbine (UWT). Fig. 1.5 presents a first schematic overview of a potential island section composed by several UWTs connected in parallel with local loads and with the main grid through a local circuit breaker. Additional DG units with sources of other nature might be considered. Nevertheless, the aggregated power is limited by the overall ratio storage capacity – rated power. This ratio takes into account all the storages capacities (at least the kinetic storage of the UWTs) and the overall power rating. As long as additional DG units without inherent storage resources are added, the ratio is reduced and so does the capacity for dealing with instantaneous power mismatches. A lower threshold of this ratio establishes the limit where the Universal Operation is feasible. The hardware modifications are mainly focused on making feasible the island operation. They consist on a circuit breaker that isolates the complete system after the LVRT operation and a capacitor added to the L-filter to improve the voltage regulation of the island (if not present). The circuit breaker is autonomously regulated. Its management system monitors the PCC voltage, detects any islanding and fault condition and sends the PCC voltage and information about the state of operation (grid-connected, island o synchronizing) to the UWTs through a communication link. This is the only communication link considered in this work. The maximum latency of the communication should assure the right performance of the UWTs. In case the system is composed by just one UWT or in low power urban applications, where distances are quite reduced, the communication link is removed and the circuit breaker regulation is just implemented in the UWT.

The greatest part of the efforts made in this work is driven to the control area of the UWT. As shown in Fig. 1.5, the control is divided into the MS controller and the GS controller. The key point of the proposed control modification resides in a high versatility with a common structure to deal with all the requirements of each mode. The proposed strategy is briefly summarized in the following lines. The control is divided into stages from outer to inner controllers. The top level is on charge of the power balance. Fig. 1.6 presents a drawing with the power flow and the more representative elements that take part on it. In grid-connected, the UWT behaves as a grid-feeding system where the injected power is fixed by the maximum power point tracking (MPPT) algorithm of the MS controller. Then, the GS controller just injects the same amount of power (minus power losses) to get an energy balance. On contrary, the island operation is more challenging. The UWT should now behave as a grid-forming system, controlling the local voltage and frequency. However, in order to optimize the iteration with other parallel sources and avoid circulating currents, the voltage and frequency regulation is smoothened with some droop constants. The power transfer is fixed in the GS controller by the local loads. The MS controller should them readapt the power it injects into the DC-link to get the desired energy balance. However, it is difficult to have a perfect match between current generation and consumption. For that purpose, the control strategy takes advance of the kinetic storage of the rotor, the braking chopper and the pitch angle to deal with power mismatches. In case of more consumption than generation, this negative power mismatch is resolved with kinetic energy, decelerating the rotor. The rotor speeds up in the opposite case. The breaker chopper is also employed for dealing with positive power mismatch. The system can additionally make use of the pitch control to carry out a further regulation of the generated power, provided that the dynamics of its actuation does not allow acting over transients. It is then employed to enhance the steady-state response. If the kinetic storage upper or lower limits are reached, the system should trip out and the power supply disappears. In order to minimize the probability of this to happen, the power sharing strategy establishes that systems with more energies reserves should participate with more power. This logically adds an extra degree of regulation of the storage reserves without any direct communication between the involved parts.

This Thesis is mainly enclosed in the Italian public project entitled "*Universal small wind-turbines (grid-connected, stand-alone, micro-grid)".* This Thesis contributes in two of the seven key issues of the project:

- Development and implementation of the most proper control techniques to control the active and reactive power flow between MS and GS systems and to operate with different grid connection conditions and wind conditions; a power sharing algorithm will be included in the control system to manage the power exchange also in case on microgrid mode.

- Implementation of the algorithms on digital board based on embedded-on-chip systems.

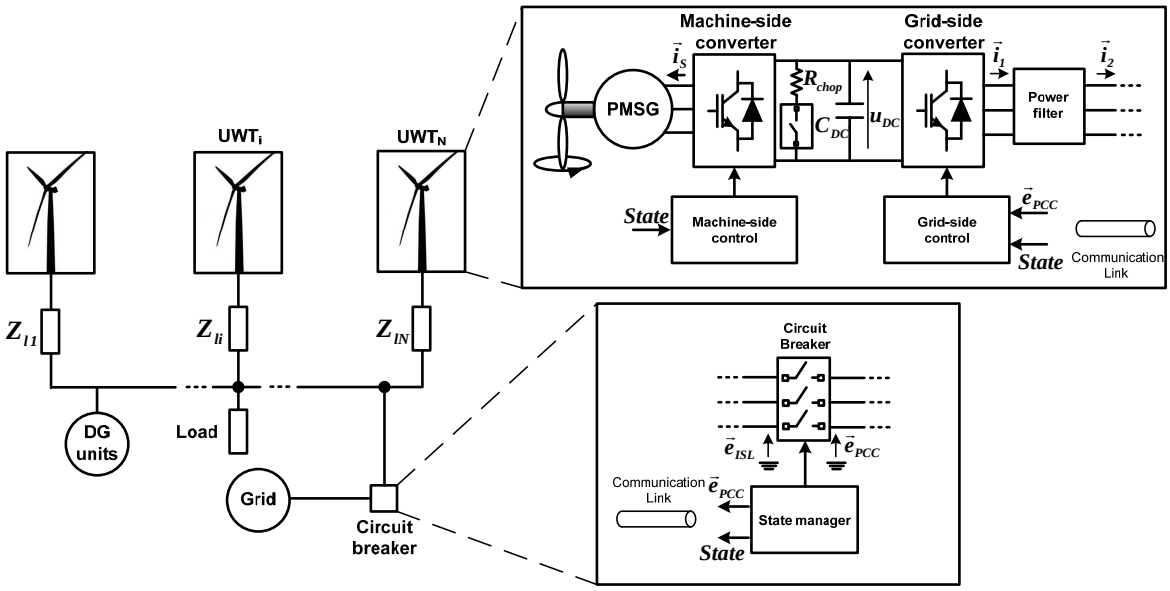

Fig. 1.5: Aggregation of several UWTs and the local circuit breaker with their respective schemes of control.

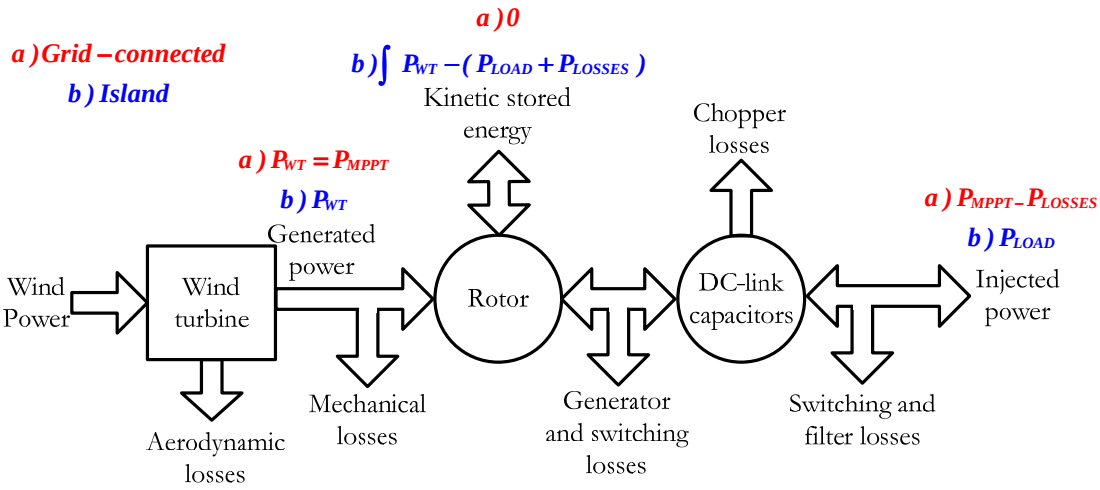

Fig. 1.6: Flowchart of the power transfer through the elements of a WT.

1.3. Related publications.

As a result of the work developed in this Thesis, several conference and journal publications have been carried out. They are collected in function of the topic they contribute as follows: Universal operation philosophy (1, 2 and 3), voltage and current control (4 and 5), synchronization (6, 7 and 8) and sensorless control of machine side converter under disturbances (9 and 10).

1. M. Rizo, M. Liserre, E. Bueno, F.J. Rodríguez and F. Huerta, *"Universal wind turbine working in grid-connected and island operating modes"*, Math.Comput.Simul., no. 0, 2012.

2. M. Rizo, E. Bueno, A. Dell'Aquila, M. Liserre and R.A. Mastromauro, *"Generalized controller for small wind turbines working grid-connected and stand-alone"*, 2011 International Conference on Clean Electrical Power (ICCEP), 2011.

3. M. Rizo, M. Liserre, E. Bueno, F.J. Rodríguez and C. Giron, *"Universal Operation of Wind Turbine Systems without Storage",* Submitted to IEEE Transactions on Sustainable Energy

4. M. Rizo, M. Liserre, E. Bueno, F.J. Rodríguez and C. Giron, *"Voltage Control Architectures for the Universal Operation of DPGS",* Submitted to IEEE Transactions on Power Electronics.

5. M.Rizo, M. Liserre, E. Bueno, A. Rodríguez and F.J. Rodríguez,*"Different Approaches of Distortion-Free Stationary Reference Frames Saturators"* To be submitted.

6. F.A.S. Neves, M.C. Cavalcanti, H.E.P. de Souza, F. Bradaschia, E.J. Bueno and M. Rizo, *"A generalized delayed signal cancellation method for detecting fundamental-frequency positive-sequence three-phase signals",* IEEE Transactions on Power Delivery, vol. 25, no. 3, 2010.

7. F.A.S. Neves, H.E.P. de Souza, F. Bradaschia, M.C. Cavalcanti, M. Rizo and F.J. Rodriguez, *"A space-vector discrete fourier transform for unbalanced and distorted three-phase signals",* IEEE Transactions on Industrial Electronics, vol. 57, no. 8, 2010.

8. M. Rizo, F. Huerta, E. Bueno and M. Liserre, *"A synchronization technique for microgrid reclosing after islanding operation",* IECON 2012 - 38th Annual Conference on IEEE Industrial Electronics Society, 2012.

9. M. Rizo, A. Rodriguez, E. Bueno and F.J. Rodriguez, *"Robustness analysis of wind turbines based on PMSG with sensorless vector control",* IECON 2010 - 36th Annual Conference on IEEE Industrial Electronics Society, 2010.

10. M. Rizo, A. Rodriguez, E. Bueno, F.J. Rodriguez and C. Giron, *"Low voltage ride-through of wind turbine based on interior permanent magnet synchronous generators sensorless vector controlled"*, 2010 IEEE Energy Conversion Congress and Exposition (ECCE), 2010.

1.4. Document structure.

The document of this Thesis is organized in five Chapters and the Appendix.

Chapter 2 contains the knowledge review of the power controller for grid-connected and island operations, the voltage controller of LCL and LC filters, the power sharing strategies and the regulation of unbalanced conditions. The last section of this chapter presents the objectives of the Thesis.

Chapter 3 introduces the proposed general control structure for both GS and MS converters and establishes the bandwidth of each loop. Besides, it covers the description of the power filter setup, the DC-link voltage controllers and the GS voltage control for the Universal Operation. Regarding the latter, an extensive comparison of several voltage control architectures attending the Universal Operation issues is carried out.

Chapter 4 presents the GS power controller. The GS power control is analyzed from the point of view of the control philosophy: current and voltage controlled. Accurate models are provided for tuning the regulator to meet the imposed requirements. Furthermore, a power sharing strategy is proposed with the aim of efficiently managing the total kinetic energy and extending the island operation until the recovery of the grid. Finally, a statistical study, which supplies accurate data regarding the real improvement over power supply reliability ratios when using the Universal Operation of WTs, is developed. It analyzes the probability of cover an interruption as function of the wind profile and load consumption and the reduction of the power supply interruption.

The contents of Chapter 5 are related to the treatment of unbalanced conditions. First of all, the relation between unbalanced and distorted control references is analyzed. Based on that study, the power control has dotted of a dual phase structure and an interesting novel saturator philosophy is proposed for avoiding the distortion of voltage and current references under unbalanced conditions. Besides, a power control block is implemented for controlling the oscillating power during unbalanced conditions by means of the injection of negative sequence voltage.

Chapter 6 collects the synchronization technique proposed for the Universal Operation. The key point of this strategy resides on the implementation of a virtual impedance in each unit that provides two beneficial features: it counteracts the voltage drop across the filter output impedance and it can be configured to again share the power as function of the kinetic storage.

Chapter 7 contains the experimental and simulation results that validate the theoretical approaches.

Finally, Chapter 8 summarizes the conclusions obtained from the development of the Thesis and presents the future works.

The Appendix introduces the inner control of the MS: a sensorless vector control of the PMSG.

Chapter 2.

Knowledge Review and Thesis Objectives

The work of this Thesis is mainly oriented to the research of control algorithms to make feasible the Universal Operation of WTs without extra storage systems. This chapter makes an extensive review of the most relevant previous works regarding the power control and power sharing of isolated and grid-connected systems, voltage control of LC and LCL filters and control performance under unbalanced conditions, etc. Then, the Thesis objectives are settled down following those research paths that still contains weak points not only for the Universal Operation but also for other issues in common with grid-connected DG systems.

2.1. Knowledge review.

2.1.1. Inner controllers: current and voltage controls.

Before getting deeper, it is important to first review the existing types of VSC control philosophies. The control philosophy of a converter is mainly given by the ac variable under control in the loop: current or voltage. In those cases where both voltage and current are regulated, the variable that defines the philosophy of control is the outer one. Attending to the above mentioned, it can be distinguished between VCVSCs and CCVSCs. The power supply reliability can be increased with VCVSCs, like DVR, UPS or grid-connected converters working in stand-alone mode within a microgrid, as UWTs. The voltage stability and harmonic distortion are a matter of CCVSCs, such as STATCOMs, active filters and any DG source connected to the main grid. Fig. 2.1 contains the CCVSC and VCVSC topologies along with their respective general controllers.

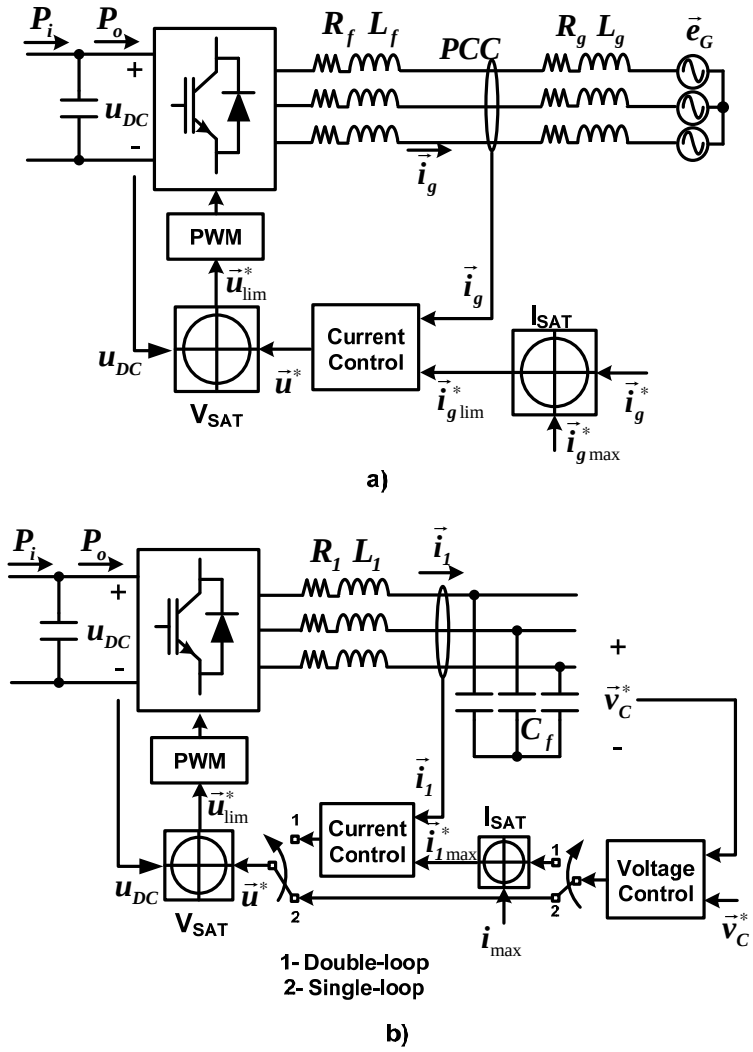

Fig. 2.1: a) Scheme of a general CCVSC with its respective inner control loop and b) VCVSC topology and general block diagram of capacitor voltage control.

In this subsection, previous works focused on the control of the voltage across the filter capacitor are reviewed. The voltage controller plays a great role in the universal controller. No matter the operation mode (grid-connected, island or synchronization) or the selected power control architecture, it is always the inner block and the basis for performing a good regulation. Several works have been published regarding the voltage control of LC and LCL filters. In the great majority of works, the employ of the LC filter is preferred due to its better voltage regulation and power factor. On the other hand, the LCL-filter supposes a good trade-off between the island and grid-connected operations. Actually, any LC can be viewed as a LCL if the feeder or the transformer impedances are taken into account. Fig. 2.2 depicts a diagram block of the control plant constituted by the LCL filter. As shown, in this case, the PCC voltage is considered as the disturbance of the control loop. The currents and the capacitor are sampled.

There are several ways to implement the voltage control. The most classic one consists on implementing it in the synchronous reference frames or dq-axis. By applying the

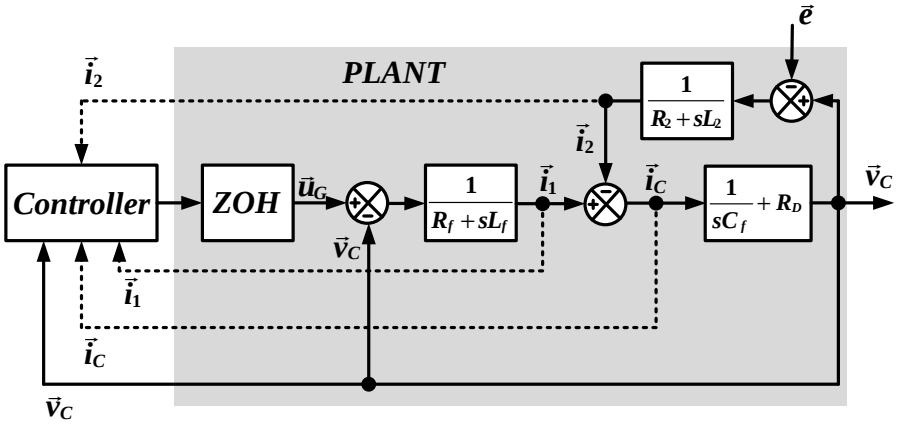

Fig. 2.2: Block diagram of the plant for the voltage control in the continuous-time domain.

transformation into this rotating axis, the ac variables become dc quantities. Then, they can be easily regulated through PI controllers. It is quite weird to use single-loop architectures in dq-axis under the inability of this option to cancel the cross-coupling terms. Therefore, the voltage control is additionally complemented with an inner current control of the converter current or the capacitor current as in [Balaguer, *et al.*, 2011], [Mehrizi-Sani, *et al.,* 2010] and [Kim, *et al.,* 2011]. One of the main advantages of the control in the dq-frames is the direct coupling with the active and reactive powers. Nevertheless, there are still many drawbacks associated to the control in dq-axis.

- The cross-coupling cancellation terms does not ideally decouple the dynamics between the d and q axis.

- The efficiency of the control is quite sensitive to the performance of the Phase-Locked Loop (PLL) of the synchronization system. Besides, the additional transformation into the dq-axis slightly increases the computational weight of the controller.

- The most crucial aspect resides in the simultaneous control of positive and negative sequences. The control of UWTs should provide optimum performance under unbalanced loads in island operation and unbalanced faults during grid-connected operation. The control of the negative sequences demands the definition of an additional dq-axis rotating in clockwise and the insertion of an additional PI controller working in that negative sequence frames. Besides, the synchronization system has to be equipped with a sequence detector and it not always provides a good decoupling between sequences and axis. Moreover, these sequence detectors are based on the generation of quadrature signals. Then, the settling time is limited by the time required in the sequence detection, close to a quarter of the fundamental period of the grid.

The previous statements make clear that the implementation of the voltage control over the dq-frames is very poor. The regulation of ac signals in the stationary reference frames or αβ-axis seems to solve the drawbacks described above. There are no cross-coupling terms, high dependence on PLL and the control of positive and negative sequences is done with just

one Proportional + Resonant (PR) controller without the need of defining extra virtual axis and using sequence detectors. PR controllers offer an infinite gain at the control frequency and provide zero error in steady-state. There are lots of possible configurations the voltage controller can attend to. They can be simply classified as: single-loop and double-loop. Fig. 2.3 contains both control architectures. The single-loop strategies contain just one feedback, the capacitor voltage. Double-loop control architectures additionally contain an internal feedback of the converter current or the capacitor current. In case of double-loop architectures, it has to be distinguished between inner and outer controllers. The outer controller, which regulates the capacitor voltage, consists on a PR controller while the inner controller can be implemented with a P or a PR. In [Loh, *et al.,* 2003], a voltage control based on a double-loop is analyzed from the point of view of the variable under control in the inner loop focused on UPS applications. The derivative behavior of the capacitor current can increase the bandwidth in contrast with the integral behavior of the converter current. A similar study is carried out in [Li, *et al.,* 2007] and [Li, 2009] for DVR applications. Besides, the single-loop architecture is also studied with the possibility of adding a feedforward of the voltage reference. Although the feedforward improves the settling time, the resonance damping of the filter becomes poorer. In fact, the addition of the inner current loop can further damp the filter resonance. The general closed-loop scheme proposed in [He, *et al.*, 2012] shows that a double-loop scheme is equivalent to a single-loop architecture with two virtual impedance terms in parallel. These terms are linked with the internal and external impedances. The former is configured attending to damping purposes while the latter can be employed for harmonic cancellation.

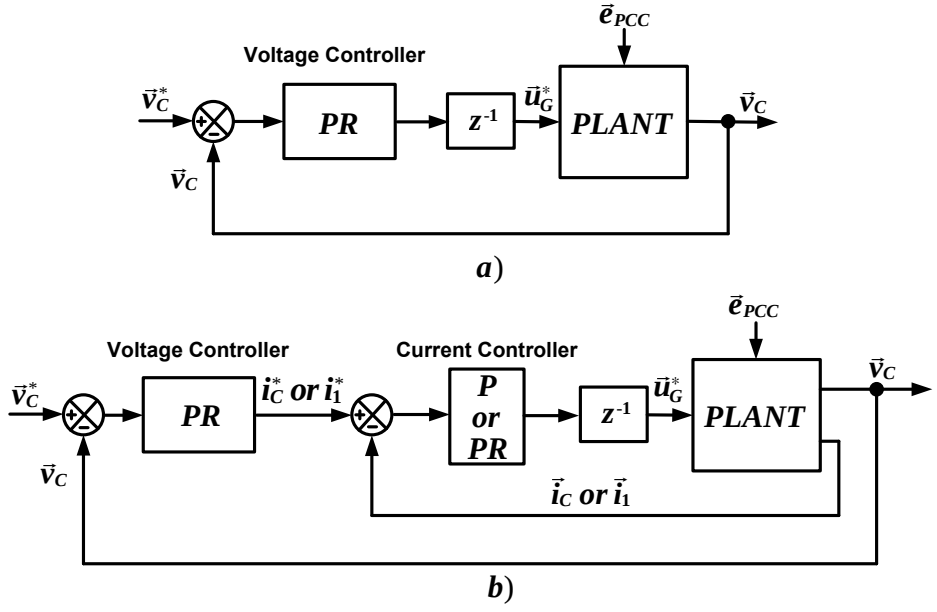

Fig. 2.3: Voltage control in the stationary reference frames: a) Single-loop architecture and b) double-loop architecture.

2.1.2. Power Control in grid-connected mode.

As illustrated in the previous subsection, it is clear that the system must adopt the control philosophy of VCVSCs during the island operation. However, the Universal Operation also contemplates the grid-connected operation after the resynchronization process when the grid fault is cleared. In the case of the grid-connected operation, the tendency is usually to follow a control in current source [Kazmierkowski, *et al.*, 1998]. An example where the control scheme leaves the VCVSC philosophy in island mode to adopt a CCVSC can be found in [Balaguer, *et al.*, 2011]. In [Yao, *et al.*, 2010], the voltage controller is kept and its reference is supplied by an outer current controller (which gives the current source identity) regulating the output current of an LC filter.

However, since the development of the droop control and the standardization of the reconnection of isolated DG areas [IEEE-1547.4, 2011], the VCVSC is also gaining importance in grid-connected applications [Katiraei, *et al.*, 2006], [Lasseter, 2002], [Li, *et al.*, 2004], [Li, *et al.*, 2009], [Hasanzadeh, *et al.*, 2010], [Mohamed, *et al.*, 2008], [Mastromauro, *et al.*, 2009] and [Vasquez, *et al.*, 2009a] under the premise of smooth operation mode transitions. For that purpose, the droop control is readapted by adding an integrator in the voltage magnitude-reactive droop in [Brabandere, 2006] and [Guerrero, *et al.*, 2009]. Works like [Guerrero, *et al.,* 2011] and [Vasquez, *et al.*, 2009b] are examples where the VCVSC regulation philosophy is used in both island and grid-connected mode.

Further discussion about the power controller focused on the management of unbalanced conditions is given in subsection 2.1.3.

2.1.3. Power Control in island mode.

Regarding the island operation, each DG unit should actively participate in the regulation of the local voltage and share the load power demands with the rest of parallel sources. If every parallel source adopts a grid-forming strategy (with fixed voltage magnitude and frequency references), the non ideal measurement of voltage and frequency leads to a control struggle between them. The use of frequency and voltage droops in the power control, as in the primary frequency control of synchronous generators, smoothes the connection and interaction of parallel sources. The concept of "plug & play" is satisfied with this control strategy improving the autonomy of each parallel source and the versatility of the isolated system. The traditional frequency and voltage droops are expressed by (2.1) and shown in Fig. 2.4. The droop curve is characterized by the droop constants, k_{Pf} and k_{QV}, and the base points, (P_G^*, ω^*) and (Q_G^*, V_C^*). These points belong to the droop curve independently the value of the slope.

$$\omega - \omega^* = k_{Pf}\left(P_G^* - P_G\right)$$
$$V_C - V_C{}^* = k_{QV}\left(Q_G^* - Q_G\right) \quad (2.1).$$

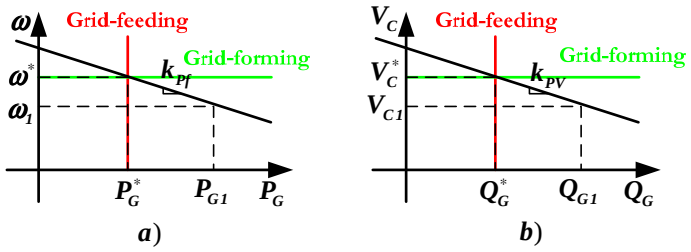

Fig. 2.4: a) Traditional active power-frequency droop and b) reactive power-voltage magnitude droop.

As shown in Fig. 2.4, the droop regulation is situated between a grid-feeding (no voltage regulation capacity) strategy and a grid-forming (no power coordination capacity between parallel sources) strategy. Actually, the requisite of regulating the local voltage during the island operation lies on the voltage controller, while the droop control is used to coordinate the different parallel sources within a higher regulation level. As a consequence of the power sharing, the regulation based on droop introduces steady-state voltage magnitude and frequency drifts, which logically affects the power quality

Two main options are reported in the bibliography for implementing the droop control. The conventional or direct droop is the most common alternative adopted by the majority of the works. It applies a voltage magnitude and frequency droops in function of the injected active and reactive power as shown in Fig. 2.4. On contrary, the second option, denominated inverse droop, fixes the active and reactive power references in function of the local voltage magnitude and frequency [Wijnbergen, *et al.*, 2005]. The inverse droop is generally used in CCVSC to add some grid-supporting capacity. With this topology and during the island operation, there is not capacity for regulating the voltage and frequency if the unit is the sole source or its rating power is high in contrast with the overall power of the parallel sources. In [Hauck, *et al.,* 2002], the inverse droop is also applied to VCVSC resulting in a more complex system.

The conventional droop control perfectly fits in the VSVSC control structure, where the voltage reference is calculated in function of the active and reactive powers. In [Brabandere, 2006] and [Zhang, *et al.,* 2010], a Dynamic Phasor Model is obtained for describing the dynamics of the non-linear plant. In [Guerrero, *et al.,* 2004], a small-signal analysis model is constructed around a bias-point. Both procedures are equivalent. Based on the model, [Guerrero, *et al.,* 2004] proposes the addition of derivative terms for improving the transient response of the droop control while the steady-state response is not affected.

However, there are other handicaps associated to the droop control. In large power systems, the transmission line is usually characterized as highly inductive. However, this fact cannot be affirmed in low-voltage application, leading to a coupling between the active and

reactive power. A quite complex solution was proposed by [Dai, *et al.*, 2008] based on a Newton-Raphson parameter estimation and feedforward control. In [Li, *et al.*, 2009], a virtual impedance term is implemented to modify the total output impedance and remove the coupling. In [Brabandere, *et al.,* 2007], a matrix that creates virtual decoupled versions of the active and reactive power is employed. The selection of the droop slopes is not only related to stability issues but should also take into account the trade-off between power quality and power sharing [Guerrero, *et al.*, 2004] [Guerrero, *et al.*, 2005] [Guerrero, *et al.*, 2009]. As long as the droop slopes are getting higher, the sensitivity for detecting voltage and frequency deviations is increasing, which improves the efficiently when sharing the local load between the parallel sources. However, the high voltage and frequency deviations logically affect the power quality supplied to the loads. Then, the droop coefficients should be configured in order to respect the maximum voltage magnitude and frequency drifts (5% and 2%, respectively). Finally, the last drawback of the conventional droop control is associated to the presence of nonlinear loads. The conventional droop is suitable for balancing the active and reactive power but not for sharing harmonic currents.

The island operation provides an extra way of improving the power supply ratios (reducing the number of interruptions and decreasing the average duration of them). The success highly depends on the ability of dealing with power mismatch between generation and consumption of each UWT. A bad regulation of the power mismatch can bring the shutting down condition very fast. On contrary, a good strategy delays the shutting down condition or even avoids it improving the power supply reliability. It is a challenging task and not always possible to be achieved under high mismatches between load consumption and available generation. The DC-link voltage and the rotor speed are the main internal factors the island regulation should be focused on.

In [Haque, *et al.,* 2010] and [Bhende, *et al.,* 2011], the increment of the regulation capacity over the power mismatch given by storage devices is emphasized. However, the possibility of equipping each existing WT with energy storage is not feasible due to the high investment it supposes [Chen, *et al.,* 2009]. As described in Chapter 1, the power that crosses the full power converter in the island mode should be adapted in accordance with the load consumption.

In [Mlodzikowski, *et al.,* 2011], the GS converter regulates the DC-link voltage through the voltage it injects to the loads so that the load consumption is wrongly modified. This *modus operandi* where the load voltage and power are modified as function of the DC-link voltage can cause serious damages to the loads. A correct procedure should just inject the power demanded by the loads. This is achieved by keeping the island voltage at its rated value, which permanently assures the supply of the demanded power. The island voltage regulation is then carried out by the GS converter. The MS converter controls the DC-link voltage and hence, balances the power flow. Any power mismatch between generation and consumption is counteracted by the kinetic energy stored on the rotor. Positive mismatches speed the rotor up while negative ones reduce the speed. This operating principle is applied to just one WT

within an island in [Kanellos, *et al.,* 2008]. This WT performs the regulation of the island voltage while the rest acts like current sources. The aggregation of additional sources can complicate the voltage regulation. The master WT experiences a particular high negative power mismatch, as the total power is not uniformly shared, so it can run out of energy reserves and be tripped off. Then, as none of the remaining WTs participate in voltage regulation, the complete system is shut down even though the remaining WTs still contain kinetic reserves. The versatility, integrity and scalability are remarkably improved when all the parallel sources participate in the voltage regulation by using the droop control as a smooth interconnection technique.

However, the island performance is very sensitive to the tripping of one source due to the lack of kinetic storage. It is important to perform a management of the energy reserves. In [Kanellos, *et al.,* 2008], the torque reference that controls the DC-link voltage is slightly modified in function of the rotor speed. However, it only takes effects when the rotor speed is reaching its operating limits or DC-link voltage controller is saturated. By using the frequency-active power droop, the parallel sources also share the total load demands [Zhong, *et al.,* 2011].

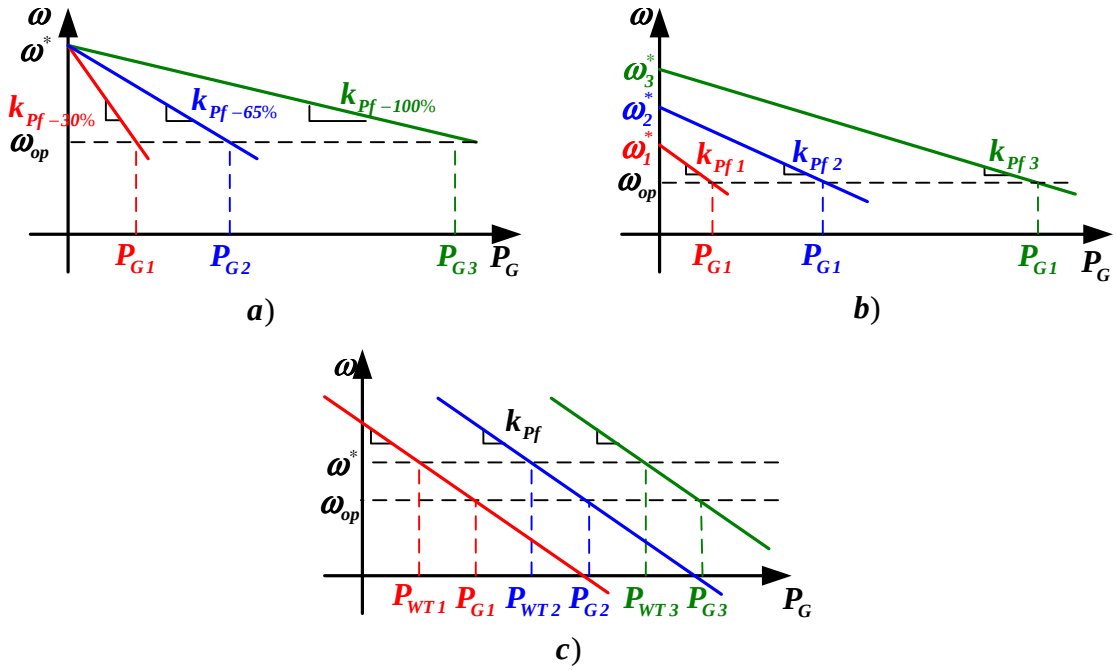

Fig. 2.5: Power sharing strategies a) Strategy proposed in [Guerrero, *et al.,* 2009] based on changing the droop slope in function of the energy reserves, b) Method proposed in [Barklund, *et al.,* 2008] where the frequency bias point and the droop gain are modified and c) Technique proposed in [Kim, *et al.,* 2011] where only the power coordinate of the bias point adopts the value of the generated power.

The droop slope, previously illustrated in Fig. 2.4, defines the sharing behavior: generous or mean. The droop curve can be online modified to readapt the injected power by a certain UWT as function of the storage reserves. In [Guerrero, *et al.,* 2009], the droop slope takes different values depending on the charge of the battery. If the charge is close to 100%, the

droop takes low values and the system has a generous behavior injecting more power at a given operating frequency, ω_{op} . On contrary, if the battery is running out of energy, the slope is configured with higher values, as shown in Fig. 2.5.a. The bias point is fixed to (ω^*,*0*), being ω^* a predefined value. Fig. 2.5.b contains the scheme proposed in [Barklund, *et al.,* 2008]. In this case, not only the slope but also the frequency coordinate of the bias point is also readapted in function of the current energy storage while the power coordinate of the bias point is still kept to zero. This logically increases the regulation over the storage. Finally, Fig. 2.5.c contains the strategy proposed in [Kim, *et al.,* 2011]. In this work, the power coordinate of the bias point adopts the value of the current power generation (i.e. mechanical power entering the generator, $P_G^* = P_{WT}$) and fixes the frequency coordinate to the nominal value ($\omega^* = \omega_0$). This modus operandi implies a partially fair fact: each UWT has to deal with the same power mismatch. It means that the negative or positive power mismatch between the total generation and the total consumption of the island is equally shared between all the DG units. Nevertheless, it would be a totally fair strategy if sharing is weighted in function of the power rating and the available storage reserves of each UW. It is important to note that the modification of the droop slope is limited by several aspects: stability and dynamics of the power loop, power quality in terms of frequency drifts, power sharing efficiency and rating power.

2.1.4. Regulation under unbalanced conditions.

The GS converter often has to deal with unbalanced conditions. The magnitudes of the three-phase variables are not longer the same and the phase displacement between them is different from 120º. The unbalance is generally given by the control disturbance (the PCC voltage in grid-connected and the current demanded by unbalanced loads in island mode). The unbalanced conditions introduce a quite challenging scenario for the control of the inverter. There are two notorious effects related each other: power oscillation and distortion of ac signals. By default, the unbalance may cause some oscillating active and reactive power components at the double of the operating frequency. As a consequence of the active power oscillation, the DC-link voltage also oscillates. If this oscillation is not well managed in the control references, the generated current and voltage can be distorted with low order harmonics, especially 3rd harmonic.

2.1.4.1. Power oscillation.

This subsection contains an enumeration of the existing works regarding the power control under unbalanced conditions in grid-connected operation. All the works make reference to Current Controlled VSC while the contributions considering a grid-connected Voltage Controlled VSC are negligible. Regarding the island operating mode, the oscillating power cannot be regulated due to the constraint of keeping a balanced voltage.

In [Akagi, *et al.,* 1984], Akagi introduces the instantaneous active and reactive power theory (PQ-theory). It relates the αβ components of the voltage and current with the active and reactive powers as in (2.2). Note that the variables have been particularized for an LCL filter with the capacitor voltage and the output current.

$$\begin{bmatrix} P_G \\ Q_G \end{bmatrix} = \begin{bmatrix} v_{C\alpha} & v_{C\beta} \\ -v_{C\beta} & v_{C\alpha} \end{bmatrix} \begin{bmatrix} i_{2\alpha} \\ i_{2\beta} \end{bmatrix} \tag{2.2}$$

The inverse of the 2x2 matrix can be used to obtain the current references in function of the active and reactive power references. However, this 2x2 matrix does not offer capacity for regulating the oscillating power. The work presented in [Rioual, *et al.,* 1996] contains an extended development of the original PQ-theory proposed by Akagi. The apparent power vector ($\vec{S}_G$) can be expressed as:

$$\begin{gathered} \vec{S}_G = P_G + jQ_G \\ \vec{S}_G = \frac{3}{2}\left(\vec{v}^{+}_{C\alpha\beta} + \vec{v}^{-}_{C\alpha\beta}\right)\left(\vec{i}^{+}_{2\alpha\beta} + \vec{i}^{-}_{2\alpha\beta}\right)^{*} = \frac{3}{2}\left(\vec{v}^{+}_{Cdq} e^{j\theta_C} + \vec{v}^{-}_{Cdq} e^{-j\theta_C}\right)\left(\vec{i}^{+}_{2dq} e^{j\theta_C} + \vec{i}^{-}_{2dq} e^{-j\theta_C}\right)^{*} \end{gathered} \tag{2.3}$$

where θ_C is the phase of $\vec{v}_C$ and the superscript + and - makes reference to positive and negative sequences. As a result of the unbalanced conditions, the active and reactive powers are not only composed of DC values but also by oscillating components at $2\omega_0$:

$$\begin{aligned} P_G &= P_{G0} + P_{GC2}\cos(2\theta_C) + P_{GS2}\sin(2\theta_C) \\ Q_G &= Q_{G0} + Q_{GC2}\cos(2\theta_C) + Q_{GS2}\sin(2\theta_C) \end{aligned} \tag{2.4}$$

P_{G0} and Q_{G0} are the DC components, P_{GC2} and Q_{GC2} the cosine oscillating components and P_{GS2} and Q_{GS2} the sine oscillating components:

$$\begin{aligned} P_{G0} &= \frac{3}{2}\left(v^{+}_{Cd}\cdot i^{+}_{2d} + v^{+}_{Cq}\cdot i^{+}_{2q} + v^{-}_{Cd}\cdot i^{-}_{2d} + v^{-}_{Cq}\cdot i^{-}_{2q}\right) \\ P_{GC2} &= \frac{3}{2}\left(v^{-}_{Cd}\cdot i^{+}_{2d} + v^{-}_{Cq}\cdot i^{+}_{2q} + v^{+}_{Cd}\cdot i^{-}_{2d} + v^{+}_{Cq}\cdot i^{-}_{2q}\right) \\ P_{GS2} &= \frac{3}{2}\left(v^{-}_{Cq}\cdot i^{+}_{2d} - v^{-}_{Cd}\cdot i^{+}_{2q} - v^{+}_{Cq}\cdot i^{-}_{2d} + v^{+}_{Cd}\cdot i^{-}_{2q}\right) \\ Q_{G0} &= \frac{3}{2}\left(v^{+}_{Cq}\cdot i^{+}_{2d} - v^{+}_{Cd}\cdot i^{+}_{2q} + v^{-}_{Cq}\cdot i^{-}_{2d} - v^{-}_{Cd}\cdot i^{-}_{2q}\right) \\ Q_{GC2} &= \frac{3}{2}\left(v^{-}_{Cq}\cdot i^{+}_{2d} - v^{-}_{Cd}\cdot i^{+}_{2q} + v^{+}_{Cq}\cdot i^{-}_{2d} - v^{+}_{Cd}\cdot i^{-}_{2q}\right) \\ Q_{GS2} &= \frac{3}{2}\left(-v^{-}_{Cd}\cdot i^{+}_{2d} - v^{-}_{Cq}\cdot i^{+}_{2q} + v^{+}_{Cd}\cdot i^{-}_{2d} + v^{+}_{Cq}\cdot i^{-}_{2q}\right) \end{aligned} \tag{2.5}$$

Then, the active and reactive power components can be expressed as function of voltage and current matrices:

$$[S]=\frac{3}{2}[v][i]$$

$$\begin{bmatrix} P_{G0} \\ P_{GC2} \\ P_{GS2} \\ Q_{G0} \\ Q_{GC2} \\ Q_{GS2} \end{bmatrix} = \frac{3}{2} \begin{bmatrix} v_{Cd}^{+} & v_{Cq}^{+} & v_{Cd}^{-} & v_{Cq}^{-} \\ v_{Cd}^{-} & v_{Cq}^{-} & v_{Cd}^{+} & v_{Cq}^{+} \\ v_{Cq}^{-} & -v_{Cd}^{-} & -v_{Cq}^{+} & v_{Cd}^{+} \\ v_{Cq}^{+} & -v_{Cd}^{+} & v_{Cq}^{-} & -v_{Cd}^{-} \\ v_{Cq}^{-} & -v_{Cd}^{-} & v_{Cq}^{+} & -v_{Cd}^{+} \\ -v_{Cd}^{-} & -v_{Cq}^{-} & v_{Cd}^{+} & v_{Cq}^{+} \end{bmatrix} \begin{bmatrix} i_{2d}^{+} \\ i_{2q}^{+} \\ i_{2d}^{-} \\ i_{2q}^{-} \end{bmatrix} \tag{2.6}$$

This way, the control is provided with capacity for regulating the oscillating active power. In order to perform this regulation, (2.6) indicates that the system has to inject negative sequence too. The proposed control scheme in [Rioual, *et al.,* 1996] was one of the first in adding both positive and negative sequence in the control actuation. Nevertheless, it presents a poor regulation of the negative sequence. The operating principle is to obtain the current reference matrix $[i^*]$ as function of the power reference and voltage matrices. However, the rank of $[v]$ and the number of current references is 4, so not all the power components of $[S]$ can be regulated. Then, all the active power components and the DC component of the reactive power are the selected variables to be controlled with output currents:

$$\left[i^*\right]=\frac{2}{3}\left[v'\right]^{-1}\left[S^*\right]$$

$$\begin{bmatrix} i_{2d}^{+*} \\ i_{2q}^{+*} \\ i_{2d}^{-*} \\ i_{2q}^{-*} \end{bmatrix} = \frac{2}{3} \begin{bmatrix} v_{Cd}^{+} & v_{Cq}^{+} & v_{Cd}^{-} & v_{Cq}^{-} \\ v_{Cd}^{-} & v_{Cq}^{-} & v_{Cd}^{+} & v_{Cq}^{+} \\ v_{Cq}^{-} & -v_{Cd}^{-} & -v_{Cq}^{+} & v_{Cd}^{+} \\ v_{Cq}^{+} & -v_{Cd}^{+} & v_{Cq}^{-} & -v_{Cd}^{-} \end{bmatrix}^{-1} \begin{bmatrix} P_G^* \\ 0 \\ 0 \\ Q_G^* \end{bmatrix} \tag{2.7}$$

The work presented in [Song, *et al.*, 1999] was the first one on using a dual control strategy for the positive and negative sequences. The references are taken from the PQ-theory 4x4 matrix and the regulation of each sequence is carried out with different PI controllers. The separation of sequences is made through notch filters at $2\omega_0$. In [Suh, *et al.,* 2006], the so-called separation of sequences is not really developed. Instead, a resonant controller at $2\omega_0$ is added to the PI controllers of both sequences regulators so that the infinite gain of this block helps to remove any presence of positive sequence in the negative sequence regulator and vice versa.

In [Hwang, *et al.,* 2007], the negative sequence reference is given by the output of a resonant controller implemented in the DC-link voltage controller. This novel proposal tries to create the necessary negative sequence reference directly from the DC-link oscillation.

2.1.4.2. Distortion of references.

Apart from de oscillating power, the unbalanced conditions can bring other issues related with the distortion of voltage and currents, as indicated in [Moran, *et al.,* 1992] and [Enjeti, *et al.,* 1993]. The distortion of ac control references is actually associated with a wrong "representation", concept introduced in this Thesis. A right representation basically consists on assuring that all the variables in the control loop do not contain unexpected frequency components in its spectrum. Four particular cases can be distinguished regarding the unbalanced conditions:

a) Power oscillation.

The first case is associated with those control schemes where the oscillating power is not regulated. There should be distinguished between grid-feeding and grid-forming schemes.

In grid-feeding control schemes, the GS controller has to regulate the DC-link voltage by means of the injected power. The appearance of oscillating power at $2\omega_0$ makes the DC-link voltage oscillates at the same frequency. The oscillation is transferred to the active power reference P_G^* through the DC-link controller. Then, when the current reference is calculated through a matrix of 2x2 based on the PQ-theory like in [Alfonso, *et al.,* 2000] or by a simple division by the voltage like in [Blaabjerg, et al., 2006], the results contains a non-zero sequence 3rd harmonic.

In case of power schemes based on droop control, employed for both grid-connected and island operating modes, the oscillating active and reactive power directly affects the magnitude and phase of the voltage reference. Equivalent to the previous case, the product between the cosine and sine of the phase with the oscillating magnitude produces a convolution of frequencies with a resulting 3rd harmonic component.

Both DC-link and droop controllers have been thought for controlling DC components. However, the poor representation allows the presence of oscillating terms that cause the distortion of references. In order to perform a good representation, the use of low-pass or notch filters can remove the non-desired frequency in the control variables and the distortion can be avoided. Note that the filter only removes the oscillation in the control variables, but both DC-link voltage and power still contain terms at $2\omega_0$. As a drawback, the filter forces to slow down the dynamic response. With any of the control structures presented in the previous subsection, the origin of the distortion, the oscillating power, is removed and the correct representation is assured in this case.

b) Poor performance of sequence detectors.

The sequence detector is an important element of the synchronization system of any control scheme of VSC connected to the grid. The relevance of these algorithms is notorious

in the management of the oscillating power and the positive and negative sequences. It basically provides the positive and negative sequences of any vector, voltage or current. For instance, these sequences are employed to fill the elements of the 4x4 matrix in (2.7) and to perform a dual control of positive and negatives current sequences in dq-frames [Song, *et al.*, 1999]. However, the performance of sequence detector is not always ideal. Some portion of positive sequence can be present in the calculated negative sequence and vice versa. In such conditions, the dq components of the calculated sequences contain a $2\omega_0$ term corresponding to the opposite sequence. As a consequence, the control references are again distorted with a 3rd order harmonic. In [Yazdani, *et al.*, 2006], a notch filter is used to remove the $2\omega_0$ oscillation in the dq-components of both negative and positive sequences, performing a right representation of the sequences.

c) Magnitudes and phases of three-phase vectors.

In linear control structures, three-phase vectors are generally represented in αβ-frames or in dq-frames. However, there are some especial cases where the vectors have to be represented in polar coordinates: magnitude and phase. As an illustrative example, [Parkhideh, *et al.,* 2013] makes use of the magnitude of voltage vectors for implementing a non-linear control of the oscillating power under unbalances. Although the oscillating power is quite attenuated, the representation of the magnitudes is not correct and the injected currents present an important level of distortion. A more obvious example related with this Thesis is the representation in polar coordinates required by the non-linear nature of the droop control. The magnitude and phase of any vector are usually calculated as follows:

$$U = \sqrt{(u_\alpha)^2 + (u_\beta)^2}$$
$$\theta = \tan^{-1}\left(\frac{u_\beta}{u_\alpha}\right) \qquad (2.8).$$

As shown, just one variable is used to represent each one. Under balanced conditions, all the phases have the same magnitude and the phase displacement between α and β components is fixed to 90º. Then, U and the ramp of θ (angular frequency) are constant variables. Nevertheless, the presence of negative sequence breaks the bonds between phases and they are no longer in quadrature. As a consequence, U and the ramp θ contain an oscillating term at $2\omega_0$ and the voltage signals are distorted.

d) Limitation of unbalanced vector references.

The limitation of unbalanced references bears relation with the previous case. However, it has been individually analyzed due to its great relevance. There are many situations where the control action exceeds the rating of the system and the use of saturators for limiting the control references is mandatory. Once again, the unbalanced conditions raise the complexity

and if the right technique is not employed, the limitation of unbalanced reference vectors can add low order harmonic components.

In systems based on power converters, voltage and current vectors suppose the most common ac variables for saturation. Attending to the variable to be limited, two saturators can be distinguished in Fig. 2.1. The saturator of current vectors, I_{SAT}, forces the current controller to follow only references feasible by the converter (determined by the rating of the IGBTs and their thermal limits). I_{SAT} can be temporarily activated during a transient of the disturbance or in the outer controller. In steady-state, the saturation can come from a poor configuration of the system. The voltage saturator, V_{SAT}, avoids the modulation of voltage references out of the PWM hexagon [Zhou, *et al.,* 2002]. V_{SAT} is generally activated under swells, high reactive power injections, etc. In the particular case of VCVSCs as autonomous and grid-forming systems, such as the Universal Operation of WTs, the energy balance plays a big role. If the conditions do not allow the entering power into the DC-link, P_i , reaching the injected power by the inverter, P_o , the mismatch is solved with the energy stored in the DC-link capacitor. This leads to a fall of the DC-link voltage u_{DC} which reduces the voltage capacity injection being necessary the actuation of V_{SAT}. There are several saturation methods for implementing these saturator blocks. The existing saturation techniques can be divided into two categories: scalar and vector saturation methods.

Scalar methods are characterized by saturating independently each component while vector techniques consider both components as part of the vector and jointly limit them. The most representative example of scalar saturation is the limitation of the modulating signal implicit in PWM schemes [Holtz, 1992]. The use of the scalar saturation only makes sense in the V_{SAT} block. Although it provides the maximum voltage in the PWM hexagon, the sinusoidal waveforms of the limited vector, $\vec{u}_{SS}$, are distorted with low-order harmonics no matter the presence of negative sequence, as shown in Fig. 2.6.a.

Different vector saturation techniques can be found in the literature. A virtual impedance is used to reduce the voltage reference under high current levels in [He, *et al.,* 2011], [Moon, *et al.,* 1999] and [Guerrero, *et al.,* 2007]. The application of this method is reduced to the current limitation of VCVSC with single-loop control architectures. The saturator used in [Ottersten, *et al.,* 2002], [Marwali, *et al.,* 2004] and [Zamani, *et al.,* 2012], known as the Circular Limit (CL) Method can be applied to CCVSCs and VCVSCs for limiting voltage and current references. This saturator limits the magnitude of the vector while keeps the original phase. It provides a good performance under balanced conditions. However, as already mentioned, both calculated amplitude and phase of the reference vector oscillate with presence of negative sequence. Then, if the saturator is modeled as a reduction factor, this factor is then varying along the fundamental period (T_0) inserting harmonic distortion in the limited reference, $\vec{u}_{CL}$, as depicted in Fig. 2.6.c. In UPSs, isolated grid-connected converters and CCVSC applications, the addition of low-order harmonics supposes a great power quality problem: (1) increases the peak value, (2) provokes heating, noise and reduces life on capacitors, rotating machines,

transformers and customer's equipment, (3) harmonic torques may arise and (4) excite system resonances, among others [Fuchs, *et al.,* 2008]. Besides, the harmonic injection is subject to an efficiency loss in autonomous systems like UPS and DVR, where the energy reserve is limited [Nielsen, *et al.,* 2005].

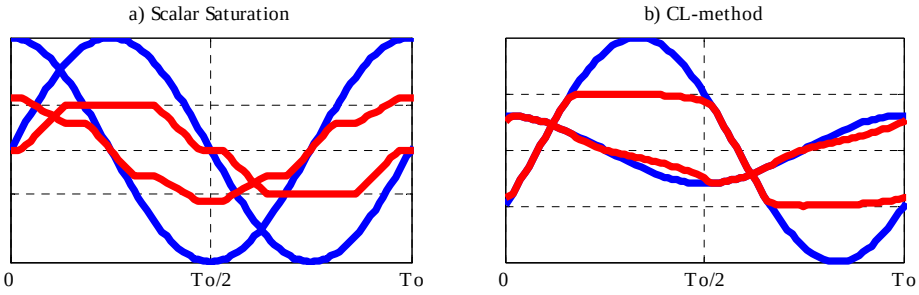

Fig. 2.6: Temporal waveforms of the input and limited references: a) Scalar Saturation and b) CL-method

Several attempts have been made to avoid the distortion caused by the negative sequence. In [Zamani, *et al.,* 2012], a notch filter at $2\omega_0$ is inserted to remove the negative sequence in dq-axis performing a good representation of the positive sequence. This logically almost avoids the operation with unbalanced variables and thus, the CL-method correctly limits the reference vector. Swapping the unbalanced reference with a predefined positive sequence reference is proposed in [Plet, *et al.,* 2011]. Nevertheless, these two solutions remove any chance of regulating the negative sequence and hence, the already mentioned power oscillations at $2\omega_0$ are unavoidable. In the particular case of [Plet, *et al.,* 2011], the loop is totally opened, losing the whole control capacity, a quite expensive prize.

2.2. Thesis objectives.

In Chapter 1, the general objectives of the Thesis have already been listed. In this section, the objectives are described in detail and grouped in four categories. They have been settled down with the intention of reinforcing the existing weak point related the Universal Operation regulation of WTs and proposing new lines of research and discussion. Next, each one of the categories is listed followed for the imposed objectives of this Thesis.

2.2.1. Developing the inner controller for the Universal Operation.

The knowledge review has shown the great number of works concerning the regulation of the voltage across the filter capacitor. Features like the bandwidth and the resonance damping are the main points under review focused on applications like UPS, microgrid units, DVRs, etc.

Regarding the Universal Operation of UWTs, the voltage controller plays a big role. It is the core of the inverter control for all the operating modes. It provides the local voltage and frequency regulation capacity during the island operation while follows the reference imposed

by the power control in grid-connected mode for both VCVSC and CCVSC schemes (with LCL-filter). In spite of its relevance, none of the existing works have treated the voltage control from the point of view of a DG unit capable of working in both operating modes. In such conditions, some of the efforts carried out in this work should be focused on analyzing the different voltage control architectures in features like:

- Power-voltage fitting: It makes reference to how both controllers fit for the grid-connected operation. It collects features like the coupling between controllers given by their respective bandwidths or the attenuation of the power plant resonance. As described in Chapter 4, the power plant for CCVSC and VCVSC schemes presents a resonance at the nominal frequency in inductive systems. Then, the damping of this resonant nature of the power controller is a matter of comparison within the voltage control analysis.

- Response under transitions between operating modes: One of the critic aspects of the Universal operation is the transient response caused during the connection and disconnection from the grid. The transient current peaks should be minimized as much as possible in order to assure the integrity of the elements of the system. This Thesis approaches the issue from the point of view of the power and voltage controllers and the synchronization system. This feature is crucial in the selection of the voltage control architecture for UWTs.

- Robustness under load changes: A study of the robustness offered by the different voltage control architectures as function of the type and value of the local load is missing in the existing works. Hence, this Thesis fixes the goal of analyzing the influence of the local load in the performance of the voltage control contributing to the existing knowledge.

2.2.2. Regulating active and reactive powers for enhancing the power supply ratios.

Many contributions have already been done regarding the power control of grid-connected DG units and isolated sources in a microgrid. However, there are still some points that can be enhanced or have not been already addressed for the Universal Operation of WTs.

The first objective on this category is focused on a study of the power control schemes of the CCVSC and VCVSC philosophies. Although the use of the CCVSC is by far more widespread, the VCVSC scheme is also taken into account for the grid-connected operation under the premise of seamless transitions with the island mode. The analysis should assess both options attending to the important aspects of the Universal Operation within the grid-connected mode: such as the bandwidth, robustness, transition between operating modes and response under unbalanced faults.

Regarding the island operation, the control functionalities change. In the GS converter, the use of the VSVSC scheme is clear, while the MS converter is on charge of the DC-link voltage

control. Many research works have been already published within the microgrid frame. However, the use of low and medium power WTs as isolated sources is still a concept under development. The main purpose of the Universal Operation is to improve the continuous power supply ratios. This is equivalent to keep the UWT under operation as much as possible. The operating time is quite related to the energy storage reserve of the UWT. As already mentioned, in order to give a direct and economical solution, the proposed strategy does not count with the installation of additional storage units. Then, the key point resides in an optimized management of the inherent storage (kinetic energy stored in the rotor) and dissipation (DC-braking chopper and pitch control) resources of the UWT. In this line, it is crucial to propose an optimum power sharing strategy in the GS controller. As a global requisite, the power sharing should be a fair strategy, i.e., the power injected by a particular UWT should be weighted by its current storage reserves, generation and power rating. This way, the power mismatch of this particular UWT can be attenuated by distributing it to the other parallel UWTs. The total storage reserves of all the UWTs of the island are jointly regulated offering an optimized performance. As restrictions, it should attend to power quality (in terms of voltage and frequency deviation) and stability issues. The power sharing strategy offers a way to regulate the rotor speed while MS controller is regulating the DC-link voltage.

Although the island and grid-connected operation modes have more repercussion, the synchronization mode also plays a great role in the Universal Operation. As global objective, it has to resynchronize the island voltage with the grid voltage. During this mode, the power controller is disabled and thus, the power is not fairly shared unless special measures are taken in the synchronization algorithm. In this dissertation, due to the limited storage reserves, implementing a distributed synchronization technique which not only provides a seamless reconnection but also fairly divides the load among the operating units is fixed as an objetive.

The experimental and simulation tests can evidence the feasibility of the proposed strategy, but they still do not assess the real impact of the Universal Operation of WTs over the power supply ratios. There are almost infinite situations regarding the values of the consumption and the generation that do affect on the power supply enhancement. In order to provide a well supported work, this Thesis fixes the objective of carrying out an accurate assessment of the efficiency of the Universal Operation attending to two key ratios: the reduction of the number of power supply interruptions and the reduction of the duration of the interruptions. Due to the nature of the variables that take part in the analysis (wind speed, load consumption and type of interruption), it should contain a strong statistical component.

2.2.3. Regulation under unbalanced conditions.

In the knowledge review section, it has been already remarked the importance of carrying out a good performance during unbalanced conditions. The oscillating power and the distortion of control references are the main issues associated to the unbalances. The power oscillation is an already solved issue in CCVSC schemes. However, the use of VCVSC for

grid-connected applications by means of the droop control still needs a further revision for regulating the oscillating power. Focusing on the distortion of references, none of the existing works gives a definitive and convincing solution.

In such conditions, in order to carry out a balanced comparison between the VSVSC and CCVSC control schemes, this Thesis addressed the objective of providing the droop control of oscillating power regulation capacity. This way, both philosophies are under the same conditions. On the other hand, one of the strong points of this Thesis resides in the introduction of the concept "representation of control variables". By means of this proposed concept, the objective of performing a distortion-free operation in any of the control task is established. The saturation of unbalances requires a special consideration due to its complexity. The objective is focused on not only proposing a distortion-free approach but also implementing several techniques optimized for different applications.

2.2.4. Conclusions of the objectives.

The objectives of this Thesis are focused on reinforcing the weak points of the control of the full-power converter topology inside the Universal Operation frame. They are related to the challenges of the island operation without storage systems, the transition between operating states and the grid-connected operation.

Chapter 3.

Control Overview of a Wind Turbine System.

This chapter is on charge of presenting an overview of the proposed control strategy for the UWT: the complete MS controller and the inner control of the GS converter. It firstly collects the main requirements of the Universal Operation to propose the control general structure and specifies the design criteria. Besides, it carries out an analysis of the power filter configuration looking for the cost-effective solution. Different voltage control architectures are extensively studied for those features that play big roles within the Universal Operation. Finally, the MS control is also briefly described on Appendix A.

3.1. Universal Operation Control.

The control of a UWT has to deal with three different operation modes: grid-connected, island and synchronization. Each operation mode implies different requirements, and logically, a fixed control structure cannot deal with all of them at the same time. On the other hand, implementing totally different control schemes for each operation mode would penalize the transition between modes. So these two statements set out a trade-off regarding the general structure of the universal control. The universal control of a wind turbine is divided into the MS and the GS controls. First of all, it is necessary to differentiate the general roles of MS and GS outer controllers in function of the operation mode.

During normal grid-connected operation, the active power transfer of the system is usually determined by a MPPT algorithm implemented in the MS control. This algorithm basically readapts the rotor speed reference in function of the wind velocity to optimize the power

coefficient. It is normally based on a mechanical model of the turbine. The GS control should then regulate the DC-link voltage by tracking the active power coming from the MS. It is quite crucial providing a faster power regulation in the GS than in the MS control, so that the DC-link control can rapidly counteract the disturbances from strong torque steps. Besides, the power control should regulate the reactive power transfer with the grid.

The regulation during the island operation is more challenging. There is a role change when disconnecting the system from the grid. The active power transfer is now fixed by the local loads. Apart from delivering the load power demands, the GS control should adopt a quasi grid-forming strategy, participating in the local voltage magnitude and frequency regulations. Moreover, the GS control should carry out a load-sharing strategy with the rest of the parallel DG units if present. The active power contribution of each unit should be adapted accordingly with the current generation and the kinetic reserves with the aim of extending the island operation. On the other hand, the MS control should readapt the power generation to track the load demands and hence, regulate the DC-link voltage. Therefore, the regulation of the DC-link is assured no matter which side of the full power converter fixes the power transfer. A clear advantage of the universal control is the power regulation enhancement under grid faults. The voltage reduction and the reactive power injection required by the grid codes dramatically reduce the active power injection capacity leading to an undesirable power mismatch during the LVRT operation. This fact can be quite troublesome in common grid-connected systems, but is easily solved by performing the island power balance strategy in UWTs. Therefore, during grid-connected fault conditions the active power is set up to the maximum, if necessary, and the island DC-link voltage control is again used. Logically, during this period the regulation capacity over rotor speed is almost zero. Finally, power quality issues should not be forgotten in both island and grid-connected control strategies.

The synchronization mode is not less important. The safety of the system during the reconnection with main grid strongly depends on an efficient synchronization procedure. When the fault that provoked the island operation has been cleared, the island is out of synchronism with the main utility. A direct reconnection will cause big transient peaks in the current affecting the safety and stability of the system. The synchronization system uses the inner voltage control to reduce the voltage drop across the circuit breaker, minimizing the current transient.

Taking into account the requisites previously exposed, the most practical solution lays on the definition of a basic control structure slightly configurable depending on the operation mode. Fig. 3.1 introduces the general control structure of the MS and GS controls for the Universal Operation.

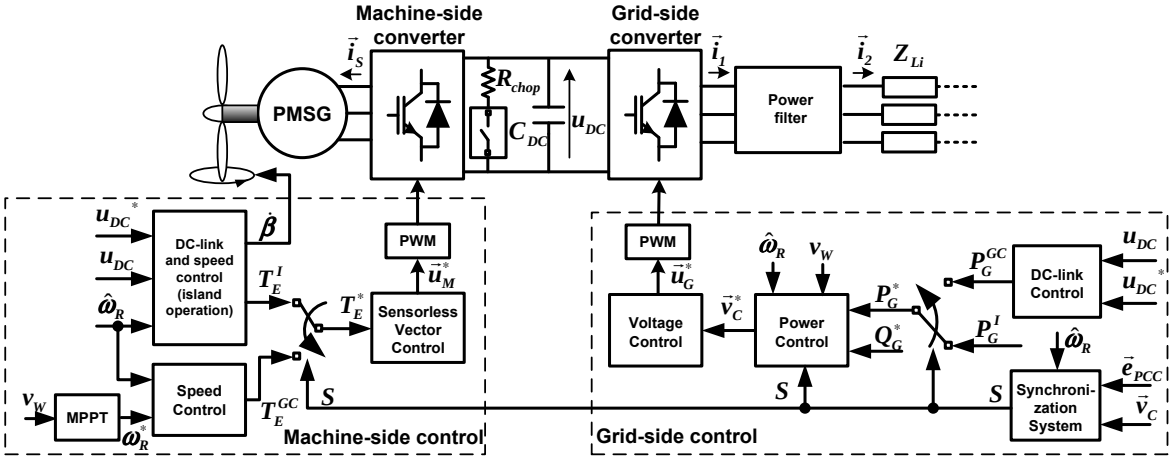

Fig. 3.1: Universal control: basic scheme.

As shown, the MS control consists of the island DC-link control, the MPPT algorithm, the speed control and the sensorless vector control for the PMSG. The GS control block contains the grid-connected DC-link voltage controller, the power controller, the voltage controller and the synchronization system. The state signal, *S*, output of the synchronization system, indicates the operation mode: 1 island, 2 synchronization and 3 grid-connected. It is employed to switch the corresponding references and modules in order to fulfill the requirements of each operation mode.

The structure based on multiple controllers in cascade needs the specification of the settling times of each control to assure a decoupling between dynamics. The dynamics of inner controller should be configured as fast as possible and then, from inner to outer controllers, slower dynamics are progressively configured. Attending to this, Table 3.1 collects the maximum and minimum settling times for each control in the particular case of the 58 kW UWT experimental (see Table 7.1). The settling times in this work are defined as the time needed to reduce the error of the signal under control below 5% under a reference step. In case of ac variables, it is referred to the magnitude error. Each restriction has an associated superscript number in function of its nature. Index (1) represents the maximum settling time for the DC-link controller during the grid-connected operation. As already mentioned, the main restriction for this controller is to provide fast enough power dynamics to track the power coming from MS. Note that fault conditions are not considered because they are managed through the island DC-link controller. The transient behavior of the MS power is mainly given by the electromagnetic torque, which in grid-connected is fixed by the speed controller. It is desired a slow rotor speed control dynamic to increase the filter capacity over the estimated speed given by the sensorless system. Therefore, the designed torque dynamics are quite smooth and not big torque step are expected. Furthermore, in some many cases, the torque reference slope is limited in the MS control loop. Then, the maximum settling time is not very demanding. Indexes (2) and (3) respectively set out the maximum responses times for the island DC-link and the speed controllers of the MS. These controllers are not in cascade each other and not used at the same time. Hence, their constraints are associated to the

current control implemented in the vector control of the MS. The restrictions given by (2) and (3) are calculated through the expression of the electric and kinetic energies respectively stored in the DC capacitors and rotor shaft. This way, the regulation assures a quick response under a critic condition, keeping the variable under control (DC-link voltage or rotor speed) in a safe range. Note that a local load change or a dip appearance requires more demanding constraints over the island DC-link voltage control than in the grid-connected case. The restriction imposed by (4) sets out the minimum settling time required for filtering the estimated rotor speed. Indexes (5) and (6) restrict the maximum and minimum settling times for assuring the controllers decoupling (the multiplying factor varies between 5 and 7).

Table 3.1: Settling times of universal controllers.

	Grid-side controls		
	Grid-connected DC-link Voltage control	Power control	Voltage control
Upper limit (ms)	500 (1)	75 (5)	15 (5)
Lower limit (ms)	375 (6)	75 (6)	-
	Machine-side controls		
	Island DC-link Voltage control	Speed control	Current control
Upper limit (ms)	76.6 (2)	827 (3)	8 (5)
Lower limit (ms)	50 (6)	700 (4)	-

(1) Maximum time to assure faster dynamics than rotor speed controller.
(2) Time needed to cause a 15% DC-link voltage fall under a 10% power mismatch between consumption and generation.
(3) Time needed to accelerate the rotor speed a 15 % under a nominal torque mismatch between load and generator.
(4) Settling time required to perform a good filtering of the calculated rotor speed.
(5) Decoupling with outer controller.
(6) Decoupling with inner controller.

3.2. Selection of power filter.

This section deliberates in the possible configuration of the power filter and gives some details for configuring it. Regarding the hardware of UWTs based on a full-power solution, the possible configurations are essentially limited to the converter, the generator and the power filter. Although the selection of converter topology and the type of generator is quite important for advanced performance in grid-connected systems, it does not play a big role in the study of the Universal Operation and it is out of scope in this Thesis. However, the power filter does suppose a key point for the voltage and power regulation of UWTs. It gives the plant for the voltage and power controllers, being able of change certain characteristics in favor of the Universal Operation. Then, the selection of hardware in this Thesis is exclusively referred to the power filter. There are two possible options taking into account the need of voltage regulation during the island operation: the LC and LCL filters. Despite the great variety of existing works using LC and LCL filters in island and grid-connected operating modes, none of them seems to make clear which one provides an optimum plant for the Universal Operation. This Thesis addresses a comparative study regarding the performance

provided by each solution over the key points of the Universal Operation and offers some guidelines to configure the values of the filter elements

3.2.1. LC-filter vs. LCL-filter.

In order to implement a robust and strong voltage controller, a capacitor element is necessary in the power filter. This capacitor gives and increments the voltage inertia which transforms the plant into a more robust system. It behaves as a voltage storage system reducing the challenges of the voltage regulation. Besides, it gives a path for a further attenuation of the switching harmonics. This implies the rejection of the classic L-filter topology. Two classic options still remain in the VSC frame, displayed on Fig. 3.2: the LC-filter and the LCL-filter. The resistors of the inductances and the damping resistor of the capacitor have been omitted in the figure. The following study analyzes these two solutions attending to the impact into the system performance, control and cost looking for the most cost-effective option.

The inductance L_2 mostly represents the plant for the power control in case of the LCL-filter while in the LC-filter the power plant consists on the line or feeder impedance (Z_{Li}), variant and unknown. In low power system, the line impedance is predominantly resistive while as long as the power rating increases, the inductive nature becomes more dominant. As a consequence, the task of implementing a power controller capable of dealing with any kind of situation is too challenging. In the LCL-filter, L_2 becomes dominant over the line impedance, providing a less sensitive plant to system changes. This fact is also applicable to the voltage control, where the resonant behavior of the filter is restricted to a narrower band of frequencies under the Z_{Li} variations in grid-connected or load changes in island operation.

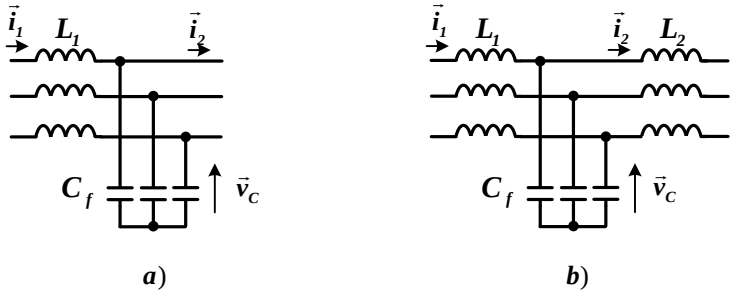

Fig. 3.2: a) LC and b) LCL filters with ideal components.

The interface between parallel VCVSCs, whose use is mandatory in island mode and optional in grid-connected, is also an aspect that plays a big role. The use of the LCL provides a smoother interface between the parallel voltage sources. This fact helps in the sharing of the active power and avoids the circulating currents. Regarding the voltage regulation during the island operation, the voltage seen by the loads is reduced by the voltage drop across L_2 in the LCL topology, especially under reactive power transferences. A virtual impedance loop can be inserted to modify the power controller output and counteract the voltage drop. The

implementation of the virtual impedance leads to two drawbacks: (1) the controller actuation is closer to the overmodulation level and the necessity of increasing u_{DC} can be a fact and (2) interface between VCVSCs get poorer. The use of the LC-filter provides a good voltage regulation capacity but circulating currents between parallel units can easily appear. The trade-off can be solved by accurately selecting both L_2 and the virtual impedance.

On the other hand, the inductance L_2 of the LCL-filter increments the cost and the order of the system. However, this filter topology is more widespread than the LC-filter in already installed grid-connected WT, so the cost is only applicable to those systems with L-filter and new ones.

Taking into account the above mentioned statements, the LCL-filter is selected in this work.

The following introduces some guidelines for adequately choosing the filter's element values. This work has taken into consideration the statements resented in [Liserre, *et al.*, 2005] and [He, *et al.,* 2011]. [Liserre, *et al.*, 2005] provides a step-by-step procedure for the design of the LCL-filter in grid-connected applications. The analyzed features are the switching noise attenuation capacity, the cost and the good performance of the in terms of response and stability margins. Besides, it suggests how to select the location of the filter resonant frequency between the switching frequency and the control band. The study presented in [He, *et al.,* 2011] is focused on the design of virtual impedance with the aim of configuring the output impedance of DG units with LC-filters for an enhanced performance in both grid-connected and island operations. As mentioned, the study can be also applied to DG-units with LCL-filters for adequately configuring the physical output impedance. The study takes into account features like the DG unit power capacity, decoupling between active and reactive powers and stability and transients performances of the power controller in grid-connected and island modes. These two last items are further improved in this dissertation during the power controller tuning.

Taking into account the faster dynamics of the voltage control, the system can be modeled as ideal controlled voltage source from the point of view of the power controller. In such conditions, the power controlled plant is constituted by the combination of the feeder impedance and the filter impedance Z_2 Regarding of the decoupling between active and reactive powers, it is desired to have an inductive Z_2. On the other hand, the power transfer capacities and the voltage regulation (for island and synchronization modes) suppose an upper limit for the magnitude of Z_2, while the sensitivity to re-circulating currents and the power control robustness fix a lower limit. Following all these statements, it is possible to configure an LCL-filter that provides an interface with other units, loads and grid in all the operating modes of the Universal Operation.

3.3. Grid-side: Voltage control.

As displayed in Fig. 3.1, the core of the grid-side controller is the voltage control. The Universal Operation strategy highly depends on the performance of this block in all the considered operating modes. However, a study taking into account the Universal Operation requirement is still missing. This section develops a wide evaluation of five control architectures with different controller blocks, current feedbacks and number of loops. The study is focused on:

- Grid-connected mode: power performance, power quality and robust stability.
- Island mode: local voltage regulation capacity and robustness under load changes.

Moreover, this work introduces a general mathematic analysis independent on the current employed as feedback, the type of controllers used and the number of loops. This common analysis provides a more accurate comparison since the special characteristics of each controller are easier to be detected.

The following list contains the 5 control architectures studied in this work, shown in Fig. 2.3:

- Architecture 1 - SL: this is the only single-loop controller considered. The controller is a PR and it does not have any current feedbacks.
- Architecture 2 - PR+P $\vec{i}_C$: contains a PR as a outer controller and proportional (P) as inner controller. The capacitor current $\vec{i}_C$ is the inner-loop feedback variable.
- Architecture 3 - PR+P $\vec{i}_I$: the outer controller is PR while the inner controller is P. The inner-loop feedback variable is the inverter current $\vec{i}_I$.
- Architecture 4 - PR+PR $\vec{i}_C$: both outer and inner controller are PRs with a $\vec{i}_C$ as feedback.
- Architecture 5 - PR+PR $\vec{i}_I$: two PRs with $\vec{i}_I$.

The LCL filter of UWT1, whose values are collected on Table 7.1, has been chosen for presenting some practical-theoretical results.

3.3.1. Mathematical approach and tuning requirements

The first step is modeling the plant, depicted in Fig. 2.2. The plant dynamics are given by the response of $\vec{v}_C$ as function of the grid-side converter voltage $\vec{u}_G$ and $\vec{e}_{PCC}$:

$$\vec{v}_C(s) = G(s)\vec{u}_G(s) + G_E(s)\vec{e}_{PCC}(s) \tag{3.1}$$

where:

$$G(s)=\frac{sC_f Z_C Z_2}{G_{den}} \quad G_E(s)=\frac{sC_f Z_C Z_1}{G_{den}} \tag{3.2}$$

with:

$$\begin{gathered} G_{den}(s)=\left[L_1 C_f s^2+C_f(R_D+R_1)s+1\right](R_2+sL_2)+(1+sC_f R_D)(R_1+sL_1) \\ Zc=\frac{(1+sC_f R_D)}{SC_f};\ Z_1=R_1+sL_1;\ Z_2=R_2+sL_2 \end{gathered} \tag{3.3}$$

In order to damp the filter resonance, a small damping resistor R_D has been placed in series with C_f. In case of double-loop control schemes, which contain current feedbacks, the model of the plant is completed with $G_I(s)$ and $G_{IE}(s)$. These last transfer functions describe the dynamics of a certain current $\vec{i}$ ($\vec{i}_C$ or $\vec{i}_1$):

$$\vec{i}(s)=G_I(s)\vec{u}_G(s)+G_{IE}(s)\vec{e}_{PCC}(s) \tag{3.4}$$

Finally, the transfer functions $G_O(s)$ and $G_{OE}(s)$ give the output current response of the plant in function of $\vec{u}_G(s)$ and $\vec{e}_{PCC}(s)$.

$$\begin{gathered} \vec{i}_2(s)=G_O(s)\vec{u}_G(s)+G_{OE}(s)\vec{e}_{PCC}(s) \\ G_O(s)=\frac{sC_f Z_C}{G_{den}};\ G_{OE}(s)=-sC_f\frac{Z_1+Z_C}{G_{den}} \end{gathered} \tag{3.5}$$

Table 3.2 collects the expressions of the inner and outer controllers, $C_I(s)$ and $C_V(s)$ respectively, and $G_I(s)$ and $G_{IE}(s)$ for each architecture. It can be noted that, as the SL architecture has no feedbacks neither inner controller, $G_I(s)$ and $G_{IE}(s)$ are null and the inner controller is set to one. The transfer functions $C_{DV}(z)$, $C_{DI}(z)$, $G_{DI}(z)$, $G_{DIE}(z)$, $G_D(z)$, $G_{DE}(z)$, $G_{DO}(z)$ and $G_{DOE}(z)$ are the results of the zero order hold (ZOH) operation of $C_V(s)$, $C_I(s)$, $G_I(s)$, $G_{IE}(s)$, $G(s)$, $G_E(s)$, $G_O(s)$ and $G_{OE}(s)$, respectively. The general control loop scheme is reported in Fig. 3.3. The discrete z^{-1} block represents the computational delay.

Table 3.2: Expressions of the different plants and voltage controllers in continuous time-domain.

	1.- Single-loop	Double-loop			
		2.- PR+P $\vec{i}_C$	3.- PR+P $\vec{i}_1$	4.-PR+PR $\vec{i}_C$	5.- PR+PR $\vec{i}_1$
$G_I(s)$	0	$sC_f\frac{Z_2}{G_{den}}$	$sC_f\frac{Z_1+Z_C}{\cdot G_{den}}$	$sC_f\frac{Z_2}{G_{den}}$	$sC_f\frac{Z_1+Z_C}{\cdot G_{den}}$
$G_{IE}(s)$	0	$sC_f\frac{Z_1}{G_{den}}$	$-\frac{sC_f Z_C}{G_{den}}$	$sC_f\frac{Z_1}{G_{den}}$	$-\frac{sC_f Z_C}{G_{den}}$
$C_I(s)$	1	k_{PI}		$k_{PI}+k_{RI}\frac{s}{s^2+\omega_0^2}$	
$C_V(s)$	$k_{PV}+k_{RV}\frac{s}{s^2+\omega_0^2}$				

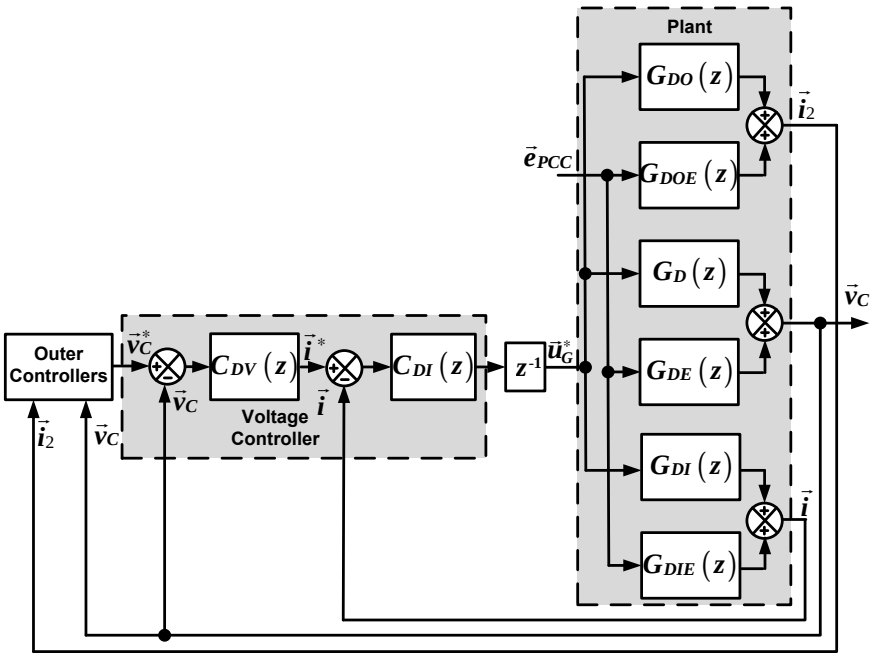

Fig. 3.3: Generalized closed-loop control scheme for each of the five voltage control architectures analyzed in this work.

The general transfer functions can be obtained by means of the scheme in Fig. 3.3. The open-loop transfer function $L(z)$, defined as the relation between the variable under control and the control error, is shown in (3.6):

$$L(z)=\left.\frac{\vec{v}_C(z)}{\vec{v}_C^*(z)-\vec{v}_C(z)}\right|_{\vec{e}_{PCC}=0}=\frac{z^{-1}C_{DI}C_{DV}G_D}{1+z^{-1}C_{DI}G_{DI}} \tag{3.6}$$

The capacitor voltage can be expressed in function of its reference $\vec{v}_C^*$ and the disturbance $\vec{e}_{PCC}$ by means of the closed-loop transfer function $T(z)$ and the closed-loop disturbance transfer function $T_E(z)$:

$$\begin{aligned} T(z)&=\frac{z^{-1}C_{DI}C_{DV}G_D}{1+z^{-1}C_{DI}\left(G_{DI}+C_{DV}G_D\right)} \\ T_E(z)&=\frac{G_{DE}+z^{-1}C_{DI}\left(G_{DI}G_{DE}+G_{DIE}G_D\right)}{1+z^{-1}C_{DI}\left(G_{DI}+C_{DV}G_D\right)} \end{aligned} \tag{3.7}$$

The sensitivity transfer function $S(z)$ is defined as the relation between the control error and the control reference:

$$S(z)=\left.\frac{\vec{v}_C^*(z)-\vec{v}_C(z)}{\vec{v}_C^*(z)}\right|_{\vec{e}_{PCC}=0}=\frac{z^{-1}C_{DI}G_{DI}}{1+z^{-1}C_{DI}\left(G_{DI}+C_{DV}G_D\right)} \tag{3.8}$$

Although the controller directly regulates the voltage and hence, the value of the output current is defined, it is important to analyze the implicit current response due to it also affects in the power dynamics. The output current $\vec{i}_2$ response is described by:

$$\vec{i}_2 = T_{VI}(z)\vec{v}_C^{*}(z) + T_{VIE}(z)\vec{e}_{PCC}(z) \tag{3.9}$$

with:

$$T_{VI}(z) = \frac{z^{-1}C_{DI}C_{DV}G_{DO}}{1 + z^{-1}C_{DI}(G_{DI} + C_{DV}G_D)}$$
$$T_{VIE}(z) = G_{DO}G_D^{-1}(T_E - G_{DE}) - G_{DOE} \tag{3.10}$$

The comparison of the voltage control architectures can be quite sensitive to the tuning of each option. In order to split between the obtained results and the controller tuning, all the controllers are configured attending to a common main points: the minimization of the settling time with a good damping ratio and a wide stability margin. Then, the analysis compares the different architectures with the fixed configuration in these and more features.

3.3.2. Grid-connected performance.

The performance of the controller in grid-connected mode is evaluated in terms of: 1) power dynamics and stability, 2) harmonic cancellation capability and 3) the inherent damping capacity of the filter resonance. However in 2) and 3) the five architectures present almost equivalent results.

The power dynamics are studied from the point of view of the power-voltage (PV) controllers fitting parameter. The PV-fitting makes reference to the decoupling between the corresponding dynamics of the power and voltage controller [Kim, *et al.,* 2011]. A fast voltage control improves the decoupling and extends the number of feasible power control configurations, especially those with high bandwidth. $T(z)$ is a sixth order transfer function for architectures 1, 2 and 3, while the order increases to eighth in architectures 4 and 5. However, the dynamic response of $\vec{v}_C$ is mainly determined by the dominant poles of $T(z)$, which makes easier the analysis. The grade of dominance of a pole is fixed by its residue. The residue of a root is defined as the weight of that root in the overall temporal response of a multi-root system. The greater the residue, the heavier the response of the root is. The magnitude of the residue is mainly given by two parameters: it is inversely proportional to the distance between the root and stability circle and directly proportional to the distance between the root and its neighbor zeros. Inspecting the closed-loop poles and zeros, it can be concluded that architectures 1 and 2 contains three dominant poles, architectures 3 and 5 have only two dominant poles and finally the power response of architecture 4 depends on five dominant poles. Verifying this statement, Fig. 3.4 shows the roots and zeros of $T(z)$ for each control architecture in the dominant area. The integral behavior of $\vec{i}_1$ penalizes the settling time when it is used in the current control in contrast with $\vec{i}_C$, which presents a derivative

nature and thus, it is more sensitive to changes in $\vec{v}_C$. The use of the PR controller in the current controller slows down the voltage response too. Architectures 1 and 2 provide the fastest and almost identically settling times, while architecture 5 presents the slowest response. Only architectures 1, 2 and 3 satisfy the bandwidth requirement imposed in Table 3.1. Regarding the overshoot, architectures 4 and 5 have poorer results. The PR in the inner loop increases the tuning complexity and hence, the desired damping ratio is difficult to be obtained.

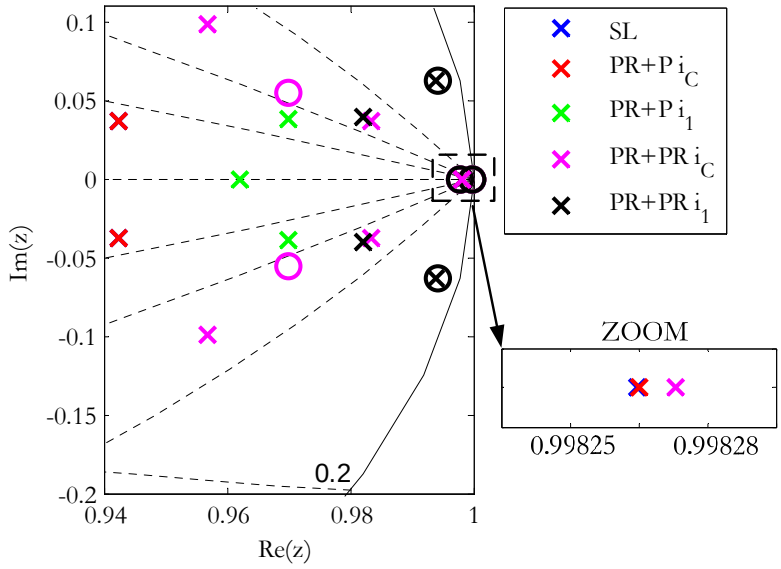

Fig. 3.4: Closed-loop poles and zeros of $T(z)$ for each voltage control architecture in the dominant area. Dominant complex conjugate poles define the power response while the simple slow pole affects the PV-fitting.

Apart from the complex conjugate roots, architectures 1, 2 and 4 contains a very slow simple pole quite near to point $1+j0$. A zoom has been carried out to accurately show their specific location. Due to the position of the zeros, the residue associated to this slow pole is greater in $T_{VIE}(z)$. As a consequence, the output current shows a long duration first order response as depicted in Fig. 3.5, leading to active and reactive powers oscillations around the fundamental frequency ω_0. In case of architectures 2 and 4, the derivative behavior of $\vec{i}_C$ introduces a zero at low frequencies in $G_{DI}(z)$, which provokes the apparition of this slow simple pole in $T_{VI}(z)$. This is a classy effect in systems without line current regulation and with a strong inductive nature. The re-adaptation of the controller's constants does not smooth this effect. Only the addition of resistive elements does. The problem is totally avoided when controlling $\vec{i}_1$. In this case, the control gets more sensitive over the line current and no slow first order responses are noticed.

Once the influence of the voltage controller over the power dynamics and the absolute stability has been verified by means of the closed-loop poles or the angles criterion, the robust stability can be analyzed with the Nyquist diagram of $L(z)$. The system under investigation is non-minimum phase and the use of the Nyquist diagram needs particular care as discussed in

[Kuo, 1991]. Fig. 3.6 shows the Nyquist diagram of $L(z)$ for each architecture. The Nyquist diagrams of control schemes 1 and 2 are almost identically. The crossing between the Nyquist diagram and the real axis gives an idea of the gain margin (GM) while the crossing with the unity circle makes reference to the phase margin (PM) [Skogestad, *et al.,* 1998]. However, the peculiarity of non-minimum phase systems makes more attractive the use of the infinite norm of the sensitivity function in order to carry out a quantitative comparison. This norm is inversely proportional to the minimum distance *d* between the Nyquist of $L(z)$ and the critic point (-1,0) as given by (3.11). The magnitude of the $S(z)$ is represented in Fig. 3.7. One more time, the corresponding curves of architectures 1 and 2 are overlapped. A good design criteria is keeping the infinite norm under 6 dβ. The infinite norms of architectures 1 to 5 are, respectively, 1.76, 1.74, 1.29, 2.49 and 2.46 dβ. The robust stability provided by architectures 1 to 3 is quite good. The use of a PR controller in the current loop increases the infinite norm, and hence, worsens the robust stability of architectures 4 and 5. It makes the system more vulnerable under any drift in the filter parameters.

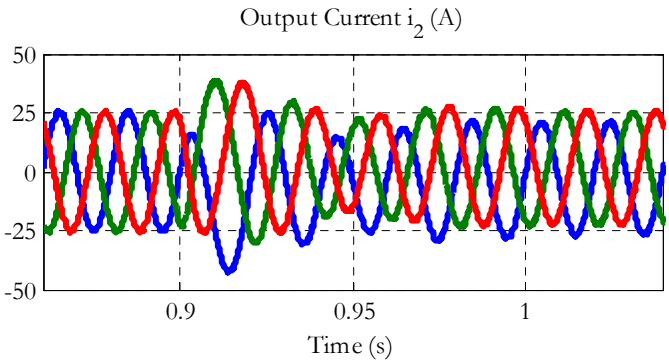

Fig. 3.5: First order behavior in the output current under disturbance transients when using architectures 1, 2 and 4.

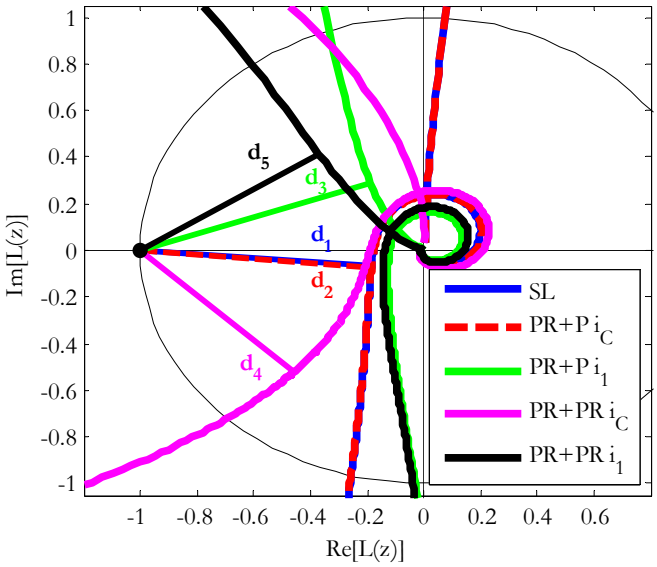

Fig. 3.6: Study of relative stability by means of the Nyquist diagram of the open-loop transfer function.

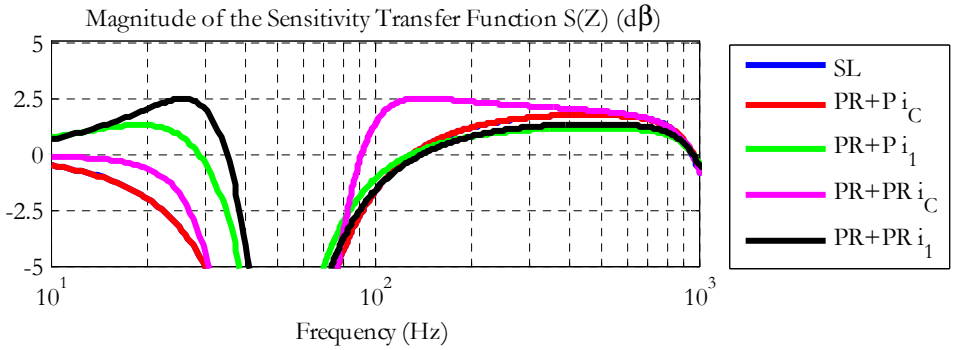

Fig. 3.7: Magnitude representation of the Bode diagram of the sensitivity transfer function of each architecture.

$$d=\frac{1}{\|S\|_\infty}=\frac{1}{\max_{\Omega}|S(\Omega)|},\ \|S\|_\infty \le 6d\beta \leftrightarrow d\ge 0.5 \tag{3.11}.$$

3.3.3. Island performance.

The performances of the controller in island operation mode are evaluated in terms of: 1) voltage regulation capacity and robustness under load changes, 2) response under frequency changes and power quality. However in the latter, the five architectures present almost equivalent results.

The regulation of the load voltage can be accurately evaluated by means of the closed-loop output impedance of the system, $Z_0(z)$. According to the Thevenin´s equivalent, it is defined as the division between the island voltage $\vec{e}_{ISL}$ and the opposite of the output current $(-\vec{i}_2)$ when the independent sources are canceled, that is $\vec{v}_C^*=0$. Note that, during the island operation, the island voltage $\vec{e}_{ISL}$ is the disturbance voltage instead of the PCC voltage. $Z_0(z)$ logically refers to the closed-loop impedance. It can be further modified by the power control or outer virtual impedance terms. The design of $Z_0(z)$ is not trivial. On one hand, from the point of view of a voltage source, it is desired to present a notch frequency behavior with the dead band around the control frequency ω_0. That way, the regulation over the island voltage is full while any disturbance in other frequency can be more or less rejected. On the other hand, from the point of view of an isolated system with several parallel power units, a small output impedance is at least desired for avoiding re-circulating currents among units. In this section, the modification carried out by the voltage controller is analyzed.

$$Z_0(z)=-\frac{\vec{e}_{PCC}}{\vec{i}_2}\bigg|_{\vec{v}_C^*=0}=-T_{VIE}^{-1} \tag{3.12}.$$

The bode diagram of $Z_0(z)$ is depicted in Fig. 3.8. The value of $Z_0(z)$ at ω_0 matches up with the output filter impendace Z_2 (see Table 7.1) regardless the control architecture. These simple voltage controllers are able to behave as ideal voltage sources when using LC filter. However, they do not have capacity to act over L_2. Focusing on the low frequency range, architectures 1, 2 and 4 keep the very low magnitude presented by Z_2, which evidences the

high sensitivity of $\vec{i}_2$ to any disturbance in such frequency ranges. The feedback of $\vec{i}_1$ provides a purely resistive behavior with a higher magnitude that reduces this effect. This logically keeps relation with the slow pole of previous section.

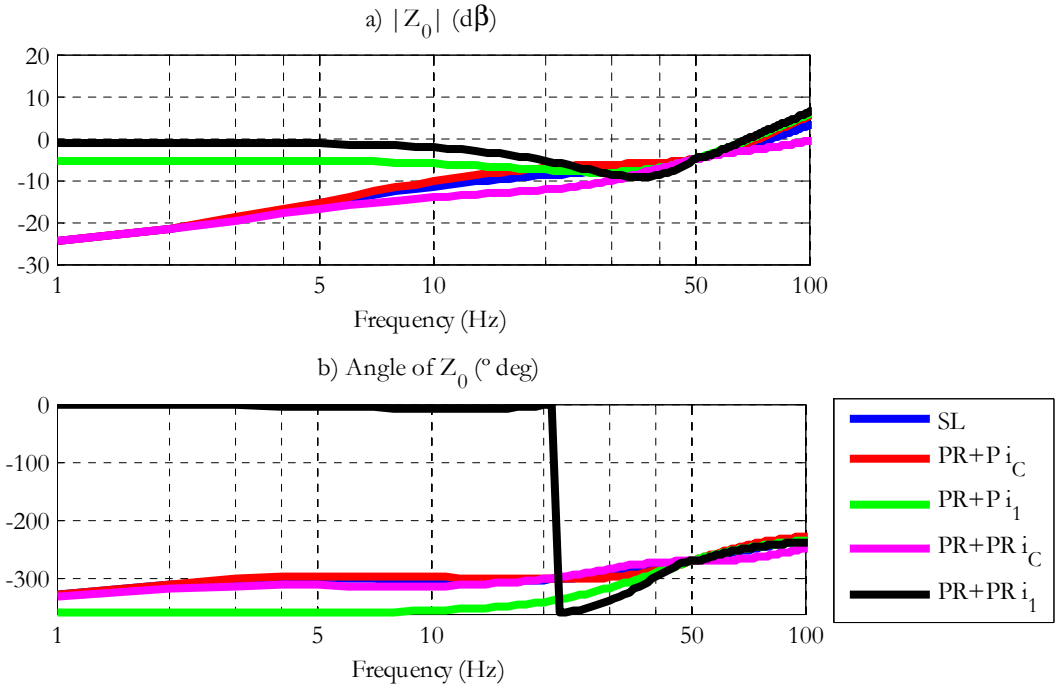

Fig. 3.8: Bode diagram of the closed-loop output impedance a) magnitude and b) angle.

As long as the number of units in parallel decreases or the total power demanded by the local load goes down, the effect of the load gets more notorious and the plant model given just by the LCL filter losses some accuracy. The effect of the local load Z_{LOAD} can be modeled by adding it to the impedance Z_2. The resistive part of the load is suspected to experience larger changes. The closed-loop poles of $T(z)$ with different resistive loads with power ratings from 6kW to 24kW are shown in Fig. 3.9. By observing the variation of the location of the dominant poles, it can be noted that loads with low power demands affects seriously to voltage dynamics. The natural frequency is the parameter more sensitive, but the bandwidth and damping ratio are also notoriously modified. Although the dominant poles of techniques 3 and 5 varies as well, their locations are always more convenient that in architectures 1, 2 and 4. Hence, the use of $\vec{i}_1$ in the current loop gives a better robustness in contrast with the use of $\vec{i}_C$ or the single-loop architecture. As long as the load power increases, the voltage response becomes more similar to the designed one. Regarding the resonant poles, high values of the load resistor (low active power consumption) improve the LCL filter resonance damping.

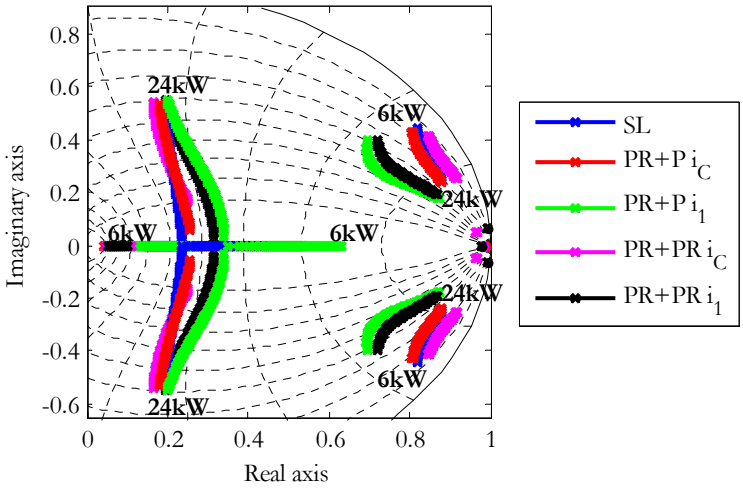

Fig. 3.9: Evaluation of the robustness of the voltage controller under different resistive loads from 24kW to 6kW by means of the closed-loop poles.

3.4. Conclusions.

This chapter has introduced the general scheme of the Universal Operation controller, which satisfies the requirements imposed for each operating mode. It has been shown that the use of an LCL filter with the right configuration provides an important robustness in the power regulation while the voltage drop across the output impedance is not very remarkable.

On the other hand, the theoretical comparative of the voltage control architectures seems to be very illustrative. The use of the PR controller on the current loop (architectures 4 and 5) is not recommended at all in contrast with the P controller (architectures 2 and 3) or the voltage single-loop (architecture 1): it generally provides worse results and makes more complex the control. The use of the filter current as feedback presents a good performance in all the analyzed features: good bandwidth, removal of power oscillations under disturbance transients and perfect performance under load changes in island mode. Waiting for an experimental validation, this makes the architecture 3 the most suitable option for the Universal Operation.

Chapter 4.

Universal Power and DC-link Voltage Controls

This chapter addresses the power control block of the GS converter and the regulation of the DC-link voltage in both grid-connected and island modes. It has been already mentioned the crucial role both blocks play inside the regulation of a UWT.

Regarding the power control, two different solutions are compared and analyzed. The first one uses the VCVSC philosophy in grid-connected and island modes. The droop control is employed for all the states of the Universal Operation with the premise of an improved response during the transitions. The study covers the obtaining of an accurate model of the plant and tuning of the controller following the requirements of section 3.1. Moreover, a power sharing strategy is proposed for increasing the power supply reliability ratios based on a fair approach where each unit contributes in function of its current generation and kinetic storage.

The second option makes use of a CCVSC philosophy in grid-connected while the VCVSC is necessarily kept in island.

The DC-link voltage control for both operating modes is also presented. The great peculiarity resides during the island operation due to the especial requirements of this state and where the pitch control, DC-braking chopper and the kinetic storage play a great role.

Finally, a statistical study, which supplies accurate data regarding the real improvement over power supply reliability ratios when using the Universal Operation of WTs, is developed. It

analyzes the probability of cover an interruption as function of the wind profile and load consumption and the reduction of the power supply interruption.

4.1. Droop control for Universal Operation.

The droop control is the VCVSC based power controller solution. It actuates over the voltage as function of some active and reactive power references. In this section, this control option is analyzed for both island and grid-connected operation modes.

Regarding the island operation, as mentioned in Chapter 3, the UWT should actively participate in the regulation of the local voltage and share the load power demands with the rest of parallel sources. The use of frequency and voltage droops, as in the primary frequency control of synchronous generators, smoothes the connection and interaction of parallel sources. The traditional frequency and voltage droops are expressed by (2.1) and shown in Fig. 2.4. On the other hand, during the grid-connected operation, the droop control is employed to supply the voltage reference that achieves a zero steady-state error in P_G and Q_G. The voltage and frequency are given by the grid and the UWT behaves as a grid-feeding system. In this mode, the power dynamics are uniquely fixed by the UWT and they should mainly guarantee a good settling time, robust stability and damping ratio. Therefore, the UWT permanently behaves as a voltage source (even in grid-connected mode), given that the voltage control dynamics are much faster. The power control structure is then kept constant in both operating laying on the premise of enhancing the transient response the connection and reconnection from the grid.

Fig. 4.1 depicts a simplified scheme where the apparent power transfer between the UWT and the PCC is described. The UWT is represented as an ideal voltage source with $\vec{v}_C$ and so does is done with PCC voltage (unbalanced and distorted conditions are not considered). The interface impedance is composed by Z_{Li} and Z_2. Generally, as explained in Chapter 3, the magnitude of Z_{Li} is negligible in regard with the magnitude of Z_2. Therefore, only the filter impedance is taken into consideration. The active and reactive power transfers of the UWT can be related with the magnitude and phase differences between the two voltages. As $\vec{e}_{PCC}$ is taken with null phase, the phase displacement is directly θ_C. Expression (4.1) collects the relation in steady-state.

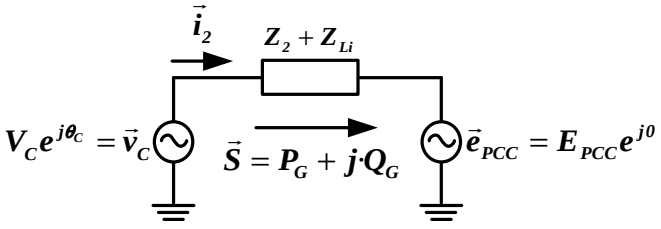

Fig. 4.1: Apparent power transfer between two voltage sources.

$$P_G = \frac{V_C^2}{R_2^2 + (\omega_0 L_2)^2}\left[R_2\left(V_C - E_{PCC}\cos\theta_C\right) + \omega_0 L_2 E_{PCC}\sin\theta_C\right]$$
$$Q_G = \frac{V_C^2}{R_2^2 + (\omega_0 L_2)^2}\left[\omega_0 L_2\left(V_C - E_{PCC}\cos\theta_C\right) - R_2 E_{PCC}\sin\theta_C\right] \quad (4.1).$$

In the following sections, the dynamics of the plant for the droop control are studied, the control parameters are configured and a power sharing strategy is proposed.

4.1.2. Dynamic phasor and small signal analysis.

The analysis developed in this subsection is based on the works [Zhang, *et al.,* 2010] and [Brabandere, 2006]. The objective is to obtain the dynamic power response of the system shown in Fig. 4.1 by means of a dynamic phasor model (DPM). The current vector $\vec{i}_2$ is given by:

$$L_2 \frac{d\,\vec{i}_2}{dt} = \vec{v}_C - \vec{e}_{PCC} - R_2\vec{i}_2 \quad (4.2).$$

By transforming each quantity to dq-frames:

$$L_2 \frac{d\,i_{2d}}{dt} = v_{Cd} - E_{PCC} - R_2 i_{2d} + \omega_0 L_2 i_{2q}$$
$$L_2 \frac{d\,i_{2q}}{dt} = v_{Cq} - R_2 i_{2q} - \omega_0 L_2 i_{2d} \quad (4.3).$$

where $v_{Cd} = V_C\cos(\theta_C)$ and $v_{Cq} = V_C\sin(\theta_C)$. The apparent power vector $\vec{S}$ is denoted by:

$$\vec{S} = P_G + jQ_G = \frac{3}{2}\vec{v}_C\left(\vec{i}_2\right)^*$$
$$P_G = \frac{3}{2}\left(v_{Cd} i_{2d} + v_{Cq} i_{2q}\right) \quad (4.4).$$
$$Q_G = \frac{3}{2}\left(v_{Cq} i_{2d} - v_{Cd} i_{2q}\right)$$

The power response given by (4.3) and (4.4) is clearly non linear. Small signal deviations are considered around the operating points of V_C, θ_C, i_{2d}, i_{2q}, P_G and Q_G, denoted with subscript 0:

$$V_C = V_{C0} + \Delta V_C \quad i_{2d} = i_{2d0} + \Delta i_{2d} \quad P_G = P_{G0} + \Delta P$$
$$\theta_C = \theta_{C0} + \Delta\theta_C \quad i_{2q} = i_{2q0} + \Delta i_{2q} \quad Q_G = Q_{G0} + \Delta Q$$
$$\Delta v_{Cd} \approx \left(\cos\theta_{C0}\Delta V_C - V_{C0}\sin\theta_{C0}\Delta\theta_C\right) \quad (4.5).$$
$$\Delta v_{Cq} \approx \left(\sin\theta_{C0}\Delta V_C + V_{C0}\cos\theta_{C0}\Delta\theta_C\right)$$

Inserting (4.5) into (4.4), neglecting second order deviations and cancelling the operating point values:

$$\begin{aligned}\Delta P=&\frac{3}{2}[V_{C0}\cos\theta_{C0}\Delta i_{2d}+V_{C0}\sin\theta_{C0}\Delta i_{2q}+i_{2d0}\left(\cos\theta_{C0}\Delta V_C-V_{C0}\sin\theta_{C0}\Delta\theta_C\right)\\&\cdots+i_{2q0}\left(\sin\theta_{C0}\Delta V_C+V_{C0}\cos\theta_{C0}\Delta\theta_C\right)]\\\Delta Q=&\frac{3}{2}[V_{C0}\sin\theta_{C0}\Delta i_{2d}-V_{C0}\cos\theta_{C0}\Delta i_{2q}+i_{2d0}\left(\sin\theta_{C0}\Delta V_C+V_{C0}\cos\theta_{C0}\Delta\theta_C\right)\\&\cdots-i_{2q0}\left(\cos\theta_{C0}\Delta V_C-V_{C0}\sin\theta_{C0}\Delta\theta_C\right)]\end{aligned} \tag{4.6}$$

Repeating the previous step with (4.3) and applying the Laplace operator, Δi_{2d} and Δi_{2q} are obtained in function of ΔV_C and $\Delta\theta_C$ as:

$$\begin{aligned}\Delta i_{2d}=&\left[\frac{\left(R_2+sL_2\right)\cos\theta_{C0}+\omega_0 L_2\sin\theta_{C0}}{\left(R_2+sL_2\right)^2+\left(\omega_0 L_2\right)^2}\right]\Delta V_C+V_{C0}\left[\frac{\omega_0 L_2\cos\theta_{C0}-\left(R_2+sL_2\right)\sin\theta_{C0}}{\left(R_2+sL_2\right)^2+\left(\omega_0 L_2\right)^2}\right]\Delta\theta_C\\\Delta i_{2q}=&\left[\frac{\left(R_2+sL_2\right)\sin\theta_{C0}-\omega_0 L_2\cos\theta_{C0}}{\left(R_2+sL_2\right)^2+\left(\omega_0 L_2\right)^2}\right]\Delta V_C+V_{C0}\left[\frac{\left(R_2+sL_2\right)\cos\theta_{C0}+\omega_0 L_2\sin\theta_{C0}}{\left(R_2+sL_2\right)^2+\left(\omega_0 L_2\right)^2}\right]\end{aligned} \tag{4.7}$$

Considering that the magnitude of Z_2 is not too big, just small phase and magnitude differences between $\vec{v}_C$ and $\vec{e}_{PCC}$ are required to deliver certain active and reactive powers:

$$\begin{aligned}V_{C0}&\approx E_{PCC}\\\cos\theta_{C0}&\approx 1\ ;\ \sin\theta_{C0}\approx\theta_{C0}\approx 0\end{aligned} \tag{4.8}$$

Using (4.7) and (4.8), the DPM of the droop plant results in:

$$\begin{bmatrix}\Delta P\\\Delta Q\end{bmatrix}=\begin{bmatrix}G_{P\theta}(s) & G_{PV}(s)\\G_{Q\theta}(s) & G_{QV}(s)\end{bmatrix}\begin{bmatrix}\Delta\theta_C\\\Delta V_C\end{bmatrix} \tag{4.9}$$

where:

$$\begin{aligned}G_{P\theta}(s)&=\frac{3}{2}\frac{\omega_0 L_2}{\left(R_2+sL_2\right)^2+\left(\omega_0 L_2\right)^2}\left(E_{PCC}\right)^2\\G_{PV}(s)&=\frac{3}{2}\frac{\left(R_2+sL_2\right)}{\left(R_2+sL_2\right)^2+\left(\omega_0 L_2\right)^2}E_{PCC}\\G_{QV}(s)&=\frac{G_{P\theta}(s)}{E_{PCC}}\\G_{Q\theta}(s)&=-E_{PCC}G_{PV}(s)\end{aligned} \tag{4.10}$$

As suspected, the filter impedance has a great weight in the model described by (4.10). However, it also hints an important dependence on E_{PCC}, which can affect the predetermined control dynamics under voltage dips and swells. Fig. 4.2 contains the actual active and reactive power dynamics when two steps are carried out in θ_C (0.1 s) and V_C (0.5 s) in the system of Fig. 4.1. The magnitude of both steps is 1% ($\Delta\theta_C$ =0.0314 rad and ΔV_C =3.27 V). To assess the accuracy of the obtained model, the actual power responses are overlapped with the

resulting ones in (4.9). As shown, the active and reactive power dynamics perfectly match up under steps on θ_C and V_C, verifying the continuous-time domain transfer functions of (4.10).

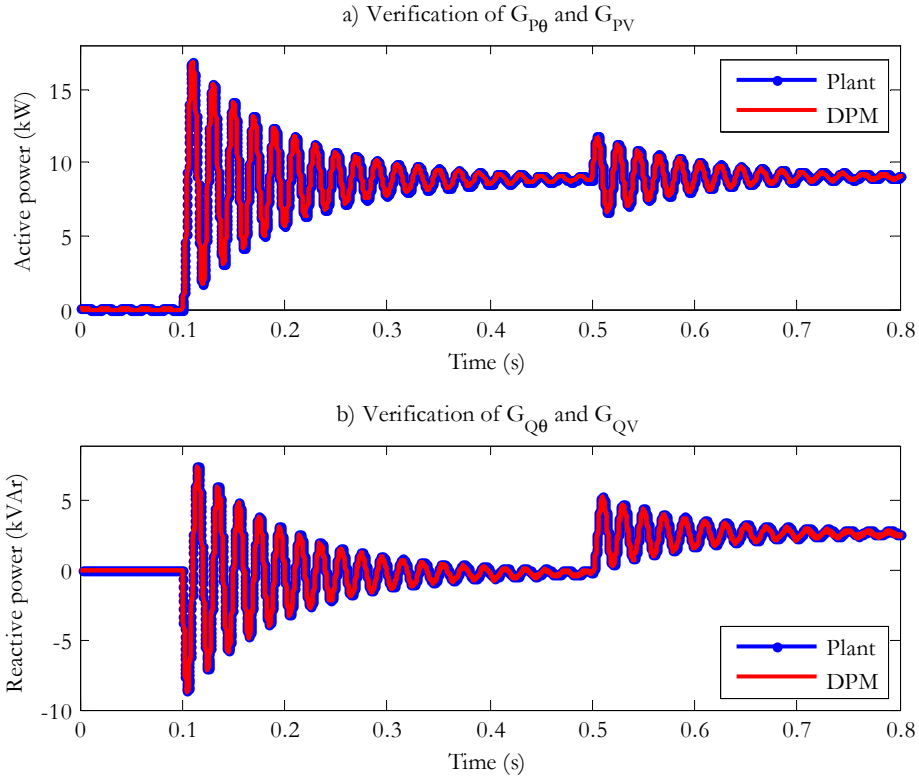

Fig. 4.2: a) Comparison between the actual and obtained active power responses under a magnitude and phase voltage steps and b) Comparison between the actual and obtained reactive power responses under a magnitude and phase voltage steps.

In order to evaluate the weight of V_C and θ_C on P_G and Q_G, the gain of $G_{P\theta}(s)$, $G_{PV}(s)$ $G_{QV}(s)$ and $G_{Q\theta}(s)$ are analyzed with the help of their Bode diagrams, shown in Fig. 4.3. The weight of V_C over the active power is fixed by the product between the magnitude of its deviation and the steady-state gain of $G_{PV}(s)$:

$$G_{PV,ss} = \lim_{s \to 0} G_{PV}(s) \tag{4.11}.$$

Analogously, the influence of θ_C on P_G is given by $G_{P\theta,ss}$ and the step magnitude of $\Delta\theta_C$. Considering the steady-state gains displayed in Fig. 4.3 for a mainly inductive filter impedance Z_2 ($\omega_0 L_2 >> R_2$) and supposing that the step magnitude of ΔV_C is quite greater than $\Delta\theta_C$, it can be concluded that the steady-state value of P_G mainly depends on θ_C and the Q_G is dominated by V_C. This statement can be verified on Fig. 4.2 and makes sense (2.1). Both steps provoke coupling transient responses in P_G and Q_G, but only $\Delta\theta_C$ modifies the steady-state value of P_G and only ΔV_C changes the steady-state value of Q_G.

A resonant behavior at ω_0 can be appreciated on the Bode diagram of each transfer function This fact is corroborated with the waveforms of the transient response, which

contains an oscillation at ω_0 with low damping, as depicted by Fig. 4.2. This effect is easily explained with the common denominator of the transfer functions, knowing the inductive behavior of Z_2. The physical explanation is: under a change in the voltage drop across an inductive element, the transient current contains an exponentially decreasing amplitude-modulating component that differently affects each current phase. It can be seen as a exponentially decreasing DC component that transiently provokes a power oscillation at ω_0. The value of R_2 can be used to damp the resonant behavior at the expense of increasing the losses and the coupling between active and reactive power. As mentioned in 3.3.2, this resonance behavior can be damped using the current i_1 as internal feedback variable.

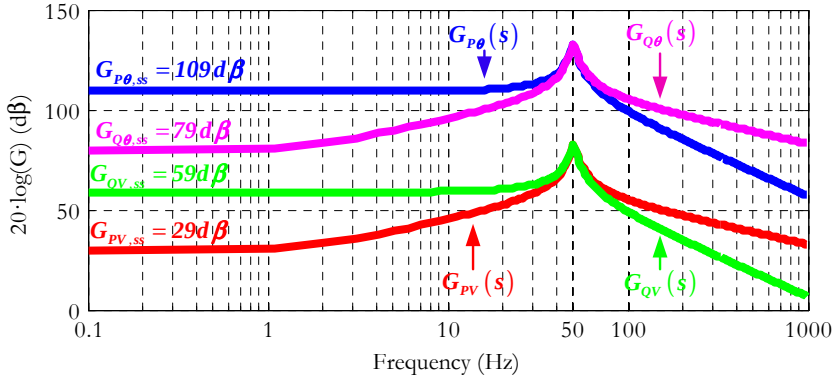

Fig. 4.3: Bode diagram of the transfer functions that define the droop control plant.

It has been verified by means of Fig. 4.2 that the obtained model accurately represents the power transfer between two voltage sources. However, the supposed conditions are not always satisfied or accurate:

(1) the voltage source $\vec{e}_{PCC}$ has been represented as a stiff voltage like it would be connected to a strong grid

(2) the model does not consider the presence of unbalanced or distorted conditions and

(3) the model has been constructed by means of a small-signal approach around a bias point.

In such conditions four different scenarios are considered:

- The marginal power rating of the UWT supposes a big portion of the overall island capacity. In this scenario, premise (1) is not fulfilled and the dynamics of $\vec{e}_{PCC}$ are coupled to $\vec{v}_C$. The presented model is not as accurate as models like the developed in [He, *et al.,* 2011], which takes into account the iteration between parallel units. However, in this scenario, considering the output of the impedance serves as a good decoupling between units and supposing a load with predominant resistive nature, the dynamics of the presented model are still considered valid. The extreme case of this scenario is given

when the UWT is the sole power source of the island. This situation can be reduced to a voltage control robustness issue.

- Connection to a weak grid. The influence of the power control actuation $\vec{v}_C^*$ over $\vec{e}_{PCC}$ is not negligible and premise (1) is again not satisfied. In order to minimize this effect, the control tuning should also attend to robust restrictions.

- Presence of negative sequence. The presence of unbalanced conditions can be very common during grid faults or in island operation as a consequence of a load unbalance. In case of the island operation, the strategy should keep injecting balanced voltages. However, during the grid-connected operation, the injection of balanced voltages causes high oscillations at $2\omega_0$ in the power and the DC-link voltage that could lead to the instability of the system. In such conditions, it is necessary to modify the power controller response to minimize the power oscillation by the injection of negative sequence voltage.

- Different bias-points. Premise (3) is impossible to be fulfilled and small-signal approaches are generally adopted as an approximation. By limiting the magnitude of Z_2, the variation of V_{C0} and θ_{C0} in function of the operation conditions is reduced.

Other assumptions have been also taken into account, but the system configuration makes the dynamics invulnerable to them. For instance, the inductive nature of Z_2 is assured in the design of the LCL filter assuring a good power decoupling.

The transfer functions $G_{P\theta}(z)$ and $G_{QV}(z)$ represent the discrete-time domain versions of $G_{P\theta}(s)$ and $G_{QV}(s)$ obtained by means of the ZOH, respectively:

$$\begin{aligned} G_{P\theta}(z) &= ZOH\left(G_{P\theta}(s)\right) \\ G_{QV}(z) &= ZOH\left(G_{QV}(s)\right) \end{aligned} \qquad (4.12).$$

4.1.3. Controller structure.

Fig. 4.4 contains the implementation of the VCVSC based power controller used for the Universal Operation. It is based on a direct droop control topology. P_G and Q_G are calculated by means of $\vec{i}_2$ and $\vec{v}_C$ and then filtered with a low-pass filter $F(z)$, assuring a right representation. The filtered versions, P_{GF} and Q_{GF}, mainly contain the DC components. The power decoupling is almost assured with the inductive design of Z_2. However, Z_2 is not completely inductive and small coupling between active and reactive power can be experienced during the transients. The decoupling matrix T_D [Brabandere, *et al.,* 2007] translates the power errors into a virtual power frame. It basically distributes the active and reactive power steps into voltage phase and magnitude steps accordingly with the resistive and inductive parts of Z_2 as:

$$T_D = \frac{1}{Z_2}\begin{bmatrix} \omega_0 L_2 & -R_2 \\ R_2 & \omega_0 L_2 \end{bmatrix} \quad (4.13).$$

Then, the droop strategy is implemented following (2.1). During the island operation, the P_G-ω droop is characterized by $-k_{Pf}$ while $-k_{QV}$ determine the Q_G-V_C droop. To obtain zero steady-state error in P_G and Q_G in grid-connected, at least type 1 open-loop transfer functions are required. This is equivalent to have one integrator. The P_G-θ_C loop already has an integrator to obtain $\Delta\theta$. In order to readapt the droop controller for the three different operating modes, the state signal S is employed for enabling controllers, changing the initial conditions of some integrators and switching between base variables. This way, the required versatility for working in all the operating modes is achieved with just one block. An integral controller with gain k_{IV} is enabled in the Q_G-V_C loop during the grid-connected operation. In such conditions, both P_G-θ_C and Q_G-V_C loops assure zero steady-state error adapting $\vec{v}_C$ with the voltage drop and phase displacement caused across the output impedance. Besides, a derivative controller with gain k_{Df} is also added in the P_G-ω loop (equivalent to a proportional controller in the P_G-θ_C loop) to enhance the transient response. Two saturators are applied to $\Delta\theta$ and ΔV. During the island operation, they avoid exceeding the limits imposed by the power quality requirements whereas they can be taken as an additional power limitation measures for the grid-connected mode. These limits can be fixed around 5% and 2% respectively for voltage magnitude ($\pm\Delta V_{\max}$) and frequency ($\pm\Delta\omega_{\max}$).

The outputs of the saturators are respectively added to the base phase and base magnitude following the power transfer philosophy described in Fig. 4.1. S actuates over the multiplexors (A) and (B) in order to select the base voltage V_{base} and base phase θ_{base} in function of the operating mode. V_{base} is selected via the multiplexor (A) between V^* in island mode and E_{PCC} in grid-connected. Note that in island, only positive sequence is desired in the local voltage. The multiplexer (B) selects θ_{base} between $\int \omega^* dt + \theta_{IC}$ in island mode and θ_{PCC} in grid-connected. The parameters V^* and ω^* define the base point in (2.1) and Fig. 2.4. The magnitude and phase of the PCC voltage, E_{PCC} and θ_{PCC} are obtained following the procedure of (2.8). The parameter θ_{IC} is the initial conditions of the integrator. The integrator is reset every time the system starts working in island, and θ_{IC} is configured with $\theta_{PCC\alpha}$. The purpose of this procedure is to offer a smooth transition between modes avoiding phase jumps at least in the positive sequence frame. When the fault that caused the isolated operation is cleared, the synchronization mode is activated. The multiplexors (C) and (D) configure the capacitor voltage reference to follow $\vec{e}_{PCC}$. Note that during this process, the droop control outputs are not taken into account. When the island voltage is again synchronized with the grid, the breaker is closed. Immediately after a reconnection, S also resets to 0 the integrator that provides $\Delta\theta$ and the controller is again ready to work in grid-connected mode.

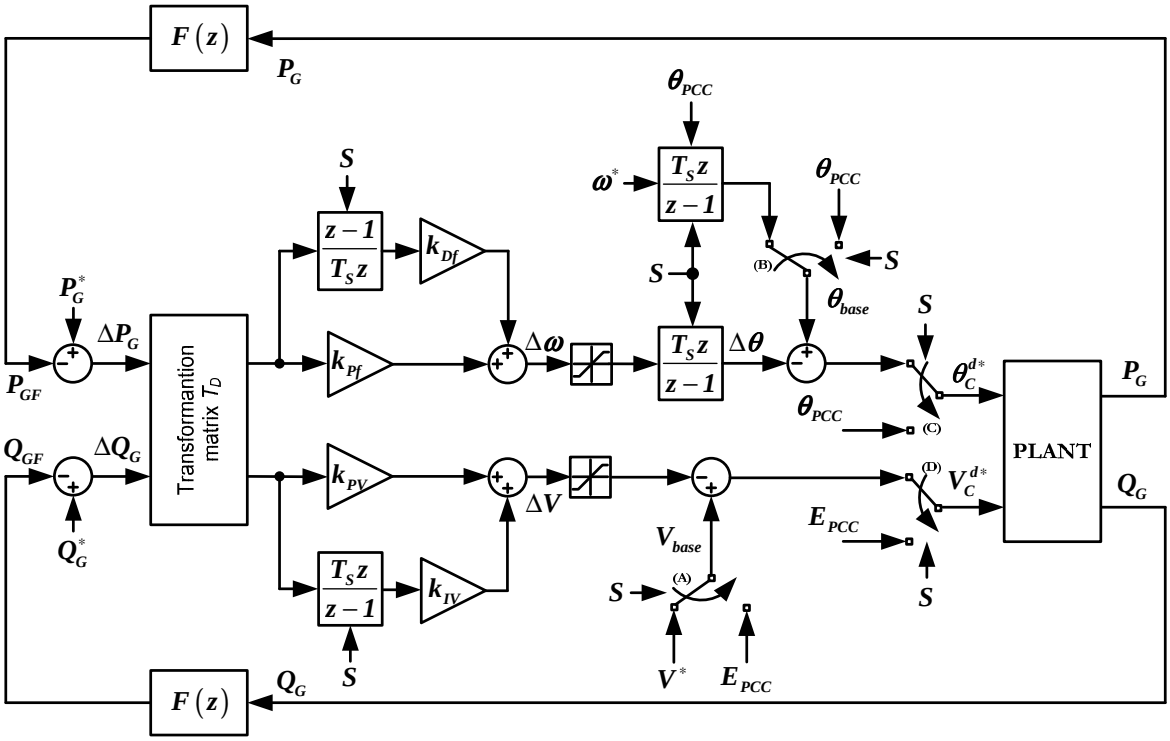

Fig. 4.4: Power controller based on droop control for Universal Operation.

The actuation of the droop control is denominated as $\vec{v}_C^{d*}$. This reference regulates the DC component of the active and reactive powers.

4.1.4. Power dynamics.

This section studies the droop dynamics and robust stability in function of the controller parameters. In grid-connected, the droop control parameters are constant and selected attending to a given power dynamics and robustness requirements. A settling time of 75 ms is desired for the power response (Table 3.1). However, as described in next section, during the island operation the values that define the droop strategy in (2.1) may vary for power sharing purposes. Therefore, in this particular case, it is important to limit the range of possible values according to stability requisites.

In such circumstances, $T_{P\theta}(z)$ and $T_{QV}(z)$ are defined as the closed-loop transfer functions (supposing neither frequency nor voltage saturation):

$$T_{P\theta}(z)=\frac{P_G^*}{P_G}=\frac{z^{-1}C_{P\theta}(z)I(z)G_{P\theta}(z)}{1+z^{-1}F(z)C_{P\theta}(z)I(z)G_{P\theta}(z)}$$
$$T_{QV}(z)=\frac{Q_G^*}{Q_G}=\frac{z^{-1}C_{QV}(z)G_{QV}(z)}{1+z^{-1}F(z)C_{QV}(z)G_{QV}(z)} \quad (4.14).$$

where z^{-1} is the computational delay to avoid the algebraic loop, $C_{P\theta}(z)$ is the PD controller in the active power loop, $I(z)$ is the phase integrator and $C_{QV}(z)$ is the PI controller in the reactive power loop:

$$C_{P\theta}(z)=k_{Pf}+k_{Df}\frac{z-1}{T_S z}$$
$$I(z)=\frac{Ts\cdot z}{z-1} \qquad (4.15).$$
$$C_{QV}(z)=k_{PV}+k_{IV}\frac{Tsz}{z-1}$$

Actually, the closed-loop transfer functions $T_{P\theta}(z)$ and $T_{QV}(z)$ are equivalent due to the cascade association between the PD controller and the integrator results in a PI. Then, it is possible to configure the same response in both power loops, which is quite interesting from the point of view of the decoupling between active and reactive power. Note that k_{Pf} is equivalent to k_{IV} and k_{Df} to k_{PV}. As expressed in (4.10), there is a factor difference (E_{PCC}) between $G_{P\theta}(z)$ and $G_{QV}(z)$ that should be taken into account. With all these considerations, the dynamics and robustness analysis is focused on $T_{P\theta}(z)$.

The first aspect to be analyzed within $T_{P\theta}(z)$ is the effect of the low-pass filter and the selection of the cut-off frequency f_C. The filter is placed to obtain the average power value and to perform a good representation of the control variables. However, it does not necessary mean that power oscillations around ω_0 and $2\omega_0$ caused by voltage or current DC components or unbalances are removed. Fig. 4.5.a, b and c depict the dominant closed-loop poles and zeros, the closed-loop step response and the bode diagram of the sensitivity transfer function expressed as $S_{P\theta}(z)=1-T_{P\theta}(z)$. These graphics have been carried out without $F(z)$ and with $F(z)$ tuned at several cut-off frequencies. It is a Butterworth Infinite Impulse Response (IIR) filter of second order. The main contribution of the filter is the damping of the 50 Hz power resonance. Note that in this particular case, a reduction of the time constant of the simple pole is also associated to the use of the filter. However, it is not correct to affirm that the filter provides faster dynamics. Higher gains can be selected when the filter is not present leading to a greater control bandwidth. On the other hand, the filter also inserts a couple of complex conjugate roots and zeros, which are getting faster as long as f_C is increased. However, the simple pole, whose position mainly provides the settling time, becomes slower with high values of f_C as it can be verified in the second zoom of Fig. 4.5.a and in Fig. 4.5.b. This trade-off is solved with the sensitivity transfer function $S_{P\theta}(z)$. As explained in section 3.3.2, the infinite norm of $S_{P\theta}(z)$, $\|S_{P\theta}\|_\infty$, is a good tool to measure the robust stability of the system, even valid for non-minimum phase systems. A reasonable robust system should keep $\|S_{P\theta}\|_\infty$ below 6 dβ [Skogestad, *et al.,* 1998]. The cut-off frequency of 40 Hz is chosen because it provides the lowest $\|S_{P\theta}\|_\infty$, approximately 4.1 dβ. Note that the enhancement in terms of robustness given by the filter also depends on the value of k_{Pf}.

The next parameter to be analyzed is the proportional gain k_{Pf} (equivalent to k_{IV} in the reactive loop). Fig. 4.6.a, b and c represent the same plots than in the filter analysis. Small values of k_{Pf} moves the complex conjugate poles of the filter towards their corresponding conjugate zeros, but also slow down the simple pole and thus, the settling time. In such

conditions, the simple pole becomes dominant and the power response can be considered as a first-order response. High values of k_{Pf} make the couple of complex poles dominant leading to a second-order power response. Although in such conditions the settling time would be below 25 ms, it also implies a poor decoupling with the voltage controller. Moreover, it is not recommendable to select big gains when the filter is inserted because it worsens the robust stability. Regarding the grid-connected operation and taking into account all these considerations, this analysis concludes with a commitment decision of k_{Pf} =1.1 10^{-4} which mainly provides a first-order power response, good robust stability and a 75 ms settling time. In case of the island operation, the upper limit is k_{STAB} = 1.3 10^{-4} while no lower limitation is required in terms of stability. The controller constant k_{Df} does not have a great influence but still can be used for slightly improving the transient power response.

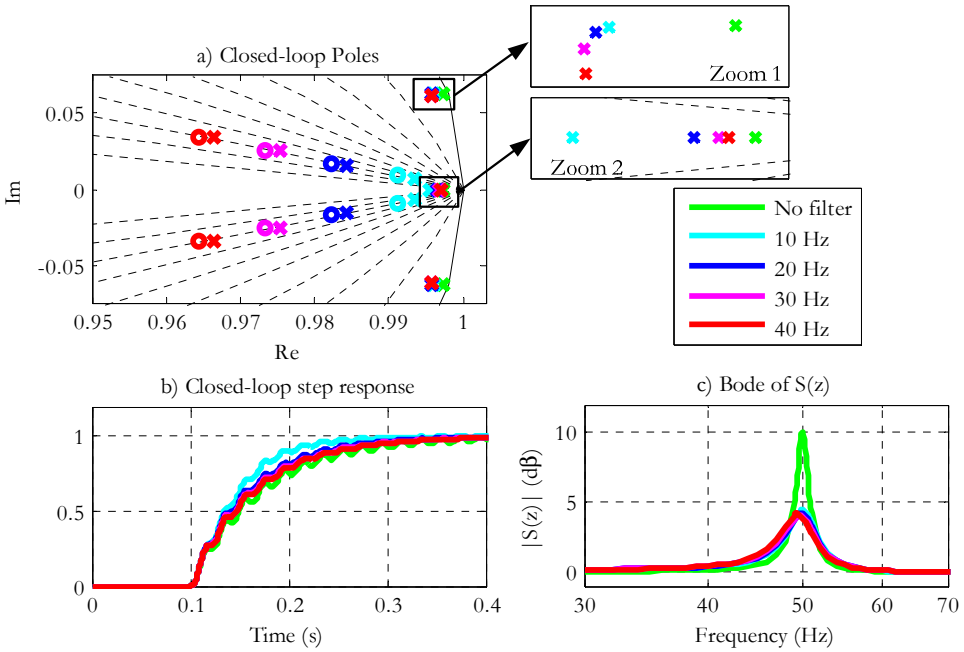

Fig. 4.5. Analysis of the effect of the presence of the filter and its cut-off frequency: a) Closed-loop poles and zeros with zoom in the 50 Hz resonant poles, b) step response of $T_{P\theta}(z)$ and c) Bode diagram of the sensitivity transfer function.

Once k_{Df} and k_{Pf} have been fixed, the reactive controller gains can be fixed as expressed by (4.16), providing exactly the same dynamics obtained in the active power loop.

$$\begin{aligned} k_{PV} &= E_{PCC} \cdot k_{Df} \\ k_{IV} &= E_{PCC} \cdot k_{Pf} \end{aligned} \qquad (4.16).$$

4.1.5. Active power sharing.

Due to the considered power level, the Universal Operation approach does not consider an island operation of many parallel sources. However, an optimum performance requires the implementation of a power sharing strategy. It is supposed that the island is mainly composed

by UWTs as parallel units, but other sources can be considered as well. The droop control constants k_{Pf} and k_{PV} are selected attending to the main island operation challenges concerning the power control: power quality, power sharing and stability.

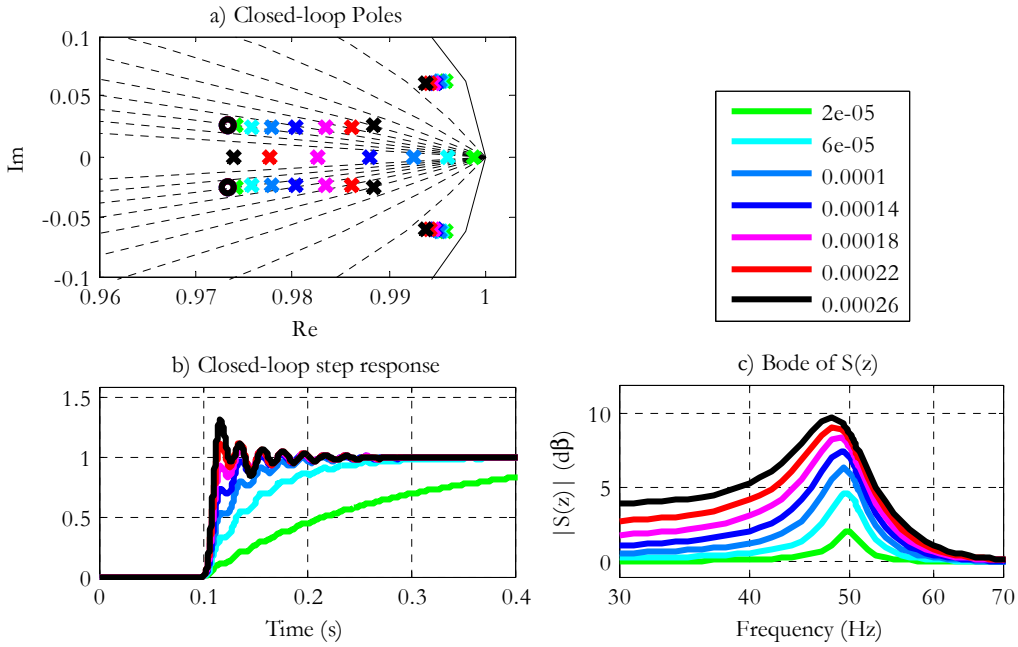

Fig. 4.6. Tuning k_{Pf} .a) Closed-loop poles and zeros, b) step response of $T_P(z)$ and c) Bode diagram of the sensitivity transfer function.

The local frequency is a common variable for every item of the island. This fact makes the use of it quite interesting as a communication resource to carry out an active power sharing strategy avoiding communication wires. In this subsection, the parameters P^*, ω^* and k_{Pf} of (2.1) are configured attending to power quality restrictions, power rating, current power generation and energy balance of each UWT. Fig. 4.7 contains the general structure of the system under study. It is composed by N units and an equivalent load. During the island mode, the unit i is independently coordinated with the P_G - ω droop:

$$\omega - \omega_i^* = k_{Pfi}\left(P_{Gi}^* - P_{Gi}\right) \tag{4.17}.$$

Then, the total power consumed in the isolated system neglecting the line losses is:

$$P_{LOAD} = \sum_{i=1}^{N} P_{Gi} = \sum_{i=1}^{N}\left(P_{Gi}^* - \frac{\omega - \omega_i^*}{k_{Pfi}}\right) \tag{4.18}.$$

By working with the previous expressions, the complex system of the N parallel units can be simplified as a unique system regulated by the P_{LOAD} - ω droop:

$$\omega - \omega_{eq}^* = k_{eq}\left(P_{eq}^* - P_{LOAD}\right) \tag{4.19}.$$

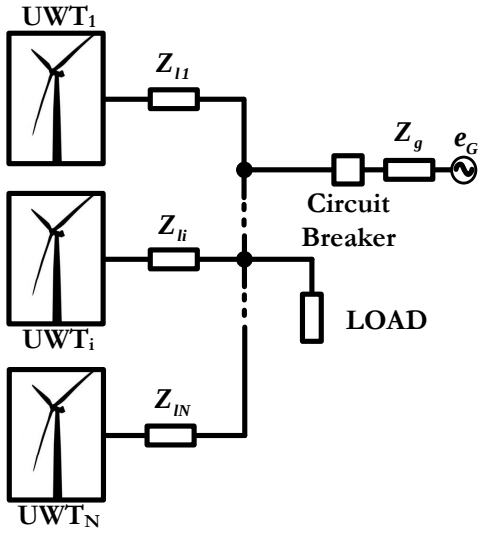

Fig. 4.7: Interconnection scheme of *N* UWTs.

$$P_{eq}^{*}=\sum_{i=1}^{N}P_{Gi}^{*};\qquad \omega_{eq}^{*}=\frac{\sum_{i=1}^{N}\left(\omega_i^{*}\prod_{\substack{j=1\\ j\neq i}}^{N}k_{Pfj}\right)}{\sum_{i=1}^{N}\prod_{\substack{j=1\\ j\neq i}}^{N}k_{Pfj}};\quad k_{eq}=\frac{\prod_{i=1}^{N}k_{Pfi}}{\sum_{i=1}^{N}\prod_{\substack{j=1\\ j\neq i}}^{N}k_{Pfj}} \tag{4.20}$$

Expressions (4.19) and (4.20) define the steady state behavior of the complex system and can be used to predict the voltage magnitude and frequency deviations as function of the demanded power.

The power injection capacity of the MS is given by the rotor speed and the torque. As long as the system takes advance of the inertia storage to cover a negative power mismatch, the rotor speed is being reduced and so does the power injection capacity. The shutting down condition is reached when the rotor speed goes below the shutting down rotor speed ω_{RSDi}, expressed in (4.21). The generator can be slightly overloaded with torque references higher than the rated value to reduce ω_{RSDi}. If $\omega_{Ri}<\omega_{RSDi}$, the island DC-link controller cannot extract the required power to keep u_{DC}, which starts falling leading to the saturation of the GS controller.

$$\omega_{RSDi}=\frac{P_{Gi}}{T_{E\max i}^{*}} \tag{4.21}$$

The capacity of regulation of the kinetic storage of each unit can be actually increased by means of the power sharing strategy. This extra degree of regulation is used for keeping ω_{Ri} higher than ω_{RSDi} and extending island operating time as much as possible. The total kinetic storage of all the UWTs is a common resource and should be managed as such. In this work, the term of power generosity is introduced as the will of injecting more active power at a fixed operation condition. The UWT can contribute with more or less active power being more or

less generous. Those UWTs with high kinetic energy reserves and instantaneous wind generation should be more generous than UWTs with reduced rotor and wind speeds.

With the aforementioned aim, the parameters P_{Gi}^{*} and k_{Pfi} are modified while $\omega_i^{*}=\omega_0$. By setting $P_{Gi}^{*}=P_{WTi}$ (see Fig. 1.6), each droop curve is adapted with its corresponding current generation. The general parameter P_{eq}^{*} matches up with the total current wind generation of the island. The total power mismatch between generation and consumption can be expressed as $P_{mis}=P_{eq}^{*}-P_{LOAD}$. Then, P_{mis} is equally shared between all the UWTs (P_{mis}/N) if they have the same droop slope. The energy management factor f_{EMi} is defined in (4.22) to readapt k_{Pfi} in function of the remaining kinetic reserve, so the power mismatch is fairly distributed as function of the remaining reserve. The parameter ω_{RNi} is the rated rotor speed. Square values of the rotor speed have been used to keep the relation with the kinetic energy stored in a rotating shaft E_{Ki}, given by expression (4.4), where J is the inertia coefficient. As long as f_{EMi} takes higher values, the power contribution of the unit i is more noticeable. The operating principle consists on modifying the droop slope as function of f_{EMi}.

$$f_{EMi}=\frac{\omega_{Ri}^2-\omega_{RSDi}^2}{\omega_{RNi}^2-\omega_{RSDi}^2};\quad f_{EMi}\in[0,1] \tag{4.22}.$$

$$E_{Ki}=\frac{J_i}{2}\omega_{Ri}^2 \tag{4.23}.$$

The selection of the slope is restricted: the upper limit $k_{\max}$ is given by stability and dynamics (see previous section) and power quality [Guerrero, *et al.,* 2011] issues and the lower limit $k_{\min}$ makes reference to the power sharing performance. Fig. 4.8 shows the concept of power generosity through the modification of the droop slope and the base point. The use of both strategies has not been proposed yet due to it addresses some challenge. The point (P_{WTi},ω_0) is fixed independently of f_{EMi}. At a fixed island frequency $\omega_2<\omega_0$, high values of the droop slope reduce the power contribution to the local load. When the operating frequency is $\omega_1>\omega_0$, high values of the droop slope increment the power contribution. . In the zone – $(\omega>\omega_0)$, UWTs with high slopes are generous while in the zone + $(\omega<\omega_0)$, high slopes turn them into selfish. Therefore, the selection of the slope k_{Pfi} via the parameter f_{EMi} has to be carried out according to the operating zone as expressed in (4.24).

$$k_{Pfi}=\begin{cases}(1-f_{EMi})k_{\min}+f_{EMi}k_{\max} & if\ \omega>\omega_0\\ f_{EMi}k_{\min}+(1-f_{EMi})k_{\max} & if\ \omega<\omega_0\end{cases} \tag{4.24}.$$

4.2. PQ-theory based power control in grid-connected operation.

This subsection presents an alternative power controller for the grid-connected operation. It is a CCVSC based option, which regulates the transference of active and reactive powers

through the control of the output current $\vec{i}_2$ by applying the PQ-theory. The PQ-theory basically consists on calculating the corresponding current reference as function of the power references and the capacitor voltage. Note that now the system behaves as a current-controlled source. It logically implies a role change during the transitions between grid-connected and island modes. The power controller is now implemented with different blocks depending on the operating mode: droop control for island operation and PQ-theory based power control for grid-connected operation. Therefore, it is crucial to fix the initial conditions of each one, so that a seamless transition is assured. The theoretical approach has been already introduced in section 2.1.4.1.

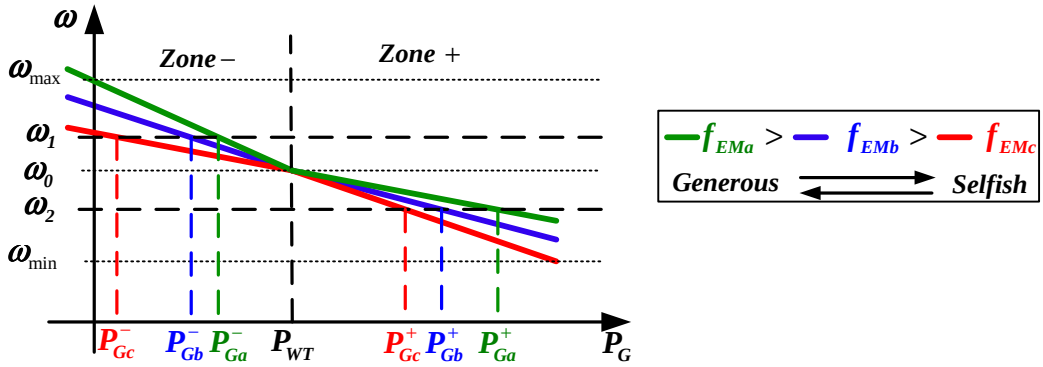

Fig. 4.8: Power generosity concept through modification of droop slopes.

Fig. 4.9 contains the block diagram of the power controller based on the PQ-theory. The operating principle is to obtain the current reference matrix $\left[i^*\right]$ as function of the power reference and voltage matrices, as expressed by (2.7).

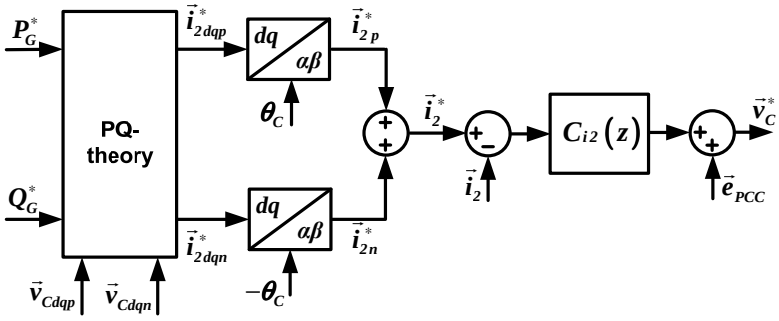

Fig. 4.9: PQ-theory based power controller.

Once the positive and negative sequence current references have been obtained in the dq-axis, they are transformed to the αβ-axis with the capacitor voltage angle. Both positive and negative sequences are regulated by means a single PR controller whose actuation is the capacitor voltage reference. In contrast with the PI controllers in dq-frames, the use of the PR allows dealing with both positive and negative sequence simultaneously. Besides, there is not any problem related with the representation of control variables under unbalanced conditions, so distortion issues are easily avoided with this solution

$$\vec{v}_C = R_2 + L_2 \frac{d}{dt}\vec{i}_2 + \vec{e}_{PCC} \tag{4.25}.$$

In contrast with the droop control, this power controller can be linearly linked to the inner voltage controller, which makes possible a more accurate study. The linearization is simply carried out by using the current references instead of the power ones. This section takes advance of the analysis carried out in section 3.3 to obtain the closed-loop response of $\vec{i}_2$. By following the control scheme of Fig. 4.9, the closed loop response of $\vec{i}_2$ can be expressed as:

$$\vec{i}_2 = T_I \cdot \vec{i}_2^{\,*} + T_{IE}\,\vec{e}_{PCC} \tag{4.26}.$$

where:

$$T_I(z) = \frac{C_{I2}(z)T_{VI}(z)}{1 + C_{I2}(z)T_{VI}(z)};\quad T_{IE}(z) = \frac{T_{VI}(z) + T_{VIE}(z)}{1 + C_{I2}(z)T_{VI}(z)}; \tag{4.27}.$$

and the current controller $C_{I2}(z)$ is given by:

$$C_{i2}(z) = k_{PI2} + k_{RI2}\frac{\sin(\omega_0 T_S)(z-1)}{z^2 - 2\cos(\omega_0 T_S)z + 1} \tag{4.28}.$$

where k_{PI2} and k_{RI2} are respectively the proportional and resonant constant. One of the advantages of taking into account the voltage loop in the study is that there is no restriction regarding the settling time of the current controller. The decoupling between controllers is already taken into account. Fig. 4.10.a, b and c respectively contain the dominant closed-loop poles and zeros, the temporal response of the magnitude of $\vec{i}_2$ and the sensitivity transfer function for several values of k_{PI2}. The order of $T_I(z)$ varies from 8th to 10th depending on the selected voltage control architecture. However, the response of $\vec{i}_2$ is actually defined by the five poles displayed in Fig. 4.10.a: 2 couples of complex conjugate poles and a simple pole. The outer couple of complex poles get closer to a couple of complex zeros as long as k_{PI2} increases so that the associated residue decreases and so does the poles dominance. In that case, the inner complex poles are dominant obtaining a fast response. As long as the value of k_{PI2} decreases, the outer couple of complex-conjugate poles is moved away from the zeros and its weight is more remarkable, slowing down the response. These facts can be appreciated in Fig. 4.10.b. $k_{PI2}=1$ offers a fast response with the lowest overshoot and optimizes the value of $\|S_I(z)\|_\infty$. Fig. 4.11 depicts the same graphs for k_{RI2}. The damping ratio is quite sensitive to k_{RI2}. Low gains make that the outer couple of complex poles get slower, the inner couple of poles faster and the effect over the single pole is negligible. As shown in Fig. 4.11.b and c, high values of k_{RI2} increase the overshoot and lead to a poor robust stability. Taking into account all these considerations, a value of 0.3 is finally selected leading to a second-order response with a power settling time of 60 ms and $\|S_I(z)\|_\infty$=6.4 dβ.

As shown in Fig. 4.9, a feedforward term with the PCC voltage is added at controller's output for several reasons. In the reconnection, it fixes the initial capacitor voltage reference

equal to the PCC voltage, so that the system initially demands zero current. This logically enhances the transient during the reconnection assuring seamless transitions. On the other hand, it also improves the response under transients, especially during grid-faults.

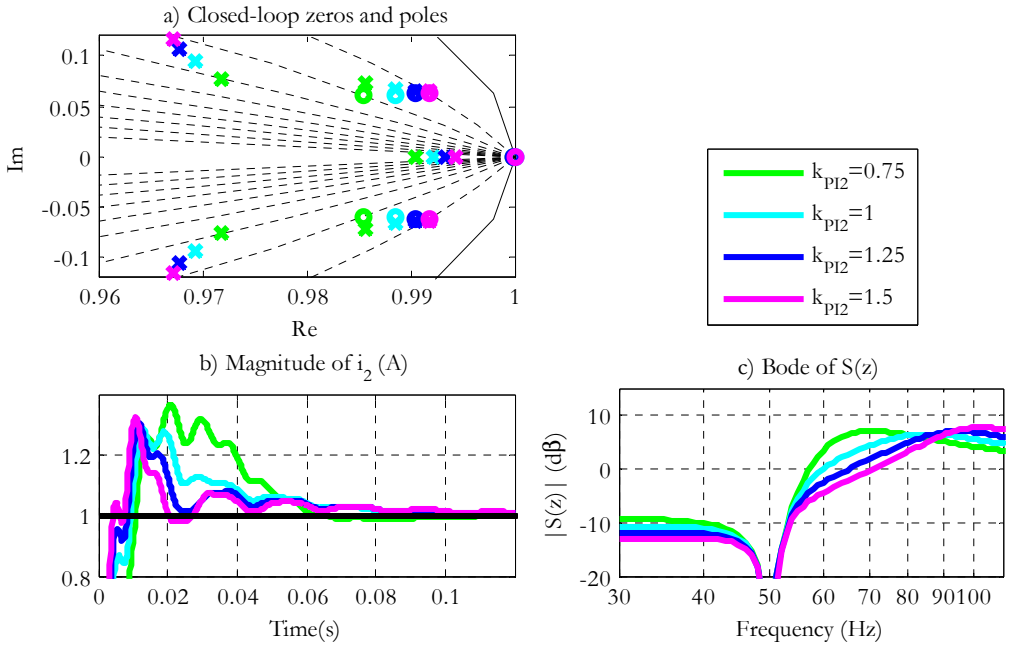

Fig. 4.10: Study of k_{PI2} : a) Dominant closed-loop poles and zeros, b) temporal response of the magnitude of the current vector under a magnitude step and c) Bode diagram of the sensitivity transfer function.

4.3. DC-link voltage control.

Up to this point, the GS voltage and power controllers have been studied in sections 3.3, 4.1 and 4.2. The MS vector control is contained on the Appendix at the end of the document. Following this order, this section is on charge of describing the DC-link voltage controller for the Universal Operation. This controller is implemented in both GS and MS controller depending on the operating mode. It is on charge of balancing the active power across the converter with the purpose of keeping u_{DC} close to its reference. During the grid-connected mode, the power transfer across the converter is fixed by the MPPT and hence, by the MS controller, so the DC-link is inserted in the GS controller to supply the power reference P_G^*. In island mode, there is a role change, and the power transfer is fixed by the GS power control with the power sharing strategy. In this mode, the DC-link controller is implemented in the MS control to give the island torque reference T_E^I (see Fig. 3.1).

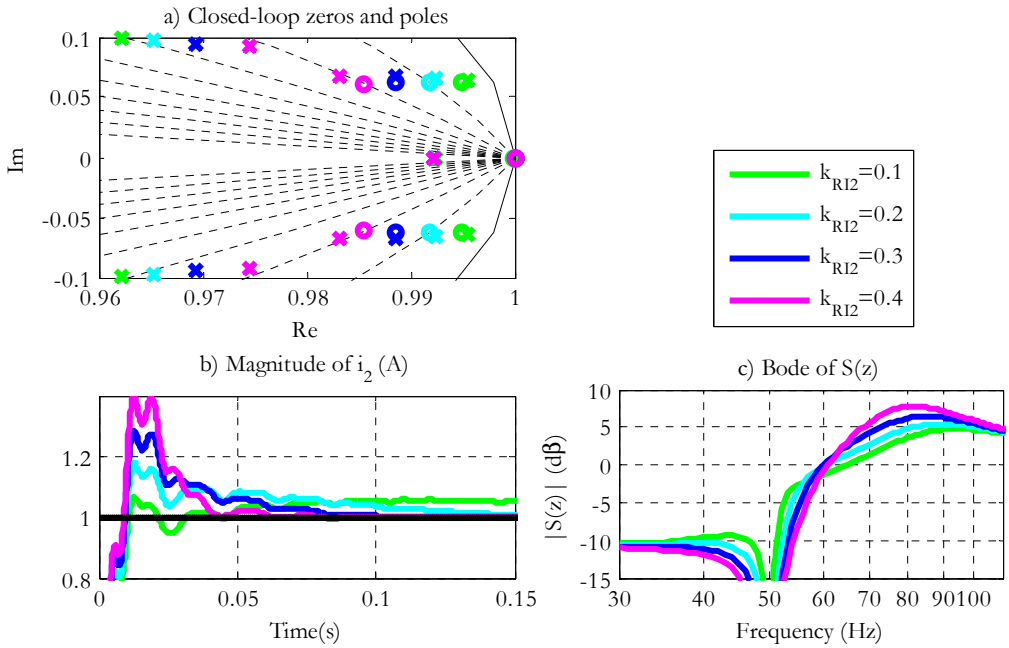

Fig. 4.11: Study of k_{RI2} : a) Dominant closed-loop poles and zeros, b) temporal response of the magnitude of the current vector under a magnitude step and c) Bode diagram of the sensitivity transfer function.

4.3.1. Grid-connected operation.

Fig. 4.12 displays the control block that regulates the DC-link voltage during a normal grid-connected operation. It is composed by a PI controller. The model to configure this controller is based on the electric energy stored on the DC-link capacitors. The output of the PI gives the grid-side power reference P_G^*. A feedforward term with the MS power can be additionally inserted for an improved transient response. As the adopted criterion indicates that a positive power flows out of the converter, after the PI controller, a minus is inserting correcting the sign of the power reference. The tuning assures the conditions imposed on Table 3.1.

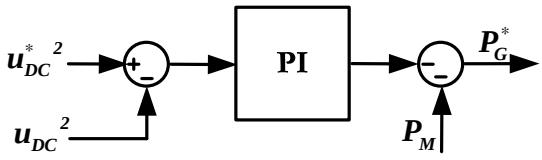

Fig. 4.12: DC-link Voltage control in grid-connected mode implemented in the GS controller

4.3.2. Island operation.

This subsection describes the block labeled as "DC-link and speed control" in Fig. 3.1. It supplies the island torque reference T_E^I and the pitch angle speed $\dot{\beta}$ following the concept represented in Fig. 1.6. It is on charge of controlling the DC-link voltage and managing the kinetic storage during the island operation and under a LVRT grid-connected operation. The DC-link voltage regulation during the island operation becomes more complex due to the power mismatch between generation and consumption. The unpredictable behavior of the power generation and the local load consumption and the great differences between them

make necessary the use of the inherent storage and dissipation capacities of a UWT. Under a negative power mismatch (consumption greater than generation), the MS controller delivers the demanded power and the kinetic storage is being reduced. However, the management of high positive power mismatches requires not only the use of the kinetic storage but also the braking chopper and the pitch control.

The operation principle of the braking chopper relies on the commutation of a resistor (R_{chop}) in the DC-bus. It is employed to dissipate the surplus of active power. The power balance is equilibrated and the DC-bus voltage is kept to its rated value. When the DC-bus voltage is higher than a certain level, the braking chopper starts commutating. As the current through the resistor is too high, it is alternatively switched on and off in order to avoid the breakdown because of the temperature. The maximum temperature is obtained at the end of the on period. The manufacturers supply a temperature limit which should not be exceeded. The braking resistor should be determined in function of the dissipated power and the temperature. When the DC-bus has gone down due to the power dissipation, the braking chopper is disabled.

Fig. 4.13 shows the combined control action over the DC-link voltage and the rotor speed. The outputs are the island torque reference and the pitch angle speed. As depicted, the torque reference can be configured from the DC-link voltage controller or from the rotor speed controller. A switch is employed to select which controller is active based on a hysteresis band of rotor speeds. If the kinetic storage is below the limit imposed by ω_{Rchop1}, the DC-link voltage gives the torque reference and the MS active power transference just follows the GS power. If the power mismatch is negative, this situation remains as the rotor speed is not expected to increase. However, under positive mismatches, the wind power can excessively increase the kinetic reserves. In order not to exceed the limit, when $\omega_R > \omega_{Rchop2}$, the rotor speed controller is activated, which is configured with $\omega_R^* = \omega_{Rchop1}$. The torque is then increased to slow down the rotor up to the reference. This surplus of power makes the DC-link voltage to increase leading to the activation of the DC-braking chopper. Once the rotor speed is below ω_{Rchop1}, the DC-link voltage is again activated. Logically, ω_{Rchop1} and ω_{Rchop2} fix the allowable limits for the kinetic storage, slightly greater than the rated speed.

Note that this procedure would be indefinitely extended unless the pitch control takes part for decrementing the captured wind power. The pitch control works by reducing the angle of attack, which reduces the induced drag as well as the cross-section. Actually, the DC-braking chopper is employed as a first and fast measure whereas the pitch control provides more dissipation capacity within a long-term response. Its slow dynamics are represented by means of the maximum pitch rate $\dot{\beta}_{\max} \approx 10^{o}/\mathrm{s}$. The pitch control is also implemented with PI controller that tries to keep the rotor speed at ω_{Rpitch}, which is usually configured with a value quite close to the rated speed. However, due to the limitations associated to the controller's actuation, it hardly ever achieves zero error tracking, especially under negative mismatches.

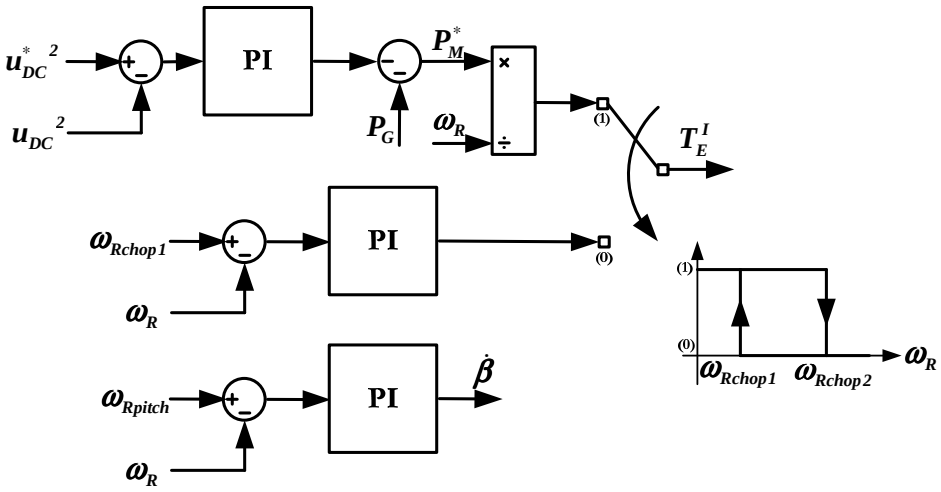

Fig. 4.13: DC-bus and speed controls during the island operation.

4.4. Statistical assessment of the power reliability improvement.

The performance in island operation is subject to the unpredictable behavior of the wind and local loads. The statistical study of this section contemplates each possible case with the aim of revealing the power quality enhancement achieved with the proposed control strategy and no energy storage devices. The power supply reliability is addressed in terms of the number of interruptions and the average duration of them. The mechanical parameters of UWT_1 of Table 7.1 have been used in this analysis [Gonzalez, *et al.*, 2007]. It is important to remark that this analysis should be taken as a first approach. The study has been particularized for just one UWT. For a first approximation, it could be extrapolated to a system with more UWTs just by aggregating the power generation and the stored energy thanks to the proposed power sharing.

4.4.1. Supply Interruption Enhancement Ratio (SIER).

This section calculates the percentage improvement in the number of interruptions, indicated by the parameter SIER. The SIER is evaluated as the probability of keeping energizing the loads by means of the UWT during the complete grid supply interruption. It is opposite to the probability of the UWT shutting down. The UWT shutting down condition during the island is given by a high power mismatch, either excess or lack of energy. The situations of high excess of energy are mainly given by very high wind speeds and/or very low load consumption. These cases are the result of a poor design of the system and not frequent at all. Then, the probability of shutting down the UWT is mainly due to the lack of energy. The shutting down probability Γ_{SD} is evaluated as:

$$\Gamma_{SD} = \Gamma\left(t_{SD} < t_{INT}\right) \tag{4.29}.$$

where the random variables t_{SD} and t_{INT} are the shutting down time and interruption duration time. The variable t_{SD} is defined as the temporal period starting from the grid

disconnection to the instant when the shutting down condition is fulfilled, i.e., when the UWT is not anymore able to supply the load power P_{LOAD}. The situation is reached when the rotor speed goes below the shutting down rotor speed ω_{RSD}, expressed in (4.21). In such conditions, the system is current limited and the required torque cannot be developed. The variable t_{INT} denotes the temporal duration of the interruption without taking into account the LVRT operation. Considering that both statistical variables – t_{INT} and t_{SD} – are independent, the joint probability density function (JPDF) $f_{INT-SD}(t_{INT}, t_{SD})$ is the product of the marginal probability density functions (PDF), $f_{INT}(t_{INT})$ and $f_{SD}(t_{SD})$, respectively. Then, (4.29) can be rewritten as:

$$\Gamma_{SD} = \int_0^{\infty} \left(\int_0^{t_{INT}} f_{INT}(t_{INT})\, f_{SD}(t_{SD})\, dt_{SD} \right) dt_{INT} \tag{4.30}.$$

The shutting down time can be obtained by evaluating the variation of the kinetic energy of the rotor during the island operation as expressed in (4.31).

$$\frac{J}{2}\left(\omega_{RSD}^2 - \omega_{RLVRT}^2\right) = \int_{t_{LVRT}}^{t_{LVRT}+t_{SD}} \left(P_{WT}(t) - \frac{P_{LOAD}}{\eta} \right) dt \tag{4.31}.$$

where ω_{RLVRT} is the rotor speed at the time the UWT gets disconnected from the grid and denotes the kinetic stored energy during the grid-connected and LVRT operations, P_{WT} is the mechanical active power of the turbine, η is the electromechanical performance of the UWT and t_{LVRT} is the duration of the LVRT operation.

One important point of this subsection is the statistical analysis of expression (4.31). In order to obtain the PDF of t_{SD}, each element of (4.31) should be statistically modeled. The shutting down time is affected by the level of generation, consumption and kinetic storage. The generation depends on the wind speed v_W and the consumption is given by the local load value. The kinetic storage depends on the power mismatch. These three items can be evaluated as random variables due to the stochastic processes that rule them are slightly affected by smooth and small variations in the period of time under study (island operation time).

The UWT power production is given by (4.32), where v_{CUTIN} is the minimum operative wind speed, v_{CUTOUT} the maximum wind speed that the UWT is allowed to operate with, R the rotor radius, ρ the air density, β the pitch angle, λ the tip speed ratio and C_P the power coefficient. The PDF of the wind speed $f_W(v_W)$ is commonly featured by the Weibull distribution expressed in (4.33), where k_S and λ_S are respectively the shape and scale parameters. It can be characterized by the average wind speed $\overline{v}_W$ and the mode wind speed v_{WMODE} (maximum probability speed). Fig. 4.14 shows the wind speed statistical distribution for $\overline{v}_W$ =7.98 m/s and v_{WMODE} = 6.28 m/s.

$$P_{WT} = \begin{cases} 0 & if\ v_W \notin [v_{CUTIN}, v_{CUTOUT}] \\ \frac{1}{2}\pi R^2 \rho C_P(\lambda, \beta) v_W^3 & else \end{cases} \quad (4.32).$$

$$f_W(v_W) = \frac{k_S}{\lambda_S}\left(\frac{v_W}{\lambda_S}\right)^{k_S-1} e^{-(v_W/\lambda_S)^{k_S}} \quad (4.33).$$

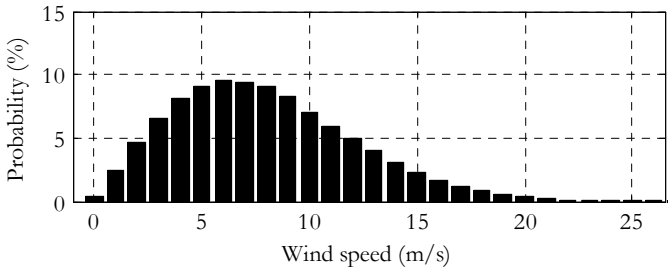

Fig. 4.14: Wind speed statistical model based on Weibull distribution.

A Gaussian distribution can be employed for statistically modeling the local load value as expressed in (4.34). Fig. 4.15 depicts the PDF of the power generation $f_{WT}(P_{WT})$ for UWT$_1$ with the wind profile of Fig. 4.14 and the PDF of the power consumption of six different loads with average power μ_P of 15, 20, 25, 30, 35 and 40 kW respectively, and standard deviation σ of 2 kW. The displayed data gives information about the statistical distribution of the power mismatch the UWT must deal with during the island operation. It is used to statistically evaluate the right term of (4.31). As shown, the statistical weight in the generation of wind speeds below v_{CUTIN} is quite remarkable and it supposes an important lost of efficiency (17.5% at 0kW). Fortunately, the rated power of the UWT also contains a strong influence on the statistical distribution of the power generation.

$$f_L(P_{LOAD}) = \frac{1}{\sigma\sqrt{2\pi}} e^{-\frac{1}{2}\left(\frac{P_{LOAD}-\mu_P}{\sigma}\right)^2} \quad (4.34).$$

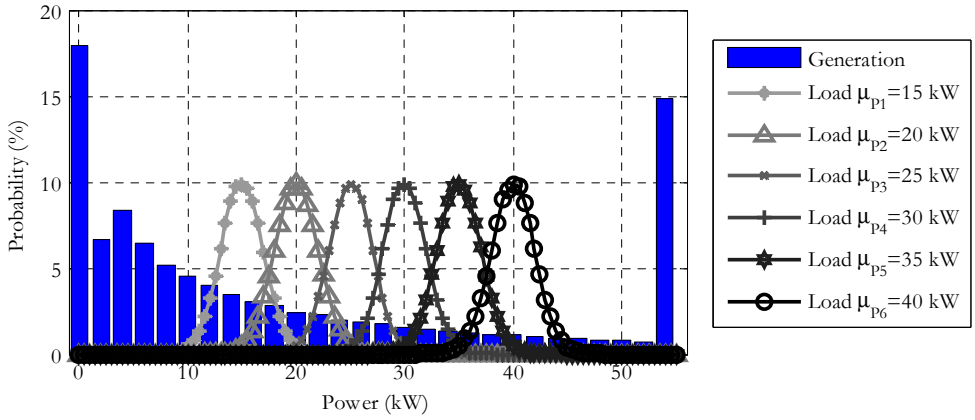

Fig. 4.15: Power generation distribution of the UWT and statistical distribution of the power consumption of six different local load scenarios

It is really important to obtain an accurate value of ω_{RLVRT} to assess the stored kinetic energy that will allow the UWT to operate when facing the island operation:

$$\frac{J}{2}\left(\omega_{RLVRT}^{2}-\omega_{RSS}^{2}\right)=\int_{0}^{t_{LVRT}}\left(P_{WT}(t)-\frac{E_{PCC}I_{2ACT}}{\eta}\right)dt \qquad (4.35).$$

where ω_{RSS} is the rotor speed in grid-connected steady state operation and depends on the MPPT algorithm and I_{2ACT} the magnitude of the active current injected into the grid. The steady state values of the main variables of a WT depend on the wind speed, as shown in Fig. 4.16. The operating range is divided into three different areas. In area I, the MPPT algorithm keeps the power coefficient at its maximum value. In area III, the rotor speed remains at the nominal value and the efficiency of the turbine starts decreasing. In area II, the power generation has reached its maximum and the pitch angle is increased, which further worsens the turbine efficiency. The active and reactive currents and t_{LVRT} are selected according to the grid codes [Fernandez, 2006]. Once ω_{RLVRT} has been statistically modeled, the statistical distribution of t_{SD} is obtained by means expression (4.31).

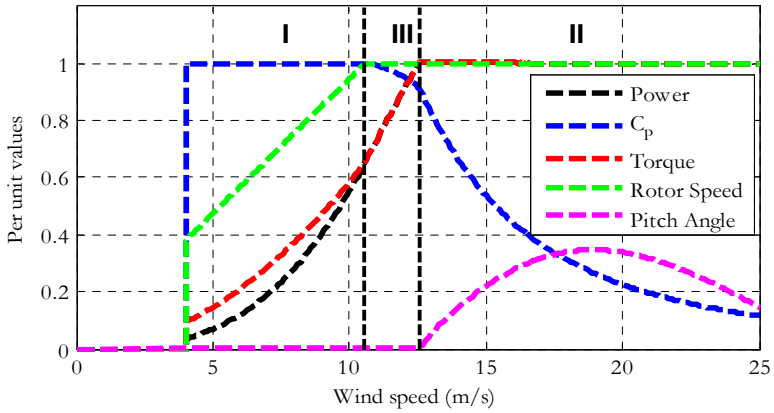

Fig. 4.16: Steady state values of the main variables of a grid-connected WT as function of the wind speed.

The use of exponential distributions for modeling t_{INT} provides an easy and accurate way for developing this study. Expression (4.36) introduces the PDF of t_{INT} as function of its average duration μ_T :

$$f_{INT}(t_{INT})=\mu_T e^{-\mu_T t_{INT}} \qquad (4.36).$$

The data shown in Fig. 4.17 is used to calculate Γ_{SD} by means of (4.30). Fig. 4.17 compares the statistic distributions of t_{SD} and t_{INT} . Three different values of μ_T have been used to contemplate both temporary and long duration power supply interruptions [Bollen, 2002]. The shutting down condition is never reached in those cases where the generation exceeds the consumption (positive power mismatch). This positive mismatch is translated into an infinite t_{SD} as a result of evaluating (4.31). The infinite power supply supposes a great weight within the statistical distribution of t_{SD} even in the 40 kW distribution load. On the

contrary, a strong probabilistic weight is also placed at low island operation times, getting higher as long as μ_P increases the negative power mismatch.

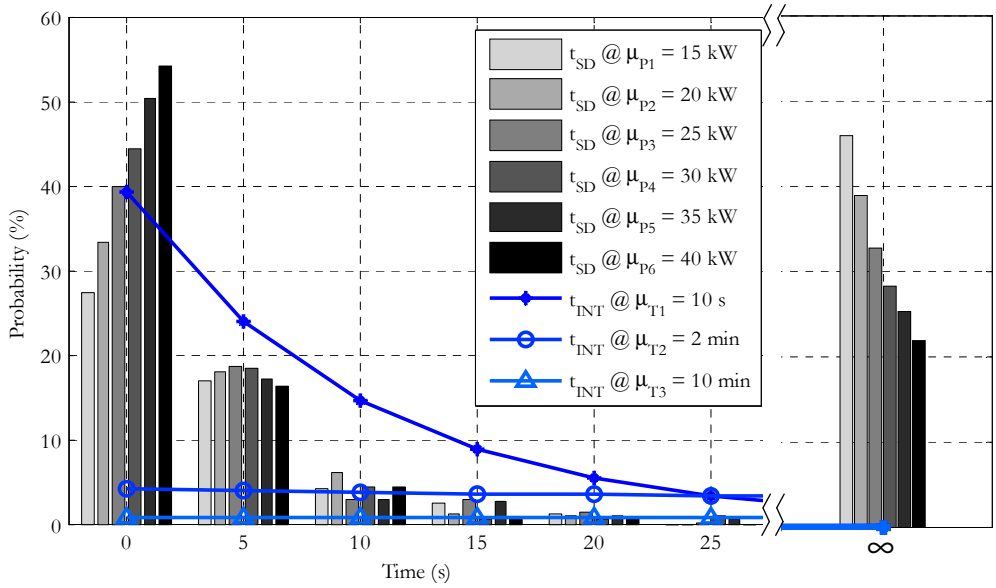

Fig. 4.17: Statistical distribution of the shutting down time for six load scenarios and duration of the power supply with three different averages: 10s, 2 min and 10 min.

The SIER parameter is given by expression (4.37). Table 4.1 collects the enhancement ratios as function of the μ_P and μ_T. As μ_P and μ_T individually increase, the SIER parameter logically becomes lower. The guaranteed minimum of SIER almost matches up with the probability of having an infinite shutting down time (Fig. 4.17). The Universal Operation can supply a load demanding almost the UWT´s rated power during a 10 min grid blackout with a probability of 22.17 %. This probably is increased up to 55 % when the interruption lasts 10 s and the load demands 0.27 p.u. This evidently makes the Universal Operation quite interesting for the DSOs.

$$SIER(\%) = (1 - \Gamma_{SD}) \cdot 100 \tag{4.37}.$$

Table 4.1: Supply Interruption Enhancement Ratio – SIER

SIER (%)		**Average Load Consumption**					
		μ_{P1}	μ_{P2}	μ_{P3}	μ_{P4}	μ_{P5}	μ_{P6}
Average Interruption Duration	μ_{T1}	56.46	49.24	43.06	38.78	33.98	30.78
	μ_{T2}	47.39	40.27	34.19	30.00	26.33	23.20
	μ_{T3}	46.25	39.08	33.04	28.58	25.46	22.17

4.4.2. Improvement of the average duration of the interruption.

In case the interruption cannot be avoided, the Universal Operation of the WT is used to reduce as much as possible the duration of the interruption before it is shut down. The

modified interruption time (taking into account only finites values of t_{SD}) is given by (4.38). The modified average interruption duration μ_T' is then given by expression (4.39). Table 4.2 collects the modified average duration values for each original average duration and load distribution. The reduction in the average interruption time obtained by means of the Universal Operation is quite remarkable, being at least 22.27 % and 60.5 % in the best case. As long as P_{LOAD} or μ_T increases, the ratio improvement given by μ_T' goes down.

$$t_{INT}' = \begin{cases} t_{INT} - t_{SD} & if \ t_{SD} < t_{INT} \\ 0 & else \end{cases} \tag{4.38}.$$

$$\mu_T' = \int_0^{\infty} \left(\int_0^{t_{INT}} (t_{INT} - t_{SD}) \, f_{INT}(t_{INT}) \, f_{SD}(t_{SD}) \, dt_{SD} \right) dt_{INT} \tag{4.39}.$$

Table 4.2: Reduced Average Duration of Interruption

μ_T' (s)		Average Load Consumption					
		μ_{P1}	μ_{P2}	μ_{P3}	μ_{P4}	μ_{P5}	μ_{P6}
Average Interruption Duration	μ_{T1}	3.95	4.64	5.26	5.69	6.19	6.52
	μ_{T2}	62.50	71-02	78.32	83.37	87.82	91.59
	μ_{T3}	321.83	364.82	401.08	427.83	446.63	466.39

4.5. Conclusions.

This chapter is mainly focused on the GS power and the DC-link voltage controls.

It firstly studies the plan for the power controllers of the CCVSC and the VCVSC solutions. Based on the theoretical models, both controllers are configured so that the design requirements (dynamics and robustness) are achieved. Besides, a novel power sharing strategy is proposed with the aim of fairly sharing the load demand among the parallel units through the readaptation of the droop slope and the active power base point. Stability and power quality issues limit the slope range and thus, the power sharing strategy.

Secondly, the control of the DC-link voltage in a UWT has been presented. It is ubicated in different sides of the full-power converter depending on the operating mode. In grid-connected mode, it is linked with the power controller of the GS while in island mode it is implemented on the MS. In this last mode, the DC-braking chopper and the pitch controller are also employed to deal with surplus of power.

Finally, the chapter presents an accurate statistical study to assess the real impact of the Univesal operation in the power quality. Taken into account the data collected in Table 4.1 and Table 4.2, which reflect a substantial improvement of the power supply capability, and the

low investement, the Universal Operation becomes a very interesting strategy under a future expansion and standardization of the island operation.

Chapter 5.

Regulation under unbalanced conditions.

This chapter collects some novel modifications to be applied to the control schemes of not only UWTs but also other kind of power systems. The covered topics are the regulation under unbalanced conditions and the synchronization with the main grid.

These modifications are firstly centered on the correct representation of control variables. Based on this concept, the distortion of control references during the simultaneous presence of positive and negative sequences is avoided. In particular, the proposed modifications are applied to the non-linear operations of a control scheme: the use of the magnitude and phase of the base voltage in the droop control or PCC voltage in the synchronization system and the use of saturators for limiting voltage and current references out of the feasible bonds of the converter. The distortion-free limitation of unbalanced references is not longer an unresolved issue with the proposed techniques.

Finally, the use of the VCVSC in grid-connected mode is a trendy topic and some developments are still required for being comparable with the CCVSC structure. A novel power controller is added in parallel with the droop control for regulating the oscillating power under unbalanced conditions. It complements the DC power regulation carried out by the droop control.

5.1. Representation of control variables.

As expressed in subsection 2.1.4.1, the presence of negative sequence brings some challenges to the control scheme. If it is not well managed, it can lead to the distortion of

control references. During the development of a control algorithm, an important step is to specify the range of frequencies each control variable should contain.

For example, the variable u_{DC} represents the DC-link voltage. The ideal case expects that the frequency spectrum of the DC-link voltage is just composed by a DC-component. In the best case there is only a very small ripple in the bus. However, the oscillating power during the presence of the negative sequences adds an unexpected frequency component at $2\omega_0$ on the DC-link voltage. Then, if the DC-link is not correctly represented by means of the variable u_{DC}, the references of the inner controllers can be distorted via the DC-link voltage controller. A simplified power control scheme is displayed in Fig. 5.1.a. The active power reference P_G^* is affected by the oscillation component of u_{DC}. P_{G2}^* is the magnitude of the oscillating component of P_G^*, expressed in (5.1), where $U_{DC,0}$ and $U_{DC,2}$ are respectively the DC component and the magnitude of the DC-link oscillation and $G_{PI}(2\omega_0)$ corresponds to the gain of the DC-link control at $2\omega_0$:

$$P_{G2}^* = -2U_{DC,0}U_{DC,2}G_{PI}(2\omega_0) \tag{5.1}$$

The vector $\vec{i}_{2,3}^*$ represents the 3rd harmonic in the current reference and it is expressed in (5.2), where E_{PCC}^+ and E_{PCC}^- are the magnitudes of the positive and negative sequences of the PCC voltage. Fig. 5.1.b shows the frequency spectrum of each variable of the loop for a better understanding of the distortion process. The waveforms of the injected current are then affected by this distorted reference.

$$\vec{i}_{2,3}^* \approx \underbrace{\frac{P_{G2}^*}{2}\frac{E_{PCC}^-}{E_{PCC}^{+2}+E_{PCC}^{-2}}e^{-j3\omega_0}}_{I_{2,3}^{*-}} + \underbrace{\frac{P_{G2}^*}{2}\frac{E_{PCC}^+}{E_{PCC}^{+2}+E_{PCC}^{-2}}e^{j3\omega_0}}_{I_{2,3}^{*+}} \tag{5.2}$$

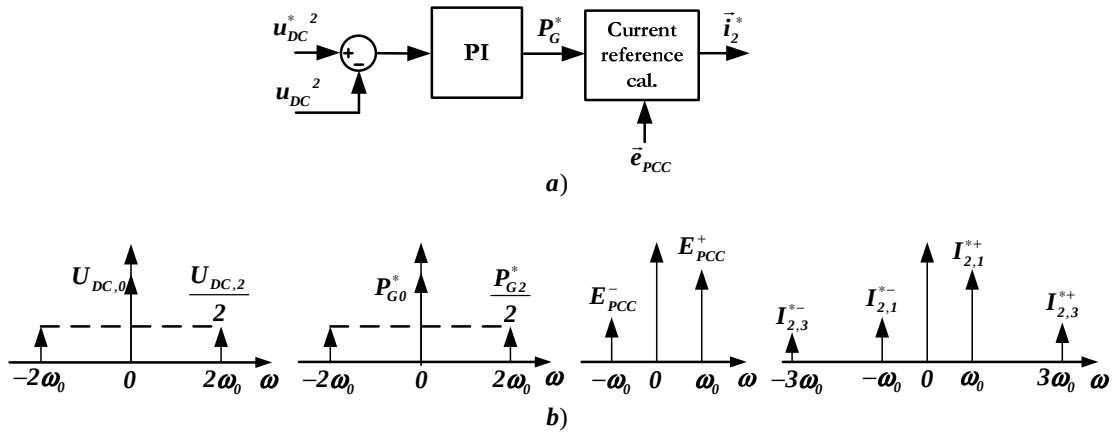

Fig. 5.1: Power oscillation and distortion in grid-feeding schemes a) Block diagram of the DC-link voltage and power controls b) Frequency spectrum of the variables that takes part in the distortion of the current reference.

The previous power control scheme makes reference to a CCVSC structure. However, the conventional droop is also subject to the distortion of references. Fig. 5.2.a displays the conventional droop. In this case, the distortion of references can be caused by three different

sources (control variables): DC-link voltage (active power reference), active power and magnitude and phase of the base voltage. The first and the second are related with the oscillating power. The third one has different nature. If the αβ components of a vector respond to equation (5.3), the magnitude of such vector is given by (5.4). The simultaneous presence of positive and negative sequences makes both magnitude and frequency to oscillate again at $2\omega_0$. Note that the oscillating term is cancelled when $U=U_\alpha=U_\beta$ and $\varphi_\alpha=\varphi_\beta\pm\pi/2$, i.e., when there is only positive or negative sequence, but not both simultaneously. This way, the components of the voltage reference are again distorted as shown in Fig. 5.2.b.

$$\begin{aligned} u_\alpha(t) &= U_\alpha\cos(\omega_0 t+\varphi_\alpha) \\ u_\beta(t) &= U_\beta\cos(\omega_0 t+\varphi_\beta) \end{aligned} \tag{5.3}$$

$$U=\sqrt{\frac{U_\alpha^2+U_\beta^2}{2}+\frac{1}{2}\sqrt{U_\alpha^4+U_\beta^4+2U_\alpha^2U_\alpha^2\cos(2\varphi_\alpha-2\varphi_\beta)}\cos(2\omega_0 t+\gamma)} \tag{5.4}$$

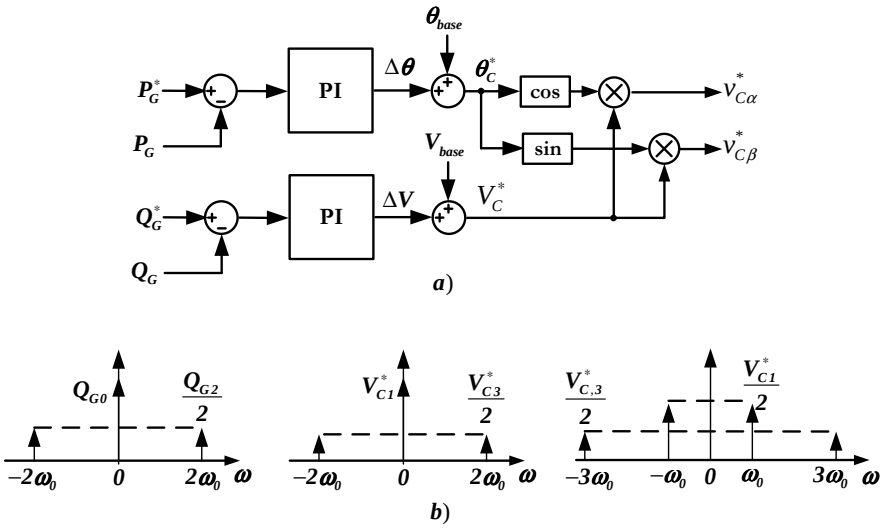

Fig. 5.2: Power oscillation and distortion in grid-forming schemes a) Block diagram of the power control and b) Frequency spectrum of the variables that takes part in the distortion of the voltage reference.

In such conditions, the problem of the distorted references is managed in this Thesis by means of the concept representation of control variables. A control scheme that performs a right representation assures that the frequency spectrum of each control variable just contains the frequencies that are really regulated. The scheme of Fig. 5.2.a does not have regulation capacity over the oscillating power. Therefore, a low pass filter should be inserted in order to only transmit the DC component, as in section 4.1.4. In case of the scheme of Fig. 5.1.a, the use of the matrix (2.7) regulates the oscillating power removing it from the control variable. In this case, the use of the low pass filter is not required. The most detrimental case for a wrong representation resides on the simultaneous presence of positive and negative sequences. The negative sequence can be represented as a $-\omega_0$ component that can provoke the oscillation of the a priori DC variables. Distorted conditions also affect to control loops with bad

representation, however the affected frequencies are located at higher bands and the effect is not so harmful in contrast with unbalanced conditions.

5.2. Droop control for unbalanced conditions.

As described in the previous section, the conventional droop control, shown in Fig. 4.4, does not present a correct representation of the control variables. The representation of the active power and its reference has just solved with the use of a low pass filter. However, the representation of the magnitude and phase of the bases voltage still requires a revision. The base voltage is configured with a predetermined magnitude, initial phase and frequency during the island operation, which does not suppose any problem. However, during the grid-connected operation, the PCC voltage can contain negative sequence. A correct representation requires the control variables to only contain the frequencies that are controlled. In this case, the magnitude and the ramp of the phase should be constants to guarantee a voltage reference without harmonic components. The base voltage and the voltage reference vectors are both represented in polar coordinates. This kind of representation has been inherited from single-phase systems. The premise of having a constant magnitude and slope is only satisfied when the vector components are in quadrature, i.e., when there are no unbalanced conditions, as expressed in (5.4). Filtering both magnitude and frequency or configuring the base voltage with the positive sequence of $\vec{e}_{PCC}$ could assure a good representation but it removes the negative sequence of the PCC voltage, so the voltage drop would be not really applied to the actual PCC voltage.

The scheme of Fig. 5.3 presents a modification of the conventional droop control for assuring a good representation and not losing the negative sequence information. Remember that the PR of the voltage controller can deal with the regulation of both positive and negative sequences. In contrast with existing works, in the proposed structure of Fig. 5.3, during the grid-connected operation the variables that represents the magnitude and phase of the base voltage are two dimensional vectors ($\vec{V}_{base}$ and $\vec{\theta}_{base}$) that respectively contain the magnitudes and phases of each components of $\vec{e}_{PCC}$, as described in (5.5).

$$\begin{aligned} \vec{e}_{PCC} &= e_{PCC\alpha} + j e_{PCC\beta} \\ e_{PCC\alpha} &= E_{PCC\alpha}\cos\left(\theta_{PCC\alpha}\right) \\ e_{PCC\beta} &= E_{PCC\beta}\cos\left(\theta_{PCC\beta}\right) \end{aligned} \qquad (5.5).$$

$$\begin{aligned} \vec{\theta}_{base} &= [\theta_{PCC\alpha}, \theta_{PCC\beta}] \\ \vec{V}_{base} &= [E_{PCC\alpha}, E_{PCC\beta}] \end{aligned}$$

The variables $E_{PCC\alpha}$, $E_{PCC\beta}$, $\theta_{PCC\alpha}$ and $\theta_{PCC\beta}$ are provided by the synchronization system, see section 6.2. Two variables are then used for expressing the magnitudes and phases of $e_{PCC\alpha}$ and $e_{PCC\beta}$. This way, no matter the presence of the unbalanced conditions, none of the variables contains oscillating components and hence, the right representation is assured. During the island operation, the vector nature is kept: $\vec{\theta}_{base} = [\int \omega^* dt + \theta_{IC\alpha}, \int \omega^* dt + \theta_{IC\beta}]$

where the phases $\theta_{IC\alpha}$ and $\theta_{IC\beta}$ (initial conditions of the integrator) are respectively configured with the values $\theta_{PCC\alpha}$ and $\theta_{PCC\alpha}+\pi/2$ at the disconnection instant. The control system is continuously synchronized with both positive and negative sequences of the grid and can add the voltage drop to each component. The output of the modified droop control $\vec{v}_C^{\,d*}$ is created in this case as:

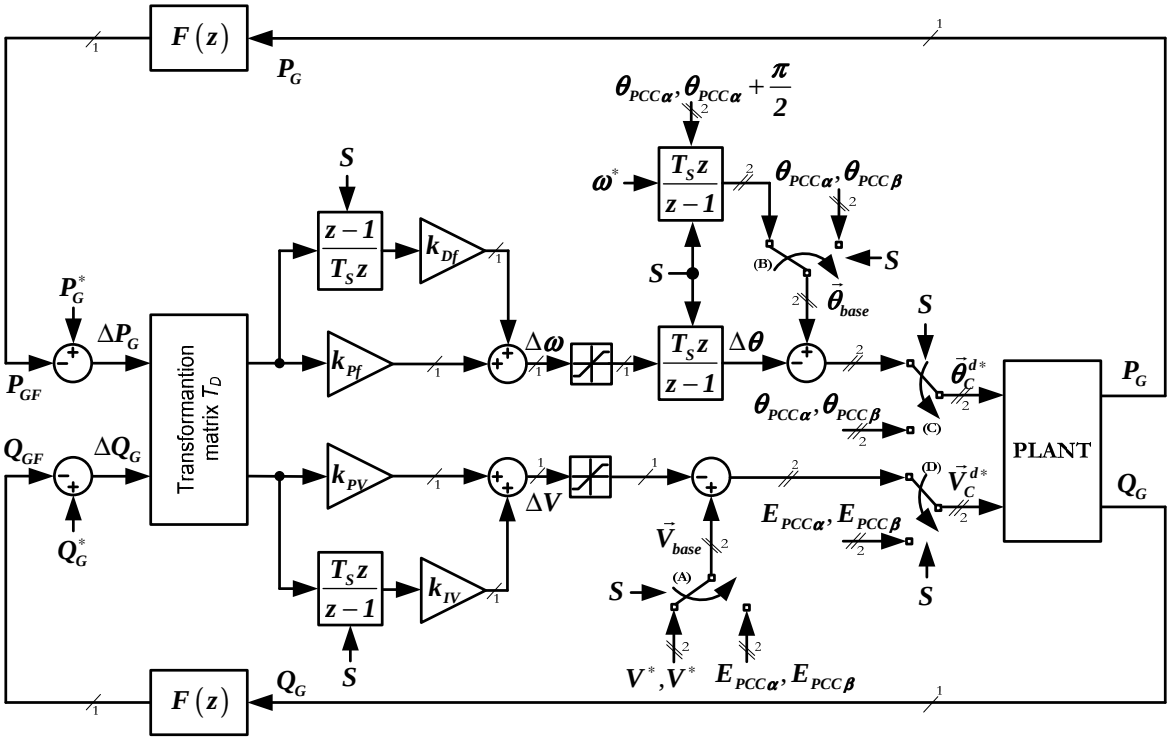

Fig. 5.3: Droop control with right representation of the magnitude and phase of the base voltage.

$$\begin{aligned} v_{C\alpha}^{d*} &= V_{C\alpha}^{d*}\cos\left(\theta_{C\alpha}^{d*}\right) \\ v_{C\beta}^{d*} &= V_{C\beta}^{d*}\cos\left(\theta_{C\beta}^{d*}\right) \end{aligned} \tag{5.6}$$

5.3. Oscillating Power Control (OPC).

Although the control structure proposed on Fig. 4.4 is continuously synchronized with positive and negative sequences of the grid for avoiding distorted voltage references, the strategy is not totally optimized for unbalanced conditions. The operation under unbalanced conditions also supposes the challenge of dealing with power oscillations at $2\omega_0$ that would make the regulation of the DC-link quite difficult. The power transfer can be written as:

$$\vec{S} = P_G + jQ_G = \frac{3}{2}\vec{v}_C\left(\vec{i}_2\right)^* \tag{5.7}$$

By substituting the output current with the voltage drop in Z_2, the active and reactive powers can be written as function of the αβ-axis components of $\vec{v}_C$ and $\vec{e}_{PCC}$:

$$P_G = \frac{3/2}{R_2 + sL_2}\left(v_{C\alpha}\left(v_{C\alpha} - e_{PCC\alpha}\right) + v_{C\beta}\left(v_{C\beta} - e_{PCC\beta}\right)\right)$$
$$Q_G = \frac{3/2}{R_2 + sL_2}\left(v_{C\alpha} e_{PCC\beta} - v_{C\beta} e_{PCC\alpha}\right) \quad (5.8).$$

In steady-state and neglecting the switching noise, P_G and Q_G contains a DC component (P_{G0} and Q_{G0}) and a oscillating component at $2\omega_0$ (P_{G2} and Q_{G2}), as indicated by (5.9). Considering that the voltage reference is only fixed by the droop control ($\vec{v}_C^{\,*} = \vec{v}_C^{\,d*}$) and that the voltage control provides a null error in steady state with negligible settling time, the αβ-axis components of $\vec{v}_C$ are given by (5.10).

$$P_G = P_{G0} + P_{G2}$$
$$Q_G = Q_{G0} + Q_{G2} \quad (5.9).$$

$$v_{C\alpha}^d = \left(\Delta V + E_{PCC\alpha}\right)\cos\left(\theta_{PCC\alpha} + \Delta\theta\right)$$
$$v_{C\beta}^d = \left(\Delta V + E_{PCC\beta}\right)\cos\left(\theta_{PCC\beta} + \Delta\theta\right) \quad (5.10).$$

Combining (5.8) and (5.10) and inspecting the oscillating terms:

$$P_{G2}^d = \frac{3/4}{R_2 + sL_2}\Big[\left(\Delta V + E_{PCC\alpha}\right)^2\cos\left(2\theta_{PCC\alpha} + 2\Delta\theta\right) - E_{PCC\alpha}\left(\Delta V + E_{PCC\alpha}\right)\cos\left(2\theta_{PCC\alpha} + \Delta\theta\right)$$
$$+\left(\Delta V + E_{PCC\beta}\right)^2\cos\left(2\theta_{PCC\beta} + 2\Delta\theta\right) - E_{PCC\beta}\left(\Delta V + E_{PCC\beta}\right)\cos\left(2\theta_{PCC\beta} + \Delta\theta\right)\Big] \quad (5.11).$$
$$Q_{G2}^d = 0$$

where P_{G2}^d and Q_{G2}^d are the oscillating active and reactive power as a consequence of the droop actuation. As $\vec{v}_C^{\,*} = \vec{v}_C^{\,d*}$, $P_{G2} = P_{G2}^d$ and $Q_{G2} = Q_{G2}^d$. As indicated in (5.11), P_{G2} is not null under unbalanced conditions while no oscillation is appreciated in the reactive power waveform regardless the presence of negative sequence. As a consequence, an oscillating component also appears in the DC-link voltage which seriously deteriorates the performance of all the system. The benefits of inserting the low-pass filter have already been studied in the previous subsection. However, this filter also brings an important drawback: it completely removes the power components at $2\omega_0$ caused by the unbalanced condition. This loss of information totally blocks any strategy in the droop control focused on the optimization of the power transfer under unbalanced conditions.

In these circumstances, the power control architecture presented in Fig. 4.4 is complemented with the Oscillating Power Controller (OPC). Fig. 5.4 presents how the droop (DC power controller) and OPC actuations are combined in parallel to carry out a complete power regulation. The input of the OPC is the oscillating power obtained as the difference between P_G and P_{GF}. As indicated by equation (5.12), the output of the OPC $\vec{v}_C^{\,opc*}$ is a purely negative sequence vector that modifies the voltage reference in order to remove the active power oscillations.

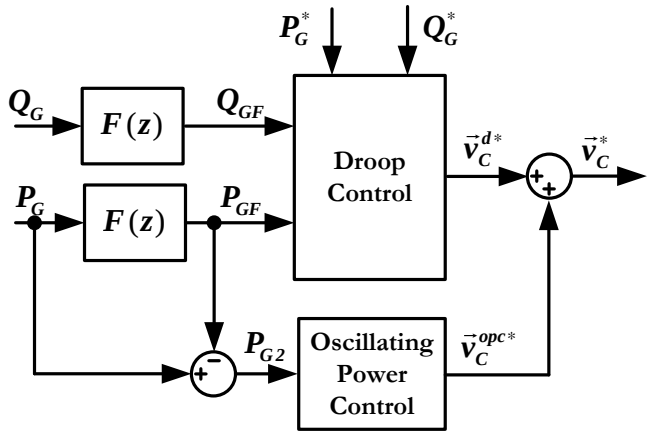

Fig. 5.4: Power regulation consisted of the droop control for tracking the DC power and the oscillating power control for removing active power oscillations under unbalanced conditions.

$$\begin{aligned} \vec{v}_C^* &= \vec{v}_C^{d*} + \vec{v}_C^{opc*} \\ v_{C\alpha}^{opc} &= V_{opc}\sin\left(\theta_{opc}\right) \\ v_{C\beta}^{opc} &= V_{opc}\cos\left(\theta_{opc}\right) \end{aligned} \tag{5.12}$$

The power transfer is now the result of the actuations of the droop control and the OPC:

$$\begin{aligned} P_{G0} &= P_{G0}^d + P_{G0}^{opc} \\ Q_{G0} &= P_{G0}^d + P_{G0}^{opc} \\ P_{G2} &= P_{G2}^d + P_{G2}^{opc} \\ Q_{G2} &= Q_{G2}^{opc} \end{aligned} \tag{5.13}$$

Equation (5.14) contains the oscillating active and reactive powers caused by the OPC actuation, respectively P_{G2}^{opc} and Q_{G2}^{opc}. The philosophy of this controller is to adjust $\vec{v}_C^{opc*}$ to cancel the term P_{G2}^d with P_{G2}^{opc} at the expense of adding oscillating reactive power Q_{G2}^{opc}.

$$\begin{aligned} P_{G2}^{opc} &= \frac{3/4}{R_2 + sL_2}\left[E_{PCC\alpha}V_{opc}\sin\left(\theta_{PCC\alpha}+\theta_{opc}\right) + E_{PCC\beta}V_{opc}\cos\left(\theta_{PCC\beta}+\theta_{opc}\right)\right] \\ Q_{G2}^{opc} &= \frac{3/4}{R_2 + sL_2}\left[E_{PCC\beta}V_{opc}\sin\left(\theta_{PCC\beta}+\theta_{opc}\right) - E_{PCC\alpha}V_{opc}\cos\left(\theta_{PCC\alpha}+\theta_{opc}\right)\right] \end{aligned} \tag{5.14}$$

Last equation can be rewritten as:

$$\begin{bmatrix} P_{G2}^{opc} \\ Q_{G2}^{opc} \end{bmatrix} = \frac{3/4}{R_2 + sL_2}\begin{bmatrix} e_{PCC\alpha} - qe_{PCC\beta} & e_{PCC\beta} + qe_{PCC\alpha} \\ e_{PCC\beta} + qe_{PCC\alpha} & qe_{PCC\beta} - e_{PCC\alpha} \end{bmatrix}\begin{bmatrix} v_{C\alpha}^{opc} \\ v_{C\beta}^{opc} \end{bmatrix} \tag{5.15}$$

where $qe_{PCC\alpha}$ and $qe_{PCC\beta}$ are respectively the quadrature signals of $e_{PCC\alpha}$ and $e_{PCC\beta}$:

$$\begin{aligned} qe_{PCC\alpha} &= E_{PCC\alpha}\sin\left(\theta_{PCC\alpha}\right) \\ qe_{PCC\beta} &= E_{PCC\beta}\sin\left(\theta_{PCC\beta}\right) \end{aligned} \tag{5.16}$$

If the signal $e_{PCC\alpha}-qe_{PCC\beta}$ and $e_{PCC\beta}+qe_{PCC\alpha}$ are further analyzed, one can find that they are in quadrature and can be expressed as:

$$\begin{aligned} e_{PCC\alpha}-qe_{PCC\beta} &= 2E_{PCC}^{+}\cos\left(\theta_{PCC}^{+}\right) \\ e_{PCC\beta}+qe_{PCC\alpha} &= 2E_{PCC}^{+}\sin\left(\theta_{PCC}^{+}\right) \end{aligned} \tag{5.17}$$

where E_{PCC}^{+} and θ_{PCC}^{+} are respectively the magnitude and phase of the positive sequence of the vector $\vec{e}_{PCC}$:

$$\begin{aligned} E_{PCC}^{+} &= \frac{\sqrt{E_{PCC\alpha}{}^{2}+E_{PCC\beta}{}^{2}+2E_{PCC\alpha}E_{PCC\beta}\sin\left(\varphi_{PCC\alpha}-\varphi_{PCC\beta}\right)}}{2} \\ \theta_{PCC}^{+}(t) &= \omega_0 t+\varphi_{PCC}^{+} \end{aligned} \tag{5.18}$$

with:

$$\begin{aligned} \theta_{PCC\alpha}(t) &= \omega_0 t+\varphi_{PCC\alpha} \\ \theta_{PCC\beta}(t) &= \omega_0 t+\varphi_{PCC\beta} \\ \varphi_{PCC}^{+} &= \tan^{-1}\left(\frac{E_{PCC\beta}\cos\left(\varphi_{PCC\beta}\right)+E_{PCC\alpha}\sin\left(\varphi_{PCC\alpha}\right)}{E_{PCC\alpha}\cos\left(\varphi_{PCC\alpha}\right)-E_{PCC\beta}\sin\left(\varphi_{PCC\beta}\right)}\right) \end{aligned} \tag{5.19}$$

Once it is known that these signals are in quadrature, E_{PCC}^{+} and θ_{PCC}^{+} can be easily obtained by means of the signals supplied by the synchronization system:

$$\begin{aligned} E_{PCC}^{+} &= \frac{\sqrt{\left(e_{PCC\alpha}-qe_{PCC\beta}\right)^{2}+\left(e_{PCC\beta}+qe_{PCC\alpha}\right)^{2}}}{2} \\ \theta_{PCC}^{+} &= \tan^{-1}\left(\frac{e_{PCC\beta}+qe_{PCC\alpha}}{e_{PCC\alpha}-qe_{PCC\beta}}\right) \end{aligned} \tag{5.20}$$

Finally, (5.15) is expressed as function of the signals X_P and X_Q.

$$\begin{bmatrix} P_{G2}^{opc} \\ Q_{G2}^{opc} \end{bmatrix} = \frac{3/2}{R_2+sL_2}\begin{bmatrix} X_P \\ X_Q \end{bmatrix} \tag{5.21}$$

where:

$$\begin{bmatrix} X_P \\ X_Q \end{bmatrix} = M\begin{bmatrix} v_{C\alpha}^{opc} \\ v_{C\beta}^{opc} \end{bmatrix}; M = E_{PCC}^{+}\begin{bmatrix} \cos\left(\theta_{PCC}^{+}\right) & \sin\left(\theta_{PCC}^{+}\right) \\ \sin\left(\theta_{PCC}^{+}\right) & -\cos\left(\theta_{PCC}^{+}\right) \end{bmatrix}\begin{bmatrix} v_{C\alpha}^{opc} \\ v_{C\beta}^{opc} \end{bmatrix} \tag{5.22}$$

Equation (5.21) defines the plant for the OPC. The signal X_P is the input of the plant and it is employed for control the oscillating power. As X_P is a sinusoidal signal at $2\omega_0$, a PR controller $C_{OPC}(z)$ tuned at that frequency is used for cancelling the power oscillations:

$$C_{OPC}(z) = k_{Popc} + k_{Ropc}\frac{\sin(2\omega_0 T_s)(z-1)}{z^2 - 2\cos(2\omega_0 T_s)z + 1} \quad (5.23).$$

The $\vec{v}_C^{opc*}$ is a pure negative sequence vector by imposition of the control. Then, the matrix *M* necessary forces than X_P and X_Q are signals in quadrature.

The simplified loop of the OPC is displayed in Fig. 5.5. The z^{-1} represents the computational delay. One of the main advantages of using (5.21) as a plant is removing the dependence with E_{PCC}^+, linked with the magnitude of $\vec{e}_{PCC}$. This is quite interesting from the point of the OPC dynamics during fault conditions. In order to get that independence, E_{PCC}^+ is used to obtain the real actuation of the OPC ($\vec{v}_C^{opc*}$) as function of X_P. Fig. 5.6 shows the actual implementation of the OPC controller. The vector $\vec{v}_C^{opc*}$ is obtained by inversing the matrix *M*, introduced in (5.22):

$$M^{-1} = \frac{1}{E_{PCC}^+}\begin{bmatrix} \cos(\theta_{PCC}^+) & \sin(\theta_{PCC}^+) \\ \sin(\theta_{PCC}^+) & -\cos(\theta_{PCC}^+) \end{bmatrix} \quad (5.24).$$

The inversion of matrix *M* does not suppose any problem as long as the magnitude of $\vec{e}_{PCC}$ is greater than zero. Note that the signal X_Q is also necessary for the calculation of $\vec{v}_C^{opc*}$ but no control is carried out over the oscillating reactive power. This signal is obtained by means of a quadrature signal generator (QSG) through X_P. The QSG can be implemented with a SOGI-QSG or by means of a delay. Both options provide good performances.

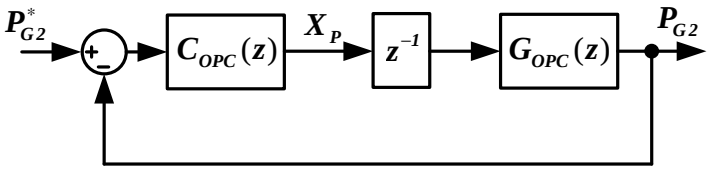

Fig. 5.5: Simplified control loop for the OPC.

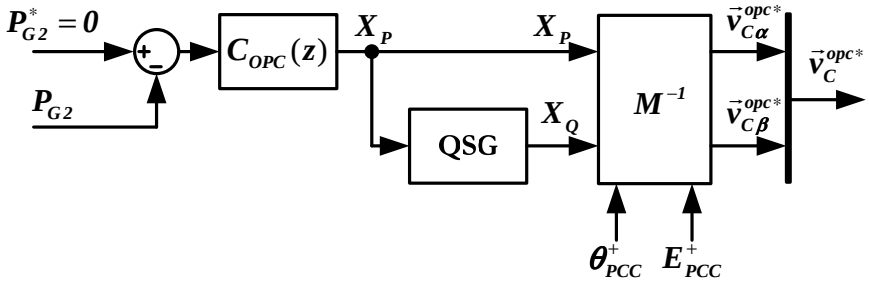

Fig. 5.6: Block diagram of the implementation of the OPC.

5.3.1. Tuning of OPC.

The loop of Fig. 5.5 is used for selecting the values of constants of C_{OPC}. The closed-loop and sensitivity transfer functions can be written as:

$$T_{OPC}(z)=\frac{z^{-1}C_{OPC}(z)G_{OPC}(z)}{1+z^{-1}C_{OPC}(z)G_{OPC}(z)}$$
$$S_{OPC}(z)=\frac{1}{1+z^{-1}C_{OPC}(z)G_{OPC}(z)} \quad (5.25).$$

The OPC and droop control are placed in parallel. Under unbalanced conditions, the OPC actuation indirectly interferes in the control of P_{G0} and the droop control causes P_{G2}, as indicated in (5.13). The configuration of the OPC should assure a minimum decoupling with the droop control so that both actuations do no tangle between them. Therefore, the regulation of P_{G0} is of first importance, so that the OPC dynamics should be tuned slower than the droop response. Fig. 5.7 analyzes the effect of k_{Popc}. Fig. 5.7.a depicts the closed-loop zeros and poles, Fig. 5.7.b the closed-loop response under a step in P_{G2}^{*} and Fig. 5.7.c contains the Bode diagram of the sensitivity transfer function. The response is given by four poles. A couple of complex-conjugate poles is placed close to the stability circle. As long as k_{Popc} increases, the associated time constant becomes larger but on contrary, the closeness to the neighbor zero reduces the impact of these poles on the total response. Then, higher values of k_{Popc} increases the settling time. Depending on the value of k_{Popc}, the other two poles can be complex with a large overshoot. As displayed in Fig. 5.7.c, low values of k_{Popc} enhance the robust stability. Considering the previous statements, k_{Popc}=2 provides a settling time of 120 ms, a 15% overshoot and $\|S_{OPC}(z)\|_{\infty}$ = 2 dβ. It perfectly satisfies all the design requirements.

Fig. 5.8 presents the same plots for k_{Ropc}. The settling time can be reduced by increasing the value of k_{Ropc}, but it will the decoupling between the droop and OPC actuations. Hence, it is quite recommendable not to increase the value of k_{Ropc} up to 0.2. This way, a good decoupling is assured while a settling time close to 125 ms in the P_{G2} response is obtained. On the other hand, the value of k_{Ropc} does not really affects the robust stability.

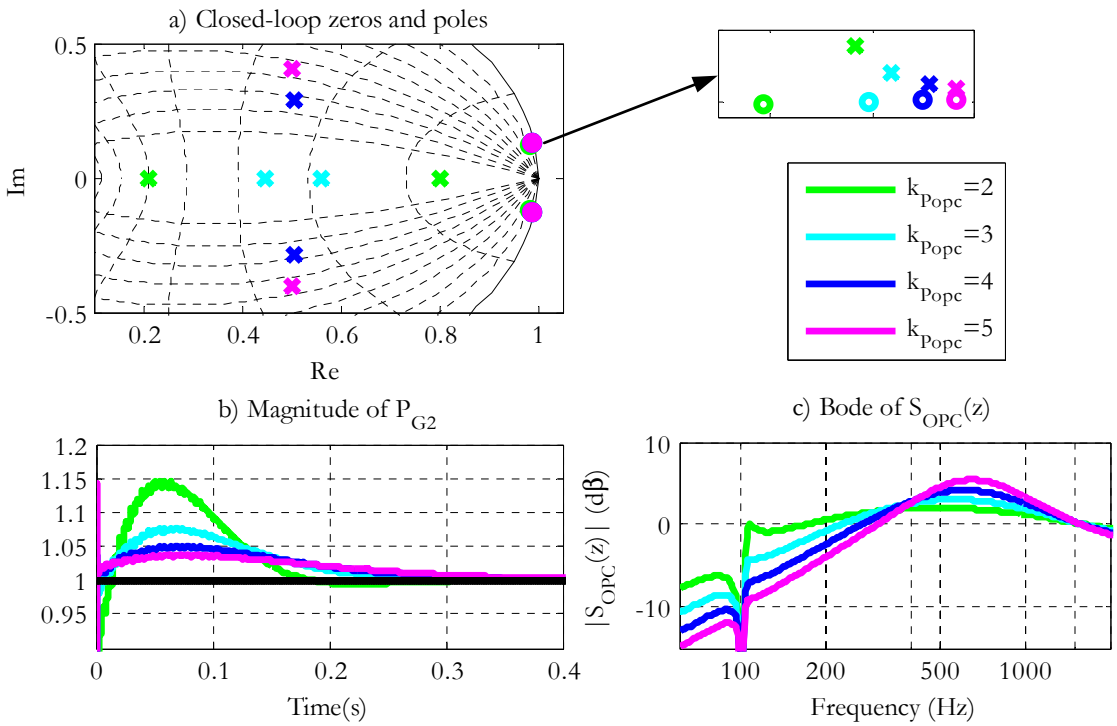

Fig. 5.7:Analysis of k_{Popc} : a) Closed-loop zeros and poles, b) Magnitude of oscillating power under a step in the reference and c) bode of the sensitivity transfer function.

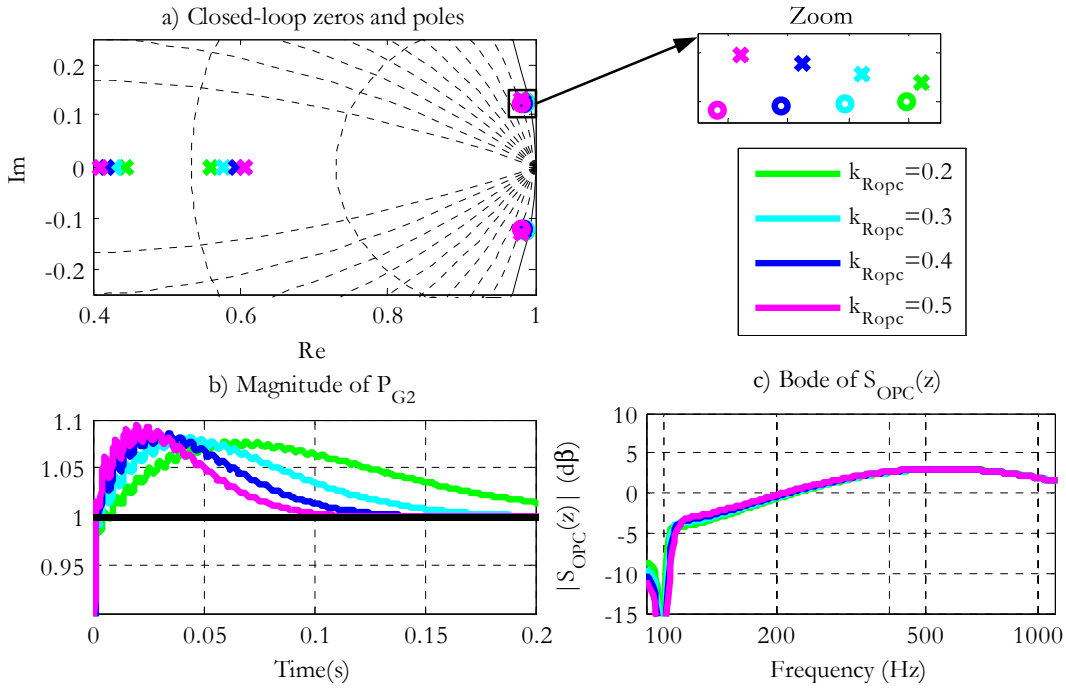

Fig. 5.8: Analysis of k_{Ropc} : a) Closed-loop zeros and poles, b) Magnitude of oscillating power under a step in the reference and c) bode of the sensitivity transfer function.

5.4. Saturation under unbalanced conditions.

The control system can take enormous actions out of the feasible operation range to counteract some undesired circumstances leading to unsafe conditions. This situation may be provoked by the effect of a transient of the control system disturbance:

- During the LVRT operation, the active power injection capacity is reduced by the presence of the voltage dip. The current references of the grid-side can exceed the rated value in order to reduce as much as possible the active power surplus in the system.

- In general drive applications, the stator voltage is directly proportional to the product of the speed and the rotor flux. During the operation at high speeds, the rotor flux of induction machines should be weakened in order not to reach the rated voltage.

- In application such as shunt converters as Dynamic Voltage Restorer (DVR) systems or universal parallel converters working in island mode, where a negative mismatch of active power may exist, the DC-link voltage tends to fall if there are no storage devices or they have been run out of energy. In these systems, the operation with low DC-link voltages is generally allowed as long as the natural voltage is not reached. However, the voltage compensation of the DVR and the power injection capacity of the isolated power system are reduced to the same extent. Therefore, the voltage actuation to be modulated can exceed the limit imposed by DC-link voltage.

The saturation process consists on the reduction of the control references and actuations to avoid the operation of the converter out of its feasible and safe range. As introduced in section 2.1.4.2, some saturation techniques have been already reported in the bibliography. The following sections introduce the definition of the trajectory and analyze the existing techniques.

5.4.1. Trajectory of a vector.

The trajectory of a rotating vector ($\vec{u}$) is defined as the geometric place consisted of the set of points taken by the vector during a period T_0 in the αβ-axis $\left(u_\alpha(t_1-T_0),u_\beta(t_1-T_0)\right)$... $\left(u_\alpha(t_1),u_\beta(t_1)\right)$. Let define balanced and unbalanced vectors as those which respectively represents balanced and unbalanced voltages or currents. The trajectory of balanced vectors corresponds to a circumference while unbalanced vectors have an elliptical trajectory. Both trajectories are centered in the origin (0,0) if no DC is present. The distance from the origin to some general point of the trajectory $\left(u_\alpha(t),u_\beta(t)\right)$ is defined as $U(t)$ while $\theta(t)$ represents the angle with the α-axis:

$$U(t)=\sqrt{\left(u_\alpha(t)\right)^2+\left(u_\beta(t)\right)^2}$$
$$\theta(t)=\tan^{-1}\left(\frac{u_\beta(t)}{u_\alpha(t)}\right) \quad (5.26).$$

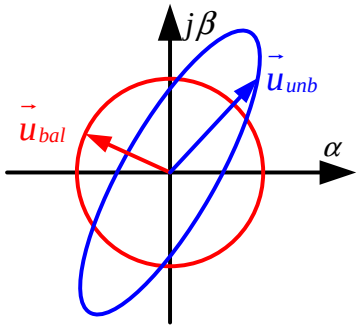

Fig. 5.9: Trajectories for balanced and unbalanced vectors.

5.4.2. Scalar Saturation.

The use of the scalar saturation only makes sense in the V_{SAT} block of Fig. 2.1. It avoids the modulation of voltage references out of the PWM hexagon. This technique is inherent to triangular carrier-based PWM schemes. It splits up the components of the reference vector $\vec{u}^*_{abc}$ and carries out an individual temporal saturation. If the absolute temporal value of one component, for instance u^*_a, is lower than the corresponding limit $|\vec{u}_{max}|$, the component is not modified in the output reference vector. In case of exceeding $|\vec{u}_{max}|$, the output component is limited to $sign(u^*_a)|\vec{u}_{max}|$. Fig. 5.10 presents the study case of the limitation of a balanced vector. Fig. 5.10.a depicts the trajectories of the input vector, the limit circle and the limited vector when using the scalar saturation, $\vec{u}^*_{SS}$. The limit circle, whose radius is $|\vec{u}_{max}| = u_{DC}/\sqrt{3}$, represents the border of the linear mode of the PWM with zero-sequence injection. The trajectory of $\vec{u}^*_{SS}$ matches up with the modulation hexagon, whose radius is $2/3\ u_{DC}$, so that the scalar saturation takes advance of all the converter feasible range. Fig. 5.10.b contains the temporal waveforms and Fig. 5.10.c the Fast Fourier Transform (FFT) of one component of $\vec{u}^*_{SS}$. It is revealed that although the scalar saturation preserves the maximum fundamental harmonic, it also adds detrimental low order harmonics such as non zero-sequence 3rd, 5th and 7th.

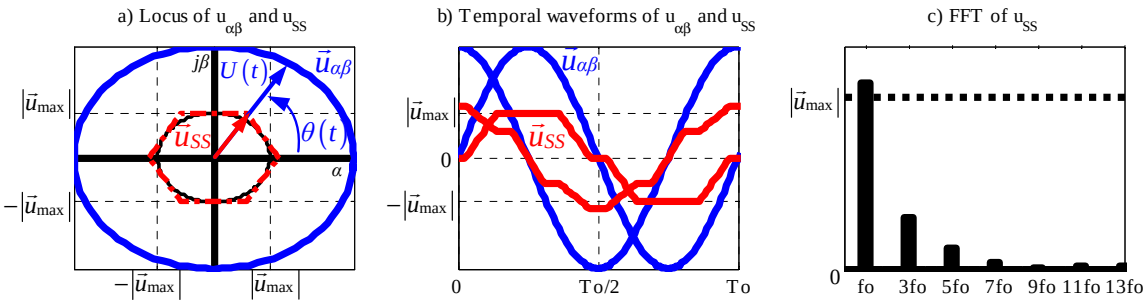

Fig. 5.10: Scalar saturation performance under balanced conditions: a) Trajectories, b) temporal waveforms of the αβ components of the input and saturated vectors and c) FFT of phase *a* of the saturated vector

5.4.3. Vector Saturation.

The most representative vector saturation technique is the Circular Limit method (CL). The rest of the existing methods contemplate some slight variations of the CL-method. It can be implemented in both V_{SAT} and I_{SAT} blocks. The goals are to keep the reference vector trajectory within the limit circle given and avoid the distortion. The operating principle is shown in Fig. 5.11. The saturator firstly obtains the instantaneous vector magnitude and phase by means of (5.26), $\hat{U}(t)$ and $\hat{\theta}(t)$. Then, when the instantaneous calculated magnitude exceeds the limit $|\vec{u}_{\max}|$, the saturation takes place. The magnitude of the limited vector remains at $|\vec{u}_{\max}|$ and the original phase is kept constant.

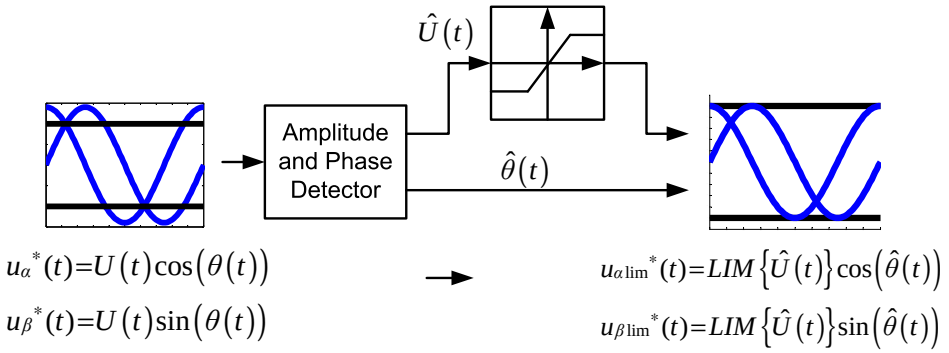

Fig. 5.11: Circular Limit method in αβ-frames

In the balanced case, it is quite easy to determine the limited trajectory: $U(t)$ is a constant value along T_0, while $\theta(t)$ is an increasing value with constant slope. Then, in steady-state conditions, if the saturation condition is fulfilled for one instant, it will be fulfilled for the complete period, performing a distortion-free saturation. Under unbalanced conditions, $U(t)$ and the slope of $\theta(t)$ contain oscillating components. The oscillations of $U(t)$ can make that the saturation condition is only fulfilled during a certain part of T_0. If the saturator is modeled as a reduction factor, this factor is then varying along T_0 inserting harmonic distortion in the limited vector $\vec{u}_{CL}^*$. This effect is shown in Fig. 5.12. The trajectories of the unbalanced vector and its limited version are depicted in Fig. 5.12.a while Fig. 5.12.b and c demonstrate that this methodology provides identical results in αβ-axis or dq-axis. Fig. 5.12.c contains the frequency spectrum of the β component.

5.4.4. Distortion-free saturation.

The previous techniques preserve the magnitude of the fundamental frequency harmonic of the input vector at the expense of distorting the voltage waveforms. The harmonic injection reduces the efficiency and affects the power quality. This situation becomes more dramatic as long as the control action $U(t)$ increases as a consequence of the saturation, so the use of anti-windups is quite recommended. The trade-off between the maximum fundamental frequency component and the distortion can be only a matter of discussion in VCVSC

depending on the application, the load and the duration of the saturation. In CCVSC, a distortion-free saturation is doubtlessly preferred.

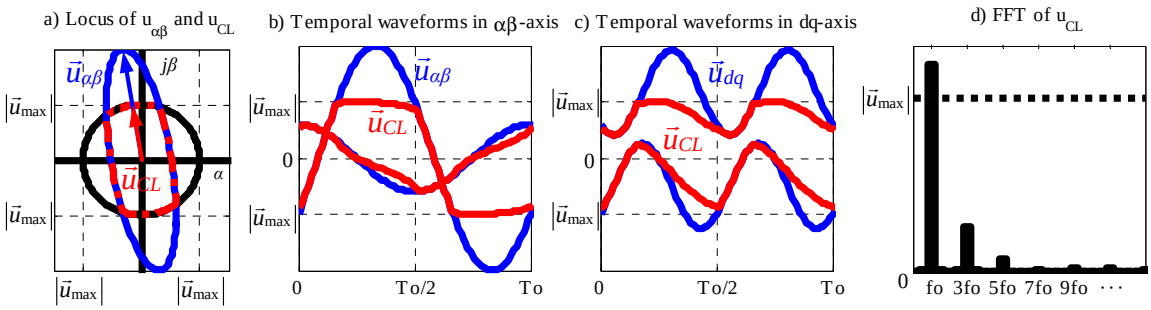

Fig. 5.12: Performance of CL-method philosophy under unbalanced conditions: a) Trajectories, b) temporal waveforms of the αβ components of the input and saturated vectors, c) temporal waveforms in the dq-axis with the corresponding 2*fo* oscillation of the negative sequence and d) FFT of the β component of the saturated vector.

The operating principle of the stationary reference frames (SRF) saturator proposed in this work is based on getting the complete trajectory of the vector along a complete period and fully readapting it to the limit circle if necessary. The reduction factor that models the saturator is then constant along the whole trajectory so that the sinusoidal waveforms are preserved. Furthermore, it can be applicable to control loops in dq-frames.

5.4.4.1. Structure of SRF saturators.

The trajectory of a general reference vector $\vec{u}^*$ is perfectly described by four DC variables: the amplitudes and phases of both components ($U_\alpha[k]$, $U_\beta[k]$, $\theta_\alpha[k]$ and $\theta_\beta[k]$). Note that the variables are now referred in the discrete-time domain. Note that now the variables are referred in the discrete-time domain. Once the trajectory has been obtained, it is possible to decide whether it should be saturated or not and define which the saturation strategy should be adopted. According to the objectives and tasks mentioned, the SRF saturator is composed of:

- Virtual Quadrature Signal Generator (VQSG): calculates the amplitudes and phases of both vector components by means of the generation of signals in quadrature.
- Trajectory Analyzer (TA): uses the amplitudes and phases to conform the trajectory and decides whether it should be saturated or not. Besides, it can be configured with different limitation strategies.

Fig. 5.13 shows a block diagram with these two elements and the expected input and output signals.

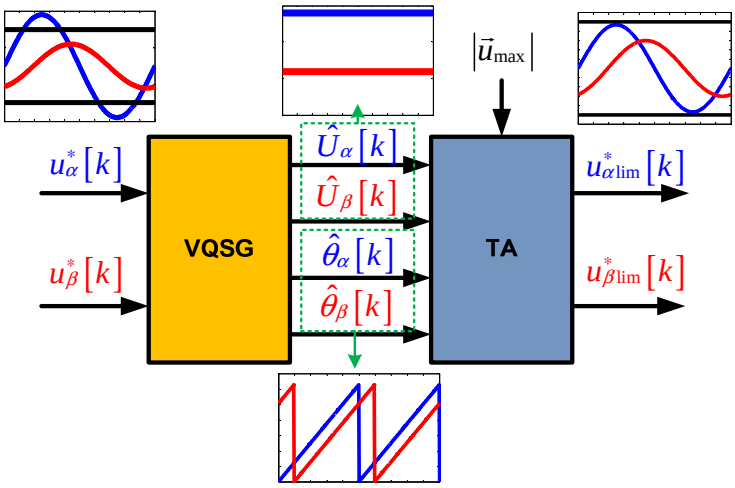

Fig. 5.13: Block diagram of the structure of the SRF saturator.

a) Virtual Quadrature Signal Generator (VQSG).

The VQSG calculates the amplitudes and phases of both vector components by means of the generation of signals in quadrature as in (5.27). The method of obtaining the quadrature signals is represented in Fig. 5.14. It comprises a delay of a quarter of the fundamental period, $N = T_0 / T_S / 4$. This technique guarantees a minimum interference over the control loop by means of a fast response with a smooth overshoot. Besides, the computation cost is reduced to two N-length buffers.

$$\begin{aligned}
\hat{U}_\alpha[k] &= \sqrt{\left(u_\alpha^*[k]\right)^2 + \left(qu_\alpha^*[k]\right)^2} \\
\hat{\theta}_\alpha[k] &= \tan^{-1}\left(qu_\alpha^*[k] / u_\alpha^*[k]\right) \\
\hat{U}_\beta[k] &= \sqrt{\left(u_\beta^*[k]\right)^2 + \left(qu_\beta^*[k]\right)^2} \\
\hat{\theta}_\beta[k] &= \tan^{-1}\left(qu_\beta^*[k] / u_\beta^*[k]\right)
\end{aligned} \qquad (5.27).$$

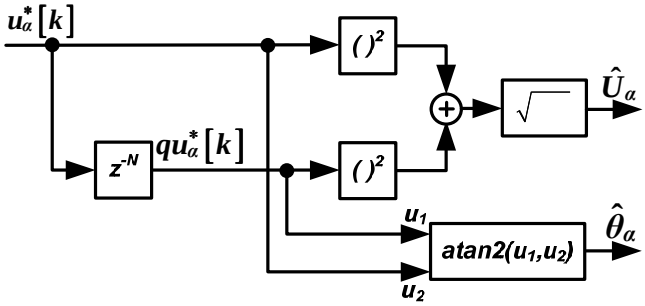

Fig. 5.14: Block diagram of the VQSG implemented in the SRF saturator for the *a*-axis.

However, if the fundamental frequency varies ($f \neq f_0$), the N-delay block does not exactly cause a 90º lag and the signals are not in quadrature [Bongiorno, *et al.,* 2008]. The use of (5.27) adds both magnitude and phase errors, $\Delta U = \hat{U} - U$ and $\Delta\theta = \hat{\theta} - \theta$, which oscillate at 2*f* and

whose magnitudes are delimited by the expressions in (5.28). For reasonable frequency variations (<5%), the oscillating errors do not suppose a problem neither for the saturator nor the control loop.

$$\max_k \Delta U_\alpha(p.u.)=\sqrt{1+\frac{1}{2}\sqrt{2+2\cos\left(\frac{\pi f}{f_0}\right)}}-1 \qquad |\Delta f|<0.2\,p.u \tag{5.28}$$
$$\max_k \Delta\theta_\alpha(p.u.)=\frac{1}{2\pi}\max_k \Delta U_\alpha(p.u.)$$

b) Trajectory Analyzer (TA).

The main purposes of the TA block are interpreting both amplitudes and phases, deciding if the associated trajectory has to be limited and if so, calculating the corresponding limited vector $\vec{u}^*_{\lim}$ based on the chosen saturation strategy. To that concern, the following steps must be followed:

1. The maximum magnitude of the input vector U_M, i.e. the maximum distance between the trajectory and the origin point (0,0) in the αβ-axis, is calculated:

$$U_M{}^2=\max_k\left[\left(u^*_\alpha[k]\right)^2+\left(u^*_\beta[k]\right)^2\right] \tag{5.29}$$

By operating with the last expression, U_M can be expressed as function of the calculated amplitudes and phases:

$$U_M{}^2=\frac{\sigma_1+\sqrt{\hat{U}_\alpha{}^4+\hat{U}_\beta{}^4+2\left(\hat{U}_\alpha\hat{U}_\beta\right)^2\sigma_2}}{2} \tag{5.30}$$

where $\sigma_1=\hat{U}_\alpha{}^2+\hat{U}_\beta{}^2$ and $\sigma_2=\cos\left(2\hat{\theta}_\alpha-2\hat{\theta}_\beta\right)$.

2. The maximum amplitude U_M is compared with the limit $|\vec{u}_{\max}|$. If it does not exceed the limit, the trajectory of $\vec{u}$ is contained within the limit circle. In that case, $\vec{u}^*_{\lim}[k]=\vec{u}^*[k]$. On contrary $(U_M>|\vec{u}_{\max}|)$, two different strategies of limitation are proposed for calculating $\vec{u}_{\lim}[k]$ and described in the following subsections.

5.4.4.2. Proportional Saturation (PS).

A common reduction factor r_{PS} is applied to both amplitudes $\hat{U}_\alpha$ and $\hat{U}_\beta$ in the calculation of the limited amplitudes $U_{\alpha\lim}$ and $U_{\beta\lim}$ while the phase of each component is not altered at all. The reduction factor r_{PS} should be low enough to make $U_{M\lim}=|\vec{u}_{\max}|$, where $U_{M\lim}$ is the maximum amplitude of $\vec{u}^*_{\lim}$. This condition is expressed by (5.31). As a consequence, the elliptical trajectory of is embraced by the limit circle.

$$\frac{\hat{U}_{\alpha\lim}{}^2+\hat{U}_{\beta\lim}{}^2+\sqrt{\hat{U}_{\alpha\lim}{}^4+\hat{U}_{\beta\lim}{}^4+2\left(\hat{U}_{\alpha\lim}\hat{U}_{\beta\lim}\right)^2\sigma_2}}{2}=|\vec{u}_{\max}|^2 \tag{5.31}$$

By replacing the saturated amplitudes $U_{\alpha\lim}$ and $U_{\beta\lim}$ with $r_{PS}\hat{U}_\alpha$ and $r_{PS}\hat{U}_\beta$, respectively, and rearranging terms in (5.31), the reduction factor is given by (5.32), where $0<r_{PS}<1$. The components of $\vec{u}^*_{\lim}$ are then calculated as in (5.33). The value of the parameter r_{PS} depends on the magnitudes $(\hat{U}_\beta,\hat{U}_\beta)$ and phases (σ_2).

$$r_{PS}=\begin{cases}\dfrac{|\vec{u}_{\max}|}{\sqrt{\sigma_1}} & if\ \sigma_2=1\\ \dfrac{|\vec{u}_{\max}|}{\hat{U}_\alpha\hat{U}_\beta}\left(\dfrac{\sqrt{\sigma_1{}^2+2\left(\hat{U}_\alpha\hat{U}_\beta\right)^2(\sigma_2-1)}-\sigma_1}{\sigma_2-1}\right)^{\frac{1}{2}} & else\end{cases} \tag{5.32}.$$

$$\begin{aligned}u^*_{\alpha\lim}[k]&=r_{PS}\hat{U}_\alpha\cos\left(\hat{\theta}_\alpha[k]\right)\\ u^*_{\beta\lim}[k]&=r_{PS}\hat{U}_\beta\cos\left(\hat{\theta}_\beta[k]\right)\end{aligned} \tag{5.33}.$$

The unbalance on the amplitudes presented by $\vec{u}^*$ is kept constant in $\vec{u}^*_{\lim}$ with the PS technique. This also means that the saturated trajectory is a reduced concentric copy of the trajectory of $\vec{u}^*_{\lim}$ as a result of applying the same reduction to both amplitudes and maintaining the phases.

5.4.4.3. Maximum Area (MA).

The saturation limits the controller actuation when it comes to reduce the tracking error and/or counteract a disturbance. The operating principle of this technique is to reduce as much as possible the saturation effect. The area swept by the trajectory of the resulting $\vec{u}_{\lim}$ is the maximum within the following restrictions: (i) the trajectory should be contained within the limit circle and the trajectory of $\vec{u}^*$, (ii) the original phase of $\vec{u}$ should be kept and (iii) the limited trajectory should still have an elliptical form avoiding distorted references. This strategy takes advance of all the possible converter actuation range without making unstable the control loop. It provides the vector with the maximum energy and remarkably reduces the wind-up effect provoked by the saturator. The surface area *S* that is swept by the trajectory of $\vec{u}_{\lim}$ is expressed by (5.34), where k_1 and k_2 are the time instants when $u^*_{\beta\lim}[k]=0$, i.e., the crossing with the α-axis. By operating with (5.34), the surface can be expressed in terms of the magnitudes and phases of the limited vector as expressed by (5.35).

$$S=2\int_{u^*_{\alpha\lim}[k_1]}^{u^*_{\alpha\lim}[k_2]}u^*_{\beta\lim}[k]\,du^*_{\alpha\lim}=2\int_{k_1}^{k_2}\left(u^*_{\beta\lim}[k]\frac{du^*_{\alpha\lim}[k]}{dk}\right)dk \tag{5.34}.$$

$$S=U_{\alpha\lim}U_{\beta\lim}\pi\left|\sin\left(\theta_{\alpha\lim}-\theta_{\beta\lim}\right)\right| \tag{5.35}.$$

Assuming that the area expressed by (5.35) is restricted by the limit circle (5.31) and the original trajectory of $\vec{u}^*$, the optimization problem of *S* is reduced to:

$$\frac{d}{dU_{\beta\lim}}\left(\frac{2\pi\left|\vec{u}_{\max}\right|U_{\beta\lim}\sqrt{\left|\vec{u}_{\max}\right|^2-U_{\beta\lim}{}^2}\left|\sin\left(\theta_{\alpha\lim}-\theta_{\beta\lim}\right)\right|}{\sqrt{4\left|\vec{u}_{\max}\right|^2+2U_{\beta\lim}{}^2\left(\sigma_2-1\right)}}\right)=0 \qquad (5.36).$$
$$U_{\alpha\lim}\in\left[0,\hat{U}_\alpha\right] \qquad U_{\beta\lim}\in\left[0,\hat{U}_\beta\right]$$

The result of (5.36) is collected in (5.37). Analogously to (5.33), the action of the MA saturator on the magnitudes $\hat{U}_\alpha$ and $\hat{U}_\beta$ can be also expressed by the factors $r_{\alpha MA}=U_{\alpha\lim}/\hat{U}_\alpha$ and $r_{\beta MA}=U_{\beta\lim}/\hat{U}_\beta$, as indicated by (5.38). Note that in this case, it has been distinguished between α and β-axis due to the saturator does not homogenously limit each vector component.

$$U_{\alpha\lim}=\begin{cases}\left|\vec{u}_{\max}\right| & if\ \sigma_2=-1\ \&\ \hat{U}_\alpha>U_{MA}\\ U_{MA} & else\,if\ \hat{U}_\alpha>U_{MA}\ \&\ \hat{U}_\beta>U_{MA}\\ 2\left|\vec{u}_{\max}\right|\sqrt{\dfrac{\left|\vec{u}_{\max}\right|^2-\hat{U}_\beta{}^2}{4\left|\vec{u}_{\max}\right|^2+2\hat{U}_\beta{}^2\left(\sigma_2-1\right)}} & else\,if\ \hat{U}_\alpha>U_{MA}\ \&\ \hat{U}_\beta\le U_{MA}\\ \hat{U}_\alpha & else\,if\ \hat{U}_\alpha\le U_{MA}\end{cases}$$
$$U_{\beta\lim}=\begin{cases}\left|\vec{u}_{\max}\right| & if\ \sigma_2=-1\ \&\ \hat{U}_\beta>U_{MA}\\ U_{MA} & else\,if\ \hat{U}_\alpha>U_{MA}\ \&\ \hat{U}_\beta>U_{MA}\\ 2\left|\vec{u}_{\max}\right|\sqrt{\dfrac{\left|\vec{u}_{\max}\right|^2-\hat{U}_\alpha{}^2}{4\left|\vec{u}_{\max}\right|^2+2\hat{U}_\alpha{}^2\left(\sigma_2-1\right)}} & else\,if\ \hat{U}_\alpha\le U_{MA}\ \&\ \hat{U}_\beta>U_{MA}\\ \hat{U}_\beta & else\,if\ \hat{U}_\beta\le U_{MA}\end{cases} \qquad (5.37).$$
$$U_{MA}=\begin{cases}\sqrt{\dfrac{-2+\sqrt{4+2\left(\sigma_2-1\right)}}{\left(\sigma_2-1\right)}}\left|\vec{u}_{\max}\right| & if\quad \sigma_2\neq 1\\ \left|\vec{u}_{\max}\right|/\sqrt{2} & else\end{cases}$$

$$u^*_{\alpha\lim}[k]=r_{\alpha MA}\hat{U}_\alpha[k]\cos\left(\theta_{\alpha\lim}\right) \qquad (5.38).$$
$$u^*_{\beta\lim}[k]=r_{\beta MA}\hat{U}_\beta[k]\cos\left(\theta_{\beta\lim}\right)$$
$$0\le r_{\alpha MA},r_{\beta MA}\le 1$$

5.4.4.4. Comparative between saturation strategies.

This subsection contains a comparative analysis of PS and MA. The advantages and downsides are studied so that the reader can assess each technique and choose the most suitable for the application. The comparative is mainly focused on the parameters r_{PS} and $r_{\alpha MA}$ - $r_{\beta MA}$, which entirely define the behavior of the saturators.

Fig. 5.15.a and b show the surface of r_{PS} in function of the magnitudes when $\sigma_2=-1$ ($\pi/2$ of phase lag between the vector components) and $\sigma_2=0.844$ (almost $\pm\pi$ of phase lag),

respectively. When $\sigma_2=-1$, the elliptical trajectory of $\vec{u}$ is totally horizontal ($\hat{U}_\alpha>\hat{U}_\beta$), vertical ($\hat{U}_\alpha<\hat{U}_\beta$) or it corresponds to a circumference ($\hat{U}_\alpha=\hat{U}_\beta$). Then, the furthest point of the trajectory from the origin is located in one of the axis. This means that the component with the minimum magnitude does not takes part in the selection of the value of r_{PS}, as indicated by (5.39). This fact can easily be appreciated on Fig. 5.15.a. As long as the value of σ_2 increases, the trajectory takes some inclination and the direction of the furthest point is not longer located in one axis. Therefore, the influence of the component with the minimum amplitude becomes more notorious as displayed in Fig. 5.15.b. The plain surface where $r_{PS}=1$ is the operating zone where no saturation is applied on $\vec{u}^*$. In general, the area of this non-saturated zone and the average value of r_{PS} decrease as long as the value of σ_2 increases. This means that those vectors with lower contamination of negative sequence suffer a softer limitation. Another interesting aspect is that the surface of r_{PS} is symmetric with respect to the plane defined by $\hat{U}_\alpha=\hat{U}_\beta$, which indicates that the value of r_{PS} does not change if the values of $\hat{U}_\alpha$ and $\hat{U}_\beta$ are switched each other.

$$r_{PS}\Big|_{\sigma_2=-1}=\frac{\left|\vec{u}^*_{\max}\right|}{\min\left(\left|\vec{u}^*_{\max}\right|,\max\left(\hat{U}_\alpha,\hat{U}_\beta\right)\right)};\ \left.\frac{\partial r_{PS}}{\partial\min\left(\hat{U}_\alpha,\hat{U}_\beta\right)}\right|_{\sigma_2=-1}=0 \tag{5.39}$$

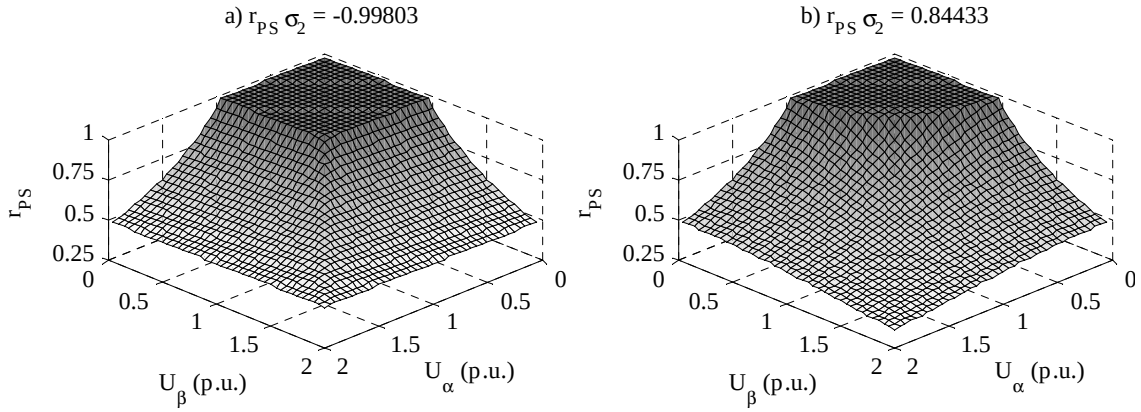

Fig. 5.15: Surface representation of the gain of the PS technique r_{PS} in function of the amplitudes with a) σ_2 = -1 and b) σ_2 = 0.84433.

On the other hand, Fig. 5.16.a and b respectively show the surfaces of the parameters $r_{\alpha MA}$ and $r_{\beta MA}$ when $\sigma_2=-1$ while Fig. 5.16.c and d display them with $\sigma_2=0.84433$. In the first case, the influence of $\hat{U}_\beta$ in the limitation of $\hat{U}_\alpha$ is null and vice versa. If $\sigma_2\neq-1$, the magnitude $\hat{U}_\beta$ affects in the limitation of $u^*_\alpha[k]$ if $\hat{U}_\beta\in[0,U_{MA}]$. Again, as long as σ_2 increases, the non-saturated area and the average value of $r_{\alpha MA}$ and $r_{\beta MA}$ decrease. In contrast with the PS, the MA does not present any symmetry in their surfaces, indicating that the vector components are treated with different saturation gains.

$$r_{\alpha MA}\Big|_{\sigma_2=-1}=\frac{\left|\vec{u}^{*}_{\max}\right|}{\min\left(\left|\vec{u}^{*}_{\max}\right|,\hat{U}_{\alpha}\right)};\quad \frac{\partial r_{\alpha MA}}{\partial \hat{U}_{\beta}}\Big|_{\sigma_2=-1}=0;$$
$$r_{\beta MA}\Big|_{\sigma_2=-1}=\frac{\left|\vec{u}^{*}_{\max}\right|}{\min\left(\left|\vec{u}^{*}_{\max}\right|,\hat{U}_{\beta}\right)};\quad \frac{\partial r_{\beta MA}}{\partial \hat{U}_{\alpha}}\Big|_{\sigma_2=-1}=0; \tag{5.40}$$

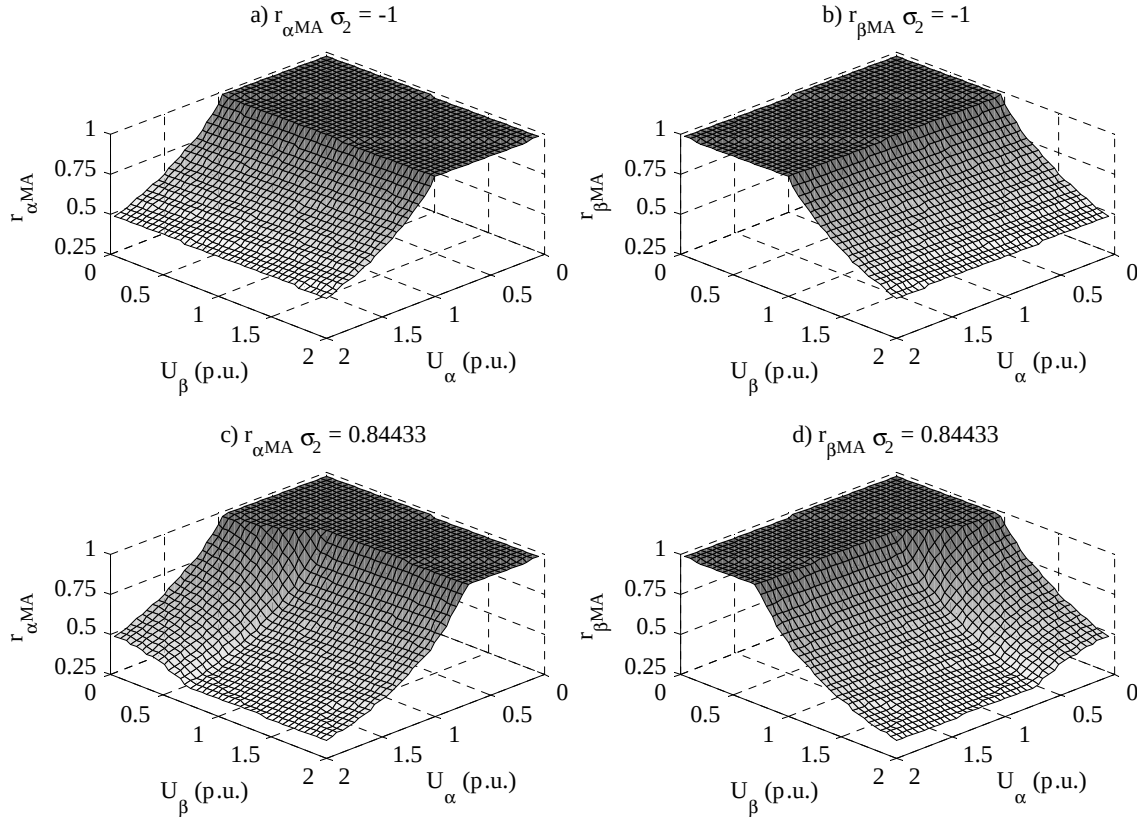

Fig. 5.16: Surface representation of the gains of the MA technique. a) $r_{\alpha MA}$ with $\sigma_2 = -1$, b) $r_{\beta MA}$ with $\sigma_2 = -1$, c) $r_{\alpha MA}$ with $\sigma_2 = 0.84433$ and d) $r_{\beta MA}$ with $\sigma_2 = 0.84433$

Comparing the surfaces obtained in the PS and MA techniques, the MA presents a wider non-saturated zone and the volume enclosed by the surfaces of Fig. 5.16 and the plane $\chi=0$ are much larger than in the PS case. This verifies the goal of supplying the vector with the maximum area. On the other hand, the symmetrical behavior of the PS technique respects much more the controller's actuation in distorted conditions. By keeping the same ratio between positive and negative sequences, the actuation over the oscillating power is not so affected. There is some kind of relation between r_{PS} and $r_{\alpha MA} - r_{\beta MA}$ (that can be easily checked with the surfaces):

$$r_{PS}=\min\left(r_{\alpha MA}, r_{\beta MA}\right) \tag{5.41}$$

As a consequence, independently of σ_2, when the vector components contain the same amplitude ($\hat{U}_\alpha = \hat{U}_\beta$), the use of PS and MA present identical results:

$$r_{PS} = r_{\alpha MA} = r_{\beta MA} \quad if\ \hat{U}_\alpha = \hat{U}_\beta \tag{5.42}$$

Fig. 5.17 depicts some representative cases of $\vec{u}^*$ with different unbalance levels and the resulting $\vec{u}_{\lim}$ in function of the adopted saturation technique. In the trajectories, the blue trace represents the trajectory of $\vec{u}^*$, the green one corresponds with the trajectory of $\vec{u}^*_{\lim}$ using PS and the red one using MA. The corresponding waveforms are also displayed where the α component is represented with solid line and the β component with dashed line. Table 5.1 collects the amplitude of each component of the input vector $\vec{u}^*$ and the value of the parameter σ_2. In case 1, both saturation techniques get the same saturated vector due to the amplitudes of $\vec{u}^\alpha$ are the same, verifying (5.42). Paying attention to Fig. 5.17.a, one could think that the resulting trajectory does not contain the maximum possible area. However, this is actually the maximum area that keeps the phases of the original components. In the case 2, the phase lag is $\pi/2$ but the magnitudes are different. As seen, the MA technique takes advance of all the available area and only limits u^*_α while $u^*_{\beta\lim} = u^*_\beta$ due to $u^*_\beta <= U_{MA}$. The PS technique applies the same reduction to both components so the limited trajectory is a reduced copy of the original one preserving the shape. The same statements mentioned for case 2 can be again applied to case 3. However, under the high unbalance between components, $U_\alpha >> U_\beta$, the use of the PS technique highly limits the β component thought its magnitude is already quite low. This can be seen as an unnecessary saturation of this axis. With the MA technique, only the component that increases the vector magnitude is saturated.

Table 5.1: Amplitudes and phase lag of the input reference vector for the three different cases.

	Case 1	Case 2	Case 3
U_α (p.u.)	1.2	1.5	5
U_β (p.u.)	1.2	0.9	0.3
σ_2	-0.921	-1	-0.921

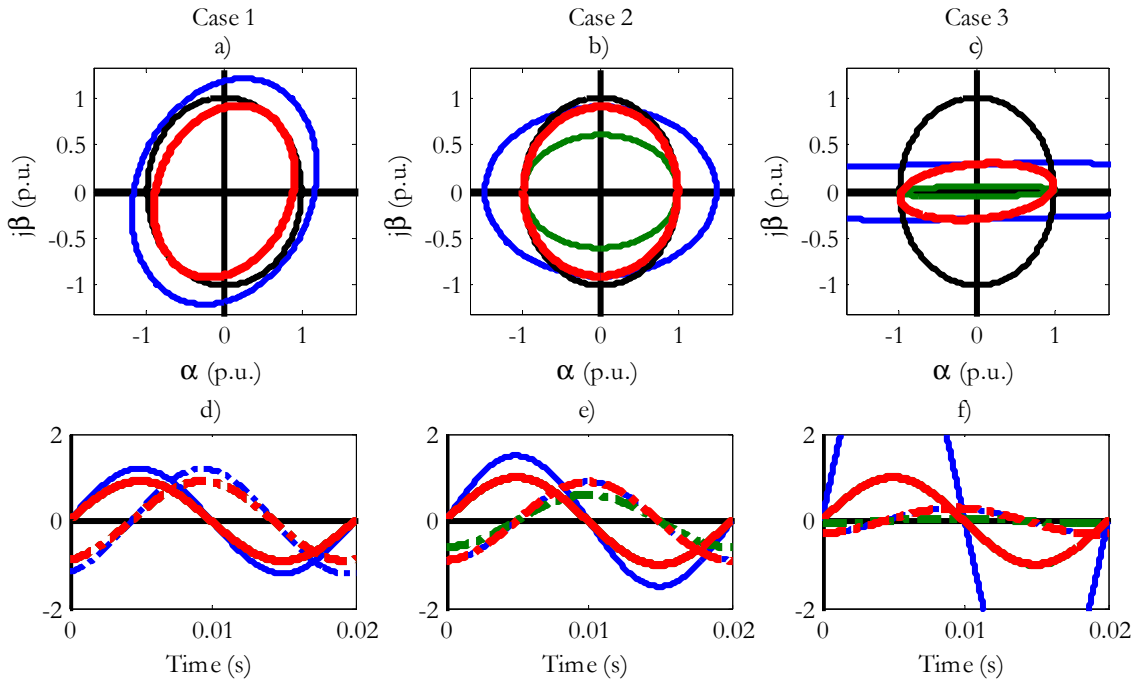

Fig. 5.17: a) Trajectories of $\vec{u}^*$ (blue), $\vec{u}^*_{\text{lim}}$ using PS (green) and $\vec{u}^*_{\text{lim}}$ using MA (red) in case 1, b) in case 2 c) in case 3, d) Temporal waveforms of the αβ components of the vectors $\vec{u}^*$ (blue), $\vec{u}^*_{\text{lim}}$ using PS (green) and $\vec{u}^*_{\text{lim}}$ using MA (red) in case 1, e) in case 2 and f) in case 3.

5.5. Conclusions.

This chapter has presented real contributions in the management of unbalanced conditions. It has been shown that a bad representation of control variables with a non linear operation leads to the apparition of harmonics.

The conventional droop controller has been revised and modified with the objective of increasing its performance in grid-connected mode. It has been dotted of a dual-phase behavior and the OPC block has been added. With the former, the distortion caused by a bad representation of control variables is avoided while the latter allows the regulation of the oscillating power. The chapter provides a theoretical study of the OPC and configures it to minimize its influence on the DC power control carried out by the droop.

One of the greatest contributions of this work is the proposed novel saturator structure. The theoretical analysis has been shown that, in contrast with previous techniques, the SRF-saturators develop a distortion-free limitation of the control references. It can be applied to the control of any converter with a fixed operating frequency (drives are logically excluded). Two different techniques have been presented with different features: PS and MA. The theoretical statements regarding the saturators are experimentally validated in Chapter 7.

Chapter 6.

Virtual impedance applied to synchronization.

Following the Universal Operation philosophy, a synchronization technique that makes use of a virtual impedance for the configuration of the voltage commands is proposed with the aim of fairly sharing the load and improving the voltage regulation accuracy.

6.1. Introduction.

During previous chapters, different solutions for the power control of a UWT during the island and grid connected modes have been studied. After an island operation and when the connection is again allowed (the fault has been cleared), the isolated grid is likely loss the synchronism with the main grid. The presence of a synchronization strategy that assures the integrity of both systems when reclosing the switch is required.

It seems obvious that the operating principle of the synchronization should be based on minimizing the voltage drop across the circuit breaker, i.e., reducing the error between the island voltage ($\vec{e}_{ISL}$) and $\vec{e}_{PCC}$ (see Fig. 1.5). This way, the current peak during the breaker reclosing is minimized. The most trivial alternative is to wait for the converging of the phases of $\vec{e}_{ISL}$ and $\vec{e}_{PCC}$. However, this option has many associated drawbacks: the synchronization time is not limited, which can cause the tripping of the sources before the reconnection, and it is not assured that both voltages contain the same magnitude, which may increase the current peak during the transition. The remaining options depend on the structure of the island. The spatial distribution of the different parallel sources can complicate the synchronization procedure. The possibility of implementing the synchronization system on a master UWT,

which controls the circuit breaker, removes the necessity of coordinating the parallel sources during the synchronization. This master UWT is on charge of bringing $\vec{e}_{ISL}$ to the desired point while the rest are still performing a semi grid-forming strategy. This fact requires the permanent availability of the master UWT and its power rating and energy reserves should be high enough to regulate $\vec{e}_{ISL}$. The existence of this overloaded master unit does not respect the versatility and reliability principles of the Universal Operation.

The synchronization system proposed in this work follows the line of the power sharing strategy of 4.1.5: fairly distribute the load as function of the remaining kinetic storage. The goal of bringing the island voltage close to the grid voltage is addressed as a common task where all the UWTs take part. The role of master is then substituted by a collaborating method. This way, the dependence level between the synchronization technique and the structure of the island is slightly reduced. However, there are still ties between these two terms. Fig. 1.5 represents the most generic case where the distribution of the UWTs and the circuit breaker requires of a communication link to perform the synchronization.

Fig. 6.1 shows an isolated system composed by N units and the synchronization strategy. The synchronization is divided in two elements: state manager and local synchronization system in each unit. The state manager can be seen as a central unit within the synchronization process. It is on charge of broadcasting $\vec{e}_{PCC}$ to all the UWTs and VCVSC units and analyzing the difference between $\vec{e}_{ISL}$ and $\vec{e}_{PCC}$. It should carry out anti-islanding tasks as well. When the phase and magnitude of the island voltage remain closer to the corresponding ones of $\vec{e}_{PCC}$, the state manager gives the command to close the circuit breaker and updates the state signal S to notify all the parallel units the current mode is grid-connected. At the same time, the UWTs receive $\vec{e}_{PCC}$ and accordingly configure their voltage reference. As described in 4.1.3, the droop control is disabled during the synchronization so each UWT can be modeled as an ideal fixed voltage plus an impedance. The line impedance of each UWT has been neglected in favor of the output impedance of the filter. Considering an ideal communication bus, every UWT receives the current value of the PCC voltage. The second element is the local synchronization system of each unit. Its main purpose is supplying the voltage reference during the synchronization process.

The purpose of this chapter is proposing a strategy for selecting the voltage reference in each unit that fairly distribute the load and achieve a seamless transition by carrying the island voltage as close as possible to the PCC voltage.

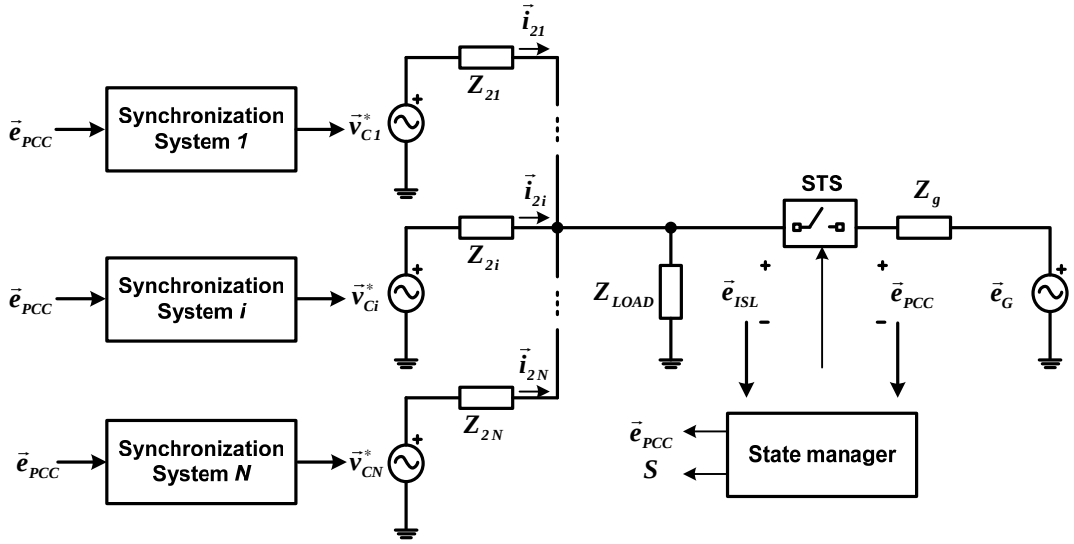

Fig. 6.1: Simplified model of isolated system with the synchronization system.

6.2. State manager.

The state manager sends both the state and the PCC voltage to each unit of the island. Apart from anti-islanding tasks, it decides when the circuit breaker has to be opened and closed. Regarding the synchronization, it is on charge of processing the PCC and island voltages to calculate their magnitudes and phases. This task is carried out by the block depicted in Fig. 6.2, to be implemented in state manager. Three fundamental blocks can be observed: second order generalized integrator for the quadrature signal generation (SOGI-QSG) [Rodriguez, *et al.*, 2006], synchronous reference frames PLL [Blaabjerg, *et al.,* 2006] and the voltage comparator. The SOGI-QSG and PLL are also implemented in the synchronization system of each UWT, depicted in Fig. 3.1.

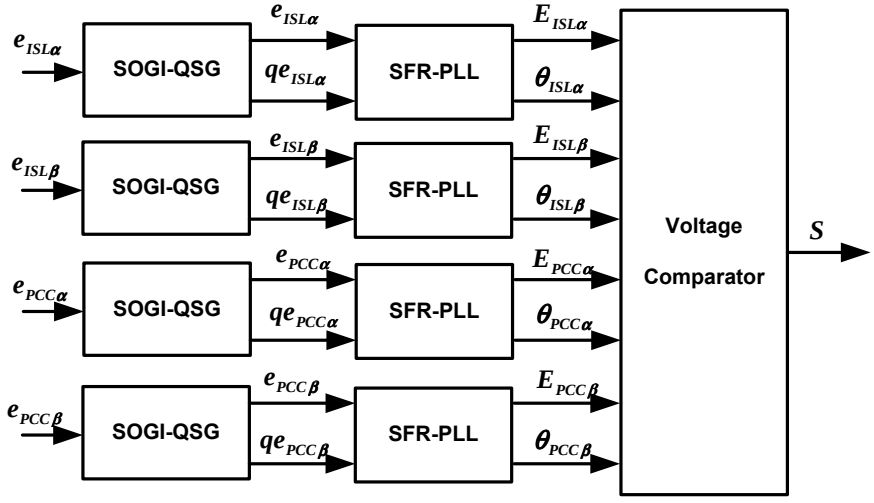

Fig. 6.2: Block diagram for comparing the island and PCC voltages.

The obtaining of a virtual quadrature signal of a certain sinusoid is quite useful for the calculation of its amplitude and phase. This operating principle is usually applied in the

synchronization of single-phase power systems to working out the phase and amplitude of the voltage. In this case, in order to assure the correctness of the synchronization even under unbalanced conditions, this philosophy has been applied reducing the problem to two single-phase systems. There are many methods in the bibliography to obtain the quadrature signal. The SOGI-QSG (see Fig. 6.3) offers a good trade-off between bandwidth and filter capacity for synchronization task. The settling time is around a half of the fundamental period while it applies noticeable attenuation of the 5th, 7th and higher harmonics. Note that this attenuation is desirable from the point of view of the PLL and it does not really affect to the synchronization performance. The discretization of the SOGI-QSG is not trivial, and in this work, the procedure suggested in [Rodriguez, *et al.*, 2008] has been followed.

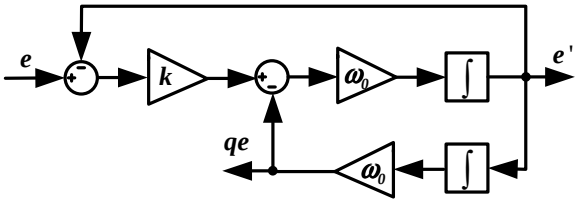

Fig. 6.3: Second Order Generalized Integrator for the quadrature signal generation (SOGI-QSG).

The scheme of Fig. 6.4 displays the PLL used in this work. It receives a voltage component and its respective quadrature signal. The phase is obtained by synchronizing with the q-axis of the each voltage, which is entered in the loop in p.u. to unlink the dynamics of the PLL and the value of the magnitude of the voltage. Information of the frequency is also collected for anti-islanding purposes.

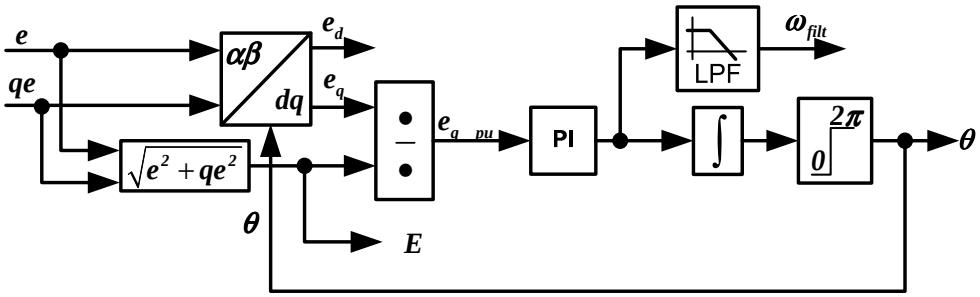

Fig. 6.4: Synchronous Reference Frames Phase-locked loop (SFR-PLL).

In these conditions, the magnitudes and phases of the αβ components of the PCC and island voltages are supplied to the voltage comparator displayed on Fig. 6.5. The absolute values of the phase and magnitude differences of each axis ($|\Delta\theta_\beta|$, $|\Delta\theta_\alpha|$, $|\Delta E_\alpha|$ and $|\Delta E_\beta|$) are calculated and stored in its corresponding buffer. Four LIFO (last input first output) buffers of L samples each are then necessary. A new sample is introduced in the buffers each control iteration, temporized by the control sampling period Ts. All the L magnitude and phase sampled errors are respectively contrasted with the magnitude and phase thresholds, $|\Delta E|_{max}$ and $|\Delta\theta|_{max}$. These thresholds represent the maximum admissible magnitude and phase of the voltage drop on the circuit breaker. In order to activate the output signal S and

thus, approve the reclosing of the isolated system, all the L magnitude and phases samples must be lower than their respective thresholds. That way, the synchronization system assures the capacitor voltage response has reached the steady state and is perfectly tracking the PCC voltage. The required time to perform the synchronization depends on: the thresholds' values, the voltage controller time response, the buffer length and Ts. The minimum time considering ideal voltage response would be $L \cdot Ts$, the required time to fill the buffers. The selection of the thresholds' values depends on the power scenario and voltage level [IEEE-1547.4, 2011].

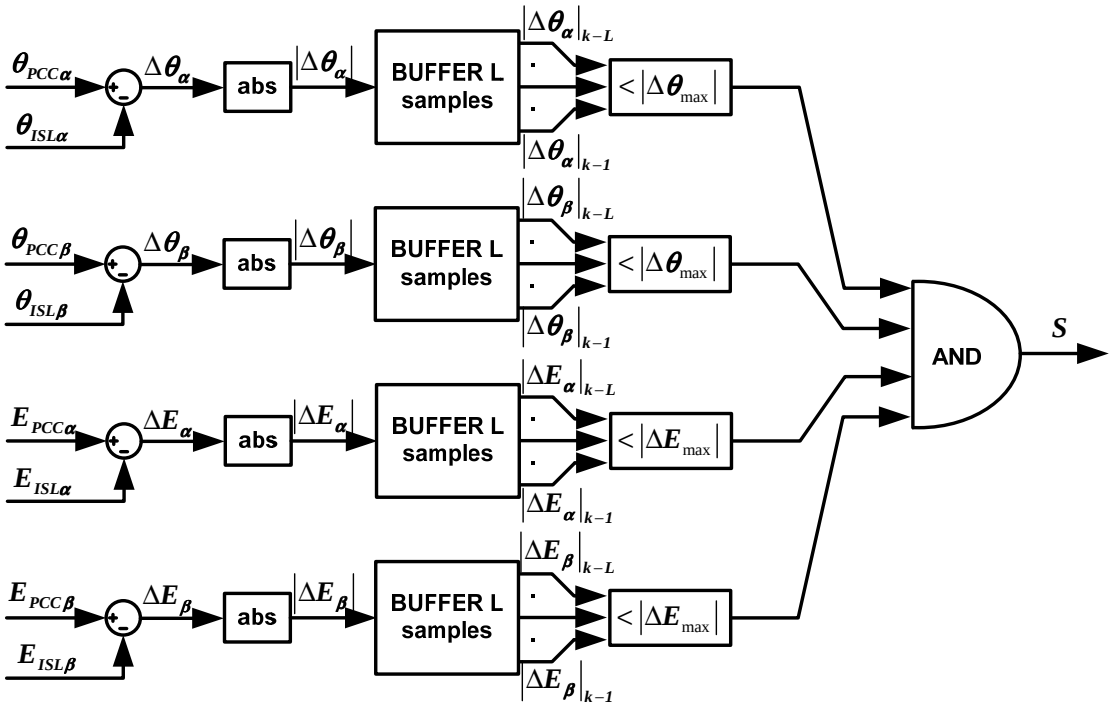

Fig. 6.5: Magnitude and phase voltage comparator.

The SOGI-QSG and SRF-PLL are also implemented in the control of each UWT to provide the base voltage as expressed by (5.5). Remember that the base voltage is employed during the grid-connected mode and also during the synchronization to create the voltage reference.

6.3. Effects of the filter output impedance.

In previous works, the local synchronization system automatically configures the voltage reference with the PCC voltage. This section analyzes the effect of L_2 over the island voltage regulation and the distribution of the load power.

The difference between capacitor voltage of the unit i, $\vec{v}_{Ci}^{*}$, and the island voltage $\vec{e}_{ISL}$ is given by the voltage drop across its filter output impedance. The steady-state island voltage can be obtained by means of the superposition theorem, where each voltage source contributes to the phasor $\vec{e}_{ISL}$ within a voltage divisor:

$$\vec{e}_{ISL} = \sum_{i=1}^{N} k_{DIVi} \cdot \vec{v}_{Ci}^{*} \tag{6.1}$$

where the factor k_{DIVi} represents the gain of the voltage divisor for the unit *i*. It can be easily expressed as:

$$k_{DIVi} = \frac{Z_{Pi}}{Z_{Pi} + Z_{2i}} \tag{6.2}$$

The impedance Z_{Pi} is the parallel of all the output impedances Z_{2j} with $j \neq i$ and the load impedance. For convenience and simplicity, the load impedance is expressed as $Z_{2N+1} = Z_{LOAD}$.

$$Z_{Pi} = \left(\sum_{j \neq i}^{N+1} Z_{2j} \right)^{-1} = \frac{\prod_{j \neq i}^{N+1} Z_{2j}}{\sum_{j \neq i}^{N+1} \left(\prod_{k \neq i,j}^{N+1} Z_{2k} \right)} \tag{6.3}$$

Then, inserting (6.3) in (6.2), the divisor factor k_{DIVi} is given by:

$$k_{DIVi} = \frac{\prod_{j \neq i}^{N+1} Z_{2j}}{\prod_{j \neq i}^{N+1} Z_{2j} + Z_{2i} \cdot \sum_{j \neq i}^{N+1} \left(\prod_{k \neq i,j}^{N+1} Z_{2k} \right)} = \frac{\prod_{j \neq i}^{N+1} Z_{2j}}{\sum_{j=1}^{N+1} \left(\prod_{k \neq j}^{N+1} Z_{2k} \right)} \tag{6.4}$$

The divisor factor is a complex value that can be expressed in polar coordinates:

$$\begin{aligned} k_{DIVi} &= M_{DIVi} \cdot e^{j\theta_{DIVi}} \\ \vec{e}_{ISL} &= \sum_{i=1}^{N} M_{DIVi} \cdot e^{j\theta_{DIVi}} \vec{v}_{Ci}^{*} \end{aligned} \tag{6.5}$$

The parameter M_{DIVi} makes reference to the magnitude variation caused in $\vec{e}_{ISL}$ as a consequence of Z_{2i} while θ_{DIVi} is related to the phase variation. Representing as well the impedances in polar coordinates as $Z_{2i} = |Z_{2i}| e^{j\theta_{2i}}$, M_{DIVi} and θ_{DIVi} respond to:

$$\begin{aligned} M_{DIVi} &= \frac{\prod_{j \neq i}^{N+1} |Z_{2j}|}{\sqrt{\left[\sum_{j=1}^{N+1} \left(\prod_{k \neq j}^{N+1} |Z_{2k}| \right) \cos\left(\sum_{k \neq j}^{N+1} \theta_{2k} \right) \right]^2 + \left[\sum_{j=1}^{N+1} \left(\prod_{k \neq j}^{N+1} |Z_{2k}| \right) \sin\left(\sum_{k \neq j}^{N+1} \theta_{2k} \right) \right]^2}} \\ \theta_{DIVi} &= \sum_{j \neq i}^{N+1} \theta_{2j} - \tan^{-1} \left[\frac{\sum_{j=1}^{N+1} \left(\prod_{k \neq j}^{N+1} |Z_{2k}| \right) \sin\left(\sum_{k \neq j}^{N+1} \theta_{2k} \right)}{\sum_{j=1}^{N+1} \left(\prod_{k \neq j}^{N+1} |Z_{2k}| \right) \cos\left(\sum_{k \neq j}^{N+1} \theta_{2k} \right)} \right], \; i \in [1, N] \end{aligned} \tag{6.6}$$

Considering that all the filter output impedances are predominantly inductive ($\theta_{2i}=\pi/2 \ \forall i\in[1,N]$), θ_{DIVi} is rewritten as:

$$\theta_{DIVi}=\theta_{DIV}\approx N\frac{\pi}{2}+\theta_{2N+1}-\tan^{-1}\left[\frac{\sum_{j=1}^{N+1}\left(\prod_{k\neq j}^{N+1}|Z_{2k}|\right)\sin\left(\sum_{k\neq j}^{N+1}\theta_{2k}\right)}{\sum_{j=1}^{N+1}\left(\prod_{k\neq j}^{N+1}|Z_{2k}|\right)\cos\left(\sum_{k\neq j}^{N+1}\theta_{2k}\right)}\right],\ i\in[1,N] \qquad (6.7).$$

The last expression indicates that the phase variation is almost the same for each unit and equal to θ_{DIV}. During the synchronization, the droop control references are not taking into account, the synchronization strategy is on charge of such task. As in this case, all the units command the same voltage reference ($\vec{e}_{PCC}$), the island voltage responds to:

$$\vec{e}_{ISL}=M_{TOT}\cdot\vec{v}_C^{\,*}\cdot e^{j\theta_{DIV}}$$
$$M_{TOT}=\sum_{i=1}^{N}M_{DIVi} \qquad (6.8).$$

The parameter M_{TOT} represents the magnitude variation between $\vec{e}_{ISL}$ and $\vec{v}_C^{\,*}$. The value of this parameter is shown in Fig. 6.6 for several active and reactive power demands of the local load Z_{LOAD} and two UWTs whose main parameters are collected on Table 7.1. The parameter is more sensitive to the reactive power. As expected, capacitive reactive power demands lead to the increment of the magnitude of $\vec{e}_{ISL}$ while inductive reactive power transfers reduces it. Besides, as long as the active power consumption is increased, the voltage drop becomes more notorious. In spite of that, the voltage reduction is still acceptable.

Expression (6.6) indicates that the weight a unit has on the island voltage is inversely proportional to the magnitude of its output impedance.

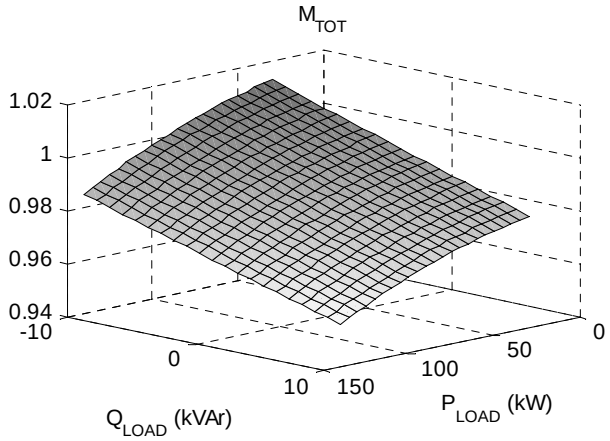

Fig. 6.6: Magnitude relation between the capacitor and island voltage due to the LCL filter output impedance in function of the active and reactive power demanded by the local load

The total current supplied to the load, $\vec{i}_{LOAD}$, is obtained by dividing the island voltage in (6.5) by the load impedance:

$$\vec{i}_{LOAD} = \frac{\vec{e}_{ISL}}{Z_{2N+1}} = \sum_{i=1}^{N} M_{IDIVi} \cdot e^{j\theta_{IDIVi}} \cdot \vec{v}_{Ci}^{\,*}$$

$$M_{IDIVi} = \frac{M_{DIVi}}{|Z_{2N+1}|} = \frac{\prod_{j\neq i}^{N} |Z_{2j}|}{\sqrt{\left[\sum_{j=1}^{N+1}\left(\prod_{k\neq j}^{N+1}|Z_{2k}|\right)\cos\left(\sum_{k\neq j}^{N+1}\theta_{2k}\right)\right]^2 + \left[\sum_{j=1}^{N+1}\left(\prod_{k\neq j}^{N+1}|Z_{2k}|\right)\sin\left(\sum_{k\neq j}^{N+1}\theta_{2k}\right)\right]^2}} \qquad (6.9).$$

$$\theta_{IDIVi} = \theta_{DIVi} - \theta_{2N+1} = \sum_{j\neq i}^{N+1}\theta_{2j} - \tan^{-1}\left[\frac{\sum_{j=1}^{N+1}\left(\prod_{k\neq j}^{N+1}|Z_{2k}|\right)\sin\left(\sum_{k\neq j}^{N+1}\theta_{2k}\right)}{\sum_{j=1}^{N+1}\left(\prod_{k\neq j}^{N+1}|Z_{2k}|\right)\cos\left(\sum_{k\neq j}^{N+1}\theta_{2k}\right)}\right],\ i\in[1,N]$$

where the parameters M_{IDIVi} and θ_{IDIVi} makes reference to the current divisor seen by the unit *i*. The particular contribution of the unit *i* to the total current is then given by $M_{IDIVi} \cdot e^{j\theta_{IDIVi}} \cdot \vec{v}_{Ci}^{\,*}$. As every local synchronization system commands the same voltage reference to every unit, the power contribution is determined by M_{IDIVi}. It defines a kind of open-loop power sharing which just depends on the filter output impedances. Analogous to M_{TOT} in the voltage divisor case, the parameter M_{ITOT} is expressed as:

$$\vec{i}_{LOAD} = M_{ITOT} e^{j\theta_{IDIV}} \vec{v}_C^{\,*}$$
$$M_{ITOT} = \sum_{i=1}^{N} M_{IDIVi} \qquad (6.10).$$

An interesting parameter to be defined is f_{IDIVi}, contained in (6.11). It indicates the power contribution of the unit *i* over the total consumption. The different f_{IDIVi}'s give the default distribution of the local load with this simple synchronization philosophy. Those units with lower impedances contribute with more power, which a priori is a beneficial fact given the relation between power rating and impedance of a power system. Note that this distribution just only depends on the filter output impedances and is independent of the load. In the case of a system conformed by the two UWTs of Table 7.1, UWT_1 would contribute with the 42% of the total power consumed while UWT_2 is on charge of the remaining 58% (f_{IDIV1}=0.42 and f_{IDIV2}=0.58).

$$f_{IDIVi} = \left.\frac{P_{Gi}}{P_{LOAD}}\right|_{\substack{\vec{v}_{Ck}^{\,*}=\vec{v}_C^{\,*} \\ k\in[1,N]}} = \frac{M_{IDIVi}}{M_{ITOT}} = \frac{\prod_{j\neq i}^{N}|Z_{2j}|}{\sum_{s=1}^{N}\prod_{j\neq s}^{N}|Z_{2j}|} \qquad (6.11).$$

6.4. Synchronization system.

The different values of the f_{IDIVi}'s define the power distribution when all the units command the same voltage reference. This default distribution does not take into account the kinetic reserves and hence, the potential risk of shutting down is high considering that the duration of the synchronization is not negligible. Besides, the parameter M_{TOT} clearly indicates that the voltage drop across filter output impedance worsens the island voltage regulation. As a consequence, $\vec{e}_{ISL}$ does never reach the PCC voltage, providing a poorer transient during the reconnection of the isolated system.

The above paragraph reveals that the efficiency of the synchronization is strictly tied to the output impedance of each UWT. It seems evident the utilization of a virtual impedance term with the aim of modify the total equivalent output impedance and this way, improve the accuracy of the synchronization and at the same time regulate the power injection of each UWT.

6.4.1. Design and implementation of the virtual impedance.

The objectives of the virtual impedance are the improvement of the synchronization accuracy and the weight of the supplied power, improving the value of the parameter M_{TOT}, defined in (6.8), and regulating each f_{IDIVi}, defined in(6.11), for a fair power sharing. The block shown in Fig. 6.7 introduces the implementation of the virtual loop by the addition of the virtual voltage term $\vec{e}_{ZV}$. The variable vector $\vec{e}_{ZV}$ increases the capacitor voltage reference in function of the output current. The system can be then modeled with an ideal voltage $(\vec{e}_{PCC})$ and an impedance whose value is $Z_{eqi} \approx Z_{2i} - Z_{Vi}$. The idea is just employ positive values of Z_V so that the synchronization accuracy cannot be worsened; only improved.

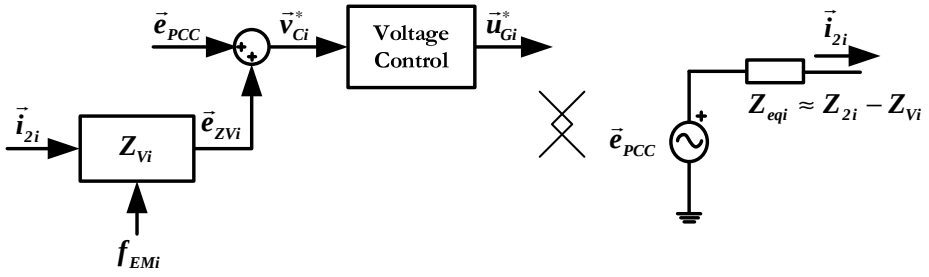

Fig. 6.7: Virtual impedance term for an accuracy and fair synchronization algorithm.

As previously mentioned, the term $\vec{e}_{ZV}$ is only activated during the synchronization, being null during the island and grid-connected modes. During the synchronization, it is configured with the steady state voltage drop the output current of the unit i creates on a virtual impedance Z_V. The steady state value makes reference to the phasor representation of Z_V, i.e. Z_V does not contain any type of dynamics. Modeling the dynamics of the virtual inductance supposes the implementation of a discrete casual derivator, which amplifies the noise of the output current. Z_V accomplishes its purpose only at the operating frequency ω_0. The values

of Z_V and $\vec{e}_{ZV}$ are expressed in (6.12). The virtual impedance is the product between the phasor output inductance L_2, the energy management factor, f_{EM}, employed for the power sharing algorithm and defined in (4.22) and a certain factor, f_{STAB}, to be configured in accordance with the desired relative stability of the system. Although the output impedance contains a resistive part, given by R_2, it is not predominant and does not take part in Z_V for simplicity. The virtual impedance and thus, the voltage reference and the supplied power, varies as function of the remaining kinetic reserves.

$$\begin{aligned} Z_{Vi} &= j\omega_0 L_{2i} f_{EMi} f_{STAB} \\ \vec{e}_{ZVi} &= Z_{Vi}\cdot\vec{i}_{2i} = j\omega_0 L_{2i} f_{EMi} f_{STAB}\left(i_{2i\alpha} + j i_{2i\beta}\right) \end{aligned} \tag{6.12}$$

From the point of view of the power balancing between units, a high value of f_{STAB} is interesting because it provides a wider range of variation in Z_V. However, the value of f_{STAB} is upper limited by stability requisites. In order to find this limit, the dynamics of the modified voltage loop, depicted on Fig. 6.8, are analyzed. As illustrated, this phasor virtual impedance adds a cross-coupling between α and β axis. The output current and capacitor voltage expressions are rewritten in (6.13) and (6.14) as function of the island voltage, which is the corresponding disturbance.

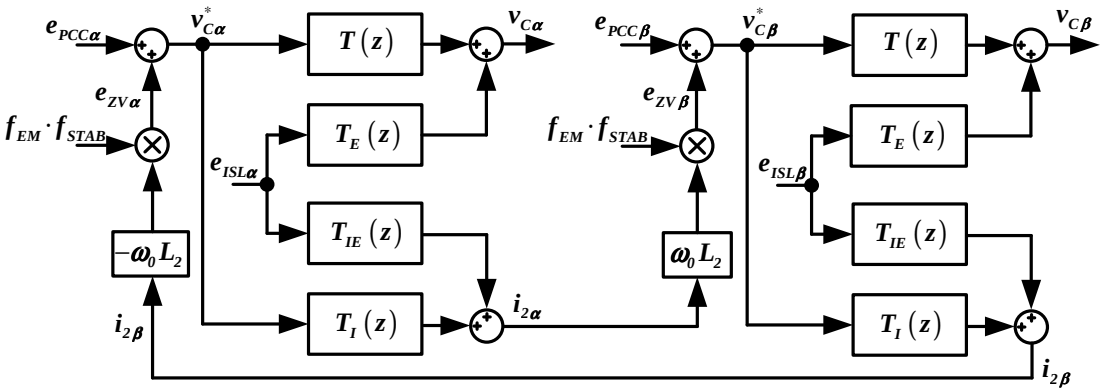

Fig. 6.8: Resulting scheme of the voltage loop with the virtual impedance.

$$\begin{aligned} i_{2\alpha}(z) &= T_I(z)v^*_{C\alpha}(z) + T_{IE}(z)e_{ISL\alpha}(z) \\ i_{2\beta}(z) &= T_I(z)v^*_{C\beta}(z) + T_{IE}(z)e_{ISL\beta}(z) \end{aligned} \tag{6.13}$$

$$\begin{aligned} v_{C\alpha}(z) &= T(z)v^*_{C\alpha}(z) + T_E(z)e_{ISL\alpha}(z) \\ v_{C\beta}(z) &= T(z)v^*_{C\beta}(z) + T_E(z)e_{ISL\beta}(z) \end{aligned} \tag{6.14}$$

The implementation of the virtual impedance configures the voltage reference as follows:

$$\begin{aligned} v^*_{C\alpha}(z) &= e_{PCC\alpha}(z) - |Z_V|\left(T_I(z)v^*_{C\beta}(z) + T_{IE}(z)e_{ISL\beta}(z)\right) \\ v^*_{C\beta}(z) &= e_{PCC\beta}(z) + |Z_V|\left(T_I(z)v^*_{C\alpha}(z) + T_{IE}(z)e_{ISL\alpha}(z)\right) \end{aligned} \tag{6.15}$$

where $|Z_V| = \omega_0 L_{2i} f_{EMi} f_{STAB}$ is the magnitude of the virtual impedance. The capacitor voltage is then represented by means of the four modified closed loop transfer functions, as

shown in (6.16). $T_D(z)$ is the direct closed-loop transfer function, $T_Q(z)$ the cross closed-loop transfer function, $T_{DE}(z)$ the direct disturbance transfer function and $T_{QE}(z)$ the cross disturbance transfer function.

$$\begin{aligned} v_{C\alpha}(z) &= T_D(z)e_{PCC\alpha}(z) - T_Q(z)e_{ISL\beta}(z) + T_{DE}(z)e_{ISL\alpha}(z) - T_{QE}(z)e_{ISL\beta}(z) \\ v_{C\beta}(z) &= T_D(z)e_{PCC\beta}(z) + T_Q(z)e_{ISL\alpha}(z) + T_{DE}(z)e_{ISL\beta}(z) + T_{QE}(z)e_{ISL\alpha}(z) \end{aligned} \tag{6.16}$$

All these transfer functions share the same roots, so the stability analysis can be reduced to $T_D(z)$ for convenience. Equation (6.17) introduces the expression of $T_D(z)$ and Fig. 6.9.a and b respectively contain its dominant zeros and roots and the response to a sinusoidal reference in function of the product $f_{EM}\,f_{STAB}$. As $f_{EM} \leq 1$, the maximum value of this product matches up with f_{STAB}. Fig. 6.9.a reveals that the system is critically stable for $f_{EM}\,f_{STAB} = 1$. As long as, $f_{EM}\,f_{STAB}$ is being reduced, the dominant poles get further the limit circle and the relative stability is increased. The parameter f_{STAB} is configured with 0.75, which provides an infinite norm of the sensitivity transfer function around 6dβ. The effect of the virtual impedance is appreciated very well in Fig. 6.9.b. As long as the magnitude of the virtual impedance is increased, the gain gets higher and the phase is reduced counteracting some part of the real voltage drop on L_2. By configuring $f_{EM} = 0$, the virtual impedance is disabled and the voltage response is again given by $T(z)$. Note as well that the use of the virtual impedance has also a clear drawback: the incremented voltage reference makes the control system works closer to the overmodulation limit.

$$T_D(z) = \left.\frac{v_{C\alpha}}{e_{PCC\alpha}}\right|_{\substack{e_{PCC\beta}=0 \\ e_{ISL\alpha}=0 \\ e_{ISL\beta}=0}} = \left.\frac{v_{C\beta}}{e_{PCC\beta}}\right|_{\substack{e_{PCC\alpha}=0 \\ e_{ISL\alpha}=0 \\ e_{ISL\beta}=0}} = \frac{T(z)}{1 + |Z_V|^2 T_I(z)^2} \tag{6.17}$$

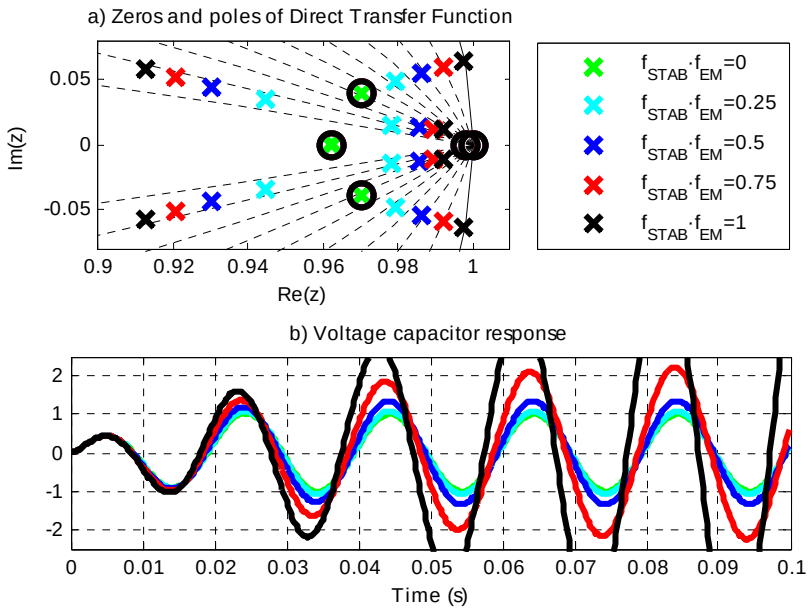

Fig. 6.9: Stability analysis in function of the parameter f_{STAB}: a) closed loop poles of $T_D(z)$ and b) $T_D(z)$ response to sinusoidal input.

To further support the study, it is necessary to focus the research on the equivalent output impedance, given by the transfer functions $T_{IDE}(z)$ and $T_{IQE}(z)$. These transfer functions give the output current through the island voltage (6.18). The direct and cross equivalent output impedances Z_{0D} and Z_{0Q} are respectively defined as the inverse of $T_{IDE}(z)$ and $T_{IQE}(z)$.

$$i_{2\alpha}(z)\Big|_{\substack{e_{PCC\alpha}=0\\ e_{PCC\beta}=0}} = T_{IDE}(z)\,e_{ISL\alpha}(z) + T_{IQE}(z)\,e_{ISL\beta}(z)$$

$$Z_{0D}(z) = \frac{e_{ISL\alpha}}{-i_{2\alpha}}\Bigg|_{\substack{e_{PCC\alpha}=0\\ e_{PCC\beta}=0\\ e_{ISL\beta}=0}} = -\frac{1}{T_{IDE}(z)} = -\frac{1+|Z_V|^2\,T_I(z)^2}{T_{IE}(z)} \qquad (6.18).$$

$$Z_{0Q}(z) = \frac{e_{ISL\beta}}{-i_{2\alpha}}\Bigg|_{\substack{e_{PCC\alpha}=0\\ e_{PCC\beta}=0\\ e_{ISL\alpha}=0}} = -\frac{1}{T_{IQE}(z)} = \frac{1+|Z_V|^2\,T_I(z)^2}{|Z_V|\,T_I(z)\,T_{IE}(z)}$$

Fig. 6.10 and Fig. 6.11 show the Bode diagram of Z_{0D} and Z_{0Q} for different values of the parameter f_{EM}. The influence of Z_V over Z_{0D} is mainly focused on the decade 10-100 Hz, while the effect out of this range is almost negligible. Out of this frequency range, the curve corresponds to the output impedance given by just the voltage control, $Z_0(z)$, expressed in (3.12) as $-T_{VIE}(z)^{-1}$. The difference between $Z_{0D}(z)$ and $Z_0(z)$ is increased as long as the UWT contains more kinetic energies to face the synchronization. The magnitude of $Z_{0D}(z)$ at ω_0 is reduced, as expected, and the system has to contribute with more power than its neighbor sources. As shown in Fig. 6.10.b, the inductive nature of the output impedance is not affected by the value of f_{EM}. The impedance $Z_{0Q}(z)$ establishes a cross-coupling between the control axes $(f_{EM}>0)$. Note that the Bode diagram for $f_{EM}=0$ has not been displayed due to $Z_{0Q}(z)\to\infty$. Although its nature is resistive at ω_0, the voltage drop across this cross impedance over the β axis, $Z_{0Q}(z)\cdot i_{2\alpha}(z)$, contains a 90º phase lead, which can be considered as an inductive behavior. As long as f_{EM} increases, the magnitude of Z_{0Q} is reduced and thus, the cross-coupling gets stronger. The dynamics given by the droop control are totally dependent of the output impedance. As during the synchronization the droop control is disabled, no additional measures have to be taken.

6.5. Further discussion.

The success and performance of the synchronization are logically quite tied to the performance of the communication link. The communication should attend to several requirements in terms of bandwidth, reliability, etc. This topic opens a new research line that is completely out of scope in this Thesis. However, the some main concerns are slightly mentioned. As the state manage has to broadcast the PCC voltage, the most convenient solution resides on a communication bus with a tree structure. The reception of the PCC voltage is then subjected to a delay, whose value is different depending on the UWT. The average value of all the different delays affects on the synchronization accuracy, while the deviation between them affects on the circulating currents limiting the value of the virtual

impedance. Supposing the average delay is fixed, the state manager can counteract it by observing the phase displacement between $\vec{e}_{ISL}$ and $\vec{e}_{PCC}$ and adding a uniformly increasing phase lead on the $\vec{e}_{PCC}$ before sending it. In [He, *et al.*, 2013], the PCC voltage is sent in dq-frames. This can be a great solution that could reduce the bandwidth demands expecting no great changes over $\vec{e}_{PCC}$ and a reduced negative sequence.

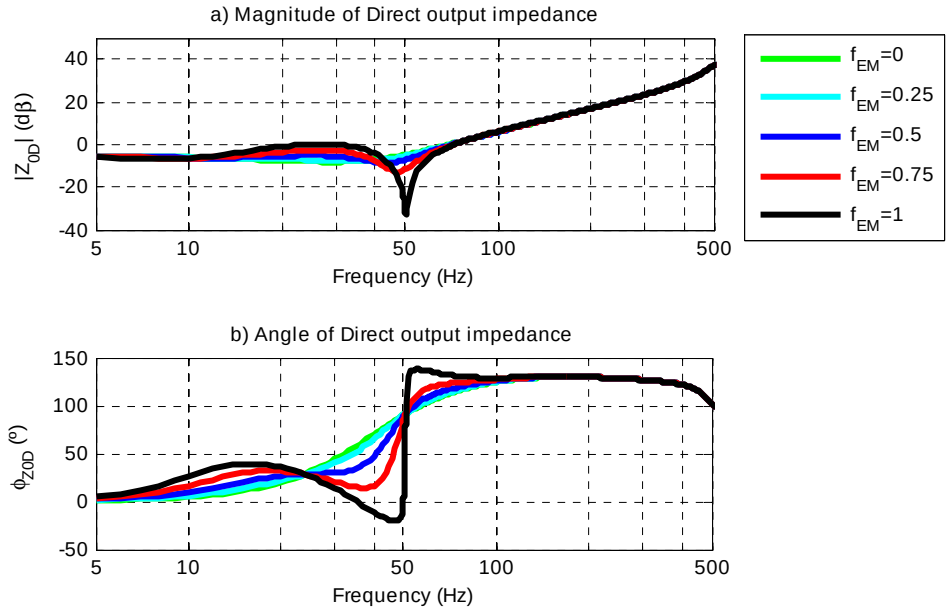

Fig. 6.10: Bode diagram of $Z_{0D}(z)$ for different energy reserves (f_{EM}): a) Magnitude and b) Phase.

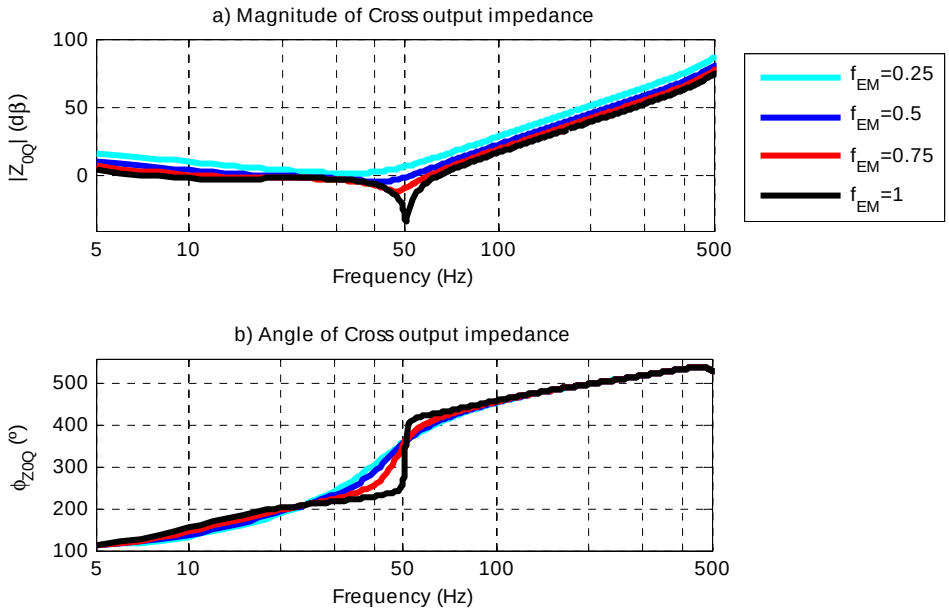

Fig. 6.11: Bode diagram of $Z_{0Q}(z)$ for different energy reserves (f_{EM}): a) Magnitude and b) Phase.

Chapter 7.

Results

This chapter presents experimental and simulation results concerning the proposed power and voltage controllers, power sharing strategies, the synchronization technique and the SRF saturators.

First of all, the setup for the experimental verification is described. Then, the VCVSC and CCVSC power controllers of Chapter 4 and Chapter 5 are analyzed and compared. The results cover the experimental verification of the grid-connected dynamics and reconnection transient, the study of the reponse under unbalanced dips and the OPC validation via simulation. The theoretical analysis of Chapter 3 regarding the voltage control is supported experimental results. The proposed SRF-saturators are compared with the most relevant previous technique with the aim of verifying its better performance it in VCVSC and a CCVSC. Finally, the synchronization strategy presented in Chapter 6 and the power sharing strategy of section 4.1.5 are tested by means of simulations results with Matlab/Simulink©.

7.1. Setup description.

This subsection describes the setup that has been used for evaluating the control algorithms proposed in this dissertation. The design of this system has been developed by the Industrial Electronics applied to Renewable Energy Systems group, GEISER, from the UAH, in collaboration with the company Sedecal Control S.L.. Its design is framed inside the project CONDOR II, entitled "Design and evaluation of protection and control solution for distributed generation systems in the presence of grid faults and disturbances".

Fig. 7.1 depicts a simplified scheme of the experimental setup. It is divided into the power electronics system and the electronic control system. The power electronics system consists of a neutral point clamped (NPC) IGBT-driven VSC of 150 kVA with a LCL filter as interface with the local loads. The potential isolated system is connected to the grid by means of a contactor used as circuit breaker locally controlled by the power electronic system. Fig. 7.2 depicts the power electronics system. Some heaters (not shown Fig. 7.2) as local loads with a total aggregated power of 12 kW are connected at the output of the LCL filter as shown in Fig. 7.1.

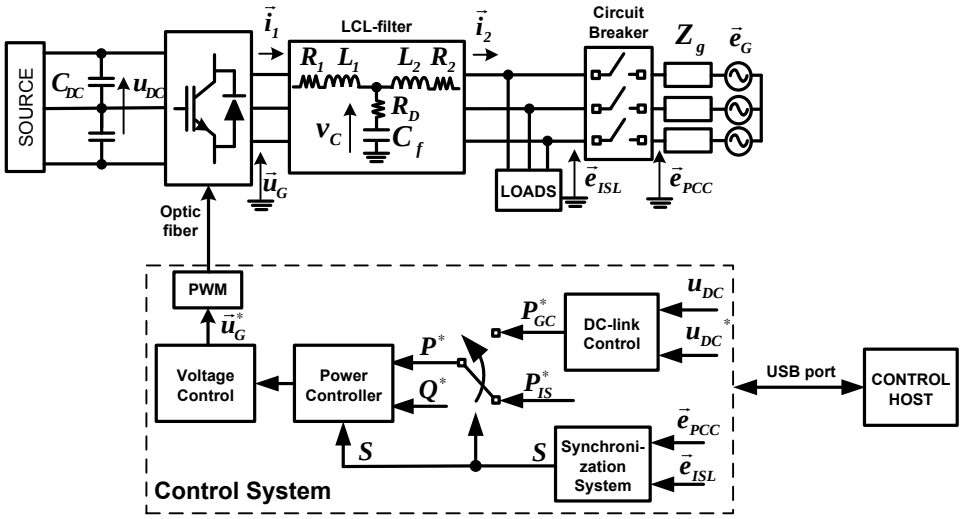

Fig. 7.1: Simplified scheme of the power electronics system and the control algorithm to be programmed in the of control electronic system.

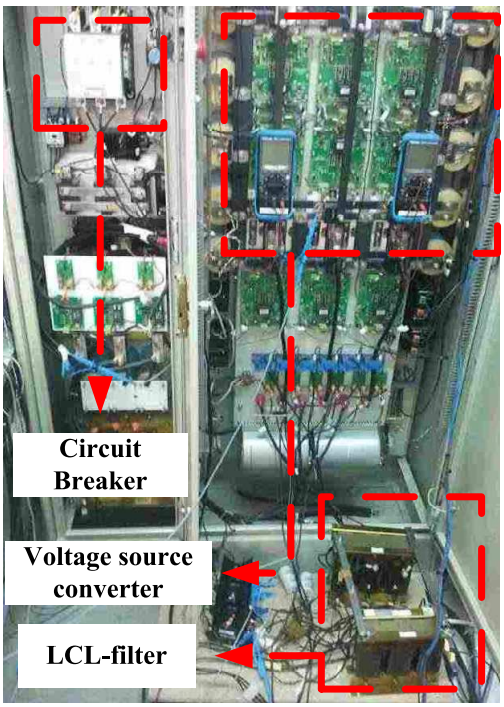

Fig. 7.2: Power electronics system: Voltage source converter, LCL filter and circuit breaker.

The control electronic system consists on the control card and a control host with user-interface application. The GS-controller to be tested is programmed in a digital control platform consisted of a FPGA + DSP [Bueno, *et al.*, 2009]. The digital platform depicted in Fig. 7.3 is composed by a floating point DSP TMS320DSK6713 from Texas Instruments® and an FPGA Spartan 3 from Xilinx®. An user-interface application executed on a PC sends the outer control references and receives the sampled variables to be displayed on-line and stored for posterior analysis apart from the visualization of alarms and states [Rodriguez, *et al.*, 2009]. The communication between the control platform and the PC is carried out by means of an USB port. The front-panel of this application is shown in Fig. 7.4.

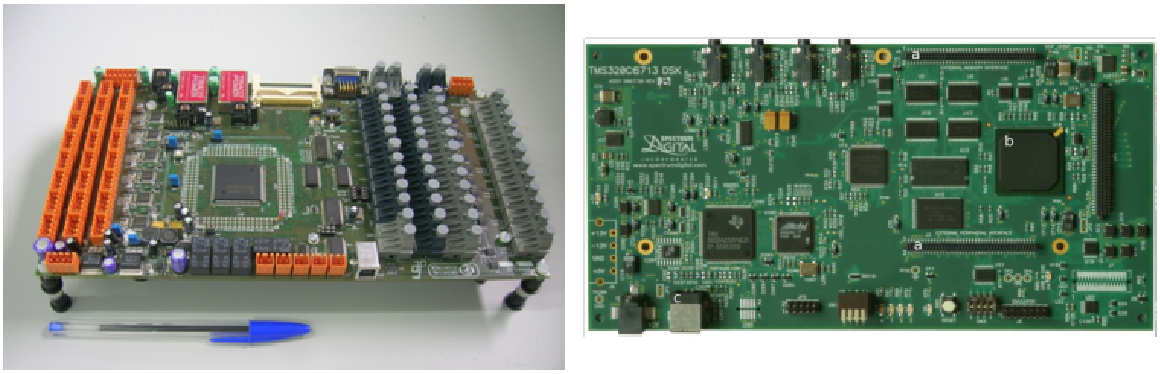

a) **b)**

Fig. 7.3: a) Control digital platform top view and b) TMS320C6713 DSP card top view.

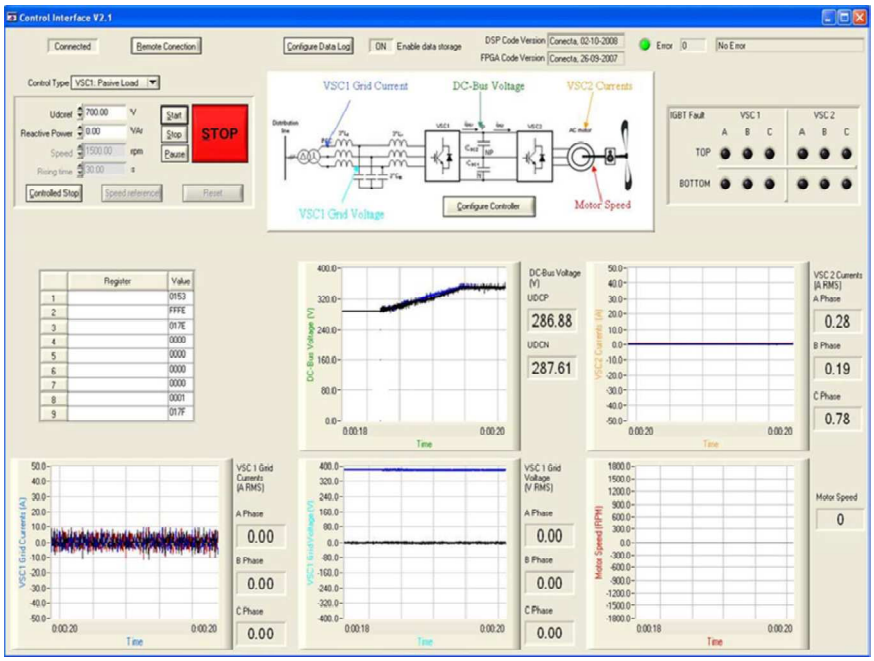

Fig. 7.4: User-interface application for sending control commands and with on-line data, visualization of registers states and alarms [Rodriguez, *et al.*, 2009].

As the setup is just constituted by one converter, only the voltage and power controllers, the synchronization and the novel saturators have been experimentally tested. The rest of

proposed approaches (power sharing between parallel units during the island operation, virtual impedance for the synchronization procedure, oscillating power controller) are validated by means simulation results.

Table 7.1 collects the parameters of two UWTs of 58 kW and 100 kW. UWT_1 serves as the principal model for the major part of the test, while UWT_2 is also used for testing the power sharing strategy and the synchronization by means of the virtual impedance. The experimental setup shares the same grid-side values as UWT_1.

Table 7.1: Main Parameters of the UWTs

	UWT_1	UWT_2
Wind Turbine Mechanic parameters		
Radio (m)	6	8.2
Gearbox Ratio	5.85	7.8
Inertia ($kg \cdot m^2$)	46.17	115.51
Machine-side Parameters		
Rated line-line Voltage (V_{RMS})	400	400
Rated Power (kW)	58	100
Rated Torque (Nm)	738	1273
Maximum Torque (p.u.)	2.0	2.0
Rated Speed (rpm)	750	750
Number of pair poles	8	8
Stator resistance (p.u.)	0.007	0.009
Stator d-axis Inductance (p.u)	0.13	0.137
Stator q-axis Inductance (p.u.)	0.43	0.589
Permanent Magnet Flux (p.u.)	0.981	0.817
Full Converter Parameters		
Rated DC-link Voltage (V)	750	850
Braking Chopper Resistance (Ω)	38.8	25.6
DC-link Equivalent Capacitor (μF)	4250	6250
Switching Frequency (Hz)	2500	2500
Grid-side Parameters		
Rated line-line Voltage (V)	400	400
Filter Inductance L_1 (p.u.)	0.416	0.511
Filter inductance L_2 (p.u.)	0.205	0.255
Filter Capacitor C_f (p.u.)	0.016	0.014
Filter Resonant Frequency (Hz)	1080	1022
Line Impedance Z_i (p.u.)	0.01	0.013
Grid impendace Z_L (mH)	0.09	

7.2. Comparative analysis between droop and PQ-theory based controls.

This section presents a brief comparative of the different performances in grid-connected provided by the droop control and the PQ-theory based control. It firstly verifies the configured dynamics and analyzes the coupling between the active and reactive powers. Then, the reconnection transient is analyzed in both power control structures. Finally, the transient responses during the LVRT operation with type-D voltage dips and the disconnection from the grid are studied.

7.2.1. Dynamics and reconnection transient.

Fig. 7.5 and Fig. 7.6 displays simulation results with temporal power responses under steps in active and reactive power references applying the previous control tunings for the droop and the PQ-theory based controls. First of all, it can be appreciated that both active and reactive powers contain the same closed-loop dynamics in both control architectures. Regarding the droop control, as expected, it is a mainly first-order response with a settling time of 75 ms, which satisfies the requirement imposed in Table 3.1. Besides, the power coupling between P_G and Q_G is quite reduced during transients and the tuning assures a good damping of the resonance at ω_0. In case of the PQ-theory based control, the powers follow a second order response with a settling time of 60 ms. In this case, both power are jointly regulated with a current controller which makes the coupling between them not negligible. The power ripple in both cases is chiefly caused by switching noise.

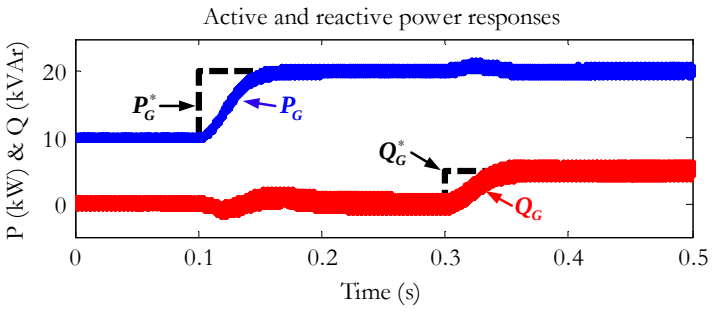

Fig. 7.5: Droop control in grid-connected: Active and reactive first-order power responses.

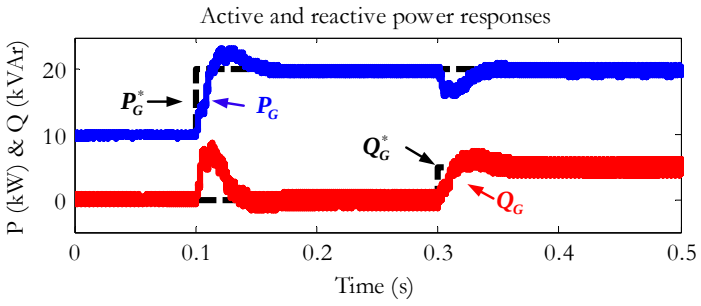

Fig. 7.6: PQ-theory based control in grid-connected: Active and reactive first-order power responses.

Fig. 7.7 contains the performance of the droop control during the reconnection with the grid for two different control tunings: k_{Pf} =10^{-4} and k_{Pf} =$1.2{\cdot}10^{-4}$. After the a period working in the synchronization mode, the magnitude and phase of the voltage across the open circuit breaker are so reduced that the re-closure does not suppose a harmful situation. The breaker is closed and the system starts performing in grid-connected mode tracking the active and reactive power references (initially 0 kW and then 6 kW). The re-closure of the breaker causes a transient peak in the active power. As depicted, as long as k_{Pf} increase, the magnitude of this peak decreases, performing a seamless transition. In case of k_{Pf} =10^{-4} the peak reaches a value close to 10.4 kW while it does not exceed 7.7 kW when k_{Pf} =$1.2{\cdot}10^{-4}$. The reason resides in the increment of the controller bandwidth that allows a faster response under any disturbance. However, the coupling with the voltage controller is poorer causing some oscillations in the steady-state power waveform. Regarding the response under the power reference step, the first-order response is verified with these experimental results. As expected, k_{Pf} =10^{-4} provides a settling time close to 75 ms while k_{Pf} =$1.2{\cdot}10^{-4}$ fast the response to 60ms.

In Fig. 7.8, the experiment has been repeated using the PQ-theory based control. In this case, the transition between island and grid-connected modes is quite dampened with a reduced current peak, offering a more seamless transient. In contrast with the droop control, the power peak reaches -4 kW. This negative value supposes transient absorption of active power during the reconnection. However, the DC-link control is able to deal with it avoiding DC overvoltages. This experiment also validates the expected second-order dynamics of the power when using the PQ-theory based control.

7.2.2. LVRT performance – OPC verification.

The next tests are focused on the analysis of the power control in grid-connected under unbalanced faulty conditions. The grid codes forces the DG units to remain connected during a voltage dip and to support the grid with reactive current injection. If the dip duration or magnitude exceeds some predetermined thresholds, the DG units can be disconnected to start working in island mode. A type-D dip has been considered due to it is the result of a phase-to-phase or single-phase voltage dip transferred through a delta-Y transformer. The phase *a* of $\vec{e}_{PCC}$ is reduced to 0.5 p.u., phase *b* remains at 0.65 p.u. with a phase shift of 21º while the magnitude of phase *c* is 0.76 p.u.. Besides, 5th and 7th harmonic components have been included with magnitudes of 0.03 p.u. and 0.01 p.u., respectively. The active and reactive power references during the LVRT operation are fixed by the grid codes attending to the magnitude of the faulty grid.

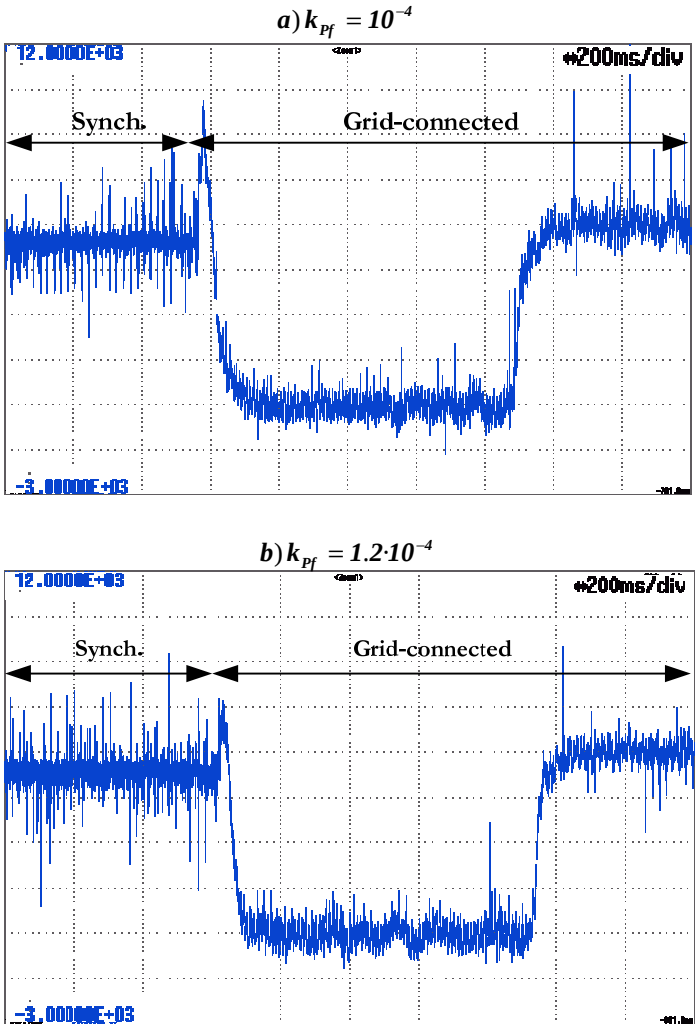

Fig. 7.7: Droop control with a) $k_{Pf} = 10^{-4}$ and b) $k_{Pf} = 1.2 \cdot 10^{-4}$: Transient power responses during grid reconnection and active power reference step.

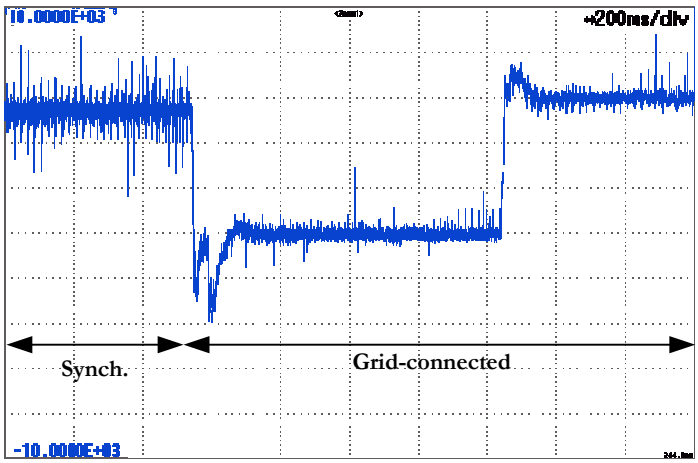

Fig. 7.8: PQ-theory based control: Transient power responses during grid reconnection and active power reference step.

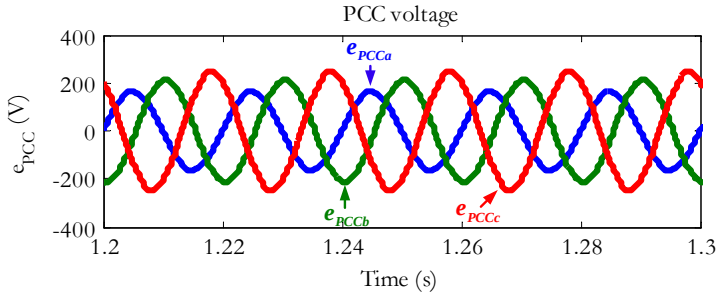

Fig. 7.9: PCC voltage during unbalanced fault.

Fig. 7.10 presents the droop control performance when its actuation is added to a based voltage where no distinction is made between the αβ components. Fig. 7.10.a and b respectively show the output current waveforms and the FFT of the phase *b*. As explained in 4.1.3, this wrong representation of an unbalanced vector leads to the apparition of a non zero-sequence third harmonic that severely distorts the injected current during the LVRT operation. This fact is independent of the harmonic content of the PCC voltage. As a consequence, the active and reactive power waveforms are not only affected by a second order harmonic (due to the unbalance) but also by a fourth order harmonic component. Depending on the nature of voltage and current third harmonics, a third order component can appear in the power waveform too.

Fig. 7.11 contains the performance of the droop control when the OPC block is disabled. Fig. 7.11.a shows the active and the reactive powers at the moment the voltage dip appears. The UWT injects a reactive power to fulfill the grid code and the rest of the available current capacity is employed to inject active power. As the voltage magnitude is reduced, the active power injection capacity is quite limited and the system usually has to deal with a surplus of power. Note that now, the open loop-gain is reduced (see expression (4.10)) and hence, the droop control provides a slower response. As mentioned in section 5.3, after the transient caused by the dip, the steady-state active power exhibits a notorious 2nd order harmonic as consequence of the unbalanced conditions while the reactive power does not oscillate. This fact verifies the expression (5.11). The active power oscillation is transferred to the DC-link voltage waveforms and worsens the system performance. Fig. 7.11.b depicts the frequency content of the active power composed by the DC and 2nd order components. The output current is displayed on Fig. 7.11.c. Taking into account Fig. 7.9, the system injects more current in the phase whose voltage magnitude is bigger. The disconnection transient raises the power peak up to 80 kW and then, active power injected by the systems is exclusively supplied to the local loads, as shown in Fig. 7.11.d.

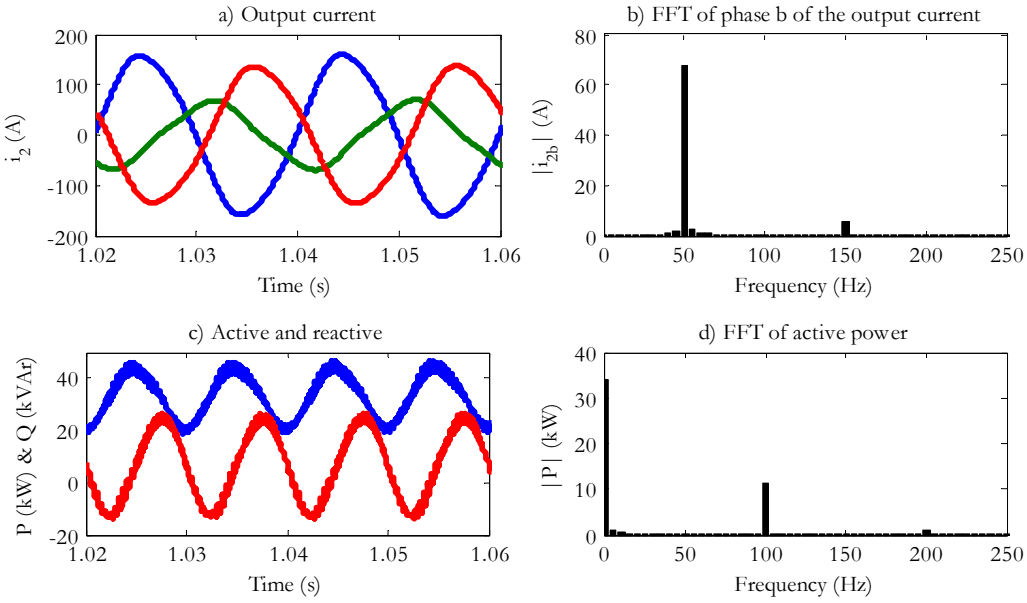

Fig. 7.10: Droop control with wrong base voltage representation under unbalanced conditions: a) Distorted output current, b) Magnitude of the FFT of phase *b* of output current, c) Active and reactive power and d) Magnitude of the FFT of the active power.

Fig. 7.12 displays the results when the droop controller actuation is complemented with the OPC. The transient caused by the dip is exactly the same than in the previous case, but in steady-state, the OPC block injects the necessary negative sequence voltage to remove any active oscillating power. As seen in Fig. 7.12.b, the frequency content of the active power is now only located at 0 Hz, avoiding harmful DC-link voltage oscillations. In this case, the system injects more magnitude in the phase whose voltage magnitude is lower. Furthermore, the disconnection transient is enhanced with a power peak close to 65 kW. Fig. 7.13 emphasizes the efficient performance of the OPC block. Initially, the OPC block is disabled so there is oscillating power. At 0.6 s, it is enabled and it swaps the oscillating active power by oscillating reactive power. At 1 s it is again disabled and the active power starts oscillating. Therefore, the "plug-and-play" philosophy is valid for the OPC block. It can be disposed in stand-by mode and activated when unbalanced conditions or power oscillations are detected.

Finally, the PQ-theory based controller is also tested under faulty unbalanced conditions. The resulting waveforms are contained in Fig. 7.14. As expected, it exhibits a faster power response under the dip transients. As well as in the previous case, the oscillating active power is totally removed at the expense of injecting oscillating reactive power. By a further analysis of Fig. 7.12 and Fig. 7.14 it can be concluded that the PQ-theory and the droop+OPC blocks share the same steady-state response. Besides, both power control schemes present identically performance during the disconnection transient.

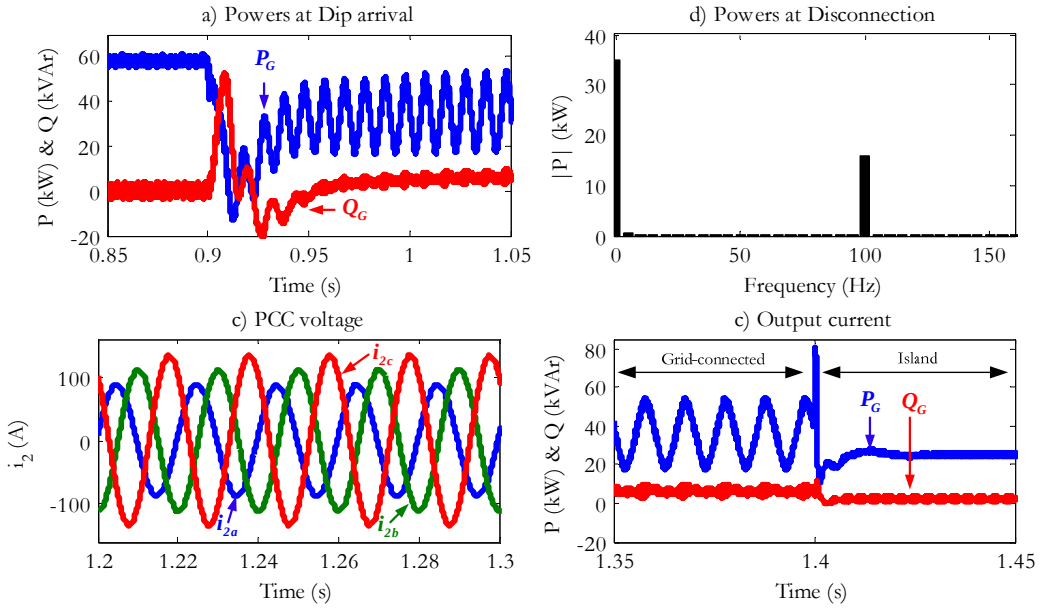

Fig. 7.11: Droop actuation without OPC against an unbalanced voltage dip: a) Active and reactive powers at dip arrival, b) FFT of the active power, c) output current and d) active and reactive powers at disconnection from main grid at the end of the LVRT operation.

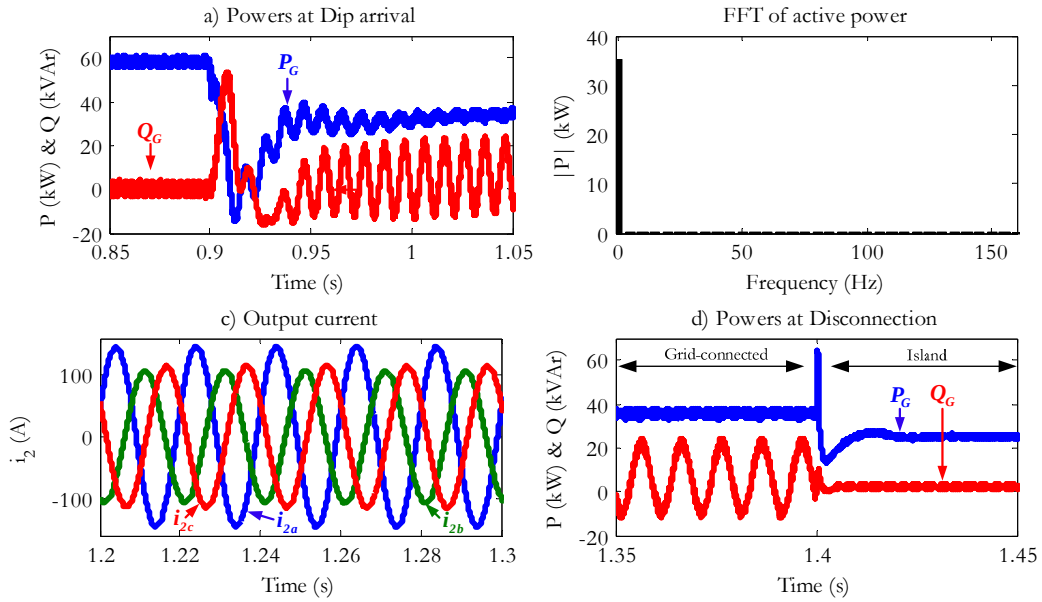

Fig. 7.12: Droop and OPC combined actuation against an unbalanced voltage dip: a) Active and reactive powers at dip arrival, b) FFT of the active power, c) output current and d) active and reactive powers at disconnection from main grid at the end of the LVRT operation.

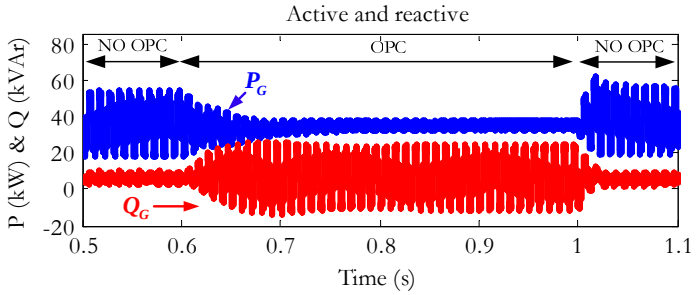

Fig. 7.13: Active and reactive powers when disabling and enabling the OPC block.

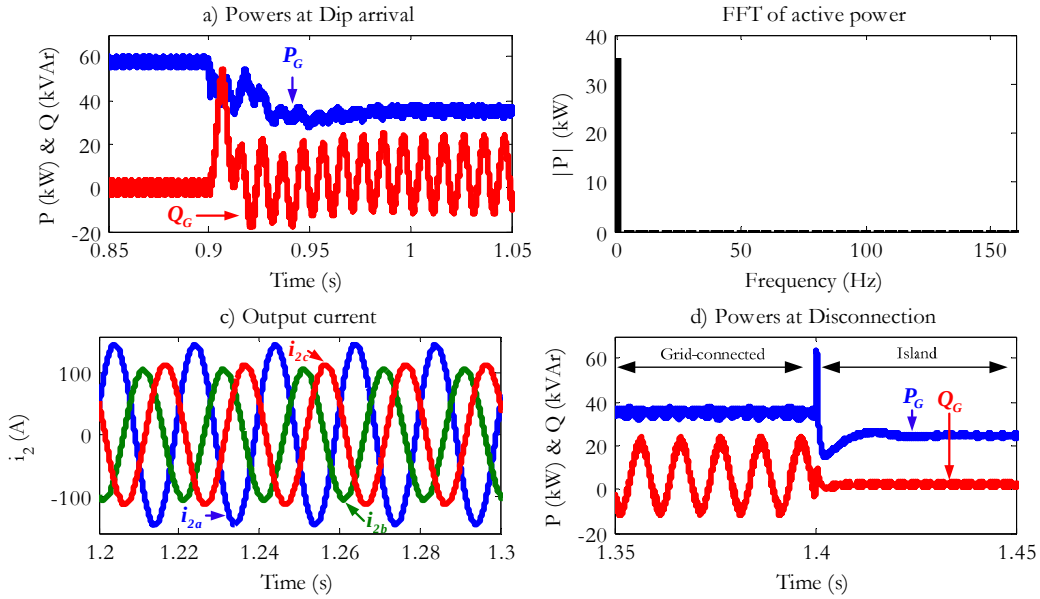

Fig. 7.14: PQ-theory based control actuation against an unbalanced voltage dip: a) Active and reactive powers at dip arrival, b) FFT of the active power, c) output current and d) active and reactive powers at disconnection from main grid at the end of the LVRT operation.

7.3. Voltage control.

The experimental tests carried out in this work follow the verification of the theoretical development of section 3.3. Generally, two waveforms are displayed for each feature analyzed with good and bad results. Besides, the performance during the transition between the operating modes is also analyzed.

7.3.1. Grid-connected performance.

This subsection verifies the statements revealed in 3.3.2. The PV-fitting feature is tested by increasing the bandwidth of the power control dynamics to appreciate the controllers decoupling. As representative cases, Fig. 7.15 and Fig. 7.16 contain the temporal evolution of the active power of architectures 2 and 5, respectively. During the island operation, the active power matches up with the load (6 kW) and after the reconnection follows (initially 0 kW and then 3 kW). As shown, the high bandwidth of the architecture 2 achieves a good decoupling

with the power control. This also happens with architectures 1 and 3. However, the use of the second PR remarkably reduces the controller's bandwidth and the poor decoupling between the power and voltage controller leads to an underdamped power response. Comparing the power and current transients during the connection with the grid, smoother transitions are achieved when using architectures 1 and 2. Again architectures 4 and 5 provide the poorest results. The power and current peaks also depends on the bandwidth of the power controller, reducing them when slow power dynamics are chosen.

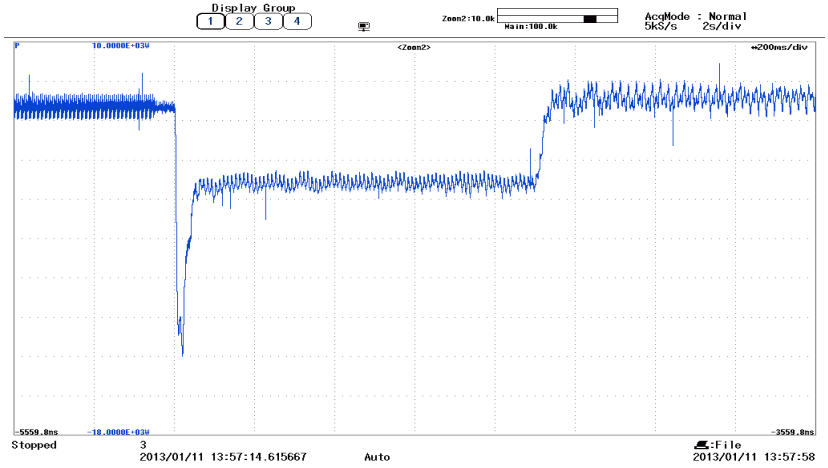

Fig. 7.15: Power waveform when using the PR ic architecture with a high bandwidth in the power controller.

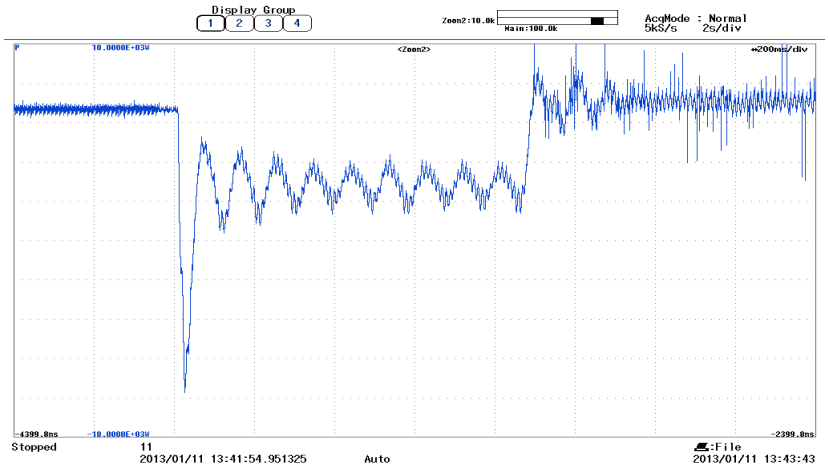

Fig. 7.16: Power waveform when using the PR+PR i1 architecture with a high bandwidth in the power controller.

As mentioned in 3.3.2, any disturbance transient excites the slow pole of techniques 1, 2 and 4 and as a result, a first order response appears on the output current. Fig. 7.17 depicts the output current and power transients under a 5% amplitude step on the PCC voltage at 0.9 s when the unit is injecting 12 kW for architectures 1 and 3. Fig. 7.17.b shows the 50 Hz oscillation produced by the DC component of the output current during the transients. This effect is totally avoided when using the filter current as inner feedback.

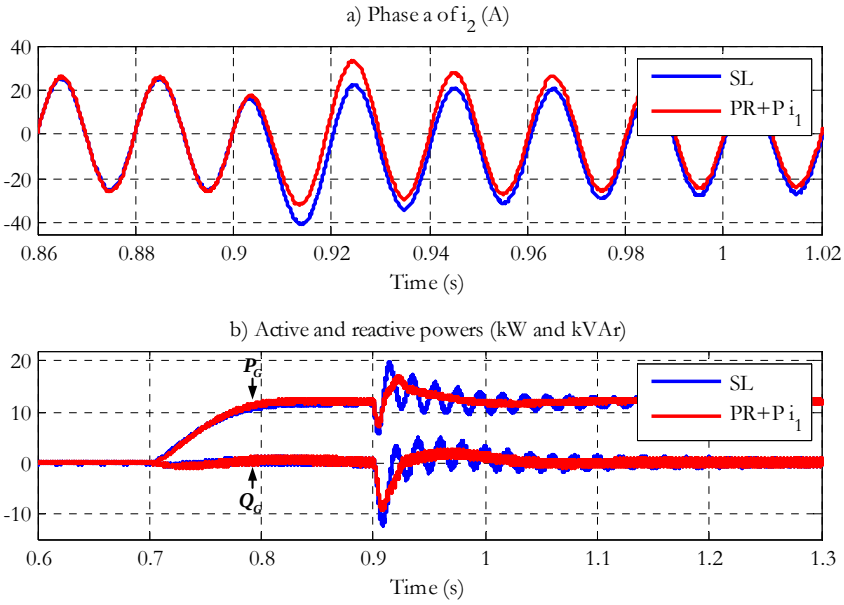

Fig. 7.17: Effect of the slow pole: a) Output current and b) Active and reactive power transfers when using architectures 1 and 3.

The robust performance is tested by carrying out a 50% variation of the filter inductance L_1. In such conditions, Fig. 7.18 and Fig. 7.19 present two representative cases: the performance of architectures 1 and 5, respectively. Although the resulting response is not the desired one, it is quite acceptable when employing the single-loop option. Something similar happens with architecture 2. As depicted by Fig. 7.19, the system is close to loss the stability when employing architecture 5. In architecture 4, the system becomes instable from the starting in the island operation.

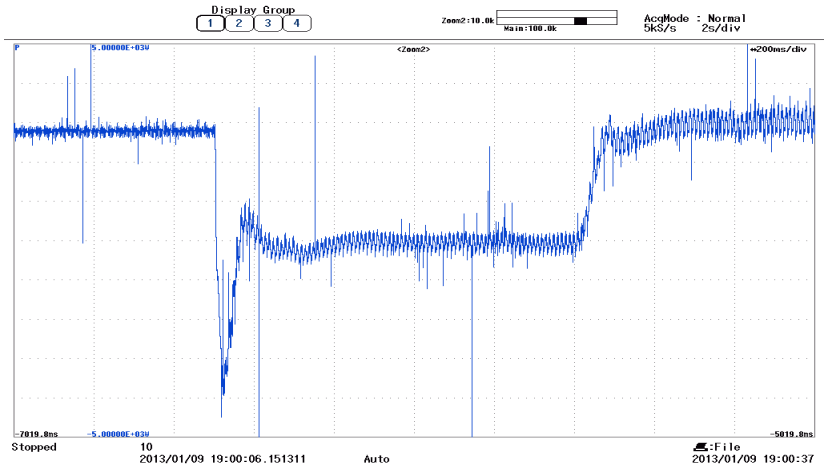

Fig. 7.18: Variation of 50% of L_1 with architecture 1.

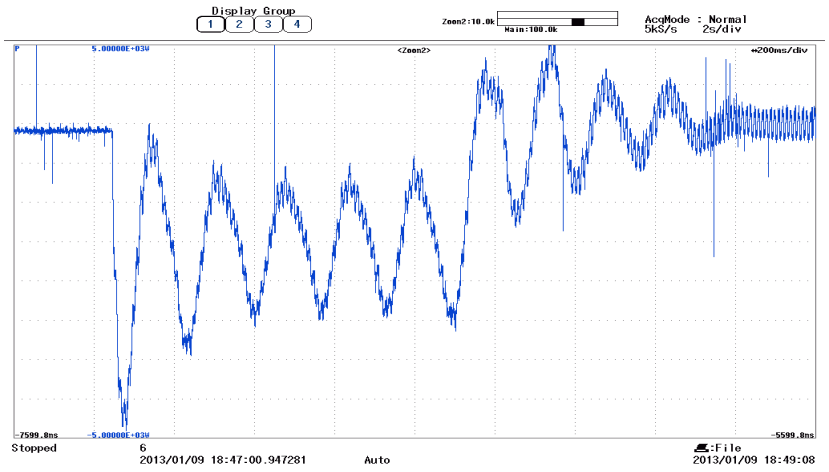

Fig. 7.19: Variation of 50% of L_1 with architecture 5.

7.3.2. Island performance.

The results presented in this subsection support the theoretical study of section 3.3.3. The island performance is checked by carrying out a resistive load step from 9kW to 3kW. Fig. 7.21 and Fig. 7.20 show the waveforms of $\vec{v}_C$ and $\vec{i}_2$ for architectures 3 and 4, respectively. As depicted, as long as the power demanded by the load decreases, the voltage dynamics become poorer. However, this effect is notoriously reduced again when using the current $\vec{i}_1$.

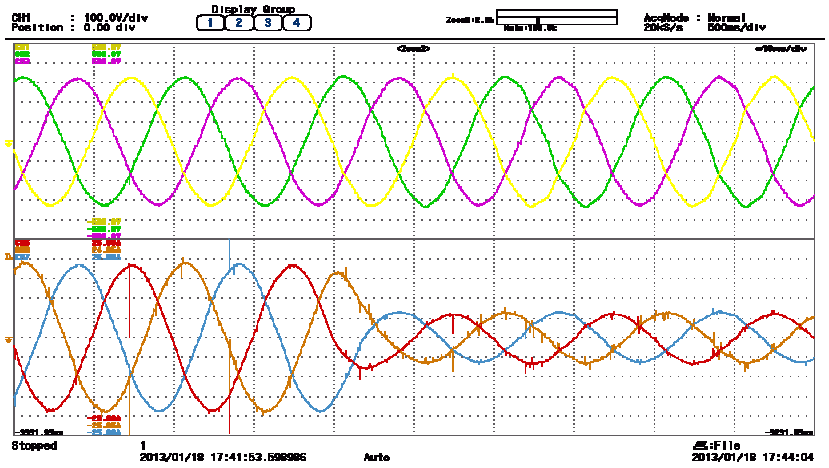

Fig. 7.20: Capacitor voltage and output current in island mode under a load reduction step of 6kW when using architecture 3.

7.4. Synchronization performance.

This subsection evaluates the improvement provided by the virtual impedance over the synchronization performance described on section 0.

The potential island is composed by two different low power UWTs (58kW and 100kW) and a local resistive load. Table 7.1 collects all the main parameters of each UWT, respectively. The resistive load demand is kept constant to 130 kW. The grid voltage is recovered in the

instant 1.5 s. In that moment, the state is automatically changed to synchronization. The parameters of the voltage comparator on the state manager are as follows: L =1000 (the errors has to be below their corresponding thresholds at least 200 ms), $|\Delta E|_{max}$ =25 V and $|\Delta\theta|_{max}$ =0.15 rad.

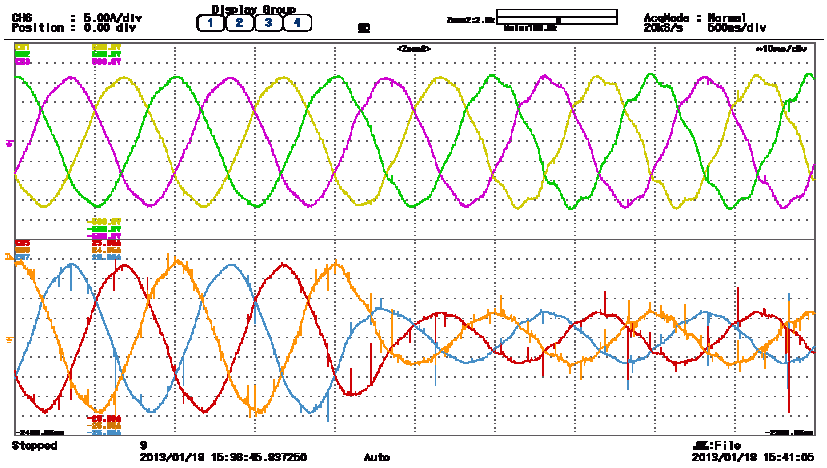

Fig. 7.21: Capacitor voltage and output current in island mode under a load reduction step of 6kW when using architecture 4.

Two different tests are presented to evaluate the improvement provided by the virtual impedance within the synchronization task. The idea is to verify the accuracy of the island voltage regulation and the fair power sharing. In both tests, the dual representation of voltages and phases described in section 6.2 is used. The tests performed and their results can be easily extrapolated to complicated island with more units in parallel.

Fig. 7.22 shows the signals related to the state manager when the virtual impedance is disabled. Fig. 7.22.a and b contains the PCC and island voltages at the beginning and end of the synchronization process. The grid voltage contains both positive and negative sequences. The worst case has been considered: 180º of initial phase error. The voltage reference is automatically changed: a strong transient is appreciated in the voltage island. Although this abrupt change on the phase reference is not a positive aspect, but still better than a smooth transition from the current phase to the PCC phase, which implies a frequency change and extended synchronization duration. As seen, at the end of the synchronization, both voltages are quite similar. Fig. 7.22.c and d depict the absolute values of the magnitude and phase differences between the PCC and island voltages together with their respective thresholds. Both magnitude errors, $|\Delta E_\alpha|$ and $|\Delta E_\beta|$, are quickly reduced approximately to 15 V while more time is required to carry $|\Delta\theta_\alpha|$ and $|\Delta\theta_\beta|$ below the desired zone. They remain at 0.133 rad, value quite close to the limit $|\Delta\theta|_{max}$, revealing the poor accuracy obtained in these conditions. In spite of that, the transient current across the circuit breaker at the reclosing, presented in Fig. 7.22.e, is acceptable.

Fig. 7.23.a and b contains the energy management factors and active power contributions of both UWTs during the three operating modes. UWT_2 has arrived to the synchronization with high kinetic reserves while UWT_1 is running out of energy. As a consequence of the active power sharing strategy, during the island operation, UWT_2 contributes with more power and the kinetic storage of UWT_1 remains constant. When the synchronization starts, as the virtual impedance has been disabled, no sharing mechanism can keep this situation and the contribution of each UWT is given by its corresponding factors $f_{IDIV1}=L_{22}/(L_{21}+L_{22})$ and $f_{IDIV2}=L_{21}/(L_{21}+L_{22})$. Consulting Table 7.1, they are 42% and 58%, which supposes an unfavorable situation for UWT_1. As shown, the UWT_1 is forced to supply more power than it can generate and thus, its storage is reduced getting closer to the shutting down condition. As the UWTs follow the unbalanced PCC voltage, the power supplied to the load during the synchronization contains an oscillating component. The use of the OPC block in the grid-connected mode assures the elimination of such power component. This effect is unavoidable if an accurate synchronization is desired. Besides, as the magnitude of the grid is lower than the rated, the local load does not receive the demanded power during the synchronization.

Fig. 7.24 and Fig. 7.25 present the signals when the virtual impedance term is enabled. Fig. 7.24.b depicts that the island and PCC voltages are perfectly overlapped before closing the breaker and no transients is detected. With the use of the virtual impedance, the voltage drop on the different output impedance is counteracted in some portion by adequately increasing the capacitor voltage. As a consequence, the magnitude and phase errors the state manager deals with are remarkably reduced and the duration of the synchronization is slightly reduced, as depicted in Fig. 7.24.c and d. Despite of this accuracy improvement, no big changes are observed on the current transient.

The second positive aspect of implementing the virtual impedance is appreciated in Fig. 7.25. The virtual impedance term of each UWT is varied as function of the remaining energies modifying the factors $f_{IDIV1}'=(1-f_{EM2})L_{22}/((1-f_{EM1})L_{21}+(1-f_{EM2})L_{22})$ and $f_{IDIV2}'=(1-f_{EM1})L_{21}/((1-f_{EM1})L_{21}+(1-f_{EM2})L_{22})$: 22.5% and 77.5%. In such conditions, the fair synchronization removes the negative power mismatch on UWT_1 to conserve the remaining storage.

7.5. Distortion-free saturation.

To verify the theoretical approach presented in section 5.4.4, the inverter has been equipped with both L and LC filters to implement the CCVSC and VCVSC schemes shown in Fig. 2.1.a and b, respectively. The values of the parameters of each configuration are collected in Table 7.2. The V_{SAT} block has been tested in VCVSC and I_{SAT} in CCVSC.

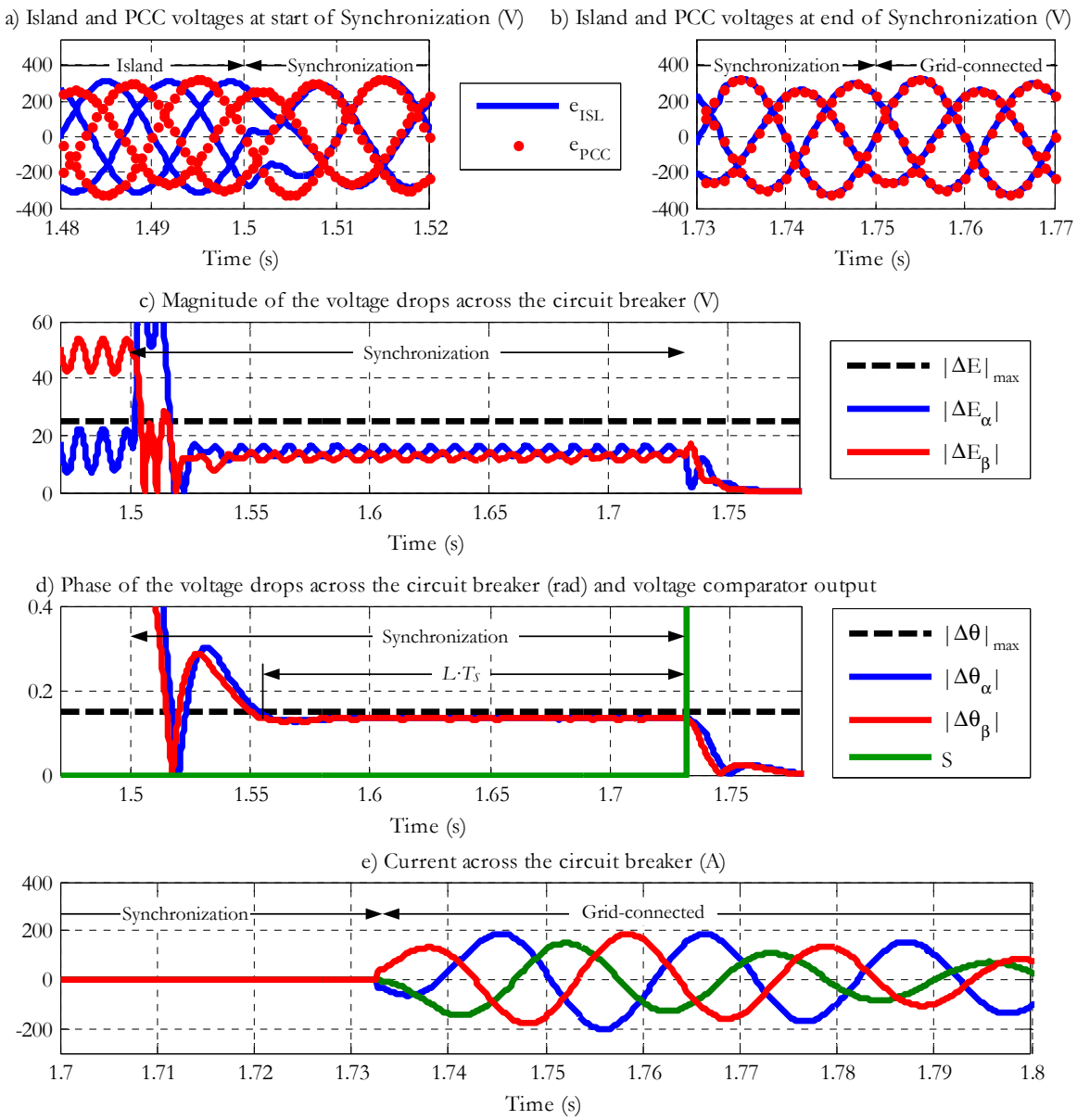

Fig. 7.22: Synchronization without virtual impedance: a) e_{ISL} and e_{PCC} at the start of the synchronization, b) e_{ISL} and e_{PCC} at the reconnection event, c) Evolution of voltage errors, d) evolution of phase errors and e) total current transient during the reconnection.

Table 7.2: Setups for testing the saturation techniques.

Parameters	VCVSC	CCVSC
Rated Power (kVA)	12	24
Rated voltage ln-ln (Vrms)	400	400
DC-bus voltage (V)	750	750
Fundamental frequency (Hz)	50	50
Switching frequency (kHz)	2.5	5
Sampling frequency (kHz)	5	10
DC-link capacitor C_{DC} (p.u.)	25.13	12.57
Filter inductance L_f (p.u.)	0.086	0.035
Filter resistance R_f (p.u.)	0.022	0.0005
Filter capacitor C_f (p.u.)	0.075	-

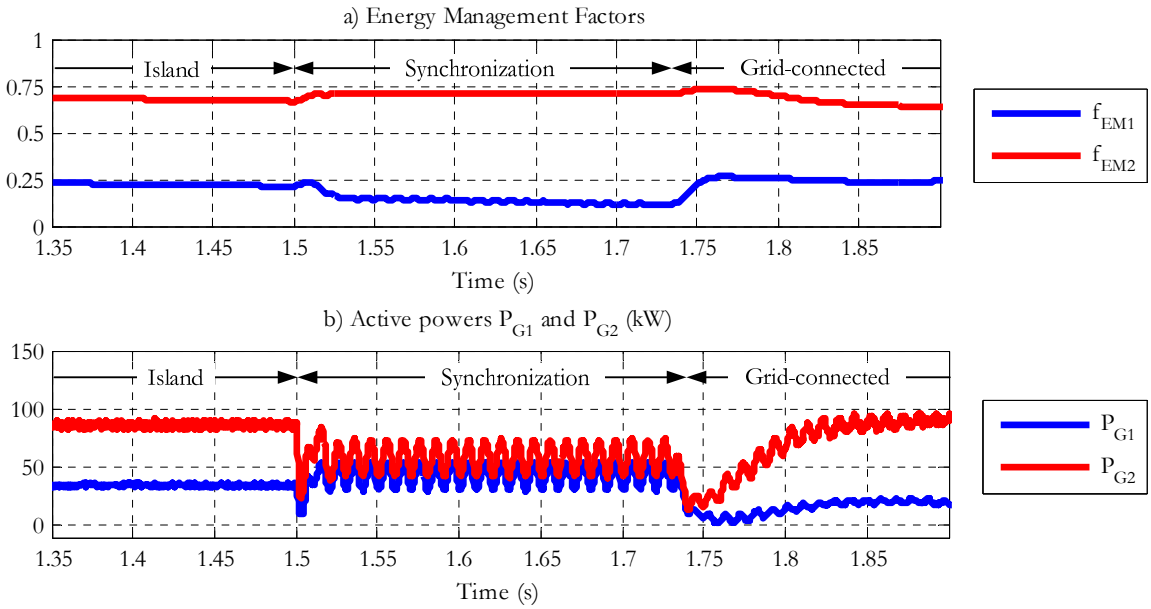

Fig. 7.23: Synchronization without virtual impendance: a) Energy management factors and b) active powers.

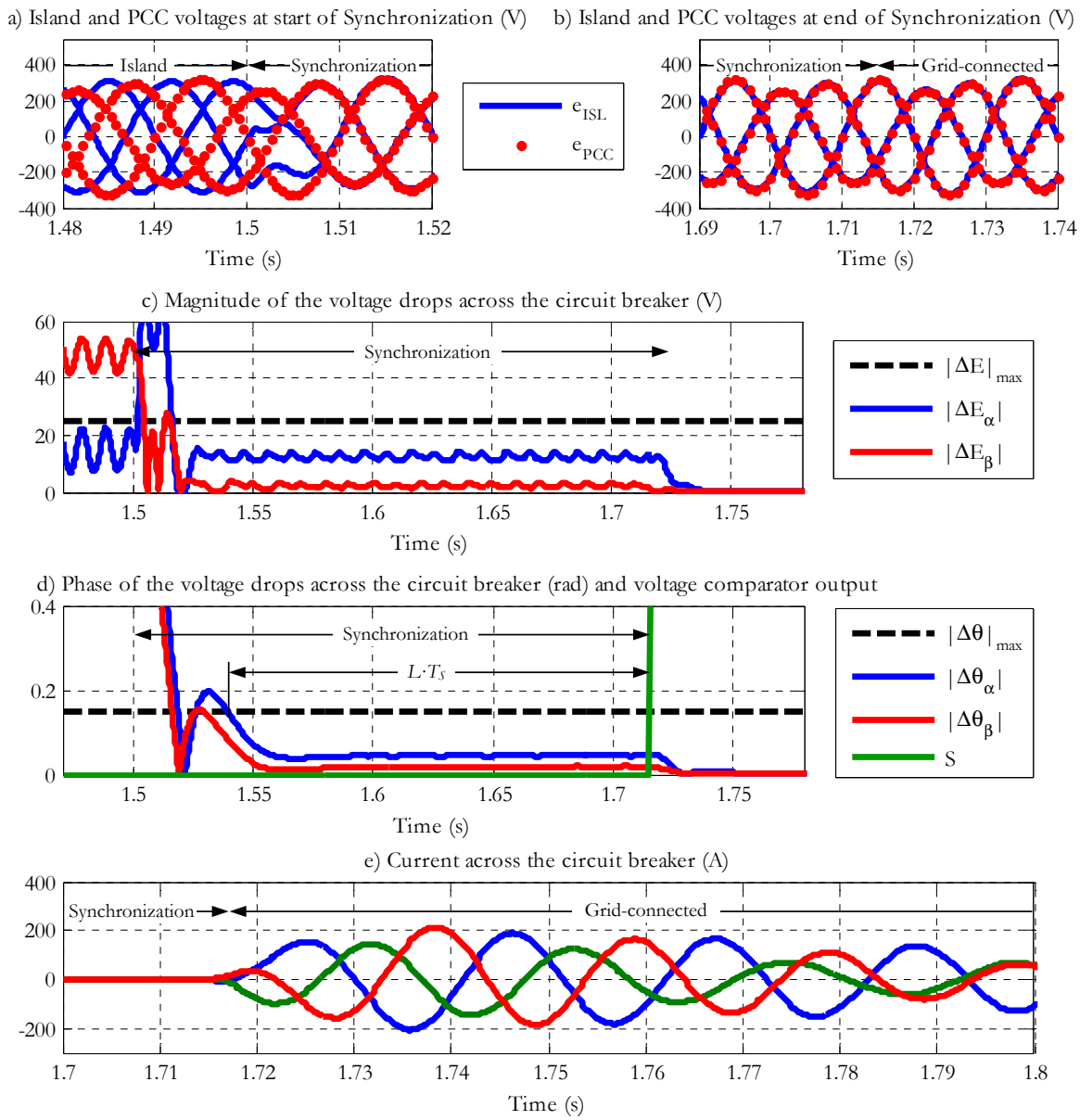

Fig. 7.24: Enhanced synchronization with virtual impendance: a) e_{ISL} and e_{PCC} at the start of the synchronization, b) e_{ISL} and e_{PCC} at the reconnection event, c) Evolution of voltage errors, d) evolution of phase errors and e) total current transient during the reconnection.

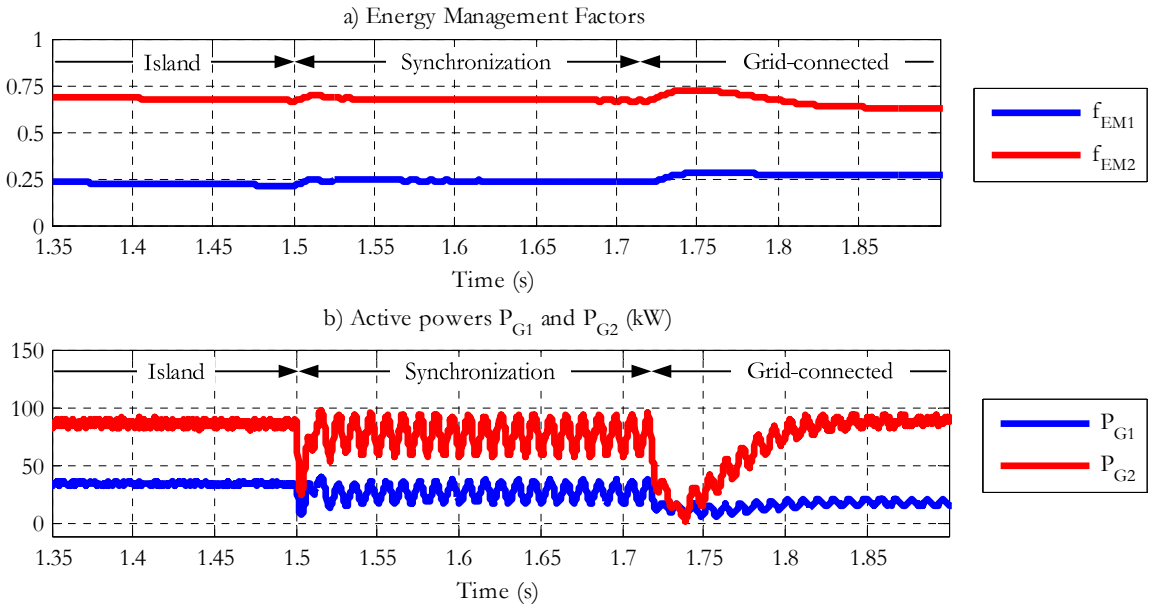

Fig. 7.25: Enhanced synchronization with virtual impedance: a) Energy management factors and b) active powers.

7.5.1. V_{SAT} in VCVSC.

The first experimental test of this subsection imitates a DVR operation with limited energy capacity, but it can be also extended to UPS and UWTs. The regulation scheme is presented in Fig. 7.26. An unbalanced voltage dip is compensated guaranteeing a continuous power supply of a 3 kW resistive load. The voltage capacity injection gets reduced when the energy stored in the DC-link capacitors is used for the power supply. The duration of the dip (1.5s) causes a remarkable fall in u_{DC} so that V_{SAT} enters in operation and the dip cannot be fully compensated. When the dip is cleared, u_{DC} recovers its operating value and the DVR stops injecting any voltage.

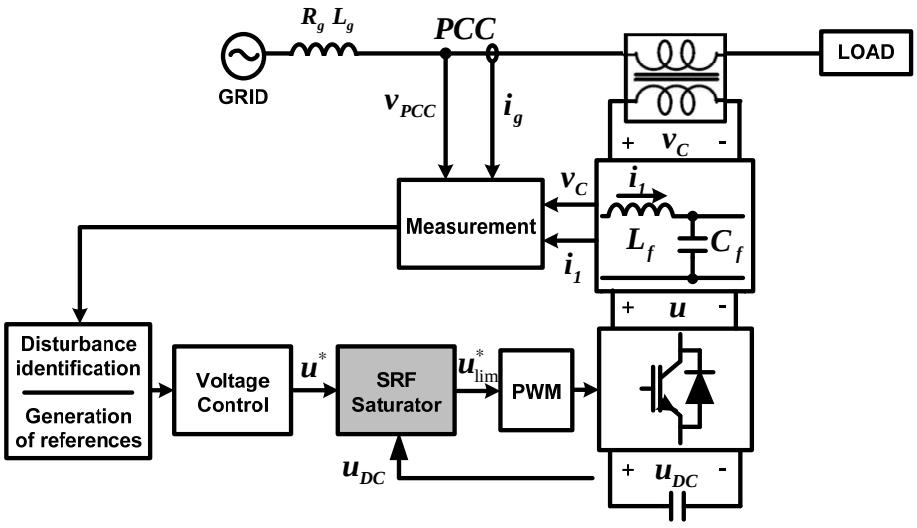

Fig. 7.26: Regulation scheme of a DVR with the proposed saturator.

Fig. 7.27 shows the results when the V_{SAT} just consists on the scalar saturation inherent to PWM schemes. Fig. 7.27.a depicts the waveforms of the converter voltage references $\vec{u}^*$ and its limited version $\vec{u}^*_{SS}$ captured by means of the interface application. The magnitude of FFT of the phase a of $\vec{v}_C$ divided by $|\vec{u}^*_{max}| = u_{DC}/\sqrt{3}$ is represented in Fig. 7.27.b. As shown, this technique provides the maximum fundamental component (up to $4/\pi$ [Holmes, *et al.*, 2003]) at the expense of mainly inserting non zero-sequence 3rd and 5th harmonics. Fig. 7.28 contains the results when the CL-method is used. The saturation performance becomes poorer: the magnitude of the fundamental component is slightly smaller and the harmonic content has notoriously increased. Fig. 7.29 and Fig. 7.30 respectively present the performance of the proposed techniques, PS and MA. As shown, the proposed saturators perfectly preserve the sinusoidal waveforms and no distortion is added. The PS uniformly saturates both α and β components while only the α component is limited with the MA method. As a consequence, the β component has a bigger magnitude. The use of anti-windups is strongly recommended.

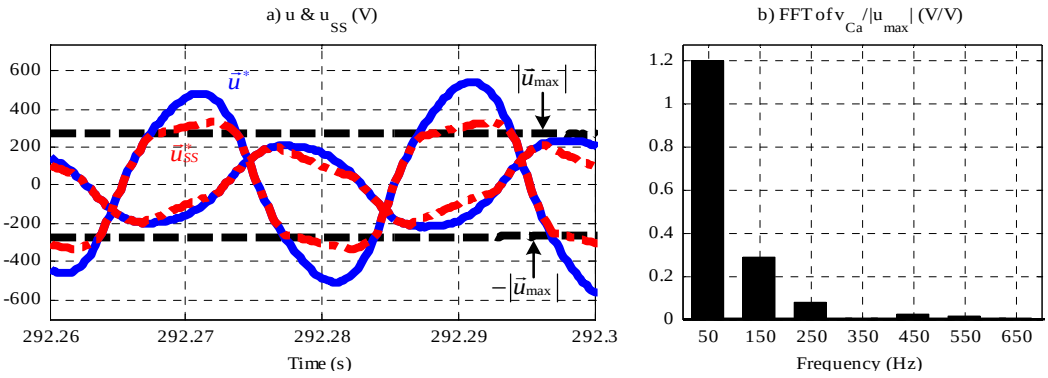

Fig. 7.27: Scalar Saturation. a) Input reference vector $\vec{u}^*$ and limited vector $\vec{u}^*_{SS}$ and b) FFT of v_{Ca}.

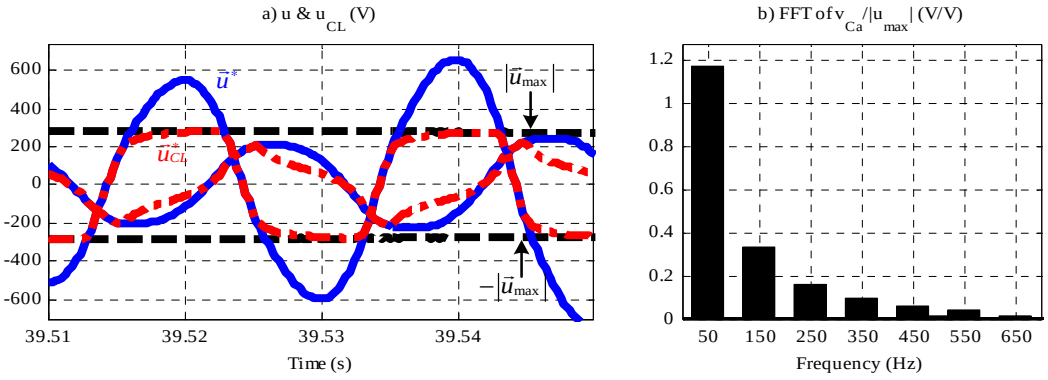

Fig. 7.28: CL-method. a) Input reference vector $\vec{u}^*$ and limited vector $\vec{u}^*_{CL}$ and b) FFT of v_{Ca}.

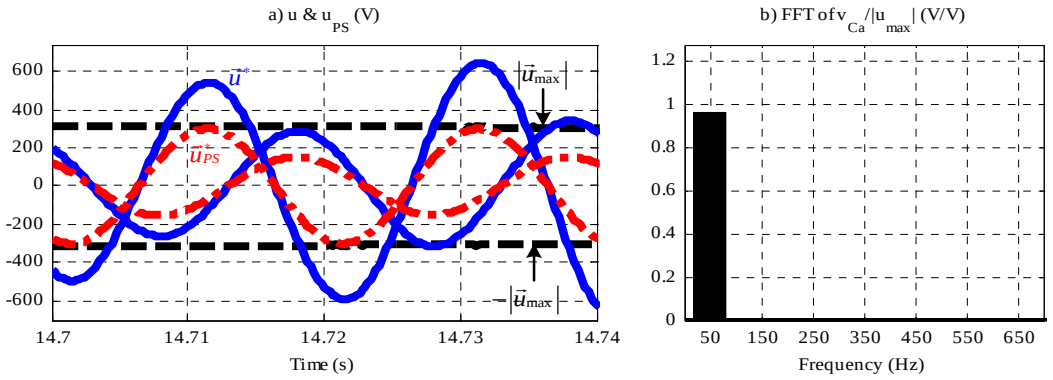

Fig. 7.29: Proportional Saturation. a) Input reference vector $\vec{u}^*$ and limited vector $\vec{u}^*_{PS}$ and b) FFT of v_{Ca}.

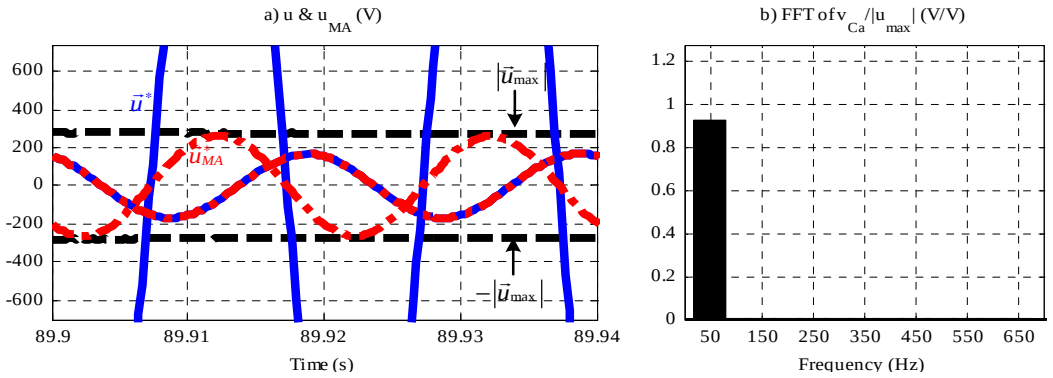

Fig. 7.30: Maximum Area. a) Input reference vector $\vec{u}^*$ and limited vector $\vec{u}^*_{MA}$ and b) FFT of v_{Ca}.

From Fig. 7.31 to Fig. 7.34 oscilloscope captures are presented with the capacitor voltage waveforms and the half of the DC-link voltage. A zoom has been inserted to make easier the appreciation of the voltage waveforms. The above mentioned statements are further verified in these graphs.

Table 7.3 collects the THD of v_{Ca} and the time derivative of u_{DC} during the actuation of each saturator. The results for the THD again make clear the benefit of the proposed techniques. Although the time derivative of u_{DC} makes reference to all injected active power, part of the difference between the results resides in the harmonics. The power wasted in the harmonic injection with the scalar saturation and the CL-method leads to a faster fall of u_{DC} and reduces the operation time in case of autonomous systems.

The efficiency of the power sharing strategy resides on the drifts of the island local frequency. .a and b respectively contain the calculated magnitudes and phases when applying the SRF-saturators with a 0.06 p.u. frequency drift. The error in the magnitude calculation is lower than 0.048 p.u., while the phases are affected by lower error of 0.0076 p.u., as described by (5.28). Fig. 7.36 depicts an oscilloscope capture of the capacitor voltages. Both graphics verifies the correct performance of the SRF-saturators with a reasonable frequency variation.

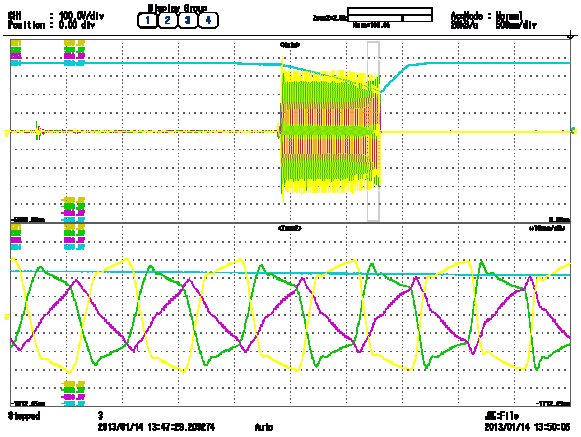

Fig. 7.31: Scalar Saturation.

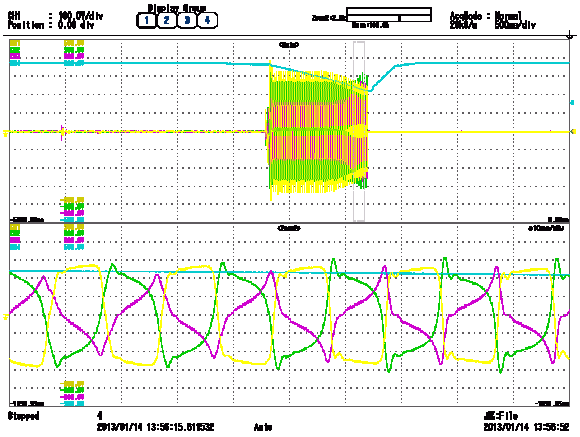

Fig. 7.32: CL-method.

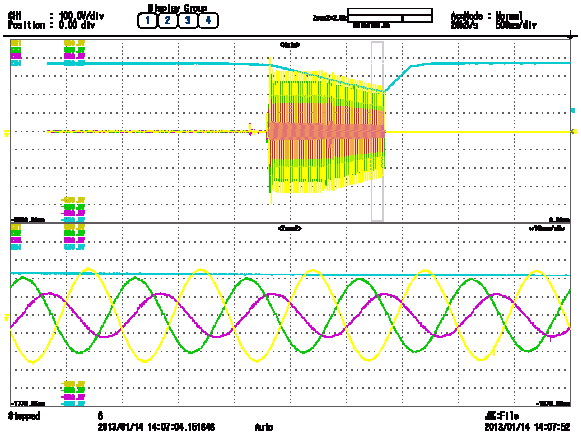

Fig. 7.33: Proportional Saturation.

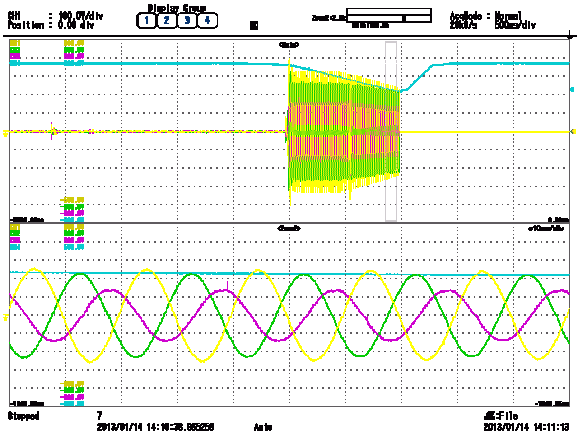

Fig. 7.34: Maximum Area.

Table 7.3: Distortion & Power Consumption in VCVSC

	Scalar Saturation	CL-method	*PS*	*MA*
THD (%)	24.89	33.78	1.81	2.15
du_{DC}/dt (V/s)	-357.26	-366.82	-280.42	-300.91

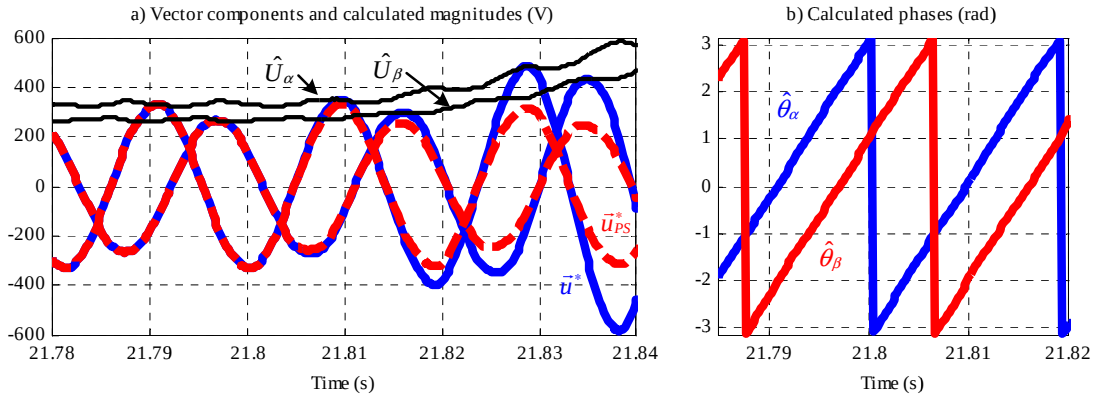

Fig. 7.35: +0.06 p.u. frequency variation: a) Reference and limited reference components with the calculated magnitudes and b) calculated phases.

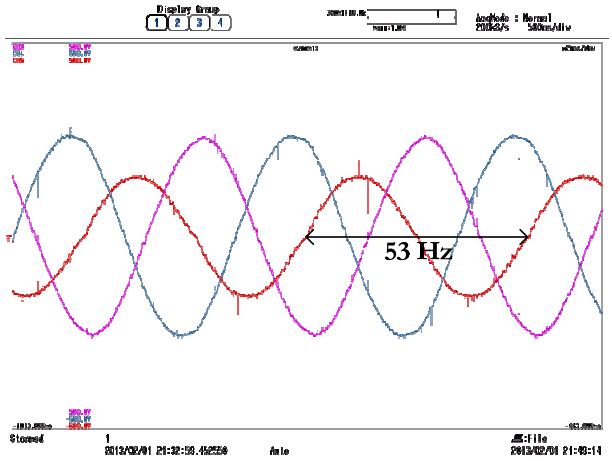

Fig. 7.36: Capacitor voltage waveforms under a limitation with a +0.06 p.u. frequency variation.

7.5.2. I_{SAT} in CCVSC.

The saturation techniques have been also compared in a UWT in grid-connected operation mode with the CCVSC based power control (see Fig. 4.9). In this case, the variable to be limited is the output current. The PCC voltage is unbalanced, the magnitude of phase a remains at 0.4 p.u. with a 5th harmonic component of 10%. The maximum current is fixed to $|\vec{i}_{2\max}|$ =49 A. The experimental test consists on carrying out a reactive power step from 10 kVAr to 50 kVAr, analyzing the performance during the short transient and in steady-state. There is no reactive power controller so the priority is given to the active power reference (which regulates the DC-link voltage). In case of using the reactive power controller, the integral part should be disabled during the saturation in order to give priority to the active current injection to assure the regulation of the DC-link voltage.

Fig. 7.37 presents the performance of the CL-method. Fig. 7.37.a shows the waveforms of the original and limited references. Again, the use of this methodology notoriously worsens the power quality of the injected currents. Fig. 15.c corroborates the addition of the non-zero sequence 3rd harmonic. The waveform of the limited current components is perfectly sinusoidal when employing the PS and MA techniques, as respectively shown in Fig. 7.38 and Fig. 7.39. One could thing that the premise of injecting the vector with the maximum amplitude by means of the MA technique is not fulfilled when comparing Fig. 7.38.b and Fig. 7.39.b. Note that these plots show the magnitude of just one phase, but not the magnitude of the vector.

Fig. 7.40, Fig. 7.42 and Fig. 7.44 contain oscilloscope captures of the output current at the moment the reactive power step takes place for the CL-method, PS and MA, respectively. Fig. 7.41, Fig. 7.43 and Fig. 7.45 depict the AC components of u_{DC}, which is a good indicator of the influence each saturation technique has over the regulation of the oscillating power. The PS saturation technique respects the ratio between positive and negative sequences given by the outer controller. As mentioned, this fact is crucial when performing a good regulation of

the oscillating power. On the contrary, the MA saturation technique does not keep the original level of unbalance of the current reference which logically affects on the regulation of the oscillating power. As shown in Fig. 7.45, the DC-link oscillation at 100 Hz is noticeably higher in this case. Table 7.4 corroborates the above mentioned statements with the THD of the output current and the magnitude of the 100 Hz oscillation for each saturation technique.

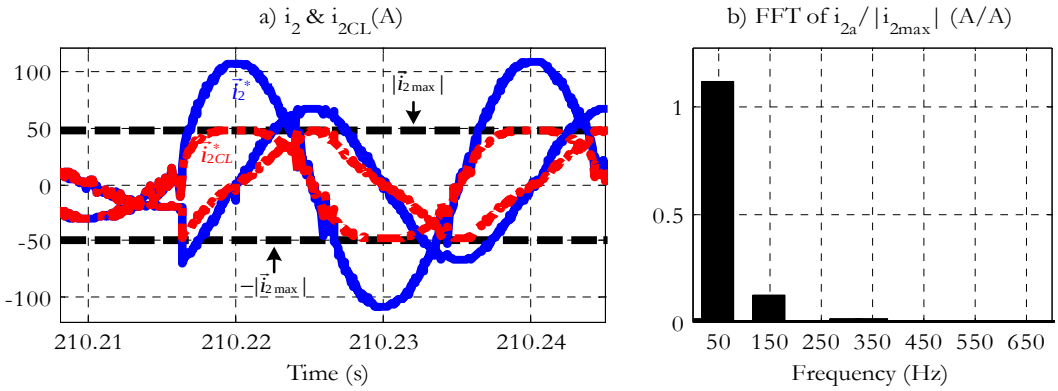

Fig. 7.37: CL-method during a 40 kVAr step for the CCVSC a) Reference and limited reference components and b) FFT of i_{2a}.

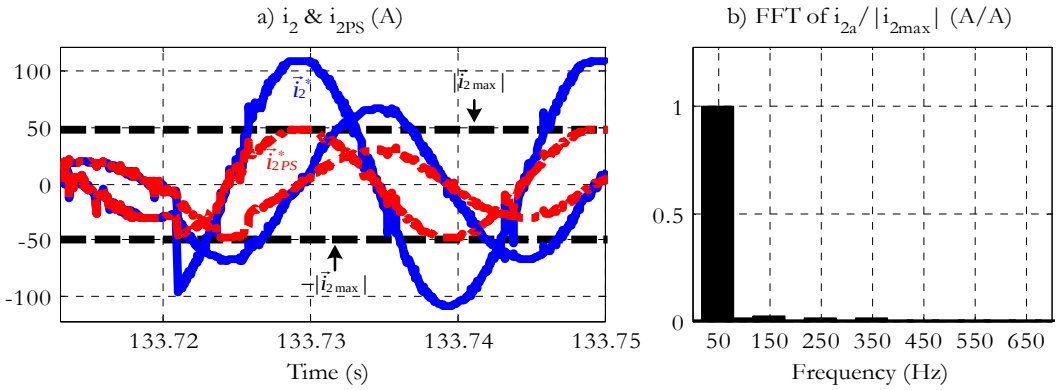

Fig. 7.38: Proportional Saturation during a 40 kVAr step for the CCVSC a) Reference and limited reference components and b) FFT of i_{2a}.

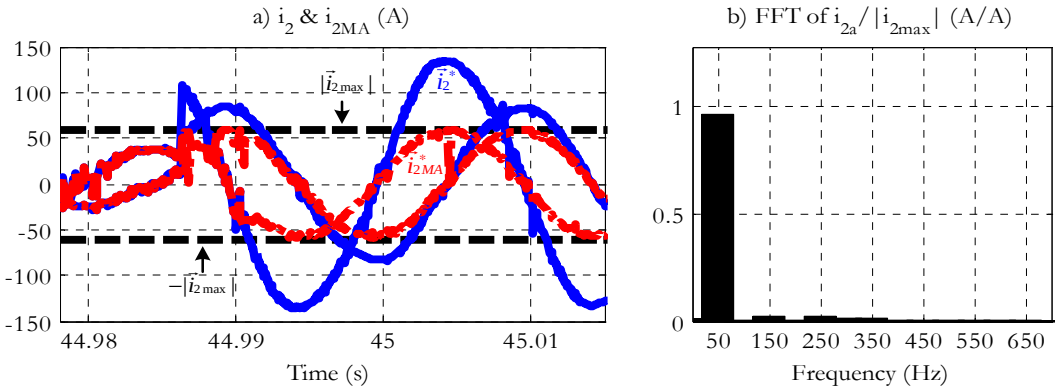

Fig. 7.39: Maximum Area during a 40 kVAr step for the CCVSC a) Reference and limited reference components and b) FFT of i_{2a}.

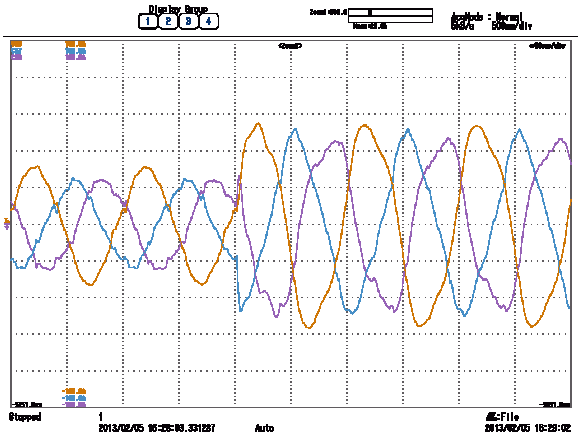

Fig. 7.40: CL-method: output current.

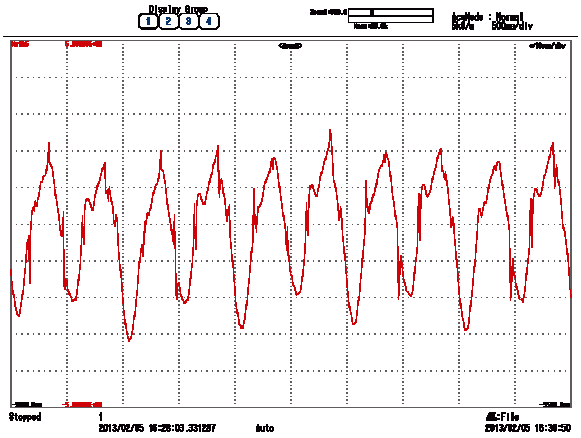

Fig. 7.41: CL-method: DC-link voltage AC component.

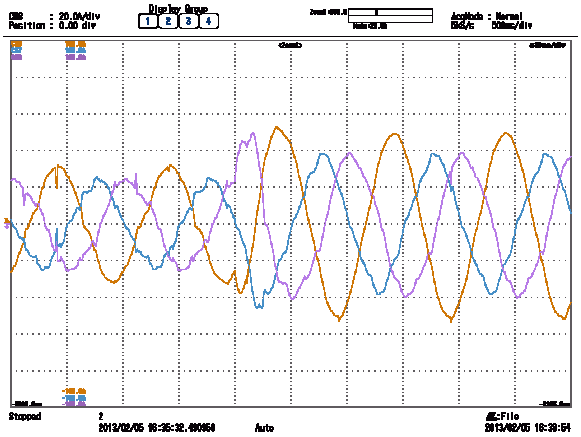

Fig. 7.42: Proportional Saturation: output current.

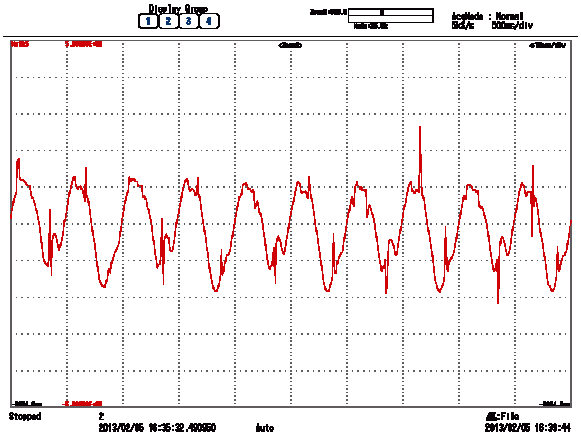

Fig. 7.43: Proportional Saturation: DC-link voltage AC component.

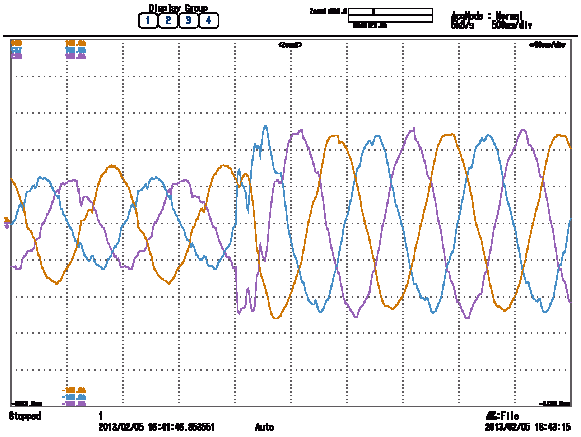

Fig. 7.44: Maximum Area: output current.

Fig. 7.45: Maximum Area: DC-link voltage AC component.

Table 7.4: Distortion & DC-link Oscillation in CCVSC

	CL-method	*PS*	*MA*
THD (%)	11.71	3.55	4.73
u_{DC} at 100 Hz (V)	1.93	0.92	5.55

7.6. Power supply reliability enhancement.

This section analyzes the performance of the proposed active power sharing and includes a statistical study of the scope of the Universal Operation regarding the power supply reliability. The fair behavior of the synchronization with the virtual impedance also fits very well in this subsection, but it has been individually analyzed in 7.3.

7.6.1. Active power sharing.

In this part, the performance of the active power sharing strategy presented in subsection 4.1.5 is tested. The setup of section 7.3 based on two UWTs is again used. The circuit breaker disconnects the island section when the LVRT operation has finished or an islanding condition is detected. Table 7.1 collects all the main parameters of each UWT, respectively. The resistive load demand is kept constant to 125 kW. A grid voltage dip appears at 1s and lasts 7.5 s. Both UWTs should first assist the grid during the LVRT operation. As the voltage magnitude remains at 0.2 p.u., the grid codes allow the breaker to be opened 0.5s after the fault appearance.

The simulation results of this section can be divided into two different case studies. In the first one, the power sharing optimization is not implemented in neither of the UWTs. Fig. 7.46.a shows the temporal evolution of the active powers of the UWTs. Fig. 7.46.b depicts the DC-link voltages and Fig. 7.46.c contains the rotor speeds. Initially, the system is connected with the grid and both UWTs are governed by the MPPT. UWT_1 injects 22 kW while UWT_2 generates 73 kW (v_{w1} = 9 m/s and v_{w2} = 11 m/s). When the voltage dip is detected, the UWTs start the LVRT operation supplying the corresponding reactive current. After that, the local breaker is opened and both UWTs instantaneously readapt the injected power to exactly fulfill the load requirements. They share it in accordance with their corresponding power ratings (P_{G1} = 47 kW and P_{G2} =78 kW). Note that the DC-link voltages are higher during the island operation to deal with high reactive loads. The power factor does not have to be close to one. The kinetic energy in UWT_1 is employed to compensate the high negative power mismatch ($P_{WT1} < P_{G1}$). As a consequence, the rotors speeds decelerate. UWT_1 reaches its shutting down condition ($\omega_{R1} < \omega_{RSD}$) at 4.85s. Since this instant, the torque reaches its maximum feasible value, $T_{E1} = T_{E1\max}$, and the MS converter does not have enough power capacity to keep u_{DC1}. Therefore, UWT_1 is firstly tripped off and then, UWT_2 cannot deal with the entire load so the voltage level of the PCC remarkably decreases. Despite there is a considerable remaining energy, UWT_2 is shut down and the power supply is interrupted. However, the duration of the supply interruption has been reduced through the Universal Operation of the WTs.

In the second case study, the Universal Operation is complemented with the proposed power sharing strategy. That way, the total negative mismatch of the island is fairly shared. The temporal waveforms have been displayed in Fig. 7.47. The system behaves as in the

previous case till the end of the LVRT operation. Then, the droop slopes are continuously readapted following a load sharing as function of the energy reserves. As UWT_2 contains great energy reserves during the entire island operation, the contribution of UWT_1 is reduced. The average value of P_{G1} is approximately 30.6 kW in contrast with 47 kW of the first case study. Then, the power mismatch UWT_1 has to deal with is lower and the power supply is assured during the entire grid interruption. When the grid fault is cleared at 8.5s, the island is resynchronized with the grid voltage. After the reclosing of the circuit breaker, both UWTs work again in grid-connected mode. In this case, the island operation of the UWTs has guaranteed the continuous power supply of the local loads. The proposed power balance strategy is more efficient as long as the number of parallel sources increase.

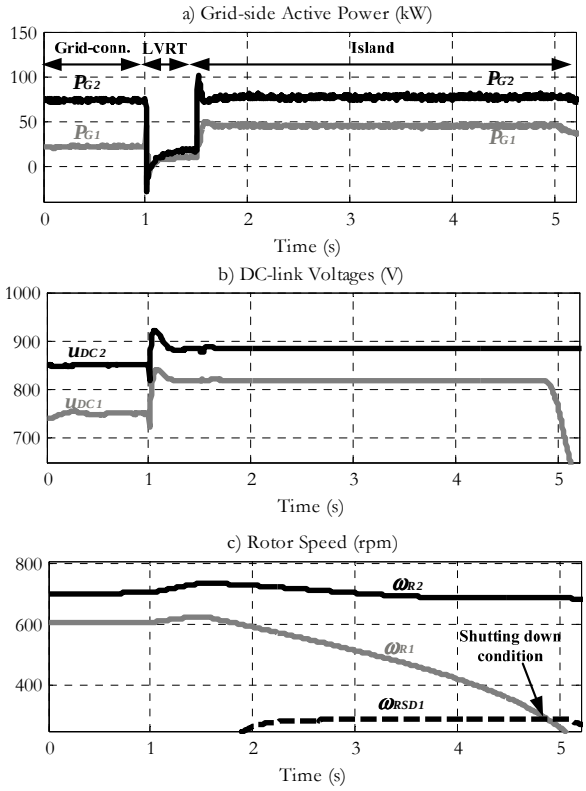

Fig. 7.46: Universal operation of 2 WTs without power balance optimization: a) Instantaneous active powers, b) DC-link voltages and c) Rotor speeds.

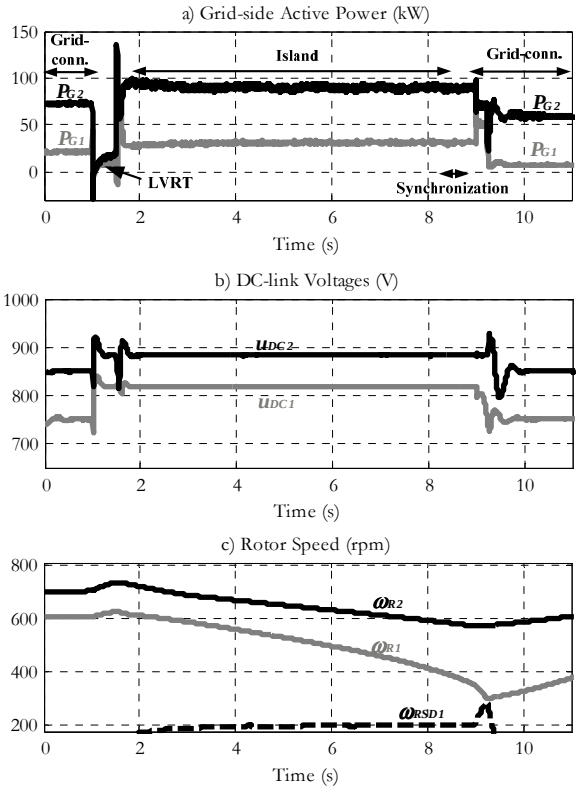

Fig. 7.47: Universal operation of 2 WTs with power balance optimization: a) Instantaneous active powers, b) DC-link voltages and c) Rotor speeds.

7.7. Conclusions and contributions.

This subsection reports the main conclusions and results of the proposed control algorithm. First of all, it is important to remark that all the control algorithms have been designed and implemented in the discrete-time domain looking to a future industrial implementation which implies dealing with the associated difficulties and limitations

It has been experimentally verified that the configuration of the power and voltage controllers satisfy the imposed design requirements. The power dynamics shown in the

experimental results have a high level of matching with the theoretical configured. This evidences the high accuracy obtained in the model. The comparison between the VCVSC and CCVSC power controllers shows in general similar results. Regarding the power coupling, the CCVSC solution presents worst results. During the reconnection transient, the VCVSC solution tends to inject more power while the transient in the CCVSC absorbs energy from the grid. However, the power overshoot are quite reduced and they do not suppose any problem. A relevant contribution of this work is the adaptation of the conventional droop control for an optimized management of unbalanced conditions during the grid connected operation. Two modifications have been proposed in this line. The first one is the addition of the OPC block. The results have been shown a good performance of this controller in the regulation of the oscillating power and the correct tuning assures the decoupling with the DC power regulation carried out by the droop block. The second modification changes the single-phase nature of the conventional droop in order to perform a correct representation of the control variables and avoid the distortion of the voltage reference. The simulation results have evidenced that the OPC block and the dual-phase behavior enhance the performance of the droop in the grid-connected mode. Distortion problems are avoided and the oscillating power is removed. As a consequence, the performance of the proposed VCVSC solution is quite similar to the CCVSC one under an unbalanced voltage dip.

This chapter also validates the theoretical statements of Chapter 3: PV-fitting and robustness in grid-connected and load change response in island mode. This reinforces the architecture 3 as the most suitable voltage control structure of the five candidates for the Universal Operation.

The simulation results have shown that the proposed synchronization strategy based on the virtual impedance implementation enhances the accuracy of the voltage regulation and thus, improves the reconnection transients and increases the power supply reliability.

The experimental results have proven that the SRF saturators provide a distortion-free saturation under unbalanced condition in contrast with the Scalar Saturation and the CL-method. The PS technique has shown a good performance in (VCVSC and CCVSC) grid-connected systems due to it does not affect the oscillating power while the MS can optimize the operation of VCVSC systems in island operation.

In this work, the power sharing has been used to add an extra regulation level of the power flow in the island operation, quite restricted a priori by the load consumption. The proposed algorithm based on the slope and base point modifications results in a fair regulation where the total power mismatch is fairly shared between all the parallel units and weighted by the particular kinetic energy of each UWT. To obtain such features, the slope adaptation has required the definition of the zone + and zone – in the droop control curve. With this power sharing strategy, the simulation results have proven the increment of the island operation time and thus, the enhancement of the continuous supply.

Chapter 8.

Conclusions and Future Work

8.1. Conclusions.

This section collects the conclusions of the dissertation.

This Thesis introduces the concept of Universal Operation of WTs. The work presented in this dissertation proposes the modification of the control of grid-connected WTs to cover all the technical challenges demanded by the Universal Operation. This way, the power supply reliability of critic loads under power interruptions in the range of minutes is improved.

As a general remark, it should be highlighted that all the proposed control algorithms have been designed and implemented in the discrete-time domain looking to a future industrial implementation dealing with the associated difficulties and limitations. A deep mathematical and theoretical development, which models every loop under analysis, precedes the configuration of the controller and serves to understand the necessities of the system.

The voltage controller, core of the GS control, has been deeply analyzed from the point of view of the Universal Operation important features: grid-connected and island performance. It has been shown that the architecture 3 (PR as outer controller and P as inner controller regulating the converter current) presents a good regular performance in all the analyzed features. It has enough bandwidth, attenuates the power resonance at the fundamental frequency and provides good robustness in grid connected. Besides, in island mode, the voltage response is less sensitive to load changes when using the converter current and thus, architecture 3. All these statements reveal that architecture 3 is the most appropriate one of all the studied ones for the Universal Operation.

Initially, the VCVSC and CCVSC power control solutions have been evaluated for the Universal Operation. However, the VCVSC solution based on the conventional droop control has needed a deep revision and modification in grid-connected to provide the same performance as the CCVSC. With the help of the DPM model, the droop control has been configured with a power response close to 100 ms, a high bandwidth in contrast with existing works. The OPC has revealed a good behavior in the regulation of the oscillating power not interfering on the steady state DC power. The application of the concept of representation of control variables gives the clue for removing the distortion. In such conditions, the droop + OPC are compared with the PQ-theory based power control. The comparative analysis has indicated that the PQ-theory based provides slightly smoother transient during the disconnection but presents worst decoupling among active and reactive power. This last issue can make the controller reach the actuation limit more frequently, and thus, the transient dynamics are affected by the saturation of the actuation. Regarding the LVRT operation with unbalanced dips, both power schemes presents identical results.

The power sharing has been used to add an extra regulation level of the power flow in the island operation. The proposed algorithm based on the slope and base point modifications results in a fair regulation where the total power mismatch is fairly shared between all the parallel units and weighted by the particular kinetic energy of each UWT. With this power sharing strategy, the simulation results have proven the increment of the island operation time and thus, the enhancement of the continuous supply.

Section 4.4 contributes with an accurate assessment of the improvement the Universal Operation adds to the power supply reliability. The study takes into account many statistical variables to provide accurate data: wind speed, local load and duration of the interruption. Two measurement ratios have been taken as reference. The SIER indicates the probability of covering the whole interruption. In case of shutting down the complete array of UWTs, the reduction of the average duration of the interruption is also calculated. The Universal Operation can supply a load demanding almost the considered UWT´s rated power during a 10 min grid blackout with a probability of 22.17 %. This probably is increased up to 55 % when the interruption lasts 10 s and the load demands 0.27 p.u. In case of not covering the interruption, the duration of the interruption is reduced up to 60 %. The results are even better as long as the aggregated power rating of the system increases. Given the low investment and presented results, the Universal Operation becomes a cost-effective strategy quite interesting for the grid operators.

The last part of Chapter 5 introduces revolutionary distortion-free saturator structure. It has been experimentally shown that the exiting saturation methods distort the control references under unbalanced conditions, among other undesired effects. The proposed SRF-saturators follow the concept of representation of control variables for avoiding the mentioned distortion. Besides, two strategies have been proposed for calculating the limited ac references. Voltage and current saturators have been studied in different control architectures:

VCVSC and CCVSC. The PS has shown a better performance in grid-connected applications (CCVSC and VSVSC) due to it preserves the relationship between positive and negative sequences, conserving the control capacity over the DC and oscillating powers. The experimental results indicate that MA technique is more suitable in island applications (VCVSC) where the negative sequence control does not makes much sense a priori, and it is really interesting to take advance of the maximum system capacity during the limitation.

Finally, Chapter 6 presents a very realistic proposal for the implementation of the voltage synchronization technique of isolated systems composed by several DG units. The need of communication links have been addressed when the physical location does not allow trivial solutions. Besides, this chapter contains a very interesting study that relates the island voltage, the power contribution and the output equivalent impedance of each system when no outer power control is considered. A virtual impedance approach for modifying the UWT equivalent output impedance has been proposed with the aim of improving the synchronization accuracy and the power sharing. The simulation results have revealed that the synchronization technique based on the virtual impedance supposes a great advance in the Universal Operation and can be extrapolated to microgrid frame.

8.2. Future Work.

This work has contributed with novel ideas and concepts which open new research lines and still needs some extra efforts to be completed.

- Experimental validation.

The experimental verification of the power sharing strategy and the synchronization strategy are missing in this report. However, it is quite important to validate the enhancement on the power reliability supply in contrast with other existing techniques and to prove the feasibility of the slope variation based on zones and the virtual impedance concept. In the particular case of the synchronization, it would be quite interesting to emulate a complex system with a communication link with a non-negligible delay.

- Droop control vs. virtual impedance.

The relation between the power distribution of the voltage sources and the output impedance suggests that the power can be controlled by a virtual impedance strategy not only during the synchronization but also during the whole island operation. As a future work, it would be interesting to implement such linear island power control method and compare its performance with the droop control. Besides, the effect of the droop control over the equivalent output impedance would help in a comparative analysis.

- Suppression of the low-pass filter of the droop control.

The performance shown by the proposed OPC completes the droop control in the power regulation during grid-connected. Since the oscillating frequency at 100 Hz is mainly removed, it is interesting to further test the droop control + OPC performance even without the low pass filter. If the OPC is able to remove the oscillating power in such conditions, the right representation of the control variables is then assured and the low pass filter can be removed. It would lead to new way of configuring the droop control.

- Addition of harmonic virtual impedance.

The virtual impedance at higher frequencies can be tuned to perform a regulation of the harmonic components of the voltage in island operation and of the output current in grid-connected mode. The conventional droop method is not really suitable to perform a power sharing of the harmonic demands of non-linear loads. The control units should balance the active and reactive power flows but at the same time deal with harmonic currents. Therefore, the virtual impedance can be configured with the purpose of sharing the harmonic current.

- Optimization of the island operation.

When a particular UWT is running out of kinetic energy, the local switch of the unit can be opened so that the power contribution of such unit is momentary zero but the system is not shut down. The UWT can operate with no load during a certain time with a big positive power mismatch. Once a certain kinetic energy is again restored, the system is locally resynchronized with the isolated microgrid and can participate again in the load supply. The application of this idea is focused on long blackouts. The future work would assess the feasibility of this proposal and the possible associated drawbacks of connecting and reconnecting the UWT so many times.

- Revision of anti-islanding algorithms.

The use of an anti-islanding algorithm is on charge of detecting any islanding condition. Unintentional islanding conditions lead to safety, commercial and power quality problems and the use an anti-islanding algorithm is mandatory. This algorithm has not been treated in this dissertation due to there are already many techniques published on the bibliography and it is not very trendy. However, it is interesting to make a complitaion of the most representative anti-islanding strategies and study which one is the most suitable for the Universal Operation.

APPENDIX

Machine-side: Sensorless vector control.

Recently, the expansion of PMSG into the variable speed WT market has become remarkable due to its operating power range, high efficiency and the torque-current ratio provided. This seems to be the tendency adopted by big WT manufacturers. The vector control scheme provides decoupled control of the torque and flux. To that purpose, the PMSG drive needs a position feedback for controlling both speed and torque. This section briefly describes the classic vector control for a PMSG and the sensorless algorithm that avoids the use of encoders.

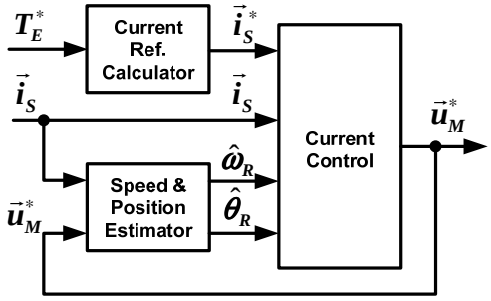

Fig. A.1 : Basic scheme of the sensorless vector control.

A.1. PMSG basic expressions.

The electrical behavior of the PMSG is given by the stator voltage expression. It is introduced in *dq*-frames in (A.1) making use of an amplitude invariant transformation.

$$\begin{aligned} u_{dS} &= r_s i_{dS} + \frac{d\lambda_{dS}}{dt} - \omega_R \lambda_{qS} \qquad \lambda_{dS} = L_d i_{dS} + \lambda_{PM} \\ u_{qS} &= r_s i_{qS} + \frac{d\lambda_{qS}}{dt} + \omega_R \lambda_{dS} \qquad \lambda_{qS} = L_q i_{qS} \end{aligned} \tag{A.1}$$

The electromagnetic torque developed by the PMSG can be expressed as:

$$T_E = \frac{3}{2} p \left(\left(L_d - L_q \right) i_{dS} + \lambda_{PM} \right) i_{qS} \tag{A.2}$$

As the employed generator contains the magnets in the interior the rotor, the *d*-axis and *q*-axis magnetic circuit differs ($L_q > L_d$). This is denominated reluctance. Finally, the mechanical motion equation of every rotating machine relations the mechanical and electromagnetic torques with the rotor acceleration and its inertia.

$$\frac{J}{p}\frac{d\omega_R}{dt} = T_E - T_M \tag{A.3}$$

A.2. Current reference calculator.

This block works out the current references by means of the torque reference (provided by the speed controller in grid-connected mode or by the DC-link controller during island and synchronization modes). There are several ways to implement this block. In this work, the aim is to maximize the torque per current ratio taking advance of the reluctance torque, so that the current range of the converter is optimized. The *q*-axis current can be expressed as:

$$i_{qS} = \sqrt{\left|\vec{i}_S\right|^2 - {i_{dS}}^2} \tag{A.4}$$

Substituting the last expression into the square of the torque equation:

$${T_E}^2 = \left(\frac{3}{2}p\right)^2 \left(\lambda_{PM} + \left(L_d - L_q\right) i_{dS}\right)^2 \left(\left|\vec{i}_S\right|^2 - {i_{dS}}^2\right) \tag{A.5}$$

The last expression is maximized in function of the stator current. Then, the couples $\left(T_E^*, i_{dS}^*\right)$ and $\left(T_E^*, i_{qS}^*\right)$ that maximize the torque per current ratio are obtained and inserted in look-up tables implementing this block.

$$\frac{d{T_E}^2}{di_{dS}} = 0 \rightarrow \left|\vec{i}_S\right|^2 - 2{i_{dS}}^2 - i_{dS}\frac{\lambda_{PM}}{L_d - L_q} = 0 \tag{A.6}$$

A.3. Current controller.

The current controller is inserted into the loop with the aim of achieve a fast current response with steady state null error. The DC components, i_{dS} and i_{qS}, are controlled with two PI controllers. In order to tune these controllers, the first step is the plant identification. Expression (A.1) can be rewritten as:

$$\begin{aligned} u_{dS} &= r_s i_{dS} + L_d \frac{di_{dS}}{dt} - \omega_R L_q i_{qS} \\ u_{qS} &= r_s i_{qS} + \frac{d\lambda_{qS}}{dt} + \omega_R L_d i_{dS} + \omega_R \lambda_{PM} \end{aligned} \tag{A.7}$$

The structure of the current plant G_C is represented in Fig. A.2.a. There is a cross-coupling between axis and the inference of the permanent magnet flux. By means of the

addition of decoupling terms and a feedforward, the modified plant $G'c$ results in a linear expression without inference between axis and external terms, as shown in Fig. A.2.b.

The discrete-time domain expression of $G'c$ is obtained by means of the ZOH. Fig. A.3 depicts the current controller scheme. The PI's constant are configured so the damping ratio of the closed-loop current response is 0.707 and the settling time is close to 5 ms. It is quite important to design the current controller with a enough bandwidth for decoupling the dynamics with the outer controllers.

A.4. Speed and position estimator.

In many motion applications, it is mandatory to monitor the rotor speed and position. Rotational encoders seriously affect in important features like the cost, maintenance and reliability. The tendency is to substitute them with a rotor speed and position estimator integrated in the control algorithm.

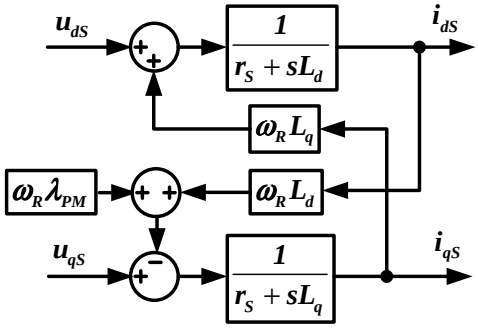

a) $G_C(s)$

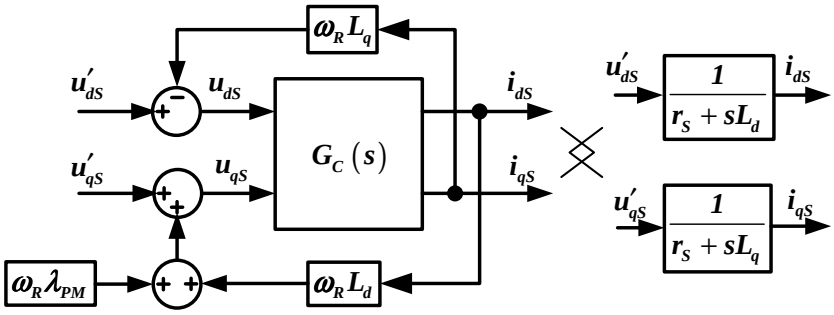

b) $G'_C(s)$

Fig. A.2 : a) Current plant and b) modified current plan by means of the decoupling and feedforward terms.

The speed estimator selected in this Thesis is based on [Boldea, *et al.,* 2005]. This method consists of an open loop stator flux estimator along with a PLL. Fig. A.4 contains the block diagram of the digital implementation proposed in this work. The aim of the estimator is to obtain the active flux in *αβ*-frames $\vec{\lambda}_A$. It is defined as the flux that contributes to develop the electromagnetic torque [Boldea, *et al.,* 2008]:

$$\vec{\lambda}_{dqA} = \lambda_{dA} = \lambda_{PM} + \left(L_d - L_q \right) i_{dS} \tag{A.8}$$

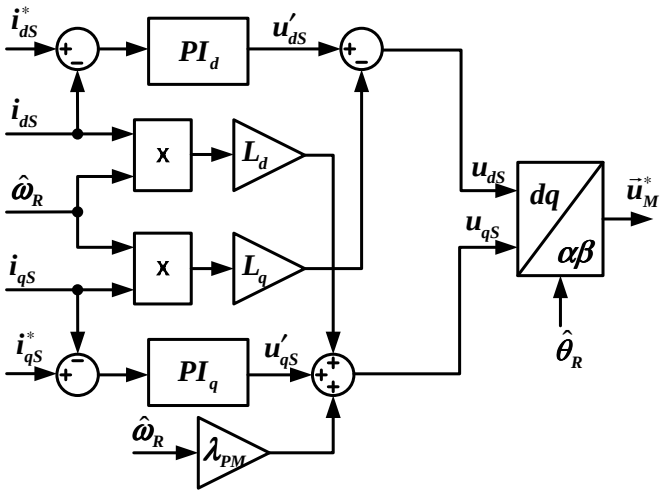

Fig. A.3 . Current controller with feedforward and decoupling terms.

As shown, $\vec{\lambda}_{dqA}$ is fully contained in the *d*-axis, so the angle of $\vec{\lambda}_A$ matches up with the rotor position. The open-loop estimator displayed on Fig. A.4 is based on two models: voltage and current models. Each one calculates an estimation of the stator flux vector, $\hat{\lambda}_V$ and $\hat{\lambda}_I$. At low rotor speeds, the current model is predominant, compensating nonlinear effects on the voltage models, whereas the voltage model becomes prevailing as the rotor speed increases. A smooth transition between both models is done by the PI, which defines the estimator dynamics too. Once $\hat{\lambda}_V$ is estimated, the active flux is worked out by:

$$\vec{\lambda}_A = \hat{\lambda}_V - L_q \vec{i}_S \tag{A.9}$$

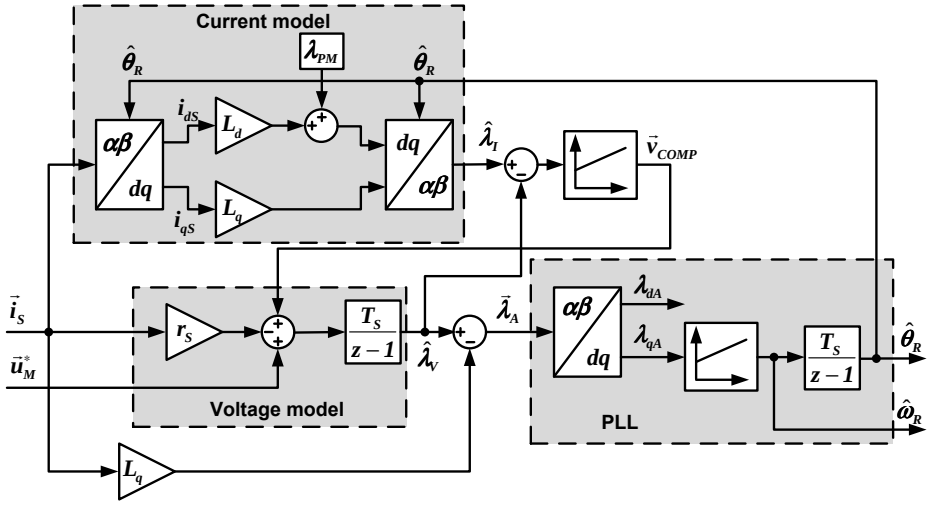

Fig. A.4 : Rotor speed and position estimator based on the calculation of the active flux [Boldea, *et al.,* 2005].

The active flux is supplied to a synchronous reference frame PLL (SRF-PLL) [Blaabjerg, *et al.,* 2006]. The *q*-axis component of the active flux is forced to zero, so that the SRF-PLL is synchronized with *d*-axis component, which indicates the rotor position. The rotor speed is

obtained from the input signal of the integrator working as a voltage-controlled oscillator (VCO).

BIBLIOGRAPHY

[Akagi, *et al.,* 1984] H. Akagi, Y. Kanazawa and A. Nabae, "*Instantaneous reactive power compensators comprising switching devices without energy storage components*", Industry Applications, IEEE Transactions on, vol. IA-20, no. 3, 1984.

[Alfonso, *et al.,* 2000] J. Alfonso, C. Couto and J.S. Martins IEEE, "*Active filters with control based on the p-q theory*", Industrial Electronics Society newsletter, ISSN 0746-1240. 47:3 (Sept. 2000) 5-10.

[Balaguer, *et al.,* 2011] I.J. Balaguer, Qin Lei, Shuitao Yang, U. Supatti and Fang Zheng Peng, *"Control for grid-connected and intentional islanding operations of distributed power generation",* Industrial Electronics, IEEE Transactions on, vol. 58, no. 1, 2011.

[Barklund, *et al.,* 2008] E. Barklund, N. Pogaku, M. Prodanovic, C. Hernandez-Aramburo and T.C. Green, *"Energy management in autonomous microgrid using stability-constrained droop control of inverters",* Power Electronics, IEEE Transactions on, vol. 23, no. 5, 2008.

[Barsali, *et al.,* 2002] S. Barsali, M. Ceraolo, P. Pelacchi and D. Poli, *"Control techniques of dispersed generators to improve the continuity of electricity supply",* Power Engineering Society Winter Meeting, 2002. IEEE, vol. 2, 2002.

[Bhende, *et al.,* 2011] C.N. Bhende, S. Mishra and S.G. Malla, *"Permanent magnet synchronous generator-based standalone wind energy supply system",* Sustainable Energy, IEEE Transactions on, vol. 2, no. 4, 2011.

[Blaabjerg, et al., 2006] F. Blaabjerg, R. Teodorescu, M. Liserre and A.V. Timbus, *"Overview of control and grid synchronization for distributed power generation systems",* Industrial Electronics, IEEE Transactions on, vol. 53, no. 5, 2006.

[Blaabjerg, *et al.,* 2006] F. Blaabjerg, R. Teodorescu, M. Liserre and A.V. Timbus, *"Overview of control and grid synchronization for distributed power generation systems",* Industrial Electronics, IEEE Transactions on, vol. 53, no. 5, 2006.

[Blaabjerg, *et al.,* 2006] F. Blaabjerg, R. Teodorescu, M. Liserre and A.V. Timbus, *"Overview of control and grid synchronization for distributed power generation systems",* Industrial Electronics, IEEE Transactions on, vol. 53, no. 5, 2006.

[Boldea, *et al.,* 2005] I. Boldea and S.A. Nasar, *Electric Drives*, 2 ed. 6000 Broken South Parkway, NW, CRC Press, 2005.

[Boldea, *et al.,* 2008] I. Boldea, M.C. Paicu and G. Andreescu, *"Active flux concept for motion-sensorless unified AC drives",* Power Electronics, IEEE Transactions on, vol. 23, no. 5, 2008.

[Bollen, 2002] M. Bollen, Understanding Power Quality Problems: Voltage Sags and Interruptions. Piscataway, NJ, IEEE Press, 2002.

[Bongiorno, *et al.*, 2008] M. Bongiorno, J. Svensson and A. Sannino, *"Effect of sampling frequency and harmonics on delay-based phase-sequence estimation method",* Power Delivery, IEEE Transactions on, vol. 23, no. 3, 2008.

[Brabandere, 2006] K. De Brabandere, *"Voltage and frequency droop control in low voltage grids by distributed generators with inverter front-end",* PhD thesis, Katholieke Universiteit Leuven, 2006.

[Brabandere, *et al.,* 2007] K. De Brabandere, B. Bolsens, J. Van den Keybus, A. Woyte, J. Driesen and R. Belmans, *"A voltage and frequency droop control method for parallel inverters",* Power Electronics, IEEE Transactions on, vol. 22, no. 4, 2007.

[Bueno, 2005] E. Bueno, "*Optimización del comportamiento de un convertidor de tres niveles NPC conectado a la red eléctrica*", PhD thesis, Universidad de Alcalá, 2005.

[Bueno, *et al.*, 2009] E.J. Bueno, A. Hernandez, F.J. Rodriguez, C. Girón, R. Mateos and S. Cobreces, "*A DSP- and FPGA-based industrial control with high-speed communication interfaces for grid converters applied to distributed power generation systems*", Industrial Electronics, IEEE Transactions on, vol. 56, no. 3, 2009.

[Chen, *et al.,* 2009] H. Chen, T.N. Cong, W. Yang, C. Tan, Y. Li and Y. Ding, *"Progress in electrical energy storage system: A critical review",* Progress in Natural Science, vol. 19, no. 3, 2009.

[Dai, *et al.*, 2008] Min Dai, M.N. Marwali, Jin-Woo Jung and A. Keyhani, "*Power flow control of a single distributed generation unit*", Power Electronics, IEEE Transactions on, vol. 23, no. 1, 2008.

[Eea, 2012] European Environment Agency. Approximated EU GHG inventory: early estimates for 2011. 2012.

[Ene, 2012] European Commission. Energy 2020: A strategy for competitive, sustainable and secure energy. 2012.

[Enjeti, *et al.,* 1993] P.N. Enjeti and S.A. Choudhury, "*A new control strategy to improve the performance of a PWM AC to DC converter under unbalanced operating conditions*", Power Electronics, IEEE Transactions on, vol. 8, no. 4, 1993.

[Estat, 2009] Eurostat Statical books. Panorama of energy. Energy statistics to support EU.

[Fernandez, 2006] J. Fernandez, *"Grid codes for wind energy in Spain and developments in Europe"*. Large Scale Integration of Wind Energy, Brussels, Belgium, November 2006-

[Fuchs, *et al.,* 2008] E.F. Fuchs and M.A.S. Mausoum, "*Power Quality in Power Systems and Electrical Machines"*. London, U.K.: Elsevier, 2008.

[GCSA, 2012] Grid connection Code for Renewable Power Plants Connected to the Electricity Transmission System or the Distribution System in South Africa.

[Gonzalez, *et al.*, 2007] A.G. González, A. González and M. Burgos, "Estimating wind turbines mechanical constants", International Conference on Renewable Energies and Power Quality, ICREPQ 07, Seville, 28-30 March, 2007.

[Gre, 2006] European Commission. Green Paper. A European Strategy for Sustainable, Competitive and Secure Energy. 2006.

[Guerrero, *et al.,* 2004] J.M. Guerrero, L.G. de Vicuna, J. Matas, M. Castilla and J. Miret, *"A wireless controller to enhance dynamic performance of parallel inverters in distributed generation systems",* Power Electronics, IEEE Transactions on, vol. 19, no. 5, 2004.

[Guerrero, *et al.,* 2005] J.M. Guerrero, L. GarciadeVicuna, J. Matas, M. Castilla and J. Miret, *"Output impedance design of parallel-connected UPS inverters with wireless load-sharing control",* Industrial Electronics, IEEE Transactions on, vol. 52, no. 4, 2005.

[Guerrero, *et al.,* 2007] J.M. Guerrero, J. Matas, L.G. de Vicuna, M. Castilla and J. Miret, *"Decentralized control for parallel operation of distributed generation inverters using resistive output impedance",* Industrial Electronics, IEEE Transactions on, vol. 54, no. 2, 2007.

[Guerrero, *et al.,* 2009] J.M. Guerrero, J.C. Vasquez, J. Matas, M. Castilla and L.G. de Vicuna, *"Control strategy for flexible microgrid based on parallel line-interactive UPS systems",* Industrial Electronics, IEEE Transactions on, vol. 56, no. 3, 2009.

[Guerrero, *et al.,* 2011] J.M. Guerrero, J.C. Vasquez, J. Matas, L.G. de Vicuna and M. Castilla, "*Hierarchical control of droop-controlled AC and DC Microgrids—A general approach toward standardization*", Industrial Electronics, IEEE Transactions on, vol. 58, no. 1, 2011.

[Hasanzadeh, *et al.*, 2010] A. Hasanzadeh, O.C. Onar, H. Mokhtari and A. Khaligh, "*A proportional-resonant controller-based wireless control strategy with a reduced number of sensors for parallel-operated UPSs*", IEEE Trans. Power Deliv., vol. 25, no. 1, 2010.

[Haque, *et al.,* 2010] M.E. Haque, M. Negnevitsky and K.M. Muttaqi, *"A novel control strategy for a variable-speed wind turbine with a permanent-magnet synchronous generator",* Industry Applications, IEEE Transactions on, vol. 46, no. 1, 2010.

[Hauck, *et al.,* 2002] M. Hauck and H. Späth, "*Control of three phase inverter feeding an unbalanced load and operating in parallel with other power sources*", Proc. International Power Electronics and Motion Control Conference, 2002.

[He, *et al.,* 2011] J. He and Y.W. Li, "*Analysis, design, and implementation of virtual impedance for power electronics interfaced distributed generation*", Industry Applications, IEEE Transactions on, vol. 47, no. 6, 2011.

[He*, et al.,* 2012] J. He and Y.W. Li, "*Generalized closed-loop control schemes with embedded virtual impedances for voltage source converters with LC or LCL filters*", Power Electronics, IEEE Transactions on, vol. 27, no. 4, 2012.

[He, *et al.*, 2013] J. He, Y.W. Li, J.M. Guerrero, F. Blaabjerg and J.C. Vasquez, *"Microgrid reactive and harmonic power sharing using enhanced virtual impedance",* Applied Power Electronics Conference and Exposition (APEC), 2013 Twenty-Eighth Annual IEEE, 2013.

[Holmes, *et al.*, 2003] D. G. Holmes and T. Lipo, "*PulseWidth Modulation for Power Converters:Principles and Practice*". Piscataway, NJ: IEEE Press, 2003.

[Holtz, 1992] J. Holtz, *"Pulsewidth modulation-a survey",* Industrial Electronics, IEEE Transactions on, vol. 39, no. 5, 1992.

[Hwang, *et al.,* 2007] J.G. Hwang, P.W. Lehn and M. Winkelnkemper, "*Control of grid connected AC-DC converters with minimized DC link capacitance under unbalanced grid voltage condition*", Power Electronics and Applications, 2007 European Conference on, 2007.

[Iea, 2002] International Energy Agency. "*Distributed Generation in a liberalized energy market*". 2002.

[Iea, 2005] International Energy Agency. "*Learning from the Blackouts. Transmission System Security in Competitive Electricity Markets*". 2005.

[Iea, 2011] International Energy Agency. "*International Energy Outlook 2011*". 2011.

[IEEE-1159, 2009] IEEE Standard 1159-2009. "*IEEE Recommended Practice for Monitoring Electric Power Quality*". 2009.

[IEEE-1547.4, 2011] *"IEEE guide for designing and operating distributed resource island systems and their connection to the grid*", IEEE P1547.4, June 2011.

[Kanellos, *et al.,* 2008] F.D. Kanellos and N.D. Hatziargyriou, *"Control of variable speed wind turbines in islanded mode of operation",* Energy Conversion, IEEE Transactions on, vol. 23, no. 2, 2008.

[Katiraei, *et al.*, 2006] F. Katiraei and M.R. Iravani, *"Power management strategies for a microgrid with multiple distributed generation units",* Power Systems, IEEE Transactions on, vol. 21, no. 4, 2006.

[Kim, *et al.,* 2011] Jaehong Kim, J.M. Guerrero, P. Rodriguez, R. Teodorescu and Kwanghee Nam, *"Mode adaptive droop control with virtual output impedances for an inverter-based flexible AC microgrid",* Power Electronics, IEEE Transactions on, vol. 26, no. 3, 2011.

[Kroposki, *et al.,* 2008] B. Kroposki, R. Lasseter, T. Ise, S. Morozumi, S. Papatlianassiou and N. Hatziargyriou, *"Making microgrids work",* Power and Energy Magazine, IEEE, vol. 6, no. 3, 2008.

[Kuo, 1991] B.C. Kuo, "*Automatic Control Systems*", Prentice Hall, Inc., Englewood Cliffs, New Jersey, USA, (1991).

[Kyo, 1998] United Nations. Kyoto Protocol to the United Nations Framework Convention on Climate Change. 1998.

[Lasseter, 2002] R.H. Lasseter, *"Microgrids",* Power Engineering Society Winter Meeting, 2002. IEEE, vol. 1, 2002.

[Li, *et al.*, 2004] Yun Wei Li, D.M. Vilathgamuwa and Poh Chiang Loh, *"Design, analysis, and real-time testing of a controller for multibus microgrid system",* Power Electronics, IEEE Transactions on, vol. 19, no. 5, 2004.

[Li, *et al.,* 2007] Yun Wei Li, Poh Chiang Loh, F. Blaabjerg and D.M. Vilathgamuwa, *"Investigation and improvement of transient response of DVR at medium voltage level",* Industry Applications, IEEE Transactions on, vol. 43, no. 5, 2007.

[Li, 2009] Yun Wei Li, *"Control and resonance damping of voltage-source and current-source converters with filters",* Industrial Electronics, IEEE Transactions on, vol. 56, no. 5, 2009.

[Li, *et al.*, 2009] Yun Wei Li and Ching-Nan Kao, "*An accurate power control strategy for power-electronics-interfaced distributed generation units operating in a low-voltage multibus microgrid*", Power Electronics, IEEE Transactions on, vol. 24, no. 12, 2009.

[Liserre, *et al.*, 2005] M. Liserre, F. Blaabjerg and S. Hansen, *"Design and control of an LCL-filter-based three-phase active rectifier",*Industry Applications, IEEE Transactions on, vol. 41, no. 5, 2005.

[Loh, *et al.,* 2003] P.C. Loh, M.J. Newman, D.N. Zmood and D.G. Holmes, *"A comparative analysis of multiloop voltage regulation strategies for single and three-phase UPS systems",* IEEE Trans. Power Electron., vol. 18, no. 5, 2003.

[Marwali, *et al.,* 2004] M.N. Marwali and A. Keyhani, *"Control of distributed generation systems-part I: Voltages and currents control",* Power Electronics, IEEE Transactions on, vol. 19, no. 6, 2004.

[Mehrizi-Sani, *et al.,* 2010] A. Mehrizi-Sani and R. Iravani, *"Potential-function based control of a microgrid in islanded and grid-connected modes",* Power Systems, IEEE Transactions on, vol. 25, no. 4, 2010.

[Mlodzikowski, *et al.,* 2011] P. Mlodzikowski, A. Milczarek and M. Malinowski, *"Control algorithm of a DC/AC converter applied in a small wind turbine",* Industrial Electronics (ISIE), 2011 IEEE International Symposium on, 2011.

[Mohamed, *et al.*, 2008] Y.A.-.I. Mohamed and E.F. El-Saadany, "*Adaptive decentralized droop controller to preserve power sharing stability of paralleled inverters in distributed generation microgrids*", Power Electronics, IEEE Transactions on, vol. 23, no. 6, 2008.

[Moon, *et al.,* 1999] M.S. Moon and R.W. Johnson, *"DSP control of UPS inverter with over-current limit using droop method",* Power Electronics Specialists Conference, 1999. PESC 99. 30th Annual IEEE, vol. 1, 1999.

[Moran, *et al.,* 1992] L. Moran, P.D. Ziogas and G. Joos, "*Design aspects of synchronous PWM rectifier-inverter systems under unbalanced input voltage conditions*", Industry Applications, IEEE Transactions on, vol. 28, no. 6, 1992.

[Nielsen, *et al.,* 2005] J.G. Nielsen and F. Blaabjerg, *"A detailed comparison of system topologies for dynamic voltage restorers",* Industry Applications, IEEE Transactions on, vol. 41, no. 5, 2005.

[Ortiz, *et al.,* 2008] A. Ortiz, M. Aredes, L.G.B. Rolim, E. Bueno and P. Rodriguez, *"A new current control for the STATCOM based on secondary order generalized integrators",* Power Electronics Specialists Conference, 2008. PESC 2008. IEEE, 2008.

[Ottersten, *et al.,* 2002] R. Ottersten and J. Svensson, "*Vector current controlled voltage source converter-deadbeat control and saturation strategies*", Power Electronics, IEEE Transactions on, vol. 17, no. 2, 2002.

[Parkhideh, *et al.,* 2013] B. Parkhideh and S. Bhattacharya, *"Vector-controlled voltage-source-converter-based transmission under grid disturbances",* Power Electronics, IEEE Transactions on, vol. 28, no. 2, 2013.

[Peng, *et al.*, 2009] F.Z. Peng, Yun Wei Li and L.M. Tolbert, "*Control and protection of power electronics interfaced distributed generation systems in a customer-driven microgrid*", Power & Energy Society General Meeting, 2009. PES '09. IEEE, 2009.

[Per, 2011] Instituto para la Diversificación y Ahorro de la Energia. Ministerio de Industria, Turismo y Comercio. Plan de Energías Renovables 2011-2020. 2011.

[Piagi, *et al.,* 2006] P. Piagi and R.H. Lasseter, *"Autonomous control of microgrids",* Power Engineering Society General Meeting, 2006. IEEE, 2006.

[Plet, *et al.,* 2011] C.A. Plet and T.C. Green, *"A method of voltage limiting and distortion avoidance for islanded inverter-fed networks under fault",* Power Electronics and Applications (EPE 2011), Proceedings of the 2011-14th European Conference on, 2011.

[Rioual, *et al.,* 1996] P. Rioual, H. Pouliquen and J. Louis, "*Regulation of a PWM rectifier in the unbalanced network state using a generalized model*", Power Electronics, IEEE Transactions on, vol. 11, no. 3, 1996.

[Rodriguez, *et al.*, 2006] P. Rodriguez, A. Luna, M. Ciobotaru, R. Teodorescu and F. Blaabjerg, *"Advanced grid synchronization system for power converters under unbalanced and distorted operating conditions",* IEEE Industrial Electronics, IECON 2006 - 32nd Annual Conference on, 2006.

[Rodriguez, *et al.*, 2008] F.J. Rodriguez, E. Bueno, M. Aredes, L.G.B. Rolim, F.A.S. Neves and M.C. Cavalcanti, *"Discrete-time implementation of second order generalized integrators for grid converters",* Industrial Electronics, 2008. IECON 2008. 34th Annual Conference of IEEE, 2008.

[Rodriguez, *et al.*, 2009] F.J. Rodriguez, C. Girón, E.J. Bueno, A. Hernandez, S. Cobreces and P. Martin, "Remote laboratory for experimentation with multilevel power converters", Industrial Electronics, IEEE Transactions on, vol. 56, no. 7, 2009.

[Skogestad, *et al.,* 1998] S. Skogestad and I. Postlethwaite, *Multivariable Feedback Control Analysis and Design*, 2 ed. Chichester etc., John Wiley & Sons, 2005.

[Song, *et al.,* 1999] Hong-Seok Song and Kwanghee Nam, *"Dual current control scheme for PWM converter under unbalanced input voltage conditions",* Industrial Electronics, IEEE Transactions on, vol. 46, no. 5, 1999.

[Suh, *et al.,* 2006] Yongsug Suh and T.A. Lipo, *"Control scheme in hybrid synchronous stationary frame for PWM AC/DC converter under generalized unbalanced operating conditions*", Industry Applications, IEEE Transactions on, vol. 42, no. 3, 2006.

[UNIFLEX-PM, 2006] UNIFLEX-PM and European Commission, "*Converter Applications in Future European Electricity Network".*

[Wessels, *et al.,* 2011] C. Wessels, F. Gebhardt and F.W. Fuchs, *"Fault ride-through of a DFIG wind turbine using a dynamic voltage restorer during symmetrical and asymmetrical grid faults",* Power Electronics, IEEE Transactions on, vol. 26, no. 3, 2011.

[Whi, 1997] European Commission, "*Energy for the future: Renewable Sources of Energy. White Paper for a Community Strategy and Action Plan*", 1997.

[Wijnbergen, *et al.*, 2005] S. Wijnbergen, S.W.H. De Haan and J.G. Slootweg, "*A system for dispersed generator participation in voltage control and primary frequency control of the grid*", Power Electronics Specialists Conference, 2005. PESC '05. IEEE 36th, 2005.

[Yazdani, *et al.,* 2006] A. Yazdani and R. Iravani, *"A unified dynamic model and control for the voltage-sourced converter under unbalanced grid conditions",* Power Delivery, IEEE Transactions on, vol. 21, no. 3, 2006.

[Yuan, *et al.,* 2002] X. Yuan, W. Merk, H. Stemmler and J. Allmeling, *"Stationary-frame generalized integrators for current control of active power filters with zero steady-state error for current harmonics",* Industry Applications, IEEE Transactions on, vol. 38, no. 2, 2002.

[Zamani, *et al.,* 2012] M.A. Zamani, A. Yazdani and T.S. Sidhu, "*A control strategy for enhanced operation of inverter-based microgrids under transient disturbances and network faults*", Power Delivery, IEEE Transactions on, vol. 27, no. 4, 2012.

[Zhang, *et al.,* 2010] Lidong Zhang, L. Harnefors and H.-. Nee, *"Power-synchronization control of grid-connected voltage-source converters",* Power Systems, IEEE Transactions on, vol. 25, no. 2, 2010.

[Zhong, *et al.,* 2011] Q. Zhong, *"Robust droop controller for accurate proportional load sharing among inverters operated in parallel",* Industrial Electronics, IEEE Transactions on, vol. PP, no. 99, 2011.

[Zhou, *et al.,* 2002] Keliang Zhou and Danwei Wang, "*Relationship between space-vector modulation and three-phase carrier-based PWM: A comprehensive analysis [three-phase inverters]*", Industrial Electronics, IEEE Transactions on, vol. 49, no. 1, 2002.